

Diss. ETH No. 27336



Protagonists and spectators  
during photocatalytic solar  
water splitting with  
oxynitride photocatalysts

Craig Lawley



DISS. ETH NO. 27336

**Protagonists and spectators during photocatalytic solar water  
splitting with oxynitride photocatalysts**

A thesis submitted to attain the degree of  
DOCTOR OF SCIENCES of ETH ZÜRICH  
(Dr. sc. ETH Zürich)

presented by

CRAIG RICHARD LAWLEY

MChem, University of Bath

Born on 03.02.1988

Citizen of the United Kingdom

accepted on the recommendation of

Prof. Dr. Thomas Lippert (examiner)

Prof. Dr. Thomas J. Schmidt (co-examiner)

# Table of Contents

Table of Contents .....	2
Abstract.....	5
Zusammenfassung.....	7
Chapter 1: Introduction.....	9
1.1. Motivation.....	9
1.2. Solar water splitting .....	12
1.3. Overpotentials .....	13
1.4. Photoelectrochemical water splitting .....	13
1.5. Requirements for semiconductor photocatalysts .....	14
1.6. Semiconductor photocatalysts .....	15
1.7. Perovskite photocatalysts .....	20
1.8. Oxynitride photocatalysts .....	21
1.9. Oxynitride thin films .....	22
1.10. Scope of this work.....	27
Chapter 2: Electronic structure of $\text{LaTiO}_x\text{N}_y$ photocatalysts and their evolution .....	29
2.1. Preamble .....	29
2.2. Introduction.....	30
2.3. Experimental Strategy.....	31
2.4. LTON thin film morphology .....	33
2.5. LTON thin film PEC characterisations .....	35
Experimental vs theoretical Density of States (DOS).....	43
Electronic structure evolution across the PECR .....	46
Conclusion.....	49
Methods.....	51
Thin Film Deposition.....	51
Angle-Resolved Photoemission Spectroscopy .....	51
Density Functional Theory .....	52
Photoelectrochemical Characterisation.....	52
Composition Analysis.....	53
2.12. Appendix .....	53

.....	53
<b>Chapter 3: Extent and nature of the surface evolution of LaTiO<sub>x</sub>N<sub>y</sub></b> .....	<b>55</b>
3.1. Preamble .....	55
3.2. Introduction.....	56
3.3. Oxynitride thin films .....	57
3.4. Experimental Strategy .....	60
3.5. Photoelectrochemical Characterisations .....	61
3.6. Neutron Reflectometry .....	64
3.7. Grazing incidence X-ray Absorption Spectroscopy .....	66
3.8. Pre-edge features.....	70
3.9. Conclusion .....	74
3.10. Experimental.....	76
3.11. Appendix .....	79
<b>Chapter 4: Oxygen and Nitrogen, the last two puzzle pieces</b> .....	<b>83</b>
4.1. Preamble .....	83
4.2. Introduction.....	84
4.3. Oxygen .....	85
4.4. Nitrogen .....	87
4.5. Titanium .....	93
4.6. Lanthanum .....	96
4.7. Conclusion .....	99
4.8. Appendix .....	100
<b>Chapter 5: Experimental platform for operando GIXAS at the solid-liquid interface</b> .....	<b>105</b>
5.1. Preamble .....	105
5.2. Introduction.....	106
5.3. Photoelectrochemical Water Splitting.....	107
5.4. Oxynitride thin films .....	110
5.5. X-ray Photoelectron Spectroscopy .....	112
5.6. <i>Operando</i> reactor cell.....	116
5.7. Tantalum L <sub>3</sub> Edge XANES .....	119
Strontium K edge XANES.....	121
Modulation Excitation X-ray Absorption Spectroscopy.....	123
<b>Conclusion</b> .....	<b>127</b>
5.12. Experimental.....	129

<b>5.13. Appendix .....</b>	<b>131</b>
<b>Chapter 6: Conclusion and Outlook .....</b>	<b>141</b>
<b>6.1. Conclusion .....</b>	<b>141</b>
<b>6.2. Outlook .....</b>	<b>145</b>
<b>List of Figures .....</b>	<b>147</b>
<b>List of Tables.....</b>	<b>155</b>
<b>Acknowledgements.....</b>	<b>157</b>
<b>Curriculum Vitae .....</b>	<b>162</b>
<b>References .....</b>	<b>164</b>

## Abstract

In order to overcome the difficulties faced with increasing global energy demands, increasing air pollution and climate change, since the majority of pre-existing technology is reliant on finite and polluting fossil fuels. As an alternative, solar water splitting offers a promising approach to address these issues, with the conversion of solar energy into chemical energy (hydrogen as an example), in a sustainable and clean manner. However, with all the research devoted to this field since the first discovery of photocatalytic water splitting using titanium dioxide and UV-light (Fujishima and Honda, 1972), to date, there still does not exist a photocatalyst, capable of efficiently splitting water under visible light irradiation for practical, large scale, low cost applications.

In several oxide materials, the substitution of nitrogen into the oxygen site leads to the formation of the corresponding oxynitride material, which also sees a significant reduction of the band gap, typically shifting the band gap from the ultra violet region towards the visible light energy range. Moreover, the edge positions of the valence band maximum and conduction band minimum for these oxynitrides are ideal for overall water splitting, as they incorporate both the water reduction and oxidation potentials. The reduced band gap and band positions mean that oxynitrides are suitable photocatalysts for solar water splitting and among some of the most promising materials for visible light driven water splitting. Although oxynitrides are considered promising, they suffer from a physicochemical evolution of the surface during initial operations conditions, therefore, limiting their long-term efficiency.

In the first half of this thesis,  $\text{LaTiO}_x\text{N}_y$  oxynitride thin films are employed to study the surface modifications at the solid-liquid interface that occur during photoelectrocatalytic water splitting. Where, soft-X-ray Angle-Resolved Photoemission Spectroscopy (SX-ARPES) is able to elucidate the electronic structure of the LTON oxynitride thin film surface layers and, its associated evolution during the oxygen evolution reaction. *Ex-situ* neutron reflectometry and grazing incidence X-ray absorption spectroscopy (GIXAS) were utilised to distinguish between

the surface and bulk signals, with a surface sensitivity of 3 nm. Here we show, contrary to what is typically assumed, that the A cations are active sites that undergo oxidation at the surface as a consequence of the water splitting process. Whereas, the B cations undergo local disordering with the valence state remaining unchanged. This surface modification reduces the overall water splitting efficiency, but is suppressed when the oxynitride thin films are decorated with a co-catalyst.

In the second half of the thesis, with a custom designed photoelectrochemical cell, we perform *operando* GIXAS on the oxynitride semiconductor SrTaO<sub>x</sub>N<sub>y</sub> during photocatalytic solar water splitting. We show that the nature of the A-site (Sr) and its evolution during operation, have large impacts on the overall stability and catalytic activity of the material, leading to an enriched BO<sub>2</sub> (Ta(OH)/TaO(OH)) like surface. However, this usually beneficial effect with respect to increased surface hydrophilicity has complications for the efficiency of the photocatalytic process, as the OH and O(OH) intermediates formed are in competition between O<sub>2</sub> generation and NO<sub>x</sub> species formation in the initial stages of operation.

To drive the advancement for the discovery of novel materials and the improvement of existing materials, that are able to fulfil all the requirements to allow efficient solar-to-hydrogen conversion, relies on the comprehensive understanding of the photocatalysts electronic structure and, its evolution over the photoelectrochemical (PEC) reaction.



## Zusammenfassung

Die solare Wasserspaltung ist ein vielversprechender alternativer Ansatz um die Schwierigkeiten zu überwinden, die mit dem steigenden globalen Energiebedarf, der zunehmenden Luftverschmutzung und dem Klimawandel verbunden sind. Da der Großteil der bereits vorhandenen Technologien auf limitierte und umweltschädliche fossile Brennstoffe angewiesen ist, kann alternativ die Umwandlung von Sonnenenergie in chemische Energie (z. B. Wasserstoff) durch die Wasserspaltung auf nachhaltige und saubere Weise realisiert werden. Bei aller Forschung auf diesem Gebiet, die es seit der ersten Entdeckung der photokatalytischen Wasserspaltung unter Verwendung von Titandioxid und UV-Licht (Fujishima und Honda, 1972) gibt, wurde noch kein Photokatalysator, mit dem Wasser effizient mit sichtbarem Licht gespalten werden kann, für eine großtechnische und kostengünstige Anwendung gefunden. Um die Entwicklung für die Entdeckung neuartiger Materialien und der Verbesserung bestehender Materialien voranzutreiben, die alle Anforderungen für eine effiziente Umwandlung von Sonnenlicht in Wasserstoff erfüllen können, ist ein umfassendes Verständnis der elektronischen Struktur der Photokatalysatoren und der photoelektrochemischen (PEC) Reaktion notwendig.

In mehreren Oxidmaterialien führt die Substitution von Sauerstoff mit Stickstoff zur Bildung des entsprechenden Oxynitridmaterials, wodurch auch die Bandlücke signifikant verringert wird. Damit wird die Bandlücke oder Absorption vom ultravioletten Bereich in Richtung von sichtbarem Licht verschoben. Darüber hinaus sind die Grenzen des Valenzbandmaximums und des Leitungsbandminimums der Oxynitride ideal für die gesamte Wasserspaltung, da sie sowohl das Wasserreduktions- als auch das Oxidationspotential beinhalten. Aufgrund der verringerten Bandlücke und Bandpositionen sind Oxynitride geeignete Photokatalysatoren für die solare Wasserspaltung und gehören zu den vielversprechendsten Materialien für von sichtbarem Licht angetriebene Wasserspaltung. Obwohl Oxynitride als vielversprechend angesehen werden, gibt es Probleme mit der Veränderung ihrer Oberfläche während der anfänglichen Betriebsbedingungen, wodurch ihre langfristige Effizienz eingeschränkt wird.

In der ersten Hälfte dieser Arbeit werden LaTiOxNy-Oxynitrid-Dünnschichten verwendet, um die Oberflächenmodifikationen an der Fest-Flüssig-Grenzfläche zu untersuchen, die während der photoelektrokatalytischen Wasserspaltung auftreten. Mit SX-ARPES (soft-X-ray Angle-Resolved Photoemission Spectroscopy) kann die elektronische Struktur der LTON-Oxynitrid-Dünnschichtoberflächenschichten und die damit verbundene Veränderung während der Sauerstoffentwicklungsreaktion untersucht werden. Ex-situ-Neutronenreflektometrie und Röntgenabsorptionsspektroskopie mit streifendem Einfall wurden verwendet, um zwischen Oberflächen- und Gesamtprobe mit einer Oberflächenempfindlichkeit von 3 nm zu unterscheiden. Hier zeigen wir, dass entgegen der typischen Annahme, die A-Kationen die aktiven Stellen sind, die infolge des Wasserspaltungsprozesses an der Oberfläche oxidieren. Die B-Kationen unterliegen einer lokalen Störung, wobei der Valenzzustand unverändert bleibt. Diese Oberflächenmodifikation verringert die Gesamteffizienz der Wasserspaltung, wird jedoch unterdrückt, wenn die Oxynitrid-Dünnschichten mit einem Cokatalysator dekoriert werden.

In der zweiten Hälfte der Arbeit führen wir mit einer speziell entwickelten photoelektrochemischen Zelle Röntgenabsorptionsspektroskopiemessungen am Oxynitrid-Halbleiter, SrTaOxNy, während der photokatalytischen solaren Wasserspaltung durch. Wir zeigen, dass die A-Stelle (Sr) und ihre Entwicklung während des Betriebs große Auswirkungen auf die Gesamtstabilität und katalytische Aktivität des Materials haben, was zu einer Anreicherung von BO<sub>2</sub> (Ta (OH) / TaO (OH)) an der Oberfläche führt. Dieser normalerweise vorteilhafte Effekt in Bezug auf eine erhöhte Oberflächenhydrophilie hat jedoch einen negativen Einfluss auf die Effizienz des photokatalytischen Prozesses, da sich aus den gebildeten OH- und O (OH) -Zwischenprodukten zu Beginn der Wasserspaltung NO<sub>x</sub>-Spezies bilden, die mit der O<sub>2</sub>-Erzeugung konkurrieren.

# Chapter 1: Introduction

## 1.1. Motivation

With increasing global population numbers and increasing living standards, as nations become more developed. This has resulted in the annual increase of global energy demands by ca. 1.7% over the last decade<sup>1</sup>. In 2017, the total energy consumption was ca. 17.9 terawatts (TW) and, expected to rise to ca. 22-23 TW by the year 2030-2040.<sup>1,2</sup> In itself, it is not a problem; however, the majority of this demand is sustained using pre-existing technology developed during the industrial revolution in the 19<sup>th</sup> century and by non-renewable fossil fuels (coal, oil, gas, nuclear). Although effective, these fossil fuels are finite, therefore, for long-term sustainability, alternative energy sources are required. To highlight this, Fig. 1.1a includes the estimated total reserves (TW) for coal (900), oil (240), gas (215) and nuclear (90-300).

These technologies are also polluting,<sup>3</sup> evidenced by the rise in CO<sub>2</sub> levels in the atmosphere<sup>4</sup>, mitigating to climate change.<sup>5</sup> The increases in inner city air pollution and its adverse effects on public health.<sup>6</sup> Bearing these factors in mind, the need for finding alternatives that are able to supply the global energy demands in a clean and a more sustainable way is crucial for long-term sustainability.

Long-term sustainability requires the independence from the reliance on fossil and nuclear fuels. Fig 1.1 summarises the alternative and sustainable technologies for the production of green energy, chemicals and their potentials. Examples of which include in no particular order: hydro, wind, tidal, biomass and geothermal (annual potential given in TW). The potentials though are relatively small individually, compared to global energy demand (17-23 TW per year). Therefore, these would all be required in parallel, in combination with fossil fuels to bridge the gaps.

We can however, see the huge potential in the utilisation of solar energy. The total potential of 173,000 TW is the continuous rate reaching the surface of the earth (part b). Which is, 10,000 times greater than the world energy consumption in 2018. Signifying, huge untapped potential to not only, meet the rising energy demands, but also provide an alternative to the combustion of fossil fuels entirely. Fig 1.1 highlights various means by which solar energy can be utilised (parts c-g). In part c, solar thermal applications,<sup>7</sup> utilise the solar energy in the form of heat. Reflective panels concentrate the solar energy to heat water or, drive electricity generating water turbines. Parts d-e include silicon and dye-sensitised based solar cells used in the direct conversion of solar energy to electricity (photovoltaic)<sup>8</sup>. Solar cells are currently considered the most promising approach for utilising solar energy<sup>9</sup>. However, these noteworthy technologies are not without their limitations. Due to the intermittent nature of the sun, these direct conversion processes are limited to the hours of daylight available.

As an alternative, solar energy can be stored in the form of chemical energy,<sup>10</sup> where it can be used as required. One promising solar fuel source is the clean energy carrier hydrogen, which can be harvested using solar energy to split water into molecular O<sub>2</sub> and H<sub>2</sub>.<sup>1, 2, 11, 12</sup> (Fig. 1.1g).

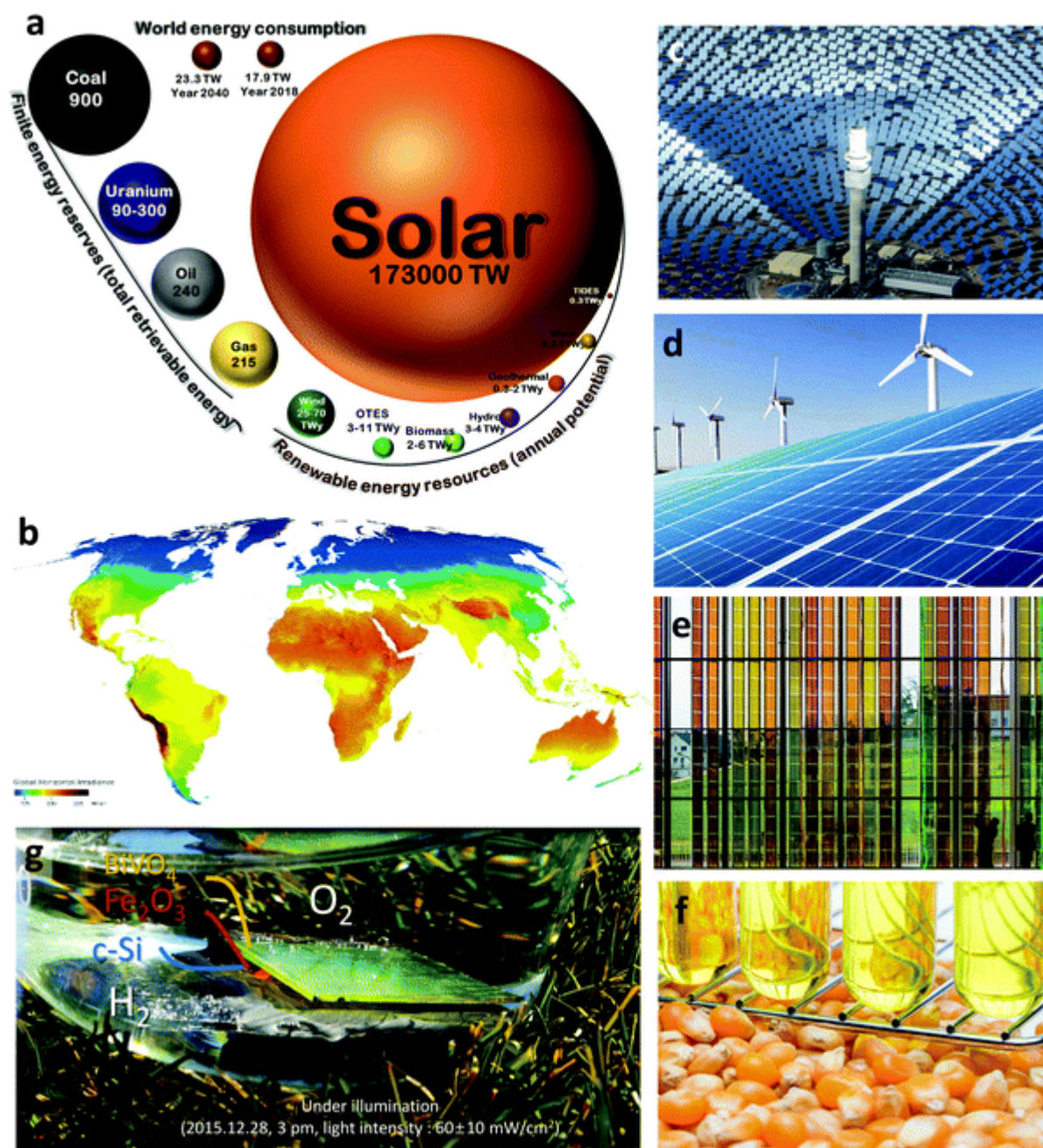
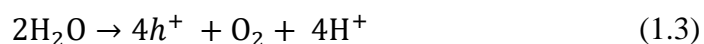


**Fig. 1.1.** (a) comparison of solar energy with other energy sources, (b) worldwide mean solar irradiance variation, (c) solar thermal plant, (d) silicon photovoltaic (PV) panels and wind turbines, (e) Dye-sensitised solar cells (DSSC), (f) biofuel production – bioethanol from corn, (g) photoelectrochemical water splitting for solar hydrogen production. Reproduced from Ref<sup>2</sup>.

## 1.2. Solar water splitting

To dissociate water into molecular  $H_2$  and  $O_2$  is energetically unfavourable, and requires a standard free Gibbs energy change of  $+237 \text{ kJ mol}^{-1}$ , corresponding to 1.23 V per electron.<sup>13</sup> Overall water splitting (Eq.1) can be separated into two half reactions, the hydrogen evolution reaction (HER) and the oxygen evolution reaction (OER), given by Eq. 1.2 and 1.3, respectively.



By applying a voltage (1.23 V) between two-electrode materials, it is possible to overcome the energy requirements to dissociate water molecules in the process known as electrolysis, depicted in Fig. 1.2. Where, the HER and OER proceed on the surface of the cathode and anode, respectively.

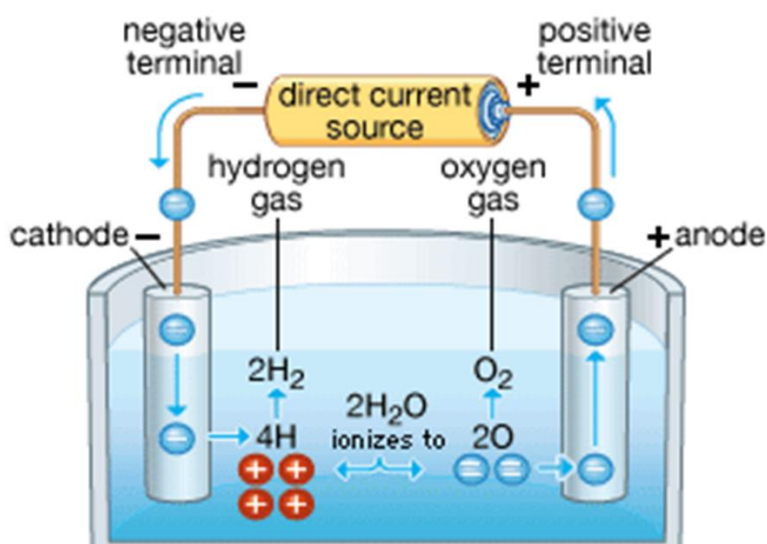


Fig. 1.2. Electrolysis of water. Adapted from Ref<sup>14</sup>

### 1.3. Overpotentials

As previously discussed, the theoretical minimum applied potential for overall water splitting corresponds to 1.23 V. However, an overpotential is usually required greater than 1.23 V. This is due to thermodynamic losses, which reduce the cells voltage efficiency. Therefore, in reality, cell voltages of 1.8 V - 2.4 V in some cases can be required to efficiently dissociate water into molecular O<sub>2</sub> and H<sub>2</sub>.<sup>15</sup> Eq. 1.4 describes the overpotential,  $\eta$ , for a cell. Defined as the difference between the actual cell potential,  $E$ , and the reversible cell potential,  $E_r$ .

$$\eta = E - E_r \quad (1.4)$$

The overpotentials are either positive or negative, depending on the process (oxidation and reduction, respectively). The reactions influence the overpotentials, however, effects such as the resistance of the electrodes and electrolyte as well as, mass transfer limitations all contribute to the overall inefficiencies of the cell (overpotentials).<sup>16</sup>

### 1.4. Photoelectrochemical water splitting

The conversion of solar energy into hydrogen via the water-splitting process assisted by semiconductor (SC) catalysts is a promising route to generate a clean, low cost and renewable energy source. In photoelectrochemical (PEC) water splitting, SC photocatalysts utilise solar light energy to generate electron/hole pairs. After reaching the surface, in contact with water, these charge carriers can be used to dissociate water molecules directly into molecular hydrogen and oxygen<sup>17</sup> according to Eq. 1.2 and 1.3, respectively.

Under light irradiation (photons) with energy greater than or equal to that of the bandgap ( $E_g$ ), the photons are absorbed and electrons are excited from the valance band (VB) to the conduction band (CB) forming electron-hole pairs ( $e^- - h^+$ ) as depicted in Fig. 1.3.

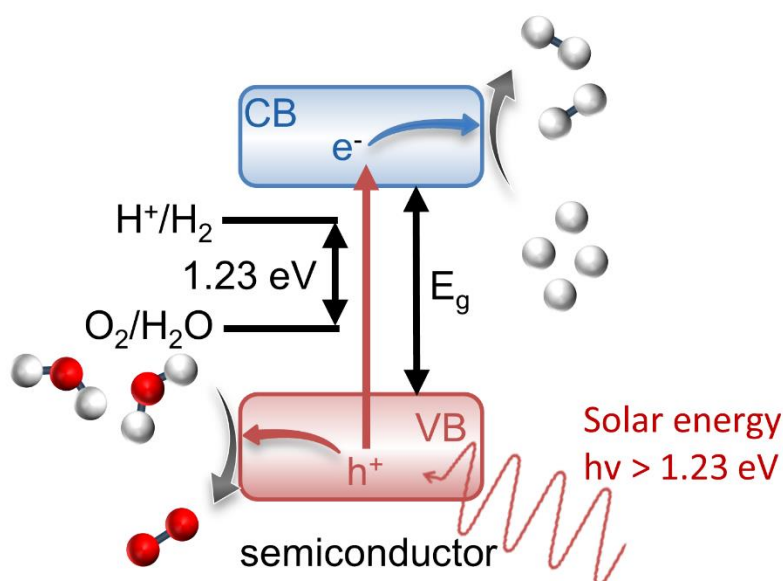


**Fig. 1.3.** Schematic representation of the photoexcitation

### 1.5. Requirements for semiconductor photocatalysts

The OER is complex, as it is a four-step reaction with each step involving the transfer of an electron (Eq. 1.1-1.3). Compared to the HER which requires two electrons, the OER is the kinetically more sluggish of the two half reactions and the bottleneck for overall efficient water splitting.<sup>18</sup>

In reality, there are significant overpotentials (as previously discussed) with respect to the ohmic resistance, the OER and, the overpotentials related to the semiconductor photocatalyst (anode/cathode for HER). Where, the overpotentials are ca. 0.46 eV higher than the theoretical minimum for overall water splitting (1.23 V). Therefore, an ideal semiconductor should have a  $E_g$  which lies in the range of ca. 1.6 – 2.4 eV<sup>19</sup>, which corresponds to a photon wavelength range of ca. 515-775 nm. Where the energy of a photon is given by:

$$E_{\text{photon}} = h\nu = \frac{hc}{\lambda} \quad (1.5)$$



Where  $E$  is the energy,  $h$  represents Planck's constant,  $\nu$  the frequency of light,  $c$  the speed of light and  $\lambda$ , the wavelength. For a photon to be absorbed  $E_{\text{photon}}$  must be equal to or, greater than the  $E_g$  of the SC photocatalyst.

Not only should the bandgap be of sufficient size, the band positions; that is the conduction band minimum (CBM) and the valence band maximum (VBM), should incorporate, both the hydrogen ( $\text{H}^+/\text{H}_2$ ) and oxygen ( $\text{O}_2/\text{H}_2\text{O}$ ) evolution redox potentials, respectively. For water reduction, the CBM must be at a potential lower than 0 V ( $\text{H}^+/\text{H}_2$ ) vs. the normal hydrogen electrode (NHE). Whereas, for water oxidation, the VBM must be at a potential higher than 1.23 V ( $\text{O}_2/\text{H}_2\text{O}$ ) vs. NHE (Fig. 1.3).<sup>20</sup> The SC themselves must also be chemically and structurally stable in the reaction, in this instance, an aqueous environment. Where in strongly basic or acidic aqueous electrolytes, in conjunction with the generated charge carriers which are not consumed in the water splitting reactions, can lead to photocorrosion of the semiconductor surface under operation conditions.<sup>21</sup>

## 1.6. Semiconductor photocatalysts

The discovery of electrochemical splitting of water was first observed in the 19<sup>th</sup> century<sup>22</sup> but it was not until the late 20<sup>th</sup> century (1972) that photochemical splitting of water into hydrogen and oxygen using titanium oxide ( $\text{TiO}_2$ ) irradiated under ultraviolet (UV) light was first observed by Honda and Fujishima.<sup>23</sup> In the past several decades since the now termed Honda-Fujishima effect was first demonstrated, extensive research in this field has been targeted at trying to find suitable and efficient water splitting photocatalysts on which the development of cost-effective and state-of-the-art technology could be based.<sup>24</sup>

Due to their relatively earth abundant, low-cost constituent elements, metal oxides have been investigated thoroughly since this discovery. The position of the VBM depends on the occupancy of the d band of the transition metal, where the VB maximum (VBM) must be higher in potential than the redox potential for oxygen evolution (1.23 V vs. NHE, Fig. 1.3) for the

material to be considered a possible candidate. Examples of  $d^0$  transition metals with an empty d band would include  $Ti^{4+}$ ,  $Zr^{4+}$ ,  $V^{5+}$ ,  $Nb^{5+}$ ,  $Ta^{5+}$  and  $W^{6+}$ . For  $d^{10}$  materials with a filled d band would include  $Ga^{3+}$ ,  $In^{3+}$ ,  $Ge^{4+}$ ,  $Sn^{4+}$ ,  $Sb^{5+}$ . Where the VB in both cases would be comprised of the O 2p states hybridised with the A cation and B cation states. The CB states for the materials with  $d^0$  electronic structure would primarily consist of the empty 3d-5d orbitals of the constituent cations. For those with a  $d^{10}$  electronic structure the d band would be filled (VB) therefore, the CB states would consist of the hybridised orbitals of the empty s and p states. A summary of materials and their respective band positions are summarised in Fig. 1.4.<sup>25</sup> The materials are aligned to the vacuum level, with the redox potentials (vs. NHE pH = 0) for water splitting are shown by the dashed black and red lines at 0 and 1.23 V, respectively. The blue and green columns portray the CB and VB states, respectively. The individual black and red lines represent the self-reduction and self-oxidation potentials, respectively. The materials are stable if the self-reduction potential of the black line is more negative than the  $H^+/H_2$  redox

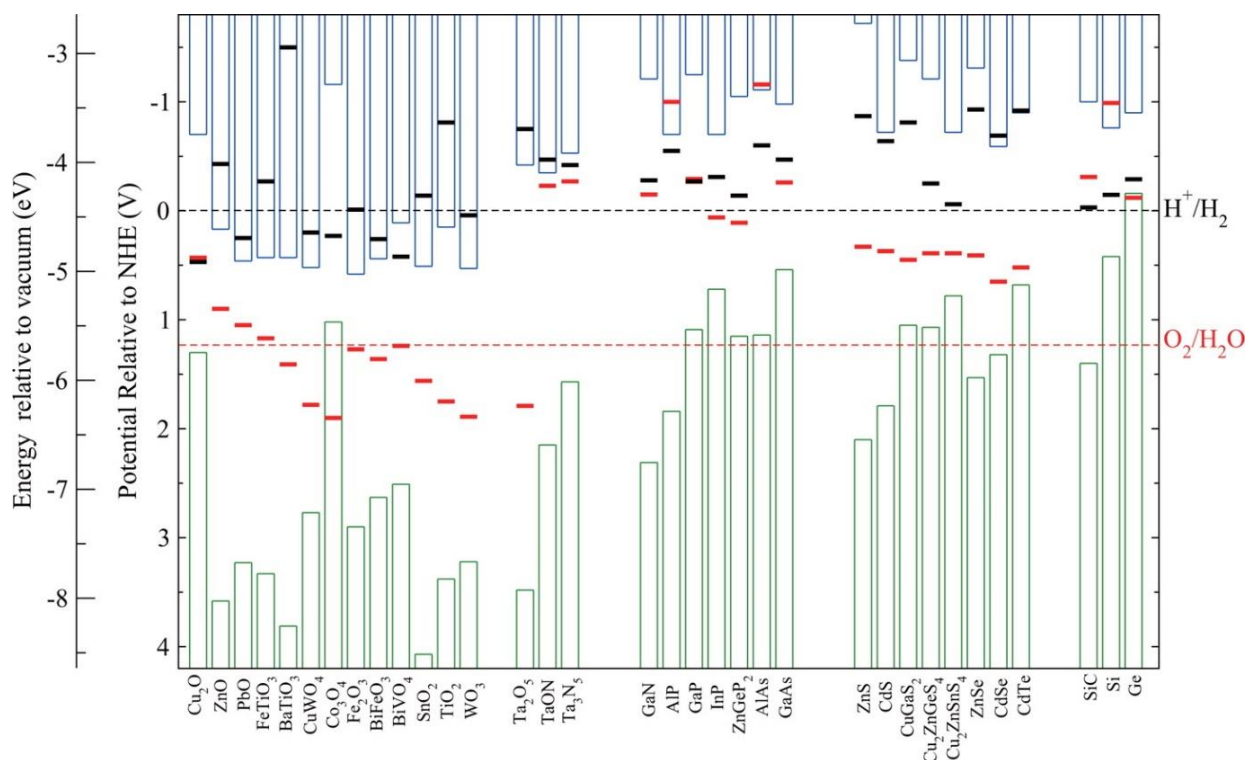


**Fig. 1.4.** The band positions of various semiconductors relative to the NHE and aligned to the vacuum level for a more accurate comparison between materials. pH = 0, 298.15K, 1 bar  
Reproduced from Ref.<sup>25</sup>

potential (0 V vs. NHE) or the CBM. The same is true for the opposite in the case of self-oxidation, the self-oxidation potential (red line) should be more positive than the  $O_2/H_2O$  redox potential (1.23 V) or the VBM. With this information, it is observable that a number of materials in Fig. 1.4 are therefore, unsuitable for water splitting due to the unfavourable alignment of their respective band positions and/or self-reduction/oxidation potentials.

In the hunt for potential photocatalysts, non-oxide SCs have been investigated (Fig. 1.4 Si, CdSe, CdTe and CdS as examples). However, stability is the main drawback for these materials due their susceptibility to photocorrosion.<sup>26</sup> Where for example, it was found that, the  $S^{2-}$  ions are more susceptible to oxidation than water.<sup>27</sup> Several approaches have successfully looked at ways to prevent/suppress the aforementioned degradation in the non-oxide SCs.<sup>26, 28, 29</sup>

We can see on the left-hand side of Fig. 1.4, that the majority of materials suited for the OER are wide band gap oxides. Due to their highly ionic nature, it results in a large separation between the CB and VB states. Therefore, many oxides tend to exhibit large bandgaps ( $E_g > 3$  eV), limiting their photo-response to the UV region of the solar spectrum<sup>17, 30</sup> (Fig. 1.5). The spectral irradiance as a function of wavelength is included in Fig. 1.5b.<sup>31</sup> A number of factors can affect the intensity, such as; the time of day, year (season), cloud coverage, altitude as well as, latitude and longitude (Fig. 1.1b). From part b, we can also observe that not all of the radiation reaches the surface of the Earth. Where, considerable amounts are either absorbed, reflected or scattered in the upper atmosphere. Therefore, UV light only contributes to a small fraction of the total solar spectrum, where ca. 42% consist of visible light and ca. 50%, infrared. The oxide photocatalysts that are active for overall water splitting possess a bandgap energy,  $E_g$ , which is too large to absorb visible light. For example, the bandgap of ZnO is ca. 3.4 eV (Fig. 1.4) which corresponds to a wavelength of ca. 365 nm. Therefore, ZnO and other wide bandgap oxides like it are limited in their photo-response. That said, significant progress has been made during the investigation of many oxide materials for their suitability as photocatalysts, examples include, but not limited to:  $NiO$ <sup>32</sup>,  $ZnO$ <sup>33, 34</sup>;  $Cu_2O$ <sup>35</sup>,  $BiVO_4$ <sup>36, 37, 38, 39</sup>;  $WO_3$ <sup>40, 41, 42</sup> and  $Fe_2O_3$ .<sup>43, 44</sup>

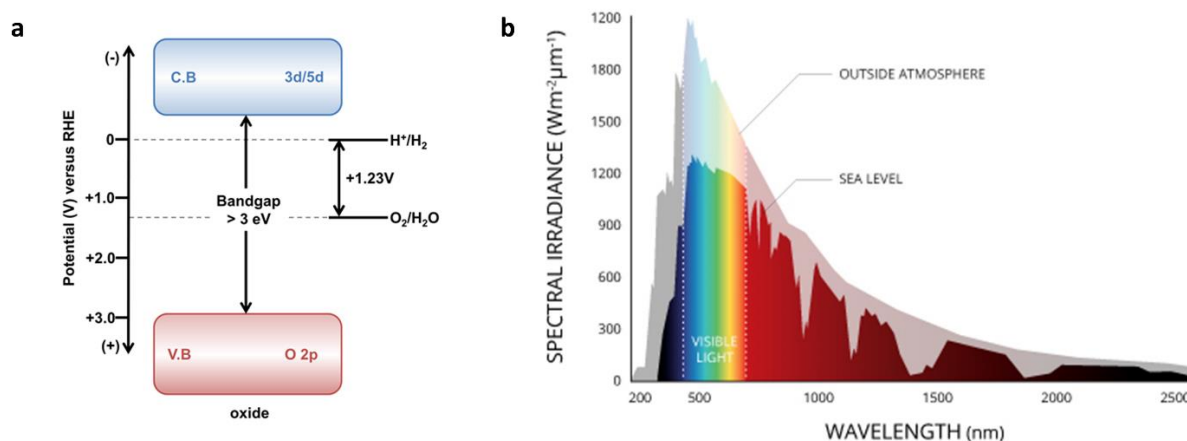


**Fig. 1.5.** (a) wide bandgap oxide semiconductor, (b) spectral irradiance of the sun, reproduced from Ref.<sup>31</sup>

The oxide materials:  $\text{WO}_3$ ,  $\text{BiVO}_4$ , and  $\text{Fe}_2\text{O}_3$  possess slightly smaller bandgaps compared to those of say  $\text{TiO}_2$ ,  $\text{KTaO}_3$ ,  $\text{BaTaO}_3$ ,  $\text{SrTiO}_3$  (Fig. 1.4.). Where the bandgaps for  $\text{WO}_3$ ,  $\text{BiVO}_4$ , and  $\text{Fe}_2\text{O}_3$  are ca. 2.6 eV (475 nm), 2.4 eV (515 nm) and 2.2 eV (560 nm), respectively. These ranges correspond to the visible light range (Fig. 1.5b) therefore, these oxide materials can utilise a greater total percentage of the solar spectrum compared to the wider bandgap oxides. However, looking at Fig. 1.4, these materials cannot reduce protons at the surface to produce hydrogen, even when absorbing visible light. This is due to the fact that, their CBM (blue) and/or the self-reduction potentials (black lines) are more positive than the hydrogen evolution potential ( $\text{H}^+/\text{H}_2$ ). Therefore, since these materials are not able to accomplish overall water splitting (Fig. 1.6a<sup>17</sup>), they are only suitable as photoanodes, to study the OER (one half of the water splitting process).

For the OER the wide bandgap oxides can be employed as photoanodes (part c). To enable water splitting using these oxides as an example, requires an additional semiconductor material connected in series in a Z-scheme, suitable for hydrogen evolution (part b and e). Where two photocatalysts are connected to a redox mediator (Ox/Red), suspended in the electrolyte (part b). The Z-scheme involves twice the number of photons ( $h\nu$ ) required for single excitation water splitting (part a). As previously discussed in section 1.4, in PEC water splitting, the SC photocatalysts utilise solar light energy to generate electron/hole pairs ( $e^-/h^+$ ). The photoexcited

holes accumulate on the surface of the SC and, subsequently consumed in water oxidation (according to Eq. 1.3). Whilst, the photoexcited electrons travel via an external circuit, transferred to a counter electrode (part c) and, subsequently consumed in water reduction (Eq. 1.2). The opposite case is also true when employed as a photocathode (part d).

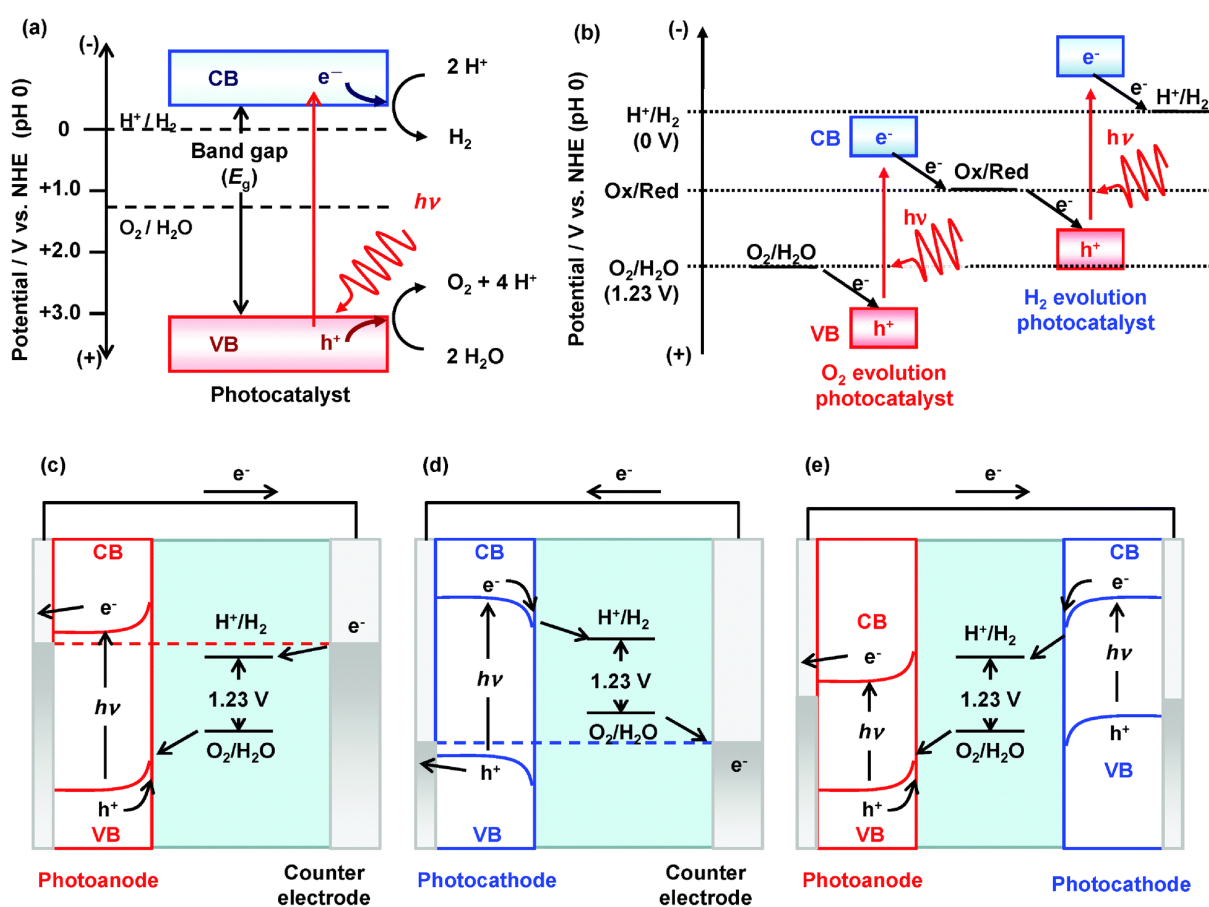


**Fig. 1.6.** Energy diagrams of photocatalytic water splitting based on (a) one-step excitation and (b) two-step excitation (Z-scheme); and PEC water splitting using (c) a photoanode, (d) photocathode, and (e) photoanode and photocathode in tandem configuration. The band gaps are depicted smaller in (b) and (e) to emphasize that semiconductors with a narrow band gap can be employed. Reproduced from Ref<sup>17</sup>

### 1.7. Perovskite photocatalysts

The ideal perovskite structure is cubic and has the general formula,  $ABX_3$ , where the A cation, is typically larger than the B cation and exhibits 12-fold coordination with the oxygen anions (in this case X). The B cation, exhibits 6-fold coordination where the B cation sits at the centre of the  $BO_6$  octahedra<sup>45</sup>, as seen in Fig. 1.7<sup>46</sup> on the top left hand corner sharing site. The perovskite structure can be modified doping at the A and/or B site. However, as the ions possess different sizes and charges, suitable choices must be made to retain the  $ABX_3$  structure. The most typical substitutions are two different but similar ions incorporated into the B site, resulting in the general formula of the perovskite changing to  $AB_{0.5}B'_{0.5}O_3$ . If the charge of the two cations, B and B' are different, the octahedral symmetry can be preserved, however, the system would become disordered resulting in the oxygen anions (blue circles) shifting towards the cations in the centre of the unit cell. Deviations from the ideal cubic structure is also possible, with orthorhombic<sup>47</sup>, tetragonal<sup>48</sup> and monoclinic<sup>49</sup> perovskites known (but not limited to).

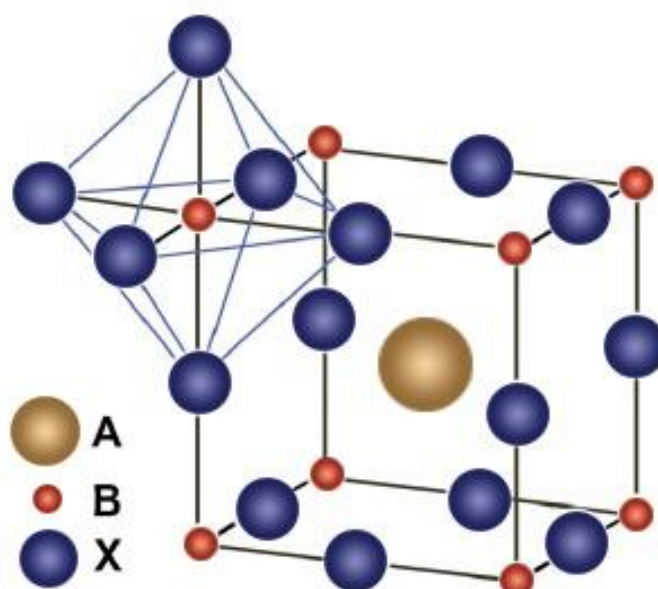


**Fig. 1.7.**  $ABX_3$  perovskite structure. Reproduced from Ref.<sup>46</sup>

Among some of the most effective photocatalysts are perovskite and perovskite-related oxides.<sup>45, 50</sup> Explained by the fact that, they provide compositional and structural flexibility<sup>51</sup>, therefore, provide opportunities to achieve higher catalytic activity<sup>52</sup> and increased sunlight absorption capabilities.<sup>53</sup> In conjunction with, control over the magnitude of the bandgap and band edges with respect the redox potentials for water splitting.<sup>54, 55</sup> Some further examples include  $\text{SrTiO}_3$ <sup>56</sup>,  $\text{La}_{1-x}\text{Sr}_x\text{CoO}_{3-\delta}$ <sup>57</sup> and  $\text{Ba}_{1-x}\text{Sr}_x\text{Co}_{1-y}\text{Fe}_y\text{O}_{3-\delta}$ <sup>57, 58, 59</sup>. Where doping of these materials leads to increased catalytic activity, chapter 5 covers this in more detail.

### 1.8. Oxynitride photocatalysts

Perovskite oxynitrides are a promising class of SC materials for solar light driven water splitting. These materials have the general formula  $\text{ABO}_{3-x}\text{N}_x$ . Examples of known A and B cations include  $\text{La}^{3+}$ ,  $\text{Sr}^{2+}$ ,  $\text{Ba}^{2+}$ ,  $\text{Ca}^{2+}$ , and  $\text{Ti}^{4+}$ ,  $\text{Ta}^{5+}$ , or  $\text{Nb}^{5+}$ , respectively. The substitution of N into the O site of the precursor oxides affects the energy position of the band edges<sup>60, 61</sup>, reducing the band gap down to the visible light energy range (Fig. 1.8). Moreover, in this class of compounds, the photogenerated electrons and holes both possess enough energy to promote the hydrogen and oxygen evolution reaction, respectively.

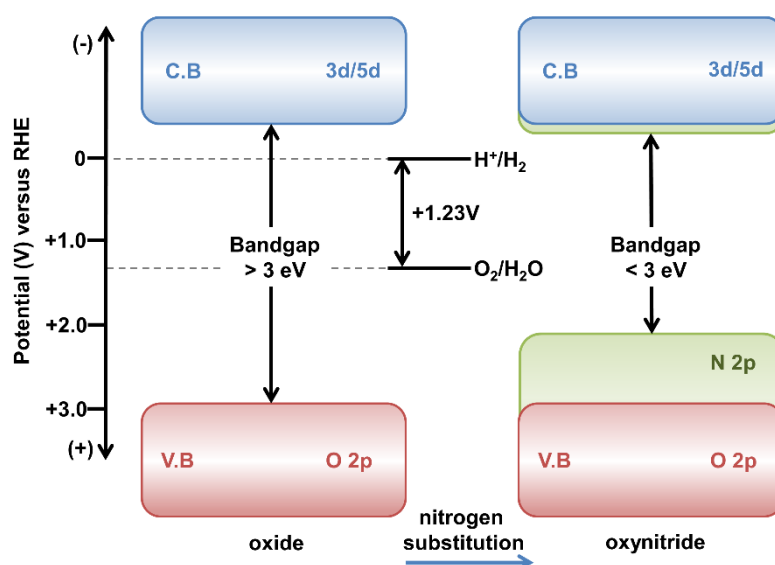


**Fig. 1.8.** Bandgap engineering with nitrogen substitution

One of the most promising and explored oxynitrides is the photocatalyst  $\text{LaTiO}_2\text{N}$  (LTON) with a bandgap of ca. 1.9-2.1 eV.<sup>61, 62</sup> Therefore, responsive in the visible region (Fig. 1.5b) unlike its wide bandgap parent oxide  $\text{La}_2\text{Ti}_2\text{O}_7$ . The assumed oxide,  $\text{LaTiO}_3$  is not stable naturally for reasons explained in chapter 2.

Most studies to date, regard to oxynitrides in the form of powders,<sup>30, 63, 64</sup> since powder development and optimisation is the primary way to device design and engineering. Depending on the nitrogen content and, choice of preparation method, can significantly influence the morphology and light absorption properties of the oxynitride photocatalyst powders.<sup>65</sup> However, specific material properties cannot be probed with powder samples, including studies of the electrode-electrolyte interface where the water splitting reaction take place. The polycrystalline oxynitrides powders do not provide any well-defined surfaces to allow the detailed studies of the solid-liquid interface where the PEC reactions take place. For that reason, thin films are ideal model systems, which allow the investigation of the surface and interface properties.

### 1.9. Oxynitride thin films

To study the physicochemical evolution of the surface of the oxynitride photocatalysts requires the use of oxynitride thin films as model systems. Thin films provide clear advantage over the corresponding powders, owing to the fact; they offer relatively wide, atomically flat, and a well-defined surface, where one can more easily distinguish between the surface and the bulk of the material (Fig. 1.9a).<sup>65, 66</sup> With respect to powders, decreasing the radius size does increase the surface area-to-bulk ratio, however, any measurements would still represent an average of the contributions from the surface and the bulk (Fig. 1.9b). The growth of oxynitride films using pulsed laser deposition (PLD)<sup>67</sup> and pulsed reactive crossed beam laser ablation (PRCLA)<sup>68, 69</sup> permit the growth of oxynitride thin films with different crystalline properties, crystallographic orientation and tuneable nitrogen contents.



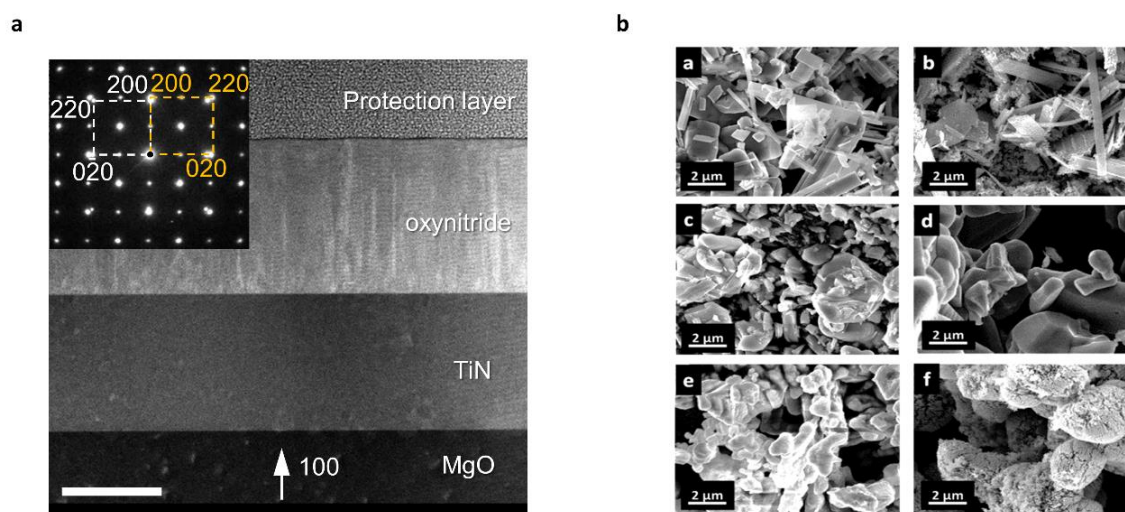


**Fig. 1.9.** (a) TEM cross-section of oxynitride thin film, adapted from Ref<sup>66</sup>, (b) SEM for  $\text{CaNbO}_x\text{N}_y$  oxynitride powders, reproduced from Ref.<sup>65</sup>

Literature pertained to LTON thin films for water splitting remains limited to date.<sup>62, 70, 71, 72, 73</sup> The following references are summarised for their contributions to date; Le Paven-Thivet et al<sup>71</sup> grew LTON films by reactive radio frequency sputtering<sup>74</sup> on Nb-doped,  $\text{Nb}:\text{SrTiO}_3$  single crystal substrates. Which were then subsequently decorated with an  $\text{IrO}_2$  co-catalyst and evaluated as photoelectrodes for water splitting. The authors compared polycrystalline, oriented and epitaxial LTON thin films and concluded that the epitaxially grown sample performed better. With the PEC performance of the films improving in line with the crystalline quality of the films. The authors also noted that the polycrystalline films contained higher nitrogen contents compared to their epitaxial counterparts, yet the epitaxial films showed superior performance. The authors also observed a degradation in their initial performance which they attributed to the surface oxidation of the LTON films and/or the dissolution of the  $\text{IrO}_2$  co-catalyst particles from the surface.

Marozau et al<sup>73</sup> established the foundations for LTON thin films grown by PRCLA onto non-conductive single crystal substrates ( $\text{MgO}$  and  $\text{LaAlO}_3$ ). However, as the template substrates were non-conductive the PEC performance of these LTON thin films were not investigated.

Pulsed reactive crossed beam laser ablation (PRCLA) is a modified version of pulsed laser deposition first described by Willmot<sup>69</sup> and a schematic of the process is given in Fig. 1.10. It is an effective technique to control the chemical activity of the plasma species (depends on choice of AT material) and background molecules (reactive gas) during the PLD process.

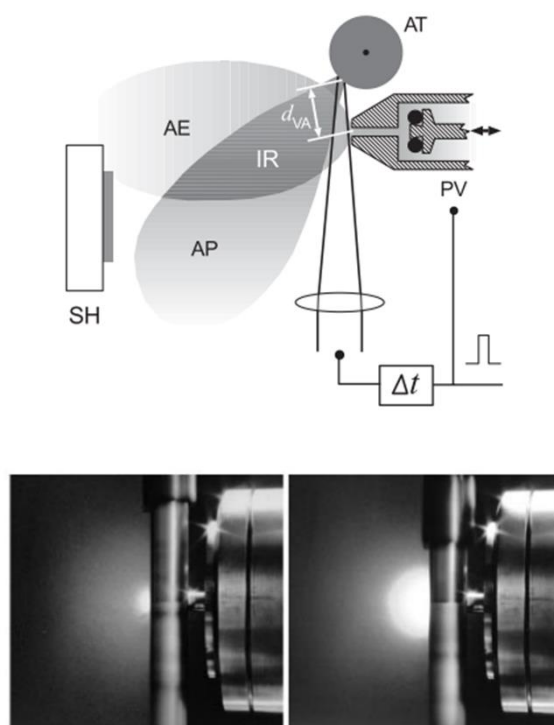


**Fig. 1.10.** Upper panel: schematic diagram of the principal of PRCLA. PV = pulsed valve; AT = ablation target; AE = adiabatic pulsed expansion; AP = ablation plume; IR = interaction region; SH = substrate heater;  $d_{VA}$  = distance from pulsed valve nozzle to point of ablation on target.  $\Delta t$  is the adjustable delay between the pulsed valve trigger and laser trigger. Lower panel: the visual effect of crossing a gas pulse with an ablation plume for a Cu plasma and an  $N_2O$  gas pulse. The left-hand image shows the appearance of the plume propagating into vacuum or when  $\Delta t$  is set so that the plume and gas pulse “miss” each other temporally. The right-hand image shows the increase in plume brightness due to its collisional excitation in passing through the densest part of the gas pulse. If one uses a constant background pressure of 20 Pa instead of a pulsed expansion, the plume also becomes brighter, but it is more localized around the point of ablation because of quenching. Reproduced from Ref.<sup>69</sup>

Rather than using a constant background pressure (gas) as common in conventional PLD, in PRCLA, a gas pulse with a reactive gas ( $\text{NH}_3$  in the case of oxynitrides), synchronized with the laser beam ( $\Delta t$  and  $PV$ ), is injected into vacuum or a low background pressure near the ablated area of the target (AE). Where upon expansion, it interacts with the generated plasma plume (AP). Resulting in increased physicochemical interactions between the gaseous environment and the plasma species.

With respect to the oxynitride thin films, PRCLA allows the growth of films with higher nitrogen contents when injecting synchronised pulses of reactive gas ( $\text{NH}_3$ ), rather than a continuous flow/background environment. This is also true for films grown by traditional PLD under a  $\text{N}_2$  background.

Pichler et al<sup>72</sup> successfully grew LTON model thin film systems incorporating a TiN-buffer layer. They found that the TiN seed layer can not only be used as a current collector for PEC measurements, but it also provides a very good template for the growth of a number of oxynitride films<sup>62</sup> making the deposition process more stable (controllable). Whilst also increasing N content in comparison to oxide substrates. An example of the oxynitride – TiN thin film multilayer structure is included in Fig. 1.9a. This work then led to the growth of a number of oxynitride thin films grown by PRCLA<sup>61, 62, 70</sup>, also setting the groundwork for the thin films used in this work.

Pichler et al<sup>70</sup> continued to explore the PEC performance of LTON thin films and initially investigated the physicochemical evolution of the surface previously reported by Le Paven-Thivet et al. The authors include X-ray photoelectron spectroscopy (XPS) data where they conclude that the detrimental surface evolution is a result of the oxidation of  $\text{Ti}^{3+}$  and nitrogen is partially depleted in the lattice position during operation. The authors also note that crystallographic quality and orientation have large impacts on the PEC performance of the LTON thin films. Showing that the highly orientated films show a 5-fold increase in efficiency compared to their polycrystalline counterparts.

Haydous et al<sup>62</sup> compared  $\text{LaTiO}_x\text{N}_y$ ,  $\text{BaTaO}_x\text{N}_y$  and,  $\text{CaNbO}_x\text{N}_y$  thin films photocatalysts grown by PRCLA with their corresponding powder counterparts. The authors noted that direct comparison of their PEC performances favours the oxynitride powders due to their increased surface area. However, when normalising the differences in surface area, with the aid of Brunauer–Emmett–Teller (BET) analysis. Due to the better crystalline quality and the grain morphologies, the oxynitride thin films can show improved charge carrier separation and the subsequent migration to the surface to be consumed in the OER.

Information regarding the growth of the oxynitride thin films used in this work and their characterisations are included where relevant in chapters 2-5.

### 1.10. Scope of this work

Despite the large contribution to the field of photoelectrochemical water splitting, there still does not exist a photocatalyst, capable of efficiently splitting water under visible light irradiation for practical, large scale, low-cost applications. To drive the advancement for the discovery of novel materials and the improvement of existing materials, that are able to fulfil all the requirements to allow efficient solar-to-hydrogen conversion, relies on the comprehensive understanding of the photocatalysts electronic structure and, its evolution over the photoelectrochemical (PEC) reaction.

Perovskite oxynitrides are a promising class of SC materials for solar light driven water splitting. These materials have the general formula  $ABO_{3-x}N_x$  (where A can be La, Sr, Ba, Ca, etc., and the B site: Ti, Ta, or Nb for example). The substitution of N into the O site of the precursor oxides affects the energy position of the band edges, reducing the band gap down to the visible light energy range. Moreover, in this class of compounds, the photogenerated electrons and holes both possess enough energy to promote the hydrogen and oxygen evolution reaction, respectively.

The work in this thesis aims to gain further insights into the electronic structure and its evolution of two promising oxynitride photocatalysts,  $LaTiO_xN_y$  and  $SrTaO_xN_y$ . With the following research questions pondered:

- What are the changes in the electronic structure and oxidation states of the materials before, during and after PEC water splitting?
- What roles do the A and B cations play during the water splitting process?
- What degree of modification do the local atomic environments undergo?
- What is the role nitrogen plays at the surface, where the reaction occurs?
- Can the surface degradation be inhibited and long-term performance improved?

To answer these research questions:

Chapter 2 elucidates the electronic structure of the LTON oxynitride thin film and, its associated evolution during the oxygen evolution reaction using a combination of soft-X-ray absorption spectroscopy (S-XAS) and soft-X-ray Angle-Resolved Photoemission Spectroscopy (SX-ARPES).

Chapter 3 takes this a step further to compare the surface and bulk evolution of the LTON thin film photocatalysts using a combination of neutron reflectometry and grazing incidence XAS (GIXAS). This chapter also builds the basis for the *operando* experimental platform in chapter 5.

Chapter 4 looks at X-ray Photoelectron Spectroscopy (XPS) data for the surface evolution with respect to the anions of LTON (O and N) the last two missing pieces of the puzzle. Since, information regarding O and N is not directly obtainable by SX-ARPES and not feasible with hard GIXAS, required to probe the A and B cations and for *operando* studies.

Chapter 5 involves the design and fabrication of an *operando* reactor cell for GIXAS measurements on thin films at the solid liquid interface. Providing an experimental platform for future *operando* studies on thin films at the solid-liquid interface. Where we explore the surface evolution of SrTaO<sub>x</sub>N<sub>y</sub> oxynitride thin film using a combination of *ex-situ* XPS and *operando* GIXAS.

## Chapter 2: Electronic structure of $\text{LaTiO}_x\text{N}_y$ photocatalysts and their evolution

### 2.1. Preamble

This chapter uses a combination of soft-X-ray angle-resolved photoemission spectroscopy (ARPES) and X-ray absorption spectroscopy (XAS) to elucidate the electronic structure of the LTON oxynitride thin films. Followed by, its evolution with respect to the OER during PEC water splitting.

The results in this chapter will be submitted for publication by the following authors: Craig Lawley, Arian Arab; Anna Hartl, Aleksandar Staykov; Thorsten Schmitt, Max Döbeli; Daniele Pergolesi, Thomas Lippert; and Vladimir N. Strocov. Entitled: “*Momentum-resolved electronic structure of  $\text{LaTiO}_x\text{N}_y$  photocatalysts by resonant soft-X-ray ARPES*” (Manuscript in preparation).

### Author Contributions

Conceptualisation, C.L., A.A.; D.P., T.L.; and V.S., Investigation, C.L., A.A.; M.D., and V.S.; Formal Analysis, C.L., A.H., V.S., and M.D.; Writing – Original Draft, C.L., A.H., and V.S.; Writing – Review & Editing, C.L., A.A.; A.H., T.S.; D.P., T.L.; M.D., and V.S.; Funding Acquisition, V.S., and T.L.; Supervision, V.S., D.P., and T.L.

## 2.2. Introduction

In several oxide materials, the substitution of nitrogen into the oxygen site leads to the formation of the corresponding oxynitride material.<sup>75</sup> This substitution results in a significant reduction of the band gap, typically shifting the band gap from the ultra-violet region towards the visible light energy range.<sup>61, 76</sup> Moreover, the edge positions of the valence band maximum and conduction band minimum for these oxynitrides are ideal for overall water splitting, as they incorporate both the water reduction and oxidation potentials.<sup>63</sup> With a band gap lying in the visible-light energy range and suitably aligned band positions, the perovskite oxynitride LaTiO<sub>2</sub>N (LTON) is a promising photocatalyst for visible-light solar water splitting.<sup>70, 71, 77</sup>

However, the surface of LTON initially evolves during operation conditions, limiting its long-term performance.<sup>66</sup> The design and discovery of new materials able to sustain an efficient solar water splitting process would represent an enormous breakthrough for the storage of solar energy in the form of a clean and renewable fuel.<sup>1, 78</sup> To drive this advancement for the discovery of novel materials and the improvement of existing materials, that are able to fulfil all the requirements to allow efficient solar-to-hydrogen conversion, relies on the comprehensive understanding of the photocatalysts electronic structure and, its evolution.

The most direct experimental method to probe the electronic structure is angle-resolved photoemission spectroscopy (ARPES), where one measures the distribution of photoelectrons as a function of their kinetic energy  $E_k$  and, emission angle  $\theta$  under irradiation of the sample by monochromatic photons with energy  $h\nu$ .<sup>79</sup> While the electron momentum (k)-integrated electronic structure of oxynitrides has already been studied with X-ray photoelectron spectroscopy,<sup>80, 81, 82</sup> no k-resolved information from ARPES experiments on these materials is available up to now. This can be explained by the fact that, standard ARPES in the VUV energy range has a probing depth of less than 0.5 nm,<sup>83</sup> which makes this technique extremely sensitive to surface contamination,



unavoidably piling up during the *ex-situ* transfer of the as-grown sample to the ARPES experiment, destroying the k-conservation. Where k is the wave vector of the electron and related to the electrons' crystal momentum and the wave velocity – pivotal in understanding the electronic structure of a material.

In this work, we overcome this difficulty by using soft-X-ray ARPES (SX-ARPES) in an energy range of a few hundreds of eV, where the probing depth increases to a few nm, which ensures the k-conservation is less susceptible to surface contamination. Moreover, the SX-ARPES energy range covers the L-edges of the transition metals and M-edges of rare-earth elements, which are characteristic components of oxynitrides (Ti and La in LTON's case, respectively). This will allow us to use resonant photoexcitation at the Ti L and La M edges, to complement the k-resolution of the ARPES experiment, by elemental and even chemical-state resolution.<sup>84, 85, 86</sup> First, we will establish the k- and chemical-state-resolved electronic structure of LTON and, second, follow its evolution associated with photocatalytic reaction.

### 2.3. Experimental Strategy

Fig. 2.1a shows the geometry and schematic representation of a typical ARPES experiment. Here, monochromatic X-rays from a synchrotron source are incident on the oxynitride thin film at an incidence angle typically of 20° (accurate alignment is crucial for angle-resolved measurements) under ultra-high vacuum (UHV) conditions. As a result, electrons emit from the sample surface in all directions in vacuum, according to the photoelectric effect (Eq. 2.1). A hemispherical electron energy analyser with a finite acceptance angle range, measures the kinetic energies of the photoelectrons at given emissions angles, providing also the momentum of the escaped photoelectrons. In this case, the energy conservation yields the binding energy  $E_B$  of these electrons back in the sample as:

$$E_B = E_k - h\nu - e\phi \quad (2.1)$$

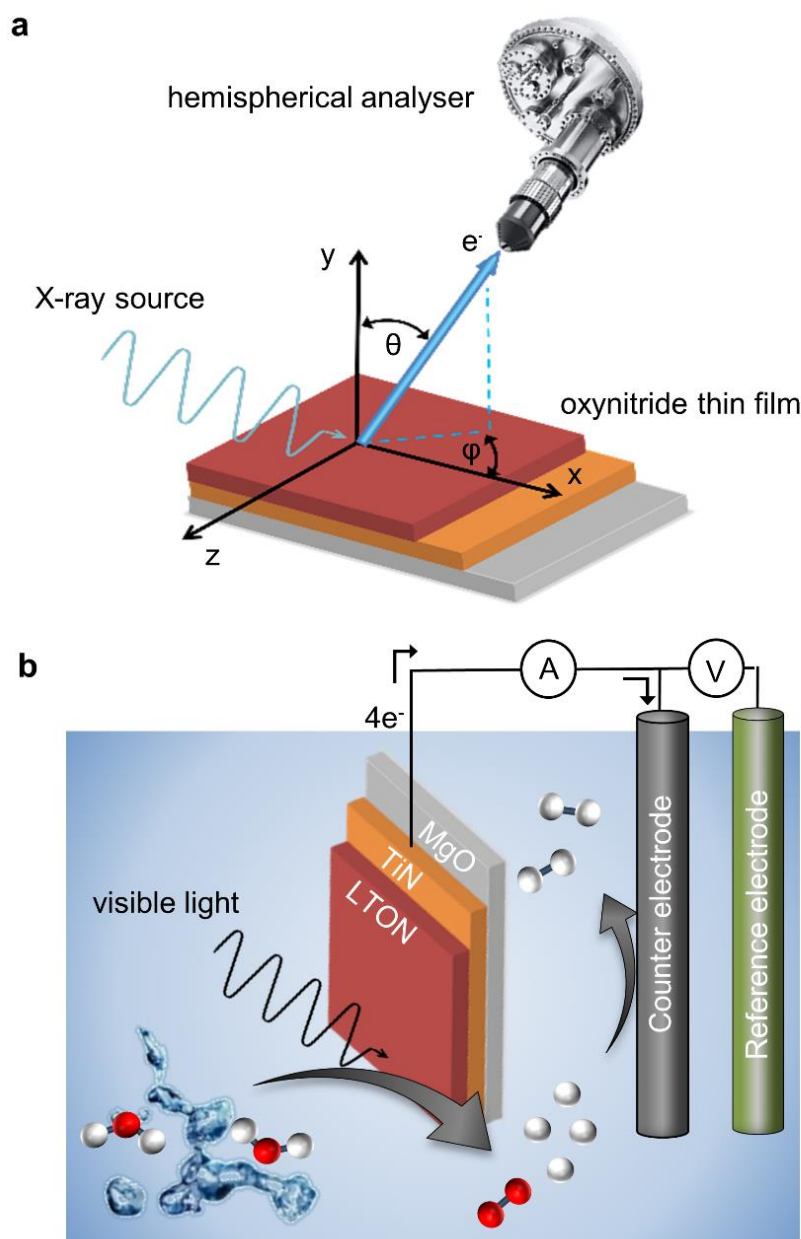


**Fig. 2.1.** (a) Schematic of an ARPES experiment showing the photoemission geometry, (b) 3-electrode configuration for the photoelectrochemical characterisations.

Where  $E_B$ ,  $E_k$ ,  $h\nu$  and  $e\phi$  are the binding energy, kinetic energy, the photon excitation energy and the work function, respectively. Equally important for the photoabsorption process, involving direct transitions, is experimental information on the electron momentum  $k$ , of the valence states.

In the ARPES experiment on crystalline systems, the surface-parallel momentum,  $k_{xy}$  is conserved and can be found as:

$$k_{xy} = 0.5124 \sqrt{E_k \sin \theta} - P_{xy} \quad (2.2)$$

Where  $p_{xy}$  is the perpendicular photon-momentum component,  $m$  is the free-electron mass and  $V_0$  the inner potential in the sample.

In this work, SX-ARPES is utilised to measure a number of LTON oxynitride photocatalyst thin films in their as grown states and after the photoelectrochemical (PEC) characterisations. Where, SX-ARPES is able to elucidate the electronic structure of the LTON oxynitride thin film surface layers and, its associated evolution during the oxygen evolution reaction.

#### 2.4. LTON thin film morphology

The LTON thin films were fabricated using a pulsed laser deposition technique described in previous works,<sup>72</sup> followed by post annealing for 1 hour under a continuous NH<sub>3</sub> flow for 1 hour. The highly ordered oxynitride LTON films were deposited on titanium nitride (TiN) coated magnesium oxide single crystal (001) oriented substrates. Rutherford back scattering (RBS) and Elastic recoil detection analysis (ERDA) determined the chemical compositions of the LTON thin films as La<sub>1.03</sub>Ti<sub>0.97</sub>O<sub>2.70</sub>N<sub>0.29</sub>. The experimental uncertainties for La and Ti are  $\pm 2\%$  (RBS) and  $\pm 7\%$  for O and N (ERDA). The full results have been included in Fig. 2.2. The O:N ratio of ca. 10 is in line with previous examples of highly ordered oxynitride thin films, since there is a trade-off between the overall nitrogen content and crystalline quality,<sup>70</sup> where films with larger N contents tend to be more disordered. From parts a-b, it can be seen that the TiN buffer layer grows (001) epitaxially oriented on the MgO substrate. Where, the (002) reflex of TiN is visible as a shoulder on the side of the peak of the substrate. Part a also

shows that, LTON grows epitaxially on the TiN buffer layer<sup>72</sup> where, the (hkl) reflexes (002) and (004) appear at the  $2\theta$  values  $22.2^\circ$  and  $45.3^\circ$ , respectively. The angular position of the (001) reflexes of the perovskite  $\text{LaTiO}_2\text{N}$  have been marked in blue as reference from the Inorganic Crystal Structure Database (ICSD). Both the (002) and (004) reflexes of the LTON thin film are slightly shifted to lower  $2\theta$  values compared to  $\text{LaTiO}_2\text{N}$ . This is due to the combined effect of a difference in N content to the stoichiometric reference and, the crystalline

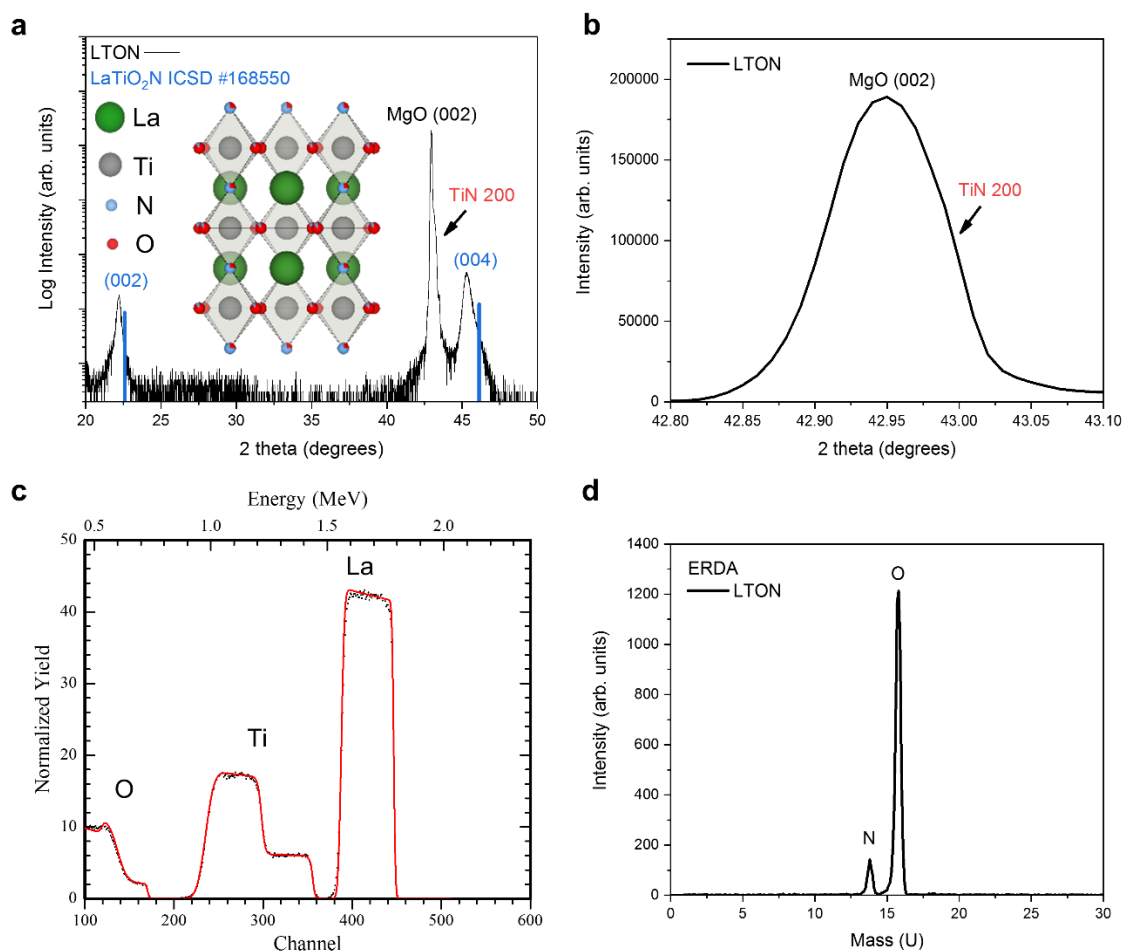


**Fig. 2.2.** (a) XRD pattern of the epitaxially grown LTON film, the  $\theta/2\theta$  scan is shown in black, with the angular position of the (001) reflexes of  $\text{LaTiO}_2\text{N}$  shown in blue for reference. The inset shows the crystal structure of  $\text{LaTiO}_2\text{N}$ , (b) zoomed region around the MgO substrate reflex for data shown in part a, (c) Rutherford backscattering (RBS) spectrum, (d) elastic recoil detection analysis (ERDA) spectrum. The cation ratios were determined by RBS and the O:N ratio by ERDA.

constrain (lattice mismatch between the substrate and film) induced by the TiN-coated MgO substrate. The perovskite structure of LTON remains stable, within a large range of N content. However, the cell parameters can significantly change since, the N content affects the B-O-B dihedral bond angle and ultimately, the overall distortion of the cell.

## 2.5. LTON thin film PEC characterisations

The photocatalytic conversion of solar energy into a clean, low cost, renewable fuel source can be realised by the splitting of water into molecular H<sub>2</sub> and O<sub>2</sub>.<sup>11,12</sup> However, the water splitting reaction is an energetically unfavourable reaction, requiring a standard Gibbs free energy change of + 237.2 kJ mol<sup>-1</sup> (1.23 eV per electron). Therefore, to produce H<sub>2</sub> and O<sub>2</sub> from water requires a light absorbing semiconductor (SC) photocatalyst to assist in the process (Fig. 2.3a). The SC material must possess a band gap larger than the theoretical minimum (1.23 eV), to account for kinetic overpotentials and, the band positions must be sufficiently positioned to account for the redox potentials for the hydrogen evolution and oxygen evolution reactions (HER and OER, respectively).<sup>13</sup>

The oxynitride LTON, satisfies these criteria with a band gap of ca. 2.1 eV.<sup>87</sup> The band gap is sufficiently large enough to absorb photons with energy  $\geq 1.23$  eV but is also responsive to visible light wavelengths (ca. 590 nm) unlike many of the wide-band gap oxide materials, which are responsive only to the UV part of the solar spectrum. Upon light irradiation (photons) with energy greater than or equal to that of the band gap, the photon is absorbed, creating electron-hole pairs. The electrons are then, excited from the valence band (VB) to the conduction band (CB) where, they travel via the TiN electrical contact buffer layer to the Pt counter electrode (Fig. 2.3a). Where the electrons can directly reduce protons to form H<sub>2</sub>. The photogenerated holes left behind in the valence band migrate to the surface of LTON where, they are then consumed in the oxidation of water, generating O<sub>2</sub>. The reference electrode sets the 0 V potential and an increasing voltage bias is applied between the working and counter electrode. The electronic current (photocurrent) between the working and counter electrodes is then

proportional to the amount of H<sub>2</sub> and O<sub>2</sub> produced. The photocurrent is defined as the current response under light conditions after the subtraction of the current response under dark conditions (light on/off). Where LTON is employed as a photoanode (working electrode) to study the OER. A platinum counter electrode is used for the HER half reaction and, a Ag/AgCl reference electrode is used to control the applied potential on the working electrode. Parts b-c, show the photocurrent density vs. applied potential curves for the LTON oxynitride thin films used in this work. Where the photocurrent is normalised to the exposed surface area (cm<sup>-2</sup>). We can see that the surface of LTON initially evolves during operation conditions, limiting its long-term performance, reflected by the reduction in photocurrent density over successive linear sweeps, before the material stabilises.

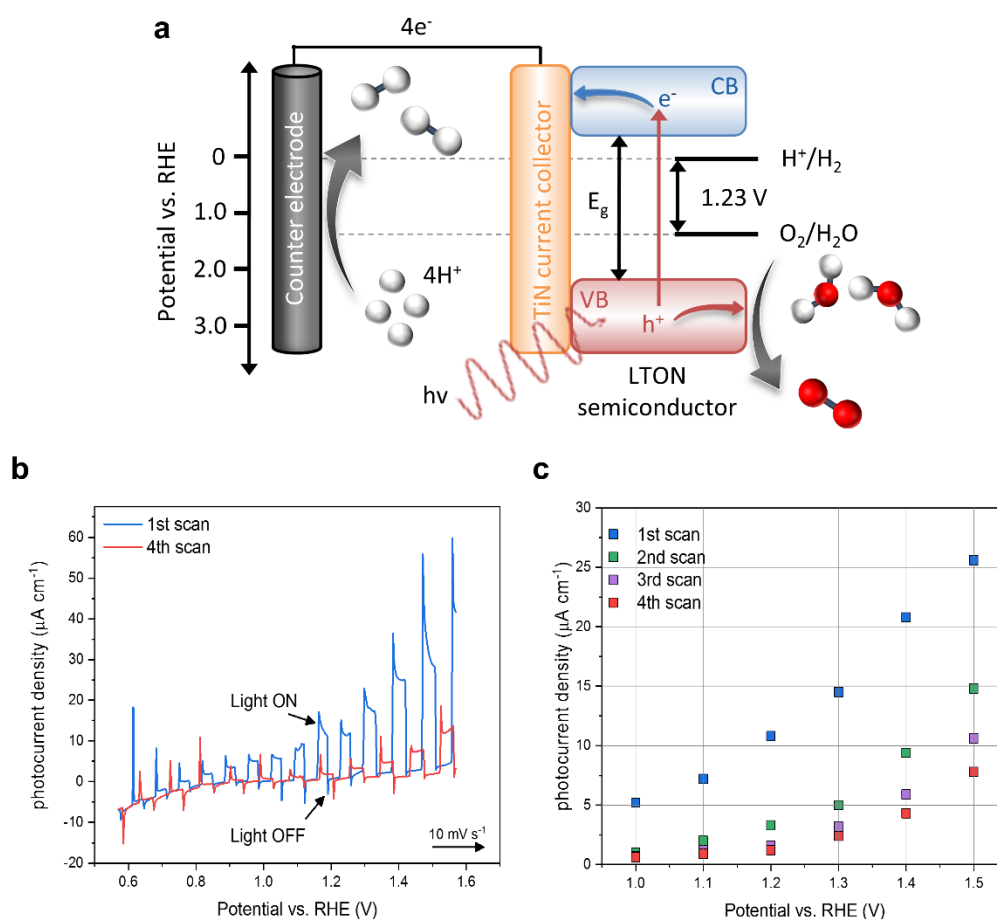


**Fig. 2.3.** (a) Energy diagram for photocatalytic water splitting, (b-c) photocurrent densities for LTON for the first four-potentiodynamic measurements.

## 2.5. SX-ARPES: Ti B cation

First, we will follow the electronic structure of the Ti ions in the B site of the perovskite LTON (ABO<sub>2</sub>N). Fig. 2.4a shows the s-XAS spectra measured at the Ti L<sub>2</sub> (460.2 eV) and L<sub>3</sub> (453.8 eV) edges. The L<sub>2</sub> and L<sub>3</sub> electronic transitions correspond to the photoexcitation from the Ti 2*p*<sub>1/2</sub> and Ti 2*p*<sub>3/2</sub> states to the unoccupied Ti 3*d* states, respectively (Fig. 2.4d). The Ti 3*d* peaks before the PECR (blue) are split by the crystal-field ( $\Delta_{\text{oct}}$ ) into the *t*<sub>2g</sub> and *e*<sub>g</sub> states. After the PECR (red) the main peaks of L<sub>2</sub> and L<sub>3</sub> edges do not exhibit any change in position (energy), which suggest no change in oxidation state for Ti. However, the peak splitting is no longer resolved, suggesting disorder surrounding the absorbing Ti cation and a lowering of symmetry of the octahedra, likely due to vacancy generation, previously been shown for LTON by measured at the Ti K edge using hard X-ray grazing-incidence X-ray absorption spectroscopy (GIXAS).<sup>66</sup> However, the K edge spectra are sensitive to 3*d*-4*p* orbital mixing. Here, the L edges involve electric dipole allowed transitions which, are insensitive to 3*d*-4*p* hybridisation and reflect the Ti *d* states, excluding multiplet effects.<sup>88</sup> Vacancy generation should result in Ti<sup>3+</sup> states which may contribute to the pre resonance small intensity seen at lower energies. However, due to the convoluted effects of the crystal field splitting, disorder, and multiplet effects. To try elucidate the extent of these changes, would require reference materials<sup>89</sup> to be measured extensively and compared experimentally and theoretically.<sup>90</sup>

With respect to the corresponding SX-ARPES data, the experimental maps of (angle-integrated) resonant photoemission (ResPE) intensity as a function of  $E_B$  and  $h\nu$  are shown in parts b and c, before and after the PECR, respectively. In the first approximation, neglecting the multiplet effects in the ResPE process,<sup>84, 85, 88, 91</sup> the resonating intensity represents the admixture of Ti weight to the VB states, with those near the bottom and top of the VB being

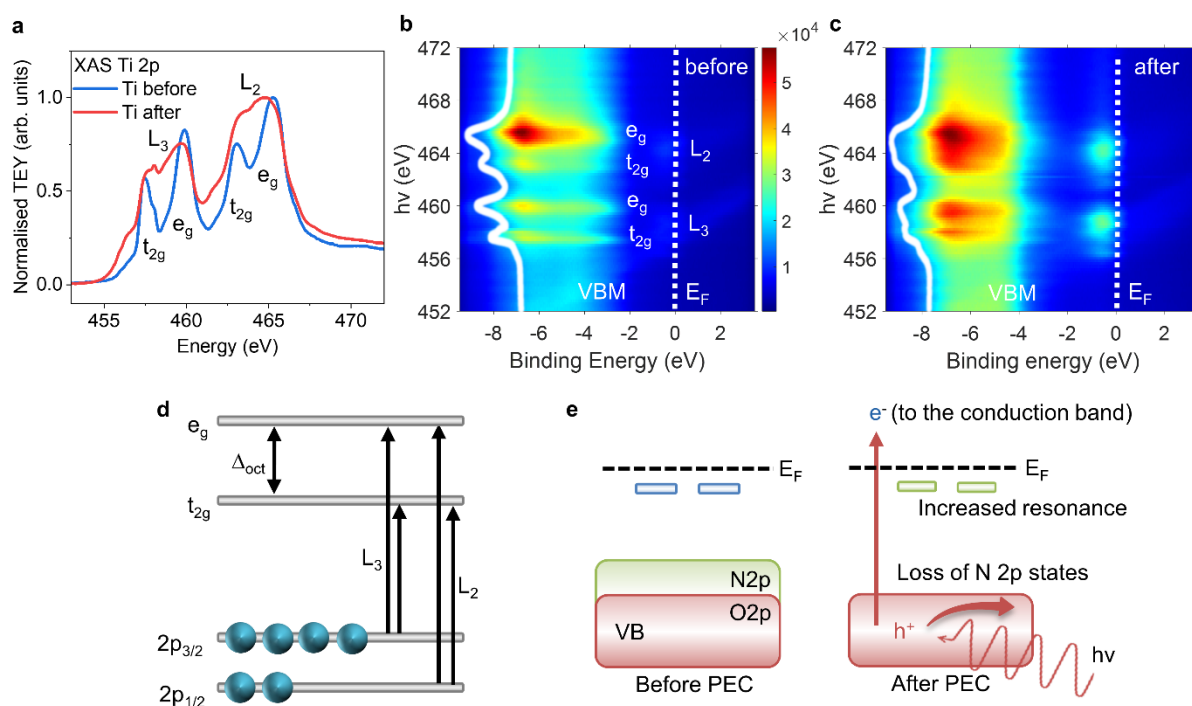


**Fig. 2.4** (a) Soft-XAS spectra for LTON showing the Ti  $L_2$  and  $L_3$  edge before and after the PECR, shown in blue and red, respectively, (b,c) Maps of angle-integrated ResPE intensity across the Ti  $L_3$  and  $L_2$  before (b) and after (c) the PECR. The solid white lines are the XAS spectra overlaid from (a). The white dashed line marks  $E_F$ . (d) schematic representation of the transition of the  $L_3$  and  $L_2$  absorption bands, (e) graphic representation for the observed changes occurring to the band structure of the surface layers of the LTON photocatalyst, where  $h\nu$ ,  $E_g$  and VBM denote the visible-light photons, the band gap and the VB maximum, respectively.

derived from the O  $2p$  and N  $2p$  states, respectively, hybridised with the Ti states. The resonant intensity appears on top of a large non-resonant spectral contribution (in Fig. 2.4b, the intensity at ca. 452-454 eV).

The XAS spectra (Fig. 2.4a) are overlaid to the ResPE maps in parts b and c as the solid white line, where the four XAS peaks correspond to the hotspots of the resonating intensity. After the PECR (Fig. 2.4c), the disorder considerably widens the XAS peaks and the resonating-intensity



hotspots in excitation energy. Moreover, after the PECR there is an increase in the  $L_3$  resonating intensity of the Ti – O<sub>2p</sub> states at the bottom of the VB. This may suggest creation of additional Ti – O 2p states and increased hybridisation between their respective valence orbitals. This observation would be in agreement with previous reports for perovskite oxynitrides with vacancy healing by O species under OER conditions<sup>20</sup> and perovskite oxides, which exhibit increases in hydrophilicity and undergo surface reconstructions during the OER, resulting in a superficial enriched BOH/O(OH) surface layer and an increase in catalytic activity.<sup>92, 93, 94</sup>

As previously described, upon the O to N substitution in LTON, N 2p states are introduced that lie higher in energy than the O 2p states, shifting the VB maximum (VBM) upwards and reducing the band gap (Fig. 2.4e). In the as grown sample (before the PECR), the VBM, which consists of Ti – N 2p states, is situated just below  $E_F$ . After the PECR (Fig. 2.4c), the N 2p derived states deplete, which results in the apparent downward shift of the VBM to its new position at ca. -4.5 eV below  $E_F$ . Furthermore, the resonating intensity near  $E_F$  dramatically increases after the PECR, indicating that new states emerge in this energy region. Consistently with the downward shift of the VB, we conjecture that these states are split off the Ti-derived states constituting the CBM of LTON. It has been suggested that LTON has a direct bandgap<sup>95</sup>, which is line with previous reports for LaTiO<sub>x</sub>N<sub>y</sub>.<sup>71</sup> However, as this is usually inferred via UV-vis spectroscopy<sup>96, 97</sup>, there are also reports for LTON through theoretical calculations suggesting it has both direct and indirect points.<sup>98</sup> As it is not possible to observe the unoccupied states using ARPES, we are unable to experimentally determine whether LTON possesses a direct or indirect bandgap. That said, the emerging states split of the CBM suggest that we observe an indirect band gap for LTON.

The observed depletion of the VBM suggests that bulk N leaves the lattice structure. It remains however, interstitial/chemisorbed on the surface in the form of  $\text{N}_2$  and  $\text{NO}_x$  species as corroborated by XPS data.<sup>70</sup> As the surface-lattice N and the OER intermediates ( $\text{OH}/\text{O}(\text{OH})$ ) likely react in competitive side reactions,<sup>94, 99, 100, 101</sup> it is possible that the increase in hydrophilicity and a superficial  $\text{B}(\text{Ti})\text{OH}/\text{O}(\text{OH})$  enriched surface layer, normally associated with the perovskite oxides, will have a more antagonistic role with respect to the oxynitrides.

We now complement the  $\mathbf{k}$ -integrated ResPE maps in Fig. 2.4 by high-statistics  $\mathbf{k}$ -resolved measurements at the Ti  $L_2$  and  $L_3$  edges, providing direct information on the band dispersions and their evolution across the PECR (Fig. 2.5).

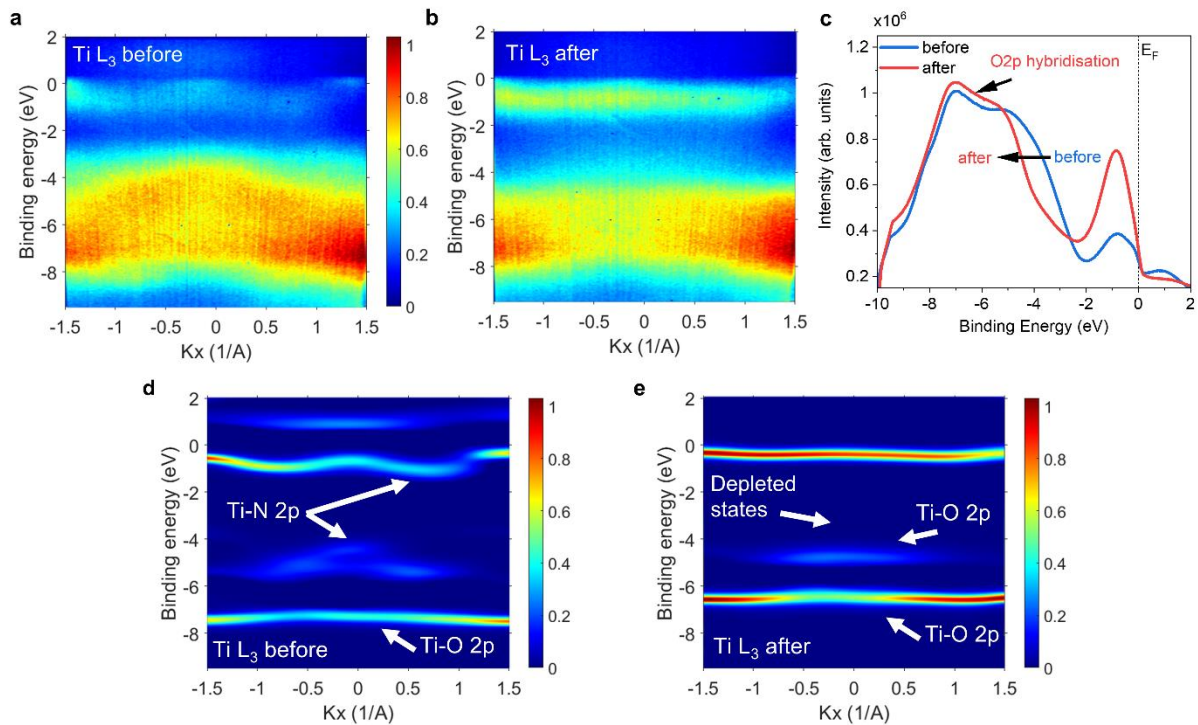


**Fig. 2.5.** (a-b) Ti  $L_3$ -edge high-statistics ARPES images acquired at  $h\nu = 465.3$  eV before (a) and after (b) the PECR; (c) angle-integrated ARPES images from a-b, (d-e) the ARPES data from a-b represented in the second derivative  $-d^2I/dE_B^2$  to enhance the band dispersions. The parallel Ti  $L_2$ -edge data are included in Supplementary Fig. 3.

Parts a-b, presents the ARPES intensity images at the  $L_3$  edge (the results at the  $L_2$  edge are similar and are presented in the Supplementary) before and after the PECR, respectively, and  $k_x$  describes the component of  $\mathbf{k}$ - parallel to the surface of LTON. The resonance emphasises the O and N 2p states hybridised with the Ti states. To discriminate the band dispersions, the angle-integrated spectral intensity is subtracted in these ARPES images from the raw intensity. Furthermore, the parts d-e emphasize the spectral peaks using the negative second derivative  $-d^2/dE_B^2$  of the (Gaussian pre-smoothed) spectral intensity (with the  $-d^2/dE_B^2 < 0$  values, having no direct physical meaning, set to zero).

We observe significant dispersions of the VB states, in particular near the VBM. The very fact of  $\mathbf{k}$ -dependent electron energies attests good crystallinity of our samples. The downward shift of the VBM after the PECR is associated with flattening of the electron dispersion in this energy region. The latter should be attributed to certain crystal-lattice degradation owing to the bulk N atoms leaving the lattice structure, mentioned above, giving another evidence to this stimulated diffusion process. We also note that the states near  $E_F$ , which we have previously assigned to the Ti-derived states split off from the CBM, scale up in intensity after the PECR but also flatten their dispersion because of the crystal-lattice degradation. The high-statistics Ti  $L_2$  measurements (Supplementary Fig. 2.9) show the same effect but with reduced resonating intensity, due to the relative strengths of the  $L_2$  and  $L_3$  transitions.

### **Resonant SX-ARPES: Lanthanum A cation**

We will now follow the electronic structure of La ions in the A site of LTON. Fig. 2.6a shows the XAS spectra for LTON measured at the La  $M_5$  (836 eV) and  $M_4$  (853 eV) edges. These

involve the electronic transitions of the La  $3d_{5/2}$  and  $3d_{3/2}$  states to the unoccupied La  $4f$  states, respectively (Fig. 2.6b). Due to selection rules<sup>102</sup> the  $3d > 4d$  transition is forbidden, as shown by the red arrow. The transition to the  $4p$  state is allowed, however, this process has much smaller cross-section compared to the  $4f$  resonance and is shifted into higher photon energies. The two main peaks in the  $3d > 4f$  XAS spectrum of LTON arise due to spin-orbit coupling, with the spin-orbit splitting between the peaks being ca. 16.2 eV, in line with previous reports.<sup>103, 104</sup> After the PECR, the splitting of these peaks increases slightly due to a reductive shift of the  $M_5$  peak in  $E_B$  of ca. 0.1-0.15 eV (Fig. 2.6a), accompanied by an increase in its energy width, with the amplitude unchanged. The  $M_4$  peak also increases its width after the PECR, but its energy does not shift and has a notable increase of its amplitude. These changes can be explained by the partial covalence between the La  $5d$  and O  $2p$  states upon the formation of LaO<sub>x</sub>/LaOH at the surface. Here, La behaves as a transition metal, albeit a poor one. It retains partial  $d$ -electron ( $5d^1$ ) density,<sup>66, 105, 106, 107, 108, 109</sup> used in hybridisation and the partial covalence between the O  $2p$  states.

With respect to the corresponding SX-ARPES data, the maps of (angle-integrated) ResPE intensity are included in Fig. 2.6d-f. The resonant intensity enhancement for La is weaker compared to the Ti resonance (Fig. 2.5c and Fig. 2.6f) which is expected since the sites of O and N, forming the VB, are situated on the octahedral sites of the Ti cation. Interestingly though, we can see resonating spectral intensity just below  $E_F$ , as also observed for the Ti resonance. This fact suggests that La  $4f$  states hybridise with the N  $2p$  ones forming the VBM, yet the majority of La resonant weight is contributed by the La – O  $2p$  hybridised states lower in the VB. We note, however, that in the case of La the multiplet effects in ResPE<sup>88</sup> are much more pronounced than for Ti, and the relation of the ResPE intensity to the La weight in the VB states becomes less direct.

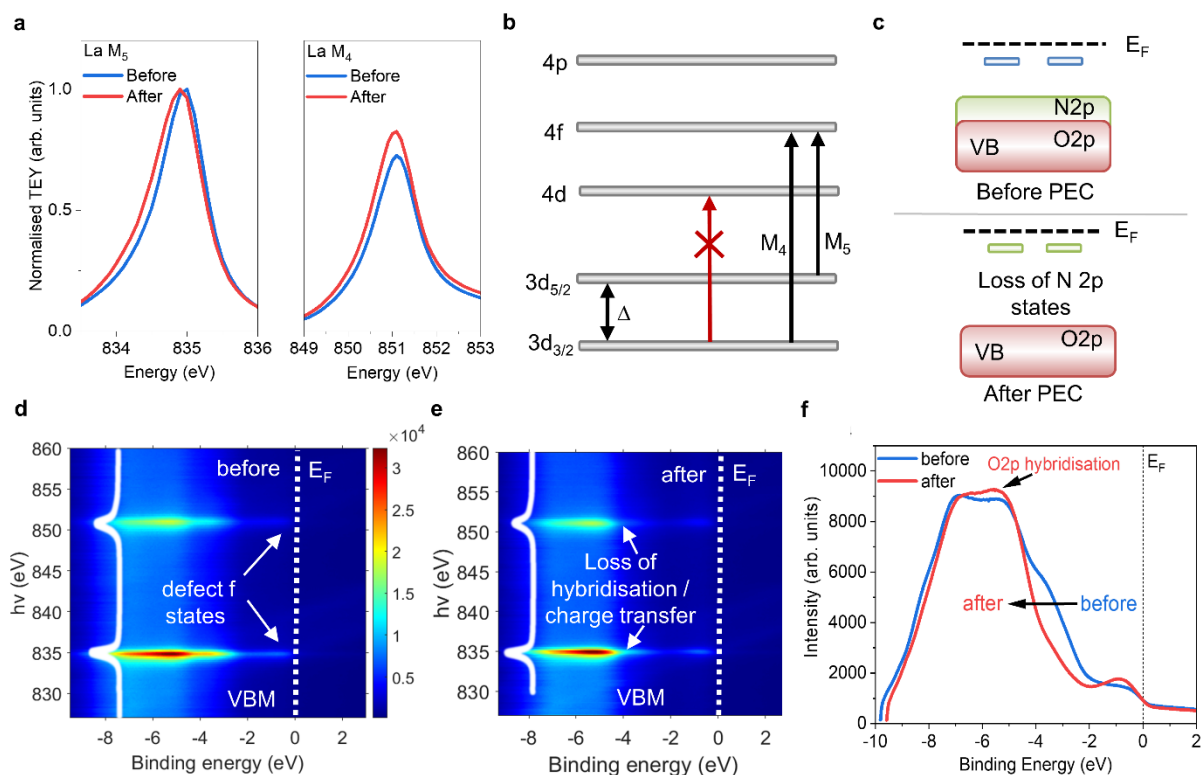


**Fig. 2.6.** (a) Soft-XAS spectra for LTON showing the La  $M_5$  and  $M_4$  edges, respectively, (b) schematic representation of the transitions of the  $M_4$  and  $M_5$  absorption bands, (c) schematic representation of the La contribution to the band structure of LTON, (d) La resonance (angle-integrated) intensity map before PEC, (e) after PEC, (f) angle-integrated plots for data shown in parts **d-e**.

### Experimental vs theoretical Density of States (DOS)

The experimental  $\mathbf{k}$ -integrated DOS is qualitatively represented by off-resonant angle-integrated ARPES spectra, albeit modulated by photoemission matrix elements depending on  $E_B$  the binding and  $h\nu$  excitation energies. Fig.2.7, parts a and b presents such spectra measured just below the Ti  $L_3$  and La  $M_5$  resonances, respectively. The gross features of both spectra are the VB extending over the  $E_B$  range from -9 to -3 eV, and a narrow band just below  $E_F$ . The

spectral modulations in the VB region are however, different because of the matrix elements<sup>110</sup> depending on  $h\nu$ .

The element-resolved partial DOS (PDOS) can qualitatively be determined from the ResPE angle-integrated spectra where, neglecting the multiplet effects,<sup>88</sup> the resonant intensity difference relative to the off-resonant spectra represents the weight of the resonating element in the electron states.<sup>84, 85, 91</sup> Such differential spectra for the Ti  $L_3$  and La  $M_5$  edges, representing the Ti and La partial DOS, respectively, are shown in Fig. 2.7c-d.

To help our understanding of LTON's electronic structure and afterwards its evolution over the PECR, we will compare the experimental data with Density-Functional Theory (DFT) calculations (see Methods) for stoichiometric LaTiO<sub>2</sub>N. Fig. 2.7e shows, the calculated total and the PDOS for Ti, O, N and La, aligned to  $E_F$ , with the work function calculated as 6.0 eV. The band gap of LaTiO<sub>2</sub>N is 1.9 eV, which is close to the experimentally reported values.<sup>75,62</sup> The calculations confirm the commonly accepted picture of LTON's electronic structure where the states near the VB bottom are formed mostly by O 2p atomic orbitals and near the VBM mostly by the N 2p orbitals. With the reservation for the matrix elements, the calculated total DOS is in a reasonable agreement with the experimental VB in Fig. 2.7a-b. Turning to the Ti PDOS hybridized mostly with the O 2p states, the calculations suggest its notable increase towards the VB bottom. This is confirmed by the experimental Ti PDOS derived from the ResPE data, Fig. 5c, that indeed scales up in this energy region. The calculated partial La PDOS is weighted towards the VB centre, which is also consistent with the ResPE results in Fig. 2.7d.

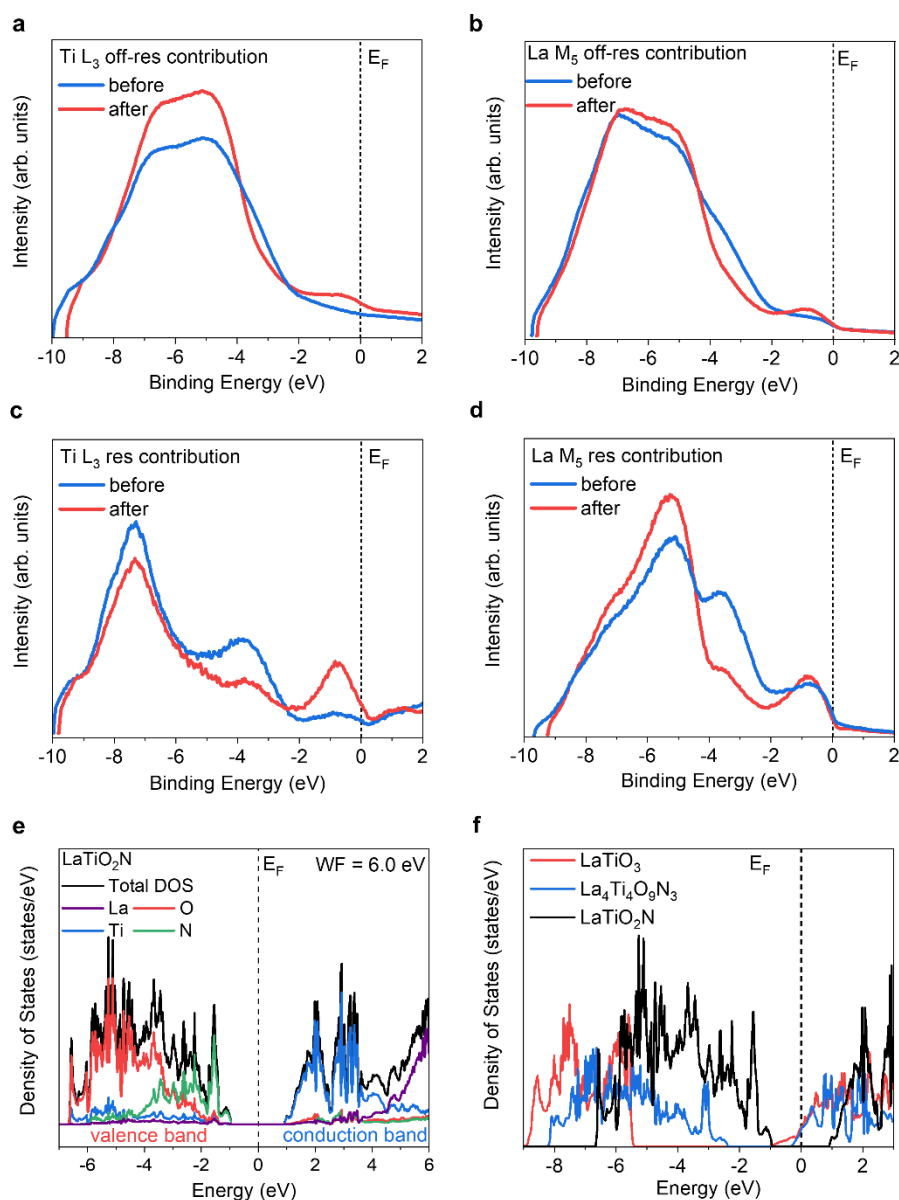


**Fig. 2.7.** Off-resonant angle-integrated ARPES spectra measured below (a) the Ti  $L_3$  edge (averaged over  $h\nu = 452\text{-}454$  eV) and (b) the La  $M_5$  edge ( $h\nu = 828\text{-}830$  eV) representing the total DOS; Resonant weight (resonant minus off-resonant spectral intensity) at (a) the Ti  $L_3$  edge ( $h\nu = 460.2$  eV) and (b) the La  $M_5$  edge ( $h\nu = 835$  eV) representing the Ti and La partial DOS, respectively. The spectra (a-d) are measured before and after the PECC; Theoretical (e) total and partial DOS for  $\text{LaTiO}_2\text{N}$  and (f) total DOS for  $\text{LaTiO}_2\text{N}$ ,  $\text{LaTiO}_3$  and  $\text{La}_4\text{Ti}_4\text{O}_9\text{N}_3$ , aligned to the fermi level.

There are however significant deviations of the experiment from the calculations: (1) the experimental VB in Fig. 2.7a is deeper in  $E_B$  by  $\sim 1.5$  eV, and (2) there is a narrow band just below  $E_F$  which, according to the Ti ResPE data in Figs. 2.4b-c and the derived Ti PDOS in Fig. 2.7c, has a large Ti weight. These observations can be reconciled with the theory if  $E_F$  shifts upwards into the Ti derived CB. This means, however, that the surface layer of our LTON sample, probed in our ARPES experiment, should be metallic. With the intrinsically semiconducting bulk of LTON, the presence of such a metallic surface layer identifies a downward band bending towards the surface.

### **Electronic structure evolution across the PECR**

Consistently with the previous works,<sup>70, 111, 112, 113</sup> our DFT calculations confirmed by the experimental ResPE data have shown that the VBM just below  $E_F$  is comprised of the Ti and La states hybridised with the N 2p ones, whereas in the bottom of the VB these states hybridise with the O 2p ones. The angle-integrated ARPES intensity for the above high-statistics measurements at the Ti  $L_3$  edge are included in Fig. 3c. Here, it is easier to follow the evolution of the DOS in LTON and the changes with respect to the OER. Confirming our observations in the ResPE maps in Fig. 2.4b-c, we observe an increase in the total resonating intensities after the PECR which suggests creation of additional O 2p states or a greater degree of hybridisation in the bottom of the VB. We also observe the downward shift of the VBM due to the loss of lattice N at/near the surface of LTON under OER conditions. The same two effects can also be observed in the La ResPE map and the angle-integrated plot, shown in Fig. 2.6 parts e and f, respectively.



In Fig. 2.7, we compare the Ti (c) and La (d) resonant contributions, representing the weight of the Ti and La hybridised states in the VB of LTON, before and after the PECR. After the PECR, we can see the depletion of the La and Ti weight at the VBM. We attribute this evolution of the spectra to the partial loss of lattice N at the surface during the OER, whereby the La N 2p and Ti N 2p states partially depleted.

For comparison with the evolution of LTON after the PECR, in Fig. 2.7f we compare the calculated total DOS for the stoichiometric LTON with that for the unstable  $\text{LaTiO}_3$  (LTO) and the anion-deficient defect structure  $\text{La}_4\text{Ti}_4\text{O}_9\text{N}_3$  (D-LTON). For the sake of clarity, only the spin-up contributions have been included in this comparison (the total DOS for LTO and D-LTON are included in the Supplementary Fig. 2.8). These materials were chosen with their respective elemental compositions to reflect possible trends to the electronic structure of LTON upon the loss of nitrogen and the creation of anion vacancies and/or changing the O/N content, as suggested by the SX-ARPES data evolution over the PECR. To more accurately compare the three materials, the energy scale of their DOS was aligned to the  $E_F$  level (energy = 0 eV). We note that the DOS of LTO and D-LTON show that  $E_F$  of these materials lies in the CB, which is composed of anti-bonding states. Their occupation is unfavourable, because it would destabilise the lattice, resulting in its reorganisation. Usually, such reorganisations proceed via phase transformations or due to vacancy formation, which explains why LTO does not exist naturally. Furthermore, we note that both LTO and D-LTON are spin polarised since Ti has the formal charge  $3^+$  in LTO, whereas D-LTON is a non-stoichiometric material (the spin-up/spin-down decomposition of their DOS is given in the Supplementary).

Comparing the total DOS in Fig 2.7f, we can see that the partial or total loss of N in the anion-deficient D-LTON or in the unstable LTO shifts the VBM downwards in energy, as we observe

experimentally. This further suggests that during the OER, the O/OH<sup>-</sup> intermediates are involved in the photocatalytic formation of nitrate and nitrite species from the surface lattice N atoms<sup>94, 99, 101</sup> whereby they leave the lattice and remain chemisorbed on the surface in the form of NO<sub>x</sub> species.<sup>70</sup> This effect is consistent with the observed suppression of electron dispersions in the CB near the  $E_F$ . Furthermore, we conjecture diffusion of O atoms to heal remnant oxygen vacancies into LTON, generated upon loss of nitrogen from the lattice structure, from the O<sup>\*</sup> and OH<sup>-</sup> reactionary intermediates generated during the OER.<sup>114</sup> This is consistent with a slight increase of the VB intensity in the off-resonant spectra, Fig. 2.7a and b, after the PECR.

However, we see for the resonant weighted contributions for Ti and La (Fig. 2.7c-d), that La shows increased resonating intensity in the bottom of the VB. Which, suggests increased La – O 2p hybridisation. Whereas, those for Ti decrease in the bottom of the VB. This can be explained by the fact that many of these oxides and oxynitride SCs exhibit a preferential AO surface termination (LaO in the case of LTON) as experimentally determined by low energy ion spectroscopy (LEIS).<sup>93, 115, 116, 117</sup> The B cation, usually a transition metal cation acting traditionally, as the active site for oxygen evolution, would be hidden below the first atomic surface layer. Therefore, surface oxygen/nitrogen vacancies, would expose the underlying transition metal cations.

Previous calculations for LaTiO<sub>2</sub>N<sup>118</sup> have also suggested that the more oxygen added to the La-O surface layer, the more the SC is self-doped with electrons (accumulation) filling the empty Ti 3d states. We see certain evidence of this effect in the La resonant spectrum (Fig. 2.7d) which shows increased O hybridisation, whereas, the Ti resonant spectrum (Fig. 2.7c) shows an increase of the Ti 3d weight at the  $E_F$  after the PECR. It was also suggested in the same work<sup>118</sup> that the evolution of the surface results in a geometrical configuration where two

N atoms leave the Ti layer and move to the La surface layer, resulting in a more stable 5 coordinated Ti configurations.

Previous work<sup>66</sup> suggests that LTON undergoes a surface reconstruction with Ti showing signs of vacancy generation (resulting in an under-coordinated Ti) with the charge surrounding Ti, conserved. Usually, such reorganisations proceed via phase transformations or due to vacancy formation. When the  $E_F$  of a material lies in the CB (Fig. 2.7f), which is composed of anti-bonding states. Their occupation is unfavourable, because it would destabilise the lattice, resulting in its reorganisation. Resulting in a surface layer that becomes more metallic in nature seen by the downward band bending in this work.

The downward band bending is contrary to our expectations, due to the fact that LTON is an n-type SC material where upward band bending would typically be assumed.<sup>119, 120</sup> This contradiction has also been observed for ZnO which exhibits downward band bending at the ZnO/air interface and after vacancy generation due to preferential O sputtering in vacuum by ion bombardment.<sup>121</sup> Which, would mean for the photoanode LTON, instead of the formation of a depletion layer and upward band bending, as typically assumed, LTON forms an accumulation layer (accumulation of electrons) and exhibits downward band bending.

### **Conclusion**

In this work, we have determined the electronic structure of the oxynitride LTON photocatalyst resolved in  $\mathbf{k}$ - and elemental character of the electronic states, and monitored its evolution through the PECD. Whereas no such information regarding oxynitrides existed to date, crucial to achieve it in the present study have been the  $\mathbf{k}$ -resolution, enhanced probing depth and

elemental/chemical-state specificity of synchrotron-radiation based SX-ARPES. By combining the SX-ARPES results with the DFT calculations, we have established that the bottom of the VB consists of La and Ti states hybridised with the O 2p states, whereas the top of the VB consists of both La- and Ti – N 2p states. Furthermore, we have identified the effect of disorder and downward band bending at the surface of LTON.

Not only have we determined the electronic structure of the LTON photocatalyst, but also monitored its evolution caused by the OER. After the PECR, we observe (a) the depletion of Ti- and La-N 2p states, (b) disorder in the local environment of Ti, likely due to O/N vacancy generation, (c) the creation of additional La - O 2p states in the VB, and (d) the formation of an electron accumulation layer in the surface region, exhibiting downward band bending. Along with the disorder and defects associated with Ti 3d states, the latter would lead to the trapping of electrons and charge recombination. Therefore, SX-ARPES has been able to confirm this effect as one of the major limitations for the oxynitride LTON's functionality.

Passivation layers and co-catalysts have shown to increase the long-term performance of oxynitrides<sup>65</sup> by reducing charge recombination as one of the benefits. However, the presence of the accumulation layer and its evolution across the PECR suggested by our results implies involvement of more complex mechanisms. The extension of our work to these buried interfaces, taking into advantage the probing depth and chemical specificity of SX-ARPES, will allow us to rationalise/correlate the evolution of their electronic structure with respect to the increase in catalytic performance usually observed with the powder photocatalysts.<sup>122, 123, 124</sup> The spectroscopic abilities of SX-ARPES highlighted by our work extend from the oxynitrides to a wide range of other thin-film and interface systems used in various functional materials.

## Methods

### Thin Film Deposition

The thin films used in this work were grown using a modified pulsed laser deposition (PLD) method known as Reactive Crossed-beam Laser Ablation (PRCLA)<sup>69</sup> following the same procedure as previously described.<sup>62</sup> A laser fluence of ca. 2.5 J cm<sup>-2</sup> was used at a repetition rate of 10 Hz. Commercially available MgO(001) substrates (10.0 x 0.5 x 0.5 mm) were used as a template to grow the TiN buffer layer and LTON thin film.

### Angle-Resolved Photoemission Spectroscopy

The ARPES measurements were performed at the SX-ARPES endstation<sup>125</sup> of the Advanced Resonant Spectroscopies (ADDRESS) beamline<sup>126</sup> situated at the Swiss Light Source, Paul Scherrer Institute, Switzerland. Resonant photoexcitations were performed at the Ti L<sub>2</sub>, Ti L<sub>3</sub> and La M<sub>4</sub>, La M<sub>5</sub> edges ( $E_0 = 460, 453, 853$  and  $836$  eV, respectively). The photon flux was ca.  $10^{13}$  photons/s and focused into a spot size of  $30 \times 75 \mu\text{m}^2$  on the sample surface at an x-ray grazing incidence angle of  $20^\circ$ . The energy resolution was set to 140 meV and the sample temperature was kept at 20 K in order to maximise the coherent spectral component.<sup>47</sup> The angle-integrated spectra were integrated within  $\pm 8^\circ$ . The XAS data were measured in total electron yield (TEY).

We also performed time dependence measurements upon X-ray irradiation, to observe if the electronic structure of LTON is modified due to exposure to the X-ray beam. Only insignificant changes have been observed (supplementary Fig. 2.10), which were comparable with the noise of the measurements and could be explained by X-ray stimulated desorption of surface

contaminations. It is also possible that these changes were a consequence of the oxidation of hydrocarbons chemisorbed on the surface during the *ex-situ* transfer of the samples.

### **Density Functional Theory**

Geometry optimisations and energy calculations were performed using DFT and Perdew-Burke-Ernzerhof (PBE)<sup>127</sup> functional implemented in the QuantumWise software package (now part of Synopsys).<sup>128</sup> A pseudopotential method was applied using numerical atomic orbitals for representation of the valence electrons. The electron correlation was taken into account using the DFT-1/2 computational approach which allows for accurate estimation of band gaps in complex oxide materials.<sup>129</sup> Workfunctions were calculated for slabs with BO<sub>2</sub> termination<sup>130</sup> using ghost atom approach and multigrid Poisson solver with Neumann boundary condition (bottom surface) and Dirichlet boundary condition (top surface). The method allows to estimate the workfunctions of polar slabs which are not accessible without complicated surface reconstruction using planewave wavefunctions. Eight BO<sub>2</sub> layers were considered in each slab. Real space grid and k-point mesh have been converged to 10<sup>-4</sup> eV energies.

### **Photoelectrochemical Characterisation**

The PEC measurements were performed using a three-electrode configuration as previously described. A KCl saturated Ag/AgCl electrode was used as the reference. The oxynitride thin film and platinum wire were utilised as the working and counter electrode, respectively. An aqueous solution of 0.5 molar NaOH was used as an electrolyte with a pH of 13. The samples were illuminated with a 150W Xe arc lamp (Newport 66477) with an AM 1.5G filter with an output intensity of 100 mW cm<sup>-2</sup>. To measure the dark and light current a chopper was used to

intermittently block the irradiation of the sample. The potentiodynamic and potentiostatic measurements were performed at a scan rate of 10 mV s<sup>-1</sup>.

### Composition Analysis

Rutherford Backscattering (RBS) and Elastic Recoil Detection Analysis (ERDA) were employed to determine the chemical compositions of the LTON thin films. RBS provides the metal ratios and oxygen content, whereas ERDA provides the nitrogen-to-oxygen ratio. The RBS measurements were conducted using a 2 MeV He beam and a silicon PIN diode detector. ERDA utilised a 13 MeV <sup>127</sup>I beam in combination with a time-of-flight spectrometer and, a gas ionisation detector. RBS data was analysed using RUMP.<sup>131</sup>

### Crystalline Properties

XRD measurements were performed using a Seifert X-ray Diffractometer with characteristic Cu K $\alpha$  radiation 0.154 nm. Theta-2theta scans were performed to determine the out-of-plane orientations of the films.

## 2.12. Appendix

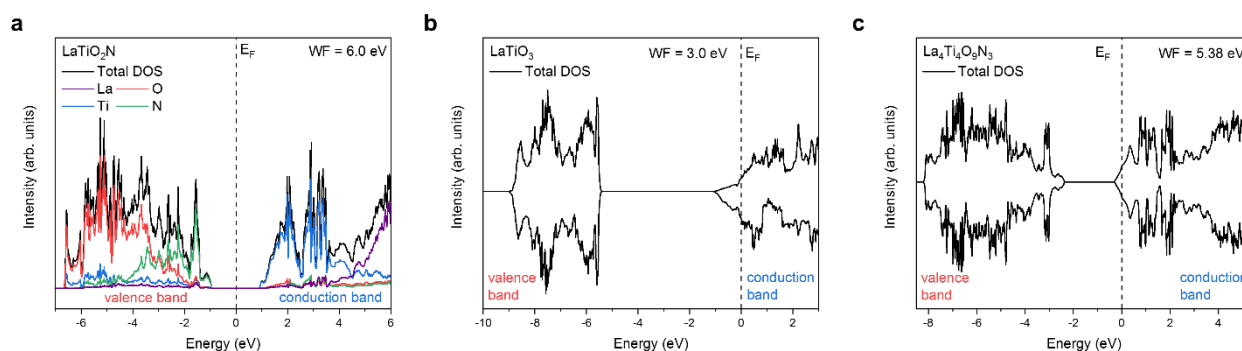


**Fig. 2.8.** Total DOS (a) LaTiO<sub>2</sub>N (b) LaTiO<sub>3</sub> (c) La<sub>4</sub>Ti<sub>4</sub>O<sub>9</sub>N<sub>3</sub> aligned to their respective fermi levels.

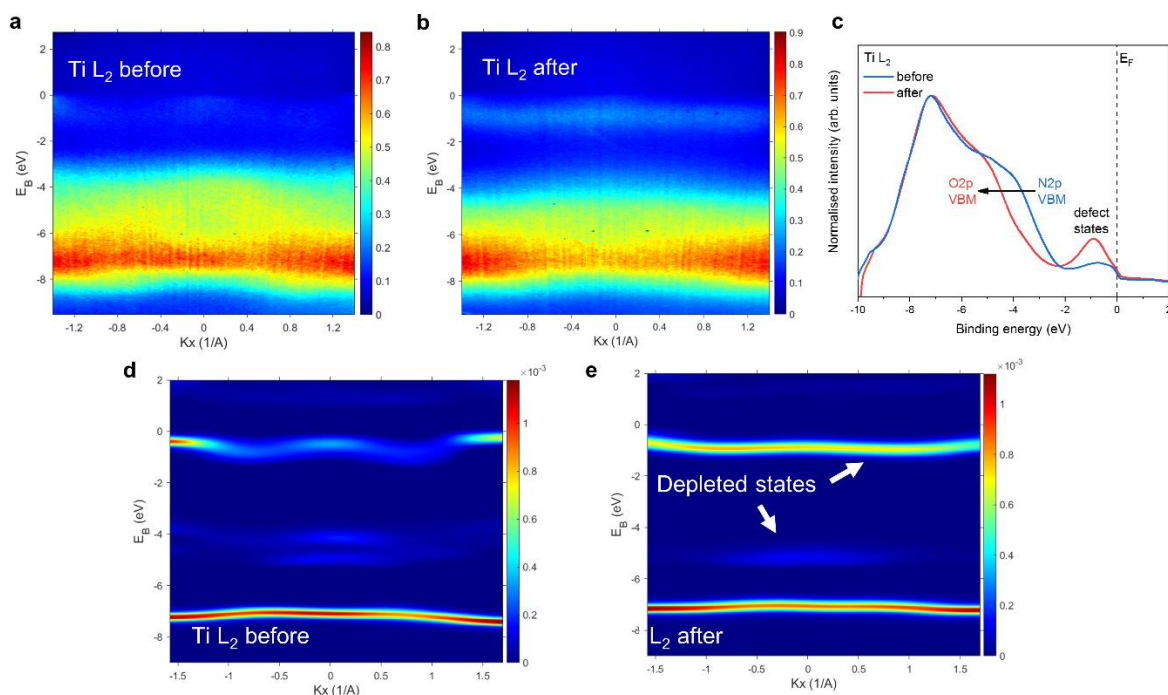


**Fig. 2.9.** (a) Ti L<sub>2</sub> edge high-statistic before PEC, acquired at 465.3 eV, (b) Ti L<sub>2</sub> edge high-statistic after PEC, (c) angle integrated plots for data shown in parts **a-b**, (d) smoothed data from part a for visual clarity of the dispersions seen near to the E<sub>F</sub>, (e) smoothed data from part b. The integrated angle range corresponds to -7.6:8.1 degrees.

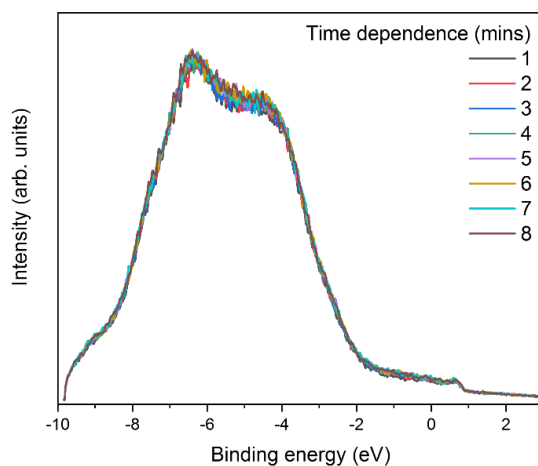


**Fig. 2.10.** Angle-integrated plot of the LTON VB measured at the Ti L<sub>3</sub> edge after exposure to the X-ray beam over time.



## Chapter 3: Extent and nature of the surface evolution of $\text{LaTiO}_x\text{N}_y$

### 3.1. Preamble

This chapter looks at the surface modifications at the solid-liquid interface that occur during photoelectrocatalytic water splitting. Where the combination of neutron reflectometry (NR) and grazing incidence X-ray absorption spectroscopy (GIXAS) are employed to distinguish between the surface and bulk signals.

The results in this chapter are published in *Nature Communications* and can be found here:

Lawley C, Nachtegaal M, Stahn J, Roddatis V, Döbeli M, Schmidt TJ, *et al.* Examining the surface evolution of  $\text{LaTiO}_x\text{N}_y$  an oxynitride solar water splitting photocatalyst. *Nature Communications* 2020, 11(1): 1178. <https://doi.org/10.1038/s41467-020-15519-y>

#### Author Contributions:

Conceptualisation, C.L., D.P., J.S., and M.N.; Investigation, C.L., M.N., V.R., M.D. and J.S.; Formal Analysis, C.L., M.N., M.D., J.S.; Writing – Original Draft, C.L. and D.P.; Writing – Review & Editing, C.L., T.S., D.P. and T.L.; Funding Acquisition, D.P., J.S., M.N., T.S.; Supervision, D.P. and T.L.

### 3.2. Introduction

To study the physicochemical evolution of the surface of the semiconductor, the use of oxynitride thin films as model systems provides a clear advantage over the corresponding powders in the fact that they offer relatively wide, atomically flat, and well-defined surface where one can more easily distinguish between the surface and the bulk of the material. With respect to powders, decreasing the nanoparticle radius size does increase the surface area-to-bulk ratio, however, any measurements would still represent an average of the contributions from the surface and the bulk. Literature pertained to oxynitride thin films for water splitting remains limited to date.<sup>62, 70, 71</sup>

Some of the prevailing surface sensitive techniques currently available are not without their limitations. Secondary Ion Mass Spectrometry (SIMS) for example involves the surface bombardment with a primary ion beam in an ultra-high vacuum. Therefore, the technique is locally destructive due to sputtering effects, which can lead to modified surface chemistry and ion implantations. X-ray photoelectron spectroscopy (XPS) is another key technique for surface characterisations, though like SIMS it requires a high vacuum environment. These environments do not simulate natural operating conditions and can alter the sample itself, whilst also ruling out future in situ and operando measurements performed in water. Recent advances in Near Ambient Pressure XPS (NAP-XPS) have been made using dip and pull methods in water and offer promising opportunities for in situ measurements, however, one must consider changes in pH values, drying and salt formation.

X-ray diffraction (XRD) is limited to long-range order and X-ray reflectivity (XRR) is not sensitive enough to distinguish between elements next to one another in the periodic table. Surface enhanced Raman spectroscopy (SERS) and more specifically tip enhanced Raman spectroscopy (TERS) is another good possibility, however, the Raman effect is also very weak, and can require a long measurement time not suitable for operando measurements. The sensitive nano tips used can be prone to unwanted chemisorption and degradation during operation conditions.

Taking into consideration the type of information that can be obtained from the current existing techniques, their limitations and practicalities, we chose for this study to employ the complementary surface sensitive techniques, neutron reflectometry (NR) and grazing incidence X-ray absorption spectroscopy (GIXAS) to probe the surface modifications of epitaxially grown LTON films (Fig. 3.1). The advantage of using neutron reflectometry and GIXAS is the fact that they are both in-situ techniques, allowing the possibility to study reactions in the presence of water. Neutron reflectometry is a non-destructive destructive<sup>132</sup> technique similar to X-ray reflectivity (XRR) for measuring the depth profile of the density of thin films. The difference between using neutrons over X-rays is that the neutrons scatter from the atomic nuclei rather than from electrons. The neutron scattering power can vary greatly between neighbouring elements and isotopes of the same element therefore, NR unlike XRR, is sensitive to neighbouring light elements (H, C, O, N) and isotopic substitution<sup>132, 133, 134</sup> and can provide depth profiles with sub-Ångstrom resolution.<sup>135</sup>

### 3.3. Oxynitride thin films

The growth of oxynitride films using pulsed reactive crossed beam laser ablation (PRCLA) described previously<sup>68</sup> allows the fabrication of thin films with different crystalline properties and tuneable nitrogen contents. Fig. 3.1 shows the structural and morphological characterisations for LTON thin films grown for this work. The crystal structure for  $\text{LaTiO}_2\text{N}$  is shown in Fig. 3.1a, Fig. 3.1b shows the X-ray diffraction (XRD) measurement for the epitaxial oxynitride LTON film deposited on titanium nitride (TiN) coated magnesium oxide ( $\text{MgO}(001)$ ) substrate. In our previous work<sup>72</sup> we demonstrated that the TiN seed layer can not only be used as a current collector for PEC measurements, but it also provides a very good template for the growth of oxynitride films making the deposition process more stable (controllable). Whilst also increasing N content in comparison to oxide substrates.

TiN possesses the same rock salt structure as MgO and has similar lattice parameters,  $a = 4.211 \text{ \AA}$  (MgO),  $a = 4.235 \text{ \AA}$  (TiN). Due to the small lattice mismatch between MgO and TiN (ca. 0.56%) this layer grows (100) epitaxially oriented with MgO(001), the (200) diffraction peak

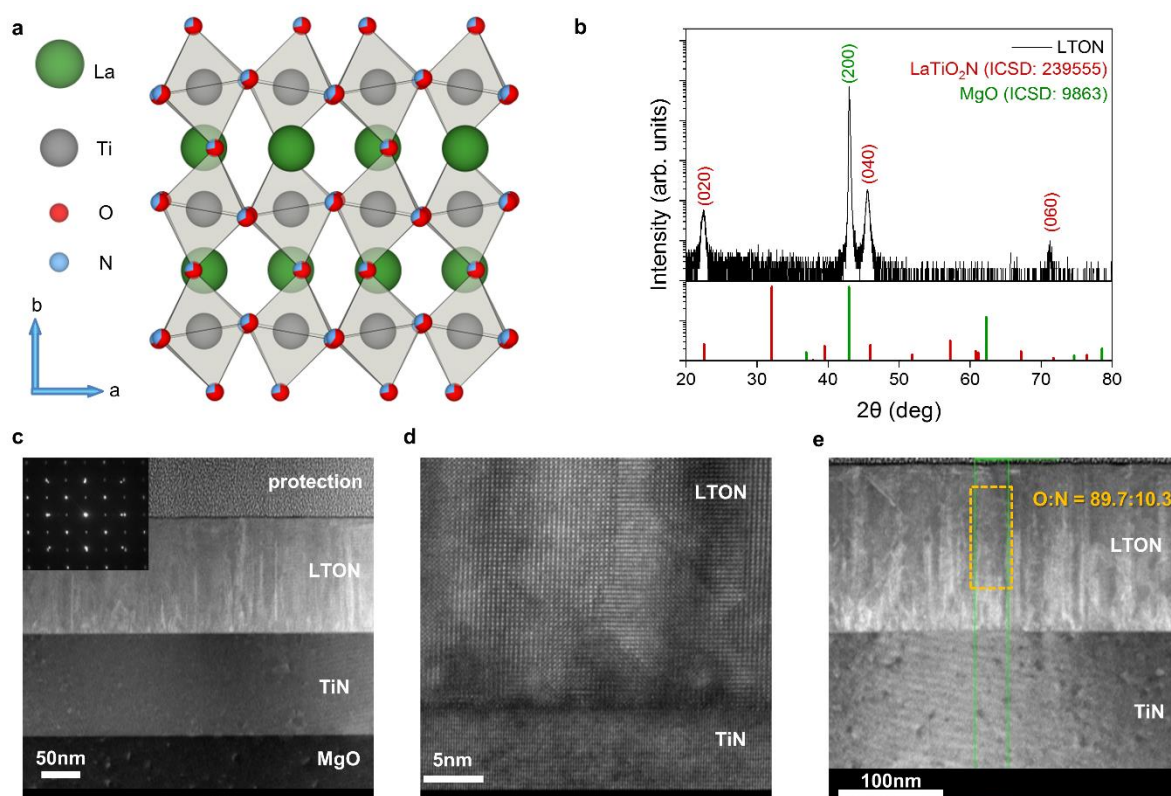


**Fig. 3.1.** (a) crystal structure of  $\text{LaTiO}_2\text{N}$ , (b) XRD pattern of the epitaxial LTON film, the  $\theta/2\theta$  is shown in black, with  $\text{LaTiO}_2\text{N}$  and MgO substrate reflexes shown below in red and green for reference. Reflections are labelled using the (hkl) notation, (c) TEM cross section of the LTON – TiN film grown on MgO, (d) High-angle annular darkfield (HAADF) image; a grain boundary (GB) is tracked with asterisks, (e) O:N ratio determined by TEM/EELS analysis.

is visible as a shoulder on the peak of the substrate. LTON has the orthorhombic perovskite structure with lattice parameters  $a=5.5731 \text{ \AA}$ ,  $b=7.8708 \text{ \AA}$ , and  $c=5.6072 \text{ \AA}$ .

The XRD pattern shows that LTON grows epitaxially on the TiN buffer layer with the (h,k,l) reflexes (0,2,0), (0,4,0) and (0,6,0) appearing at  $2\theta$  values ca. 22, 46 and 72 respectively. The MgO substrate (200) reflex has been marked in green. Fig. 4.1c shows the transmission electron microscope (TEM) cross sectional image of the epitaxially grown film, with the selected area electron diffraction (SAED) pattern inset in the top left corner. The TEM image indicates a well-defined surface and interfaces between the layers. The SAED pattern also confirms the

epitaxial growth of LTON and TiN on the MgO substrate. The protection layer seen in the cross-sectional image was applied on the sample solely for the TEM measurement. The High-angle annular dark-field (HAADF) image with atomic resolution is shown in Fig. 3.1d.

The O:N ratio for the LTON films were determined using electron dispersive spectroscopy (EDX) and are in agreement with the RBS/ERDA analysis. Although the O:N ratio is low, this is usual for epitaxially grown LTON films where there is a trade-off between crystalline quality and total nitrogen substitution/content. Films grown using larger laser fluence, tend to grow polycrystalline films with much higher nitrogen contents. The compositions of the thin films used in this work were determined by RBS/ERDA measurements (Fig 3.2). The compositions of the LTON films consist of La:Ti and O:N ratios of 1.04-1.06 and 10.3-10.7 respectively (Table 1). The experimental uncertainties on the compositions measured by RBS for La and Ti and ERDA for O and N are  $\pm 2\%$  and  $\pm 3\%$  respectively. We assume that the chemical composition of the films, while affecting the light absorption and charge migration properties, has little influence on the evolution of the physicochemical state of the surface layer.

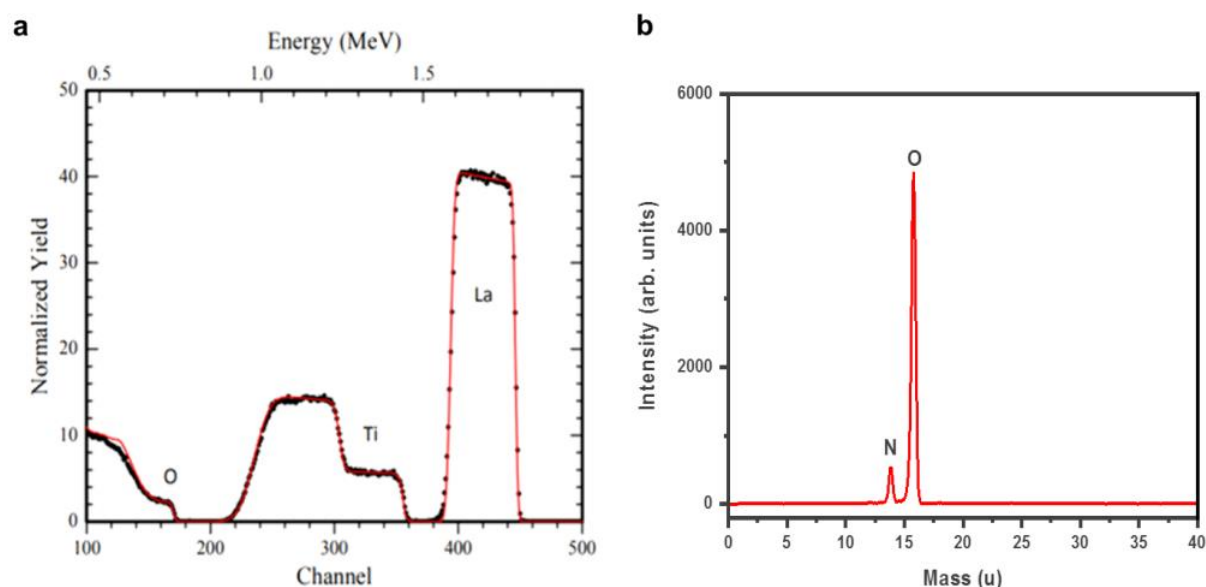


**Fig. 3.2.** (a) Rutherford backscattering (RBS) spectrum, (b) elastic recoil detection analysis (ERDA) spectrum. The cation ratios were determined by RBS whereas, the O:N ratios were determined by ERDA

**Table 1.** Compositions of LTON thin films determined by RBS and ERDA.

Film	Composition	La:Ti	O:N
LTON sample batch 1	La <sub>1.03</sub> Ti <sub>0.97</sub> O <sub>3.0</sub> N <sub>0.29</sub>	1.06(0.02)	10.3(0.7)
LTON sample batch 2	La <sub>1.02</sub> Ti <sub>0.98</sub> O <sub>3.0</sub> N <sub>0.28</sub>	1.04(0.02)	10.7(0.7)

### 3.4. Experimental Strategy

In NR, the neutron wave ( $k_0$ ) hits the sample at a given angle (Fig. 3.3). Part of the neutron wave is reflected ( $k_f$ ) and part is refracted ( $k_1$ ) (Fig. 3.3b). The scattering plane is orientated vertically ( $q_z$ ) and the incident angle ( $\omega$ ) can be by rotating the sample (Figure 3.3a). Diffuse scattering has been omitted and only the specular reflected waves are considered for easier visualisation. The depth profiles are obtained via specular NR by measuring the intensity of the reflectivity. From the reflectivity curves, scattering length density (SLD) profiles of the material are inferred.

XAS is an element specific spectroscopic technique, which allows the characterisation of the electronic structure of the absorbing atoms and of their local geometrical environment. To perform surface sensitive measurements, grazing incident X-ray absorption spectroscopy (GIXAS) were performed on the LTON thin films, while powder reference samples were measured by XAS in transmission mode. Measurements were performed at grazing incident angles varying between 0 and 1 degree at intervals of 0.1 degree (Fig. 3.3c-e). This method enables us to distinguish between the surface and the bulk of our samples, a type of characterisation that is not possible with powders samples.

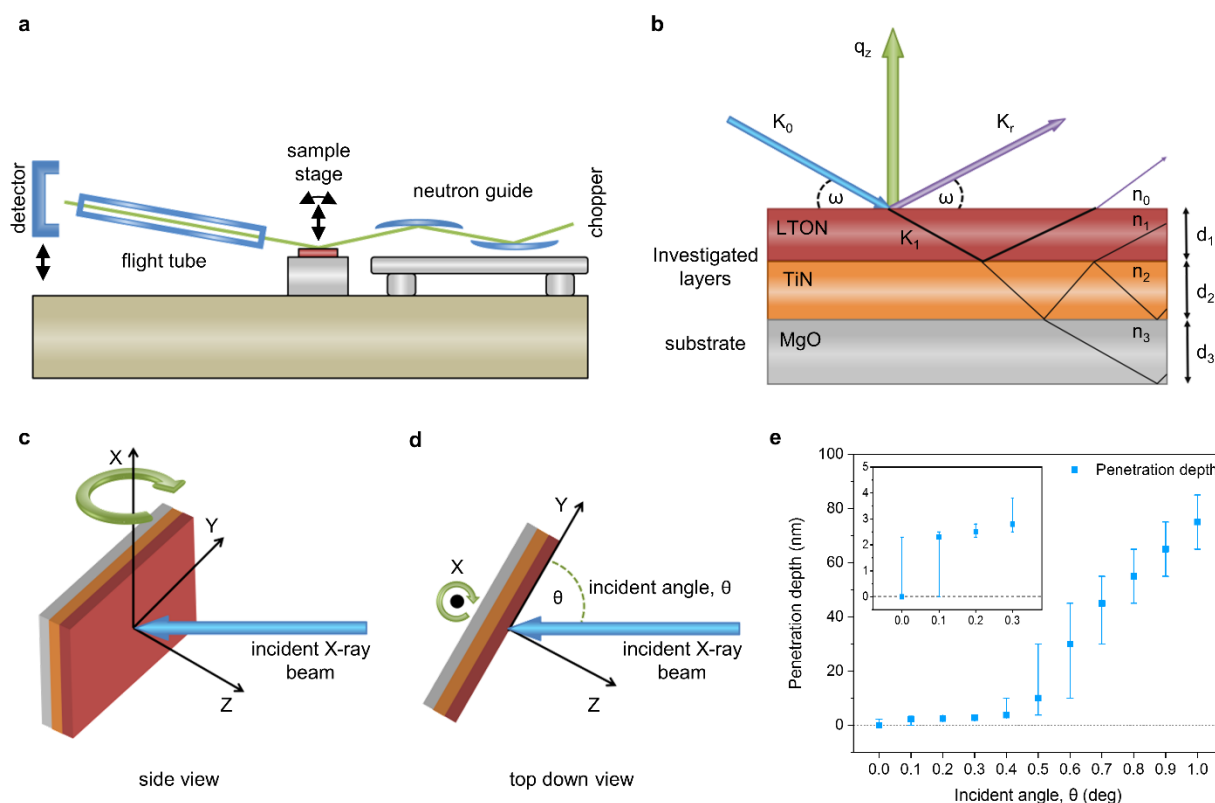


**Fig. 3.3.** (a) instrument description for AMOR time-of-flight neutron reflectometer at SINQ/PSI, (b) neutron reflectometry measurement for multilayer thin films, (c-d) surface sensitive GIXAS measurement, side view and top down respectively, (e) penetration depth of X-rays for LTON at the Ti K edge energy range as a function of incident angle, the error bars correspond to the penetration depth at a given incident angle with an error of  $\pm 0.1$  degrees. Values taken from.<sup>136</sup>

### 3.5. Photoelectrochemical Characterisations

The photocatalytic conversion of solar energy into hydrogen via the water-splitting process assisted by semiconductor catalysts is a promising route to generate a clean, low cost and renewable energy source. In these semiconductor photocatalysts, electrons are excited from the valance band to the conduction band forming electron-hole pairs ( $e^- - h^+$ ) under light irradiation

(photons) with energy greater than or equal to that of the band gap (Fig. 3.4). The photogenerated electrons are collected by the TiN seed layer and transferred to the Pt counter electrode where the excited electrons can directly reduce protons to form  $\text{H}_2$ . As for the photogenerated holes, they are consumed in the OER where they oxidise water to generate  $\text{O}_2$  at the surface of the photocatalyst. Co-catalysts can also be used in conjunction with the photocatalysts (not shown), which provide alternative active sites for the evolution of hydrogen and oxygen by acting as electron and hole scavengers for the photogenerated charges, respectively. Thus, co-catalysts can increase performance by reducing electron/hole charge carrier recombination which is a detrimental effect that suppresses the photocurrent.

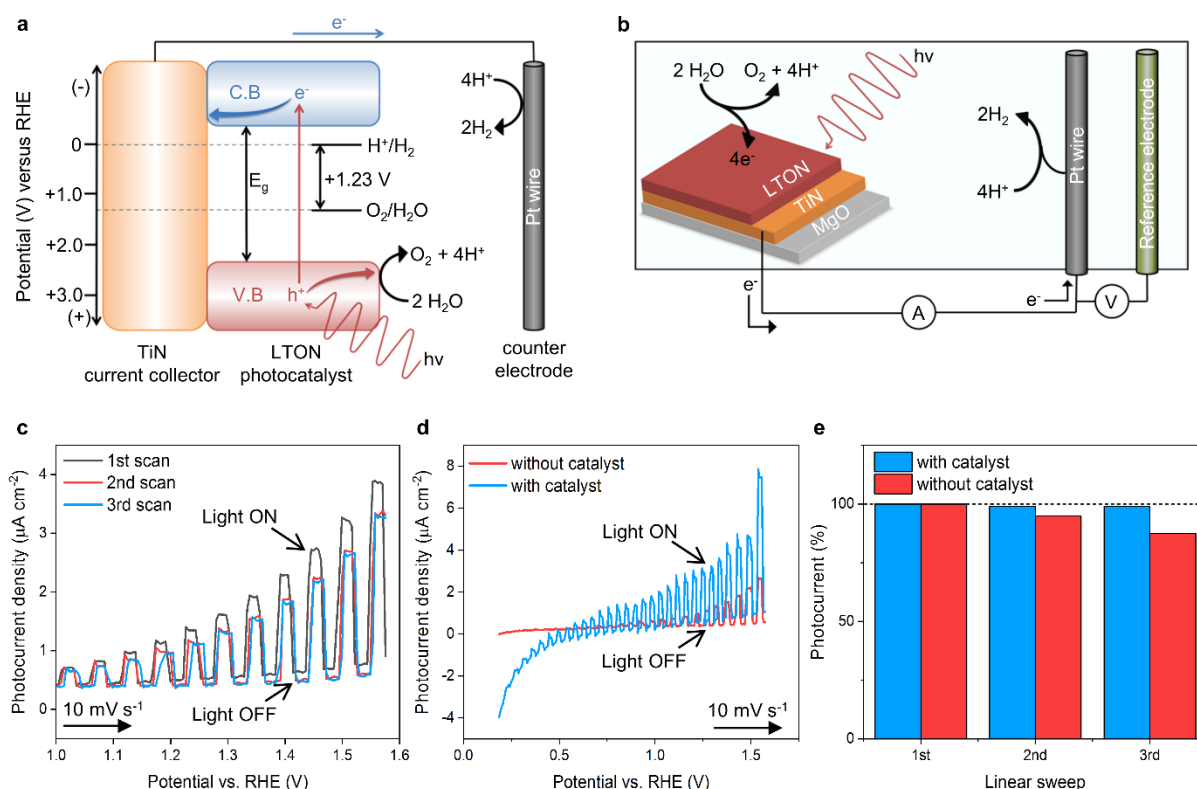


**Figure 3.4.** (a) energy diagram for the LTON semiconductor photocatalyst, (b) photoelectrochemical 3 electrode cell, (c) 3 consecutive potentiodynamic scans for LTON without catalyst, (d) stabilised photocurrent for the bare LTON film and  $\text{IrO}_2$  decorated LTON film shown in red and blue respectively, (e) the degradation from the initial photocurrent with successive potentiodynamic linear sweeps comparing the bare and  $\text{IrO}_2$  decorated LTON films values taken at 1.5 V vs RHE.



The PEC characterisations of LTON were performed with a standard 3 electrode configuration in 0.5 mol. NaOH aqueous electrolyte ( $\text{pH} = 13$ ) as shown in Fig. 3.4b. A reversible hydrogen electrode sets the 0 V potential and an increasing voltage bias is applied between working and counter electrode. The electronic current between working and counter electrodes, also called the photocurrent, is proportional to the amount of  $\text{H}_2$  and  $\text{O}_2$  produced. Fig. 3.4c shows the first three consecutive potentiodynamic current-voltage scans for LTON. From the initial scan it is apparent that there is a decrease in the measurable photocurrent density with successive sweeps. By the third scan the photocurrent density is stable however, with a photocurrent density at 1.5V vs. RHE ca. 20% less than the initial value. This degradation was previously ascribed to the surface oxidation of the epitaxial LTON film under operation conditions.<sup>71</sup>

Measurements were performed under chopped illumination allowing the distinction between the dark current when there is no illumination of the sample, and the visible-light response that can be seen by the sharp increases in current when under illumination. Fig. 3.4c shows the stabilised photocurrent density for the bare LTON sample compared to LTON decorated with  $\text{IrO}_2$  nanoparticle co-catalyst deposited onto the surface, shown red and blue respectively. Fig. 3.4e shows the degradation in photocurrent observed previously in part c as a percentage from the initial measured photocurrent during the first linear sweep for the bare LTON film compared to the  $\text{IrO}_2$  decorated film.

It is apparent that the bare LTON film is more susceptible to the degradation process compared to the sample decorated with co-catalyst, where the degradation rate is decreased and the extent of the degradation is minimised. It is shown in Figure 3.4d that in the presence of the co-catalyst, the photocurrent density is increased by a factor of ca. 2 at 1.5V vs. RHE. Optimal co-catalyst deposition conditions and cheaper alternatives to  $\text{IrO}_2$ , are currently under study. The significance of the co-catalyst here is to compare the effect of the PEC water splitting process on bare LTON thin films and those decorated with a well-known co-catalyst to compare performance and the extent of the surface modifications. To confirm and monitor any changes in, or the formation of a modified surface layer of the LTON films, neutron reflectometry measurements were performed on several LTON films *ex situ* comparing before and after PEC measurements.

### 3.6. Neutron Reflectometry

A visual description of the measurement has been included in Fig. 3.3 to compare NR results before and after PEC measurements. For one batch of samples, PEC characterisation were performed as described in the experimental section (3.10). For the second batch, the sample history was kept identical. It was exposed to the same electrolyte for the same time period and irradiated with the same light intensity. However, no external bias was applied to the film and no measureable photocurrent was observed, the reason for doing so was to try establishing which stimulus is the driving force for the observed surface degradation. The resulting reflectivity plots for the before and after comparisons of the two sets of films are shown in Fig. 3.5a-b.

It can be seen in Fig. 3.5a, that for the sample that did not evolve any oxygen there is minimal observable changes in the reflectivity curves when comparing the initial as grown film and after exposing to the electrolyte and light irradiation. At higher  $Q$  (scattering vector) values there are small deviations but they are smaller than the resolution and degree of error as the signal tends to wash out at high  $Q$  values. The difference spectrum has been provided for easier visualisation. When comparing a sample which was exposed to an external bias and evolved oxygen under OER conditions, significant changes in the reflectivity curve can be observed when comparing before and after PEC measurements (Fig. 3.5b).

These differences arise due to changes in the density of the film during operation. The extent of the changes can be described by modelling of the reflectivity curves. Figure 3.5c shows the experimental data (solid lines) from b with the corresponding model fit (dashed lines) which has been offset in the y axis for easier visualisation. From the fit, a 1D SLD profile is inferred and is portrayed in Figure 3.5d. Comparing before and after PEC the TiN layer remains unchanged, contrast differences in the SLD profile at each TiN interface arise due to the slight diffusion of oxygen to the TiN layer from the substrate and from the LTON film during growth which has also been evidenced previously by TEM and electron energy loss spectroscopy (EELS) (Appendix 3.11). Comparing before and after PEC for the LTON film, a minor

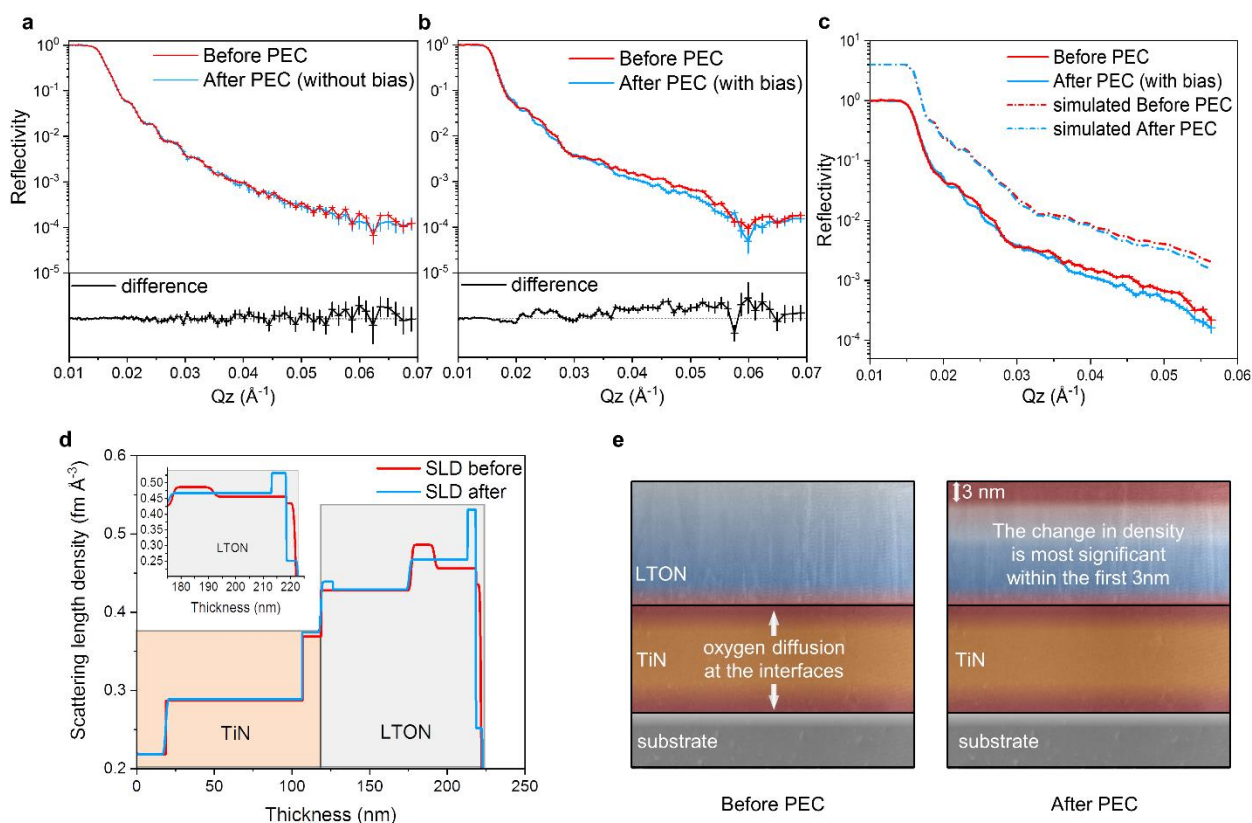


**Fig. 3.5.** (a) Reflectivity plot for a LTON film exposed to electrolyte and light intensity, yet no external bias was applied to the sample and showed no photoelectrochemical performance, (b) with applied bias, (c) experimental and corresponding model fit for data shown in b, shown by the solid and dashed lines respectively, (d) the inferred scattering length density profile as a function of depth from the corresponding fit. The inset shows the magnified region at and near to the surface of LTON, (e) depth profile of the samples before and after PEC.

difference is apparent at the  $\text{TiN}/\text{LTON}$  interface inferred by an almost negligible O:N ratio change but the largest changes in SLD profile occur at and just below the surface, as seen in Figure 3.5d and the inset. The model suggests slight nitrogen content loss in the film below the surface layers, but at the surface within the first 3 nm there is a greater degree of nitrogen loss and a slight increase in the oxygen content which would generate a small degree of vacancy formation in the film after PEC measurements. However, the quantitative analysis of the stoichiometric changes resulting in the scattering length density profile changes involve some degree of uncertainty and require additional complementary techniques to reference.

Qualitatively, the differences in the scattering length density profile confirm that a physiochemical change in the film has taken place, most significantly at and near the surface where the model suggests slight stoichiometric changes. Since no difference was observed in the film where no external bias was applied, we could conclude that the density changes observed for the oxynitride are of a direct consequence of the applied external bias and the water splitting process. The electrolyte and incident light alone has minimal/negligible effect on the LTON sample. Although NR is a powerful technique with various applicational benefits, relying solely on NR is not sufficient to elucidate the degree of changes in the LTON films.

### **3.7. Grazing incidence X-ray Absorption Spectroscopy**

For this study, we performed ex-situ GIXAS measurements on several LTON thin films before and after PEC, to probe the electronic structure of the La and Ti, A and B cations and their local environments. We saw in the previous section the suggestion by NR, that the physicochemical changes occurring in LTON are limited to the first 3 nm. In section 3.4 and more specifically, Fig. 3.3c-e, we show how GIXAS enables us to distinguish between the surface and the bulk of our samples.

Fig. 3.6 shows the X-ray absorption near edge spectroscopy (XANES) spectra for LTON measured at the lanthanum  $L_3$  edge and titanium K edge including, several powder references for both elements. Fig. 3.6a compares several La containing references, where there is no significant shift seen in the energy position of the absorption edge peak at ca. 5.49 keV for all three samples. This suggests that lanthanum exists in the commonly observed 3+ oxidation state for the prepared powders of the LaTi oxide and oxynitride materials. There are however, significant differences in intensities of the peaks for the 3 samples which are attributed to the different and perhaps non-uniform particle sizes. Different size particles possess different surface areas and as a result can exhibit partial oxidation reflected in the changes of the peak

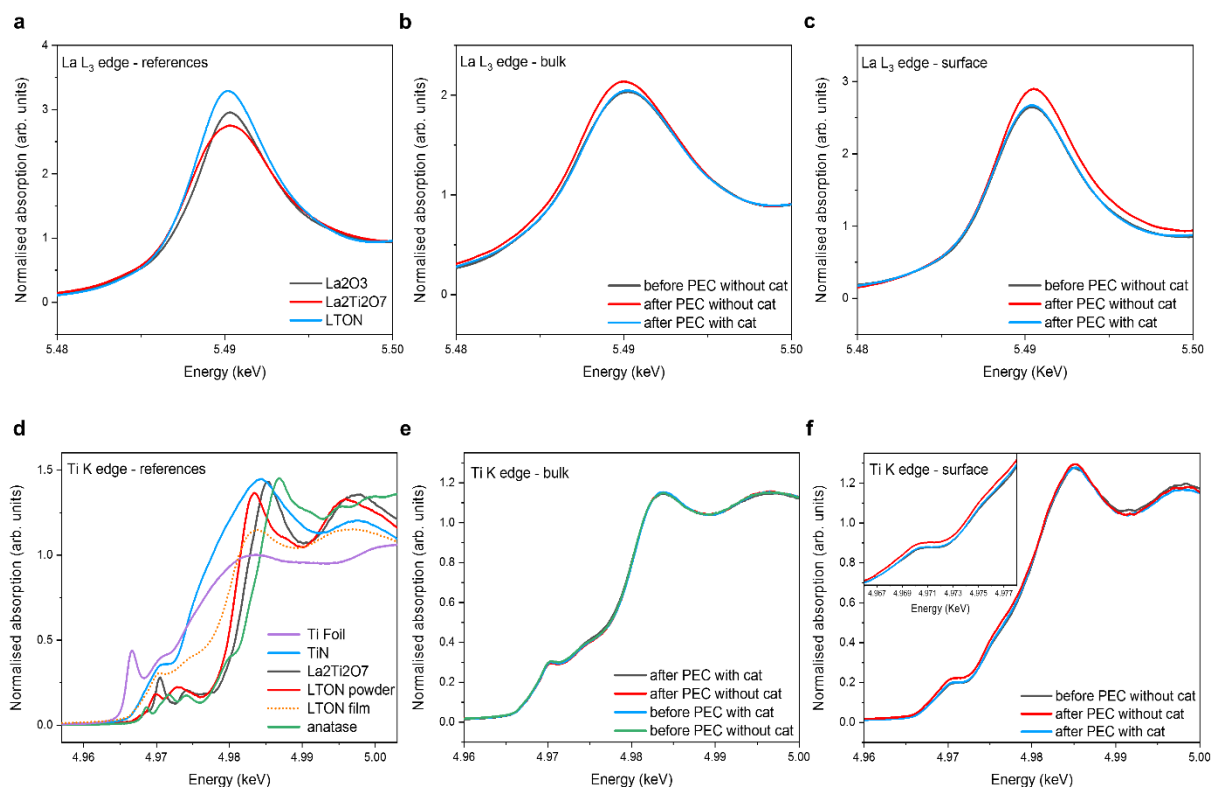


**Fig. 3.6.** (a) La containing references, (b) LTON bulk comparing La before and after PEC, (c) LTON surface comparing La before and after PEC, (d) Ti containing references, (e) LTON bulk comparing Ti before and after PEC, (f) LTON surface comparing Ti before and after PEC.

intensities. Fig. 3.6b shows the comparison of the bare LTON film with the  $\text{IrO}_2$  decorated film measured in the bulk of the sample. It can be seen that after PEC the La cations in the bulk of the bare sample undergoes both an increase in intensity and a reductive shift to lower energy. For the La cations situated at the surface however, it can be seen that there is an oxidative shift to higher energy after PEC (Fig. 3.6c). It is noteworthy that when the LTON films are decorated with the  $\text{IrO}_2$  co-catalyst, the shifts in the edge positions and intensity changes are prevented.

It has previously been shown that the looking at the second derivative plots of the La XANES and peak fitting analysis looking at peak positions and FWHMs are related with the degree of disorder and coordination environment surrounding La.<sup>137, 138</sup> The same analysis was carried

out on the La L<sub>3</sub> XANES data presented here but it did not show any significance difference comparing between before and after PEC. The analysis has been included in the appendix (section 3.11).

The biggest differences in the XANES spectra are the centroid shifts, which suggests that the La A cation sites are much more active in the water splitting process than previously believed. This was not obvious or expected for the A site and especially for La. The B cation would correctly be assumed to be more catalytically active than La, but it has been previously shown that the surfaces of these oxides and oxynitrides tend to show AO (La-O) termination rather than BO<sub>2</sub> (TiO<sub>2</sub>) surface terminations.<sup>70, 115, 139, 140</sup> The La cations are much larger than Ti (1.03-1.16 Å and 0.61-0.67 Å respectively) and so the surface would consist primarily of La-O atoms where the Ti B cations sink down slightly into the subsurface layers. Which could explain why the A site shows evidence to be the catalytically active site for the OER.

Traditionally, it is assumed that the valence state of lanthanum exists solely in the nominal 3+ integer value. However, there have been theoretical and experimental studies which suggest that this is not entirely true. It has been shown that La can exhibit a partially occupied d-orbital (5d<sup>1</sup>) with an atomic charge between the nominal valence charges +2 and +3.<sup>106, 107, 108</sup> This partial covalency between La-O would explain the observed catalytic behaviour of the A cation and the changes seen in the XANES spectra. The reductive shift in bulk of the samples may be driven by the slight loss of nitrogen/oxygen and generation of vacancies changing the partial covalency surrounding La. It is possible and worth noting that overall nitrogen contents could be retained, where nitrogen leaves the lattice but remains in interstitial sites. At the surface the La oxidative shift in centroid position could be due to the adsorption of \*O, \*OH, \*OOH intermediates under OER conditions where adjacent O decouples to release molecular O<sub>2</sub>.

Using a co-catalyst conserves the valence state of lanthanum after PEC measurements as seen by the edge positions remaining static and not shifting as seen for the bare sample by filling the role of the active site rather than the A cations. The same measurements were performed at the titanium K edge to explore the B cation site in the LTON films and are portrayed in Fig. 3.6d

and 6f. Fig. 3.6d shows a number of Ti containing references for comparison to the LTON films. As expected, the Ti valence states in the perovskite powder samples and the LTON film are a mixture of  $3^+$  and  $4^+$ . This can be seen by edge positions and peak intensities which are situated in-between those of  $\text{Ti}^{3+}$  in titanium nitride and

$\text{Ti}^{4+}$  in anatase. The comparison between the bare and co-catalyst loaded LTON films measured in the bulk before and after PEC characterisation (Fig. 3.6e) conveys that the water splitting process has no effect on the valence state of the titanium cations in the bulk of the samples. Fig. 3.6f shows the comparison of the LTON films measured at the surface with and without the co-catalyst before and after PEC measurements. It is evident from the spectra that there is no shift in the edge position, meaning that the valence state of Ti has not changed as a consequence of the water splitting process. There are however slight changes in the intensity of the pre-edge region (4.96-4.98 keV) as a consequence of the PEC measurements.

Since pre-edge features are generally related to symmetry and local coordination environments it is suggested that as a consequence of the OER there is an increase in the disorder of the Ti octahedra located at the surface of the LTON film. This type of information and data are not obtainable with some of the previously described surface sensitive techniques. Measurements were performed at various incident angles as previously discussed and the observed changes in the pre-edge for Ti were limited to within the first 3 nm of the film.

The nature of the changes in the pre-edge features will be discussed in the following section but first when comparing the bare LTON sample with the sample decorated with the co-catalyst it is noteworthy that when the co-catalyst is present the pre-edge features changes previously seen are subdued in the presence of  $\text{IrO}_2$ .

### 3.8. Pre-edge features

In order to understand the extent of the changes in the pre-edge features observed at the surface in the Ti K edge spectrum after PEC measurements as seen in Fig. 3.6f, the differential spectrum for the interested region has been produced and displayed with the original data as shown in Fig. 3.7a. The differential and, the corresponding peak analysis fit are included in Fig. 3.7b.

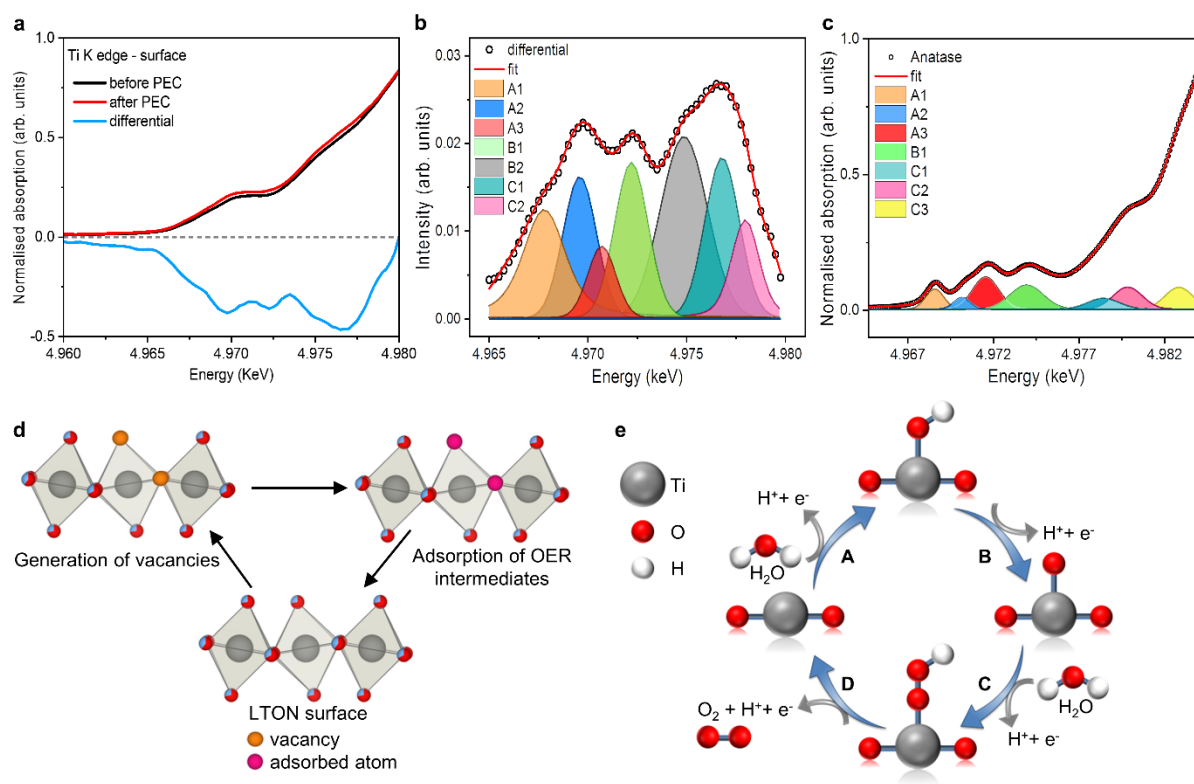


**Fig. 3.7.** (a) the bare LTON film surface before and after PEC and the differential spectra shown in black, red and blue respectively, (b) differential spectra and corresponding peak fitting analysis, (c) peak fitting analysis for measured  $\text{TiO}_2$  anatase as a reference for peak assignments, (d)  $\text{Ti}(\text{O}/\text{N})_6$  octahedra and the possible axial and equatorial positions for vacancy generation and adsorption sites, (e) schematic representation of the OER mechanism.



The pre-edge peak intensities arise due to disorder, lattice defects<sup>141, 142</sup> and a lowering of symmetry; along with orbital mixing. Therefore, the intensity of these peaks increases considerably when moving away from a perfect octahedral to tetrahedral Ti environments. The pre-edge peaks in Fig. 3.7b correspond to the 1s > 3d, 1s > 4s and 1s > 4p transitions of the core 1s electron to the unoccupied molecular orbitals of the Ti(O/N)<sub>6</sub> octahedra. Their assignments are summarised in Table 2 and discussed in more detail below.

**Table 2.** Pre edge peak positions and assignments for TiO<sub>2</sub> and LTON.

Peaks	$\Delta E$ TiO <sub>2</sub>	$\Delta E$ LTON	Peak assignment	orbitals
A1	0.0	0.0	3d-4p	B <sub>2g</sub> , a <sub>g</sub>
A2	1.6	1.7	3d-4p	b <sub>3g</sub>
A3	3.0	3.0	3d-4p	a <sub>g</sub> , b <sub>1g</sub>
B1	5.4	4.5	4p-4s	a <sub>g</sub>
B2	-	7.0	-	-
C1	9.9	9.2	4p <sub>z</sub>	b <sub>1u</sub>
C2	11.3	-	4p <sub>y</sub>	b <sub>2u</sub>
C3	14.3	-	4p <sub>x</sub>	b <sub>3u</sub>

The  $\Delta E$  of the centroid positions have been aligned by setting peak A1 to zero on the energy scale. Peaks C2 and C3 were not included in the differential peak fit model for LTON since there was no change in the pre edge intensity for those contributions. Peak B2's presence was only suggested for the LTON film.

Each peak corresponds to a certain transition and is in agreement for peak fitting analysis performed on experimentally obtained data for  $\text{TiO}_2$  (Figure 3.7c). These transitions have also previously been discussed in literature.<sup>141</sup> The exception is peak B2 which contributes to the differential fitting for the LTON thin film but has no evidence of any contribution to  $\text{TiO}_2$  pre-edge analysis.

### **Peak A1**

The peak denoted as A1 has previously been assigned to a 1s-3d transition usually forbidden in perfect octahedra but due to disorder and a lowering of symmetry, along with 4p-3d orbital mixing with neighbouring Ti atoms the peak is weakly present for LTON and in  $\text{TiO}_2$ . The intensity of this peak increases considerably as you move away from an octahedral to tetrahedral Ti environments. After PEC measurements the contribution of this peak has increased suggesting an increase in disorder of the  $\text{Ti}(\text{O/N})_6$  octahedra of the Ti atoms located at the surface.

### **Peak A2**

The peak denoted as A2 has previously been assigned to a 1s-3d quadrupole transition for  $\text{TiO}_2$  and is related to lattice defects. Perhaps more specifically for LTON with  $D_{2h}$  symmetry the A2 peak can be assigned as the 1s-3d ( $b_{3g} d_{yz}$ ) which is primarily quadrupolar in character. After PEC measurements the intensity of this peak increases. Since it has been previously assigned to defects in  $\text{TiO}_2$ , it therefore suggests that after the water splitting process the local geometry surrounding the surface and near surface Ti cations become a little more disordered. Increasing disorder lowers the octahedral  $D_{2h}$  symmetry even further, introducing more dipolar character to the A2 peak by p-d orbital mixing. This could account for the observed intensity increase of this peak as a consequence of the water splitting process.

The reason for increase in disorder could also be explained by nitrogen loss from the lattice and the formation of nitrogen/oxygen vacancies. This would lead to pentacoordinated Ti cations, lowering the symmetry and increasing p-d orbital mixing. It has been previously shown by *ab-initio* FDM calculations for TiO<sub>2</sub><sup>143</sup> that oxygen vacancies can lead to strong enhancements in the A2 peak region due to the lowering of symmetry and a spectral shift of the A1 peak for pentacoordinated Ti atoms with oxygen vacancies. This may explain why this peak is most significant for the LTON thin films but minimal in powdered anatase.

### **Peak B1**

Peak B1 is attributed to the non-local 1s to 4p-4s hybridised states with the second Ti neighbour. From the peak fitting it suggests that the B1 peak also increases in intensity after PEC which could be accounted for with the increase in disorder around the local absorbing Ti atom altering the degree of p-d mixing with neighbouring Ti atoms.

### **Peak B2**

The B2 peak which is present only in the LTON film can be explained by the existence of oxygen/nitrogen vacancies. This is supported also by the *ab-initio* FDM calculations previously described under section peak A2.<sup>143</sup> According to the calculations, the introduction of axial and equatorial oxygen vacancies leads to large peak intensities for TiO<sub>2</sub> situated at ca. 2.5-3 eV higher in energy than B1. For LTON the difference between B1 and B2 is also separated by a similar energy difference (Table 2). Since this contribution is suggested to be due to oxygen vacancies, the increase in the intensity of this peak after PEC measurements seems to suggest that the OER creates oxygen and/or nitrogen vacancies driven by the loss of nitrogen at the surface of the oxynitride films. This would agree with the NR model that the surface is comprised with an increased oxygen after nitrogen depletion.

### Peak C1

The C1 peak situated at ca. 4977.2 eV also has a large change in amplitude after PEC measurements. This peak is characterised for  $\text{TiO}_2$  as the 1s to 4p ( $B_{1u}$ ) transition which is dipolar in character. The antibonding  $B_{1u}$  molecular orbital is comprised of the Ti 4P<sub>z</sub> orbitals and N/O 2P<sub>z</sub> orbitals. The large increase for this transition may be explained by the loss of N/O and the creation of vacancies at the apical position of the Ti octahedra where the surface terminates and adsorption of intermediates during the OER takes place. The contributions of these peaks seem large due to the fitting of the difference spectra, the overall disorder of the Ti environment as a consequence of the water splitting process are quite subtle when looking at the XANES data. However, we would like to highlight the fact that the edge position does not change yet XAS is a suitable technique to detect this short-range structural information not seen by XRD or XPS. The change in stoichiometry and the increase in disorder of the environment surrounding Ti would induce changes in the degree of local strain of the films. These physiochemical changes can account for the reduced OER activity by increasing the binding energies of the \*O, \*OH and \*OOH intermediates and increasing the OER overpotentials.

### 3.9. Conclusion

We have applied complementary NR and surface sensitive GIXAS techniques to probe the detrimental surface modifications associated with oxynitrides that occur during operation. We show that thin films are ideal model systems for surface sensitive studies where one can more easily distinguish the surface signals from the bulk contributions. The physiochemical modification of the oxynitride surface was limited to the first 3nm of the bare thin film. The addition of the  $\text{IrO}_2$  co-catalyst not only increases the performances of the oxynitride sample by a factor of two but also protects the surface by preventing the observed surface modification as a direct consequence of the water splitting process. The surface modification involves the oxidation of the La A cations and a disordering of the local environment surrounding the Ti B

cations which are thought to be detrimental and the reason for the reduced performance observed in the oxynitrides.

Whereas, La undergoes a reduction in the bulk and Ti remains unaffected as a consequence of the water splitting process. These findings were unexpected because we have evidence that the A site plays a significant role in the OER and La does not exist solely in the nominal +3 valence state. Reports in literature tend to focus more on the role of the B cations, with many new materials involving doping and/or partial substitutions at the B cation sites with respect to activity. To the best of our knowledge, this is the first depiction of what is occurring at the surface and the extent of the changes with respect to each cation as a function of depth during photocatalytic water splitting.

The findings in this chapter are also in agreement with those in Chapter 2 where, sXAS and SX-ARPES suggested (a) the loss of N states, (b) charge conservation surrounding Ti, (c) generation of Ti 3d defect states, (d) reductive shift for La and an increase in spin orbit coupling, (e) increased O2p hybridisation. Here, NR suggests this effect is limited within the first 3 nm of the samples and GIXAS shows that La acts as a weak transition metal and, the Ti 3d states in the conduction band shows signs of disorder, due to vacancy generation and changing O/N-B-O/N dihedral bond angles. Where the charge around Ti is conserved. These observations can be explained by increases in surface hydrophilicity and the formation of a superficial OH/O(OH) surface layer. Typically observed and beneficial for the perovskite oxides<sup>57</sup>. However, it seems in the presence of N, the OER intermediates adopt a more counterproductive role with respect to LTON. Where nitrogen is lost from the lattice structure in the surface layer(s), and remains chemisorbed on the surface as  $\text{N}_2$  and  $\text{NO}_x$  species.<sup>70</sup>

Our findings support the idea that that La behaves as a transition metal although, a weak one, compared to Ti. It is likely then that the formation of LaOH/LaO(OH) would then not only contribute to overall  $\text{O}_2$  evolution<sup>144</sup> during the OER, but also help to stabilise and/or minimise, vacancy induced surface reconstruction.<sup>145</sup> However, as discussed for Ti, it then can also facilitate  $\text{N}_2/\text{NO}_x$  formation and drive the N loss from the surface layer on the Ti site.

### 3.10. Experimental

#### Thin film deposition

The LTON films were grown using a modified pulsed laser deposition (PLD) method called Pulsed Reactive Crossed-beam Laser Ablation (PRCLA) previously described here<sup>12</sup> using a KrF excimer laser (Lambda Physik LPX 300, 30 ns pulse width,  $\lambda = 248$  nm) to ablate a target of La<sub>2</sub>Ti<sub>2</sub>O<sub>7</sub> fabricated in our laboratory. The target to substrate distance was set at 50 mm. A laser fluence of 3 J/cm<sup>2</sup> with a laser repetition rate of 10 Hz was applied. Commercially available (001)-orientated MgO was used as a substrate (10 x 10 x 1 mm). Platinum paste was applied between the substrates and heating stage to provide good thermal conductivity. The substrate temperature was set at 750°C measured via a pyrometer. N<sub>2</sub> partial pressure of 8.0x10<sup>-4</sup> mbar was set via a gas inlet line to the vacuum chamber. NH<sub>3</sub> gas jets were injected through the piezo controlled nozzle valve of the gas pulse. The opening time of the nozzle valve was set at 400  $\mu$ s and the delay between the valve closing and the laser pulse was set at 30  $\mu$ s. The titanium nitride current collector layer was grown by conventional PLD using a commercially available TiN target under vacuum with a base pressure of ca. 5x10<sup>-6</sup> mbar. The substrate temperature was set at 750°C. A laser fluence of about 3 J/cm<sup>2</sup> with a laser repetition rate of 10 Hz was applied.

#### Photoelectrochemical characterisation

Photoelectrochemical (PEC) measurements were performed using a three-electrode configuration. The working and counter electrode were the LTON thin films and Pt wire respectively. A KCl saturated Ag/AgCl electrode was used as the reference. An aqueous solution of 0.5 molar NaOH (pH = 13) was used as an electrolyte. For the electrical contact of the LTON films, on one side of the films a small section of LTON was carefully removed to expose the TiN current collector to apply the electrical contact to the potentiostat (Solatron 1286). The electrically connected area was then insulated with epoxy and the sample then immersed into the electrolyte. The samples were illuminated with a 150W Xe arc lamp (Newport 66477) with an AM 1.5G filter with an output intensity of 100 mW cm<sup>-2</sup>. To measure the dark and light current a chopper was used to intermittently block the irradiation of the

sample. The potentiodynamic and potentiostatic measurements were performed at a scan rate of  $10 \text{ mV s}^{-1}$ .  $\text{IrO}_2$  nanoparticles were deposited by immersion in an  $\text{IrO}_2$  colloidal solution for 30 minutes. The  $\text{IrO}_2$  solution was prepared by hydrolysis of  $\text{Na}_2\text{IrCl}_6 \cdot 6\text{H}_2\text{O}$  (0.010 g) dissolved in  $\text{H}_2\text{O}$  (50 mL), and the pH was adjusted to 11-12 with  $\text{NaOH}$  (1M). The solution was heated at  $80^\circ\text{C}$  for 30 min and cooled to room temperature by immersion in an ice water bath. The pH of the cooled solution was adjusted to 10 with  $\text{HNO}_3$ . Subsequent heating at  $80^\circ\text{C}$  for 30 min resulted in a blue solution containing colloidal  $\text{IrO}_2$ .

### **Chemical Composition**

Metal ratios, oxygen content and film thickness were determined by Rutherford Backscattering (RBS). Measurements were performed using a 2 MeV He beam and a silicon PIN diode detector. Data was analysed using RUMP.<sup>43</sup> Nitrogen-to-oxygen ratios were determined by Elastic Recoil Detection Analysis (ERDA) using a 13 MeV  $^{127}\text{I}$  beam, time-of-flight spectrometer and gas ionisation detector.

### **Crystalline Properties**

XRD measurements were performed using a Bruker-Siemens d500 X-ray Diffractometer with characteristic  $\text{Cu K}_\alpha$  radiation 0.154 nm. Unlocked coupled theta-2theta scans were performed to determine the out-of-plane orientations of the films. Grazing incidence detector scans (theta=1) were also performed to determine whether a film crystalline quality is epitaxial, textured or polycrystalline.

### **Transmission electron microscopy**

TEM specimens were prepared by Focused Ion Beam (FIB) lift-out technique using a Thermofisher Scientific Helios UC instrument operated at 30 kV at the beginning of preparation followed by 5 kV and 2 kV for the final cleaning. The HAADF and Electron Energy Loss Spectroscopy images were collected with a Thermofisher Scientific (former FEI) Titan 80-300 environmental TEM operated at 300 kV, equipped with a Gatan Imaging Filter Quantum 965 ER.

### **Neutron Reflectometry**

Neutron reflectivity (NR) measurements were performed at the reflectometer AMOR at SINQ, Paul Scherrer Institut in Switzerland.<sup>44</sup> There the neutron beam is focused to the sample by elliptic reflectors leading to a divergence of 1.6°. The angular resolution is realised via the position sensitive detector. The intensity of the reflected neutron beam from the sample is measured as a function of the scattering angle and the time-of-flight from the chopper to the detector. The wavelength resolution was 5% and measurements were performed over a Q-range (1/Å) ranging between 0.005 and 0.1.

### **X-ray Absorption Spectroscopy**

XAS measurements were performed at the SuperXAS beamline at the SLS, Paul Scherrer Institut in Switzerland. The energy resolution was optimised using (111)-Si monochromator crystals. Energy calibration was performed using a thin Ti reference foil. A focused beam was used with a spot size of 100 x 100 μm<sup>2</sup>. The samples were mounted in grazing incidence to the incoming X-ray beam, with an incident angle between 0-1 degrees. XAS spectra were obtained in fluorescence yield using a 5 element SDD detector situated at 90 degrees to detect fluorescence. Data analysis was performed using the Athena and Larch software packages.<sup>45, 46</sup>



### 3.11. Appendix

#### Transmission Electron Microscopy (TEM) cross sectional image for a LTON film.

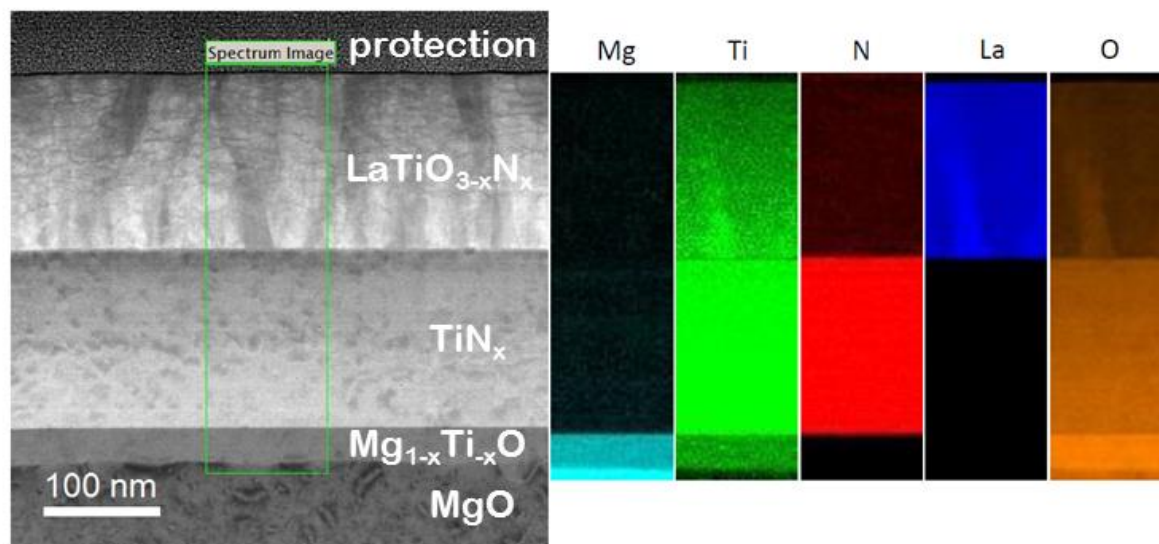


**Fig. 3.8.** Transmission Electron Microscopy (TEM) cross sectional image for a LTON film.

The TEM cross image (Fig. 3.8) signifies there is an additional layer/interface at the substrate-TiN interface. Electron energy spectroscopy (EELS) was able to determine the presence of the elements and could determine that this additional layer comprised on Mg, Ti and O. During growth of the sample, small amounts of Ti diffused into the MgO substrate and O diffused from the MgO substrate into the TiN layer.

#### La $L_3$ XANES peak fitting analysis

The The centroid positions of the peak fits (Fig. 3.9) show that after PEC in the bulk La centroid position shifts to lower energy by ca. 0.1 eV. With the co-catalyst, the centroid position remains unchanged. At the surface, the opposite trend is observed where after PEC without the co-catalyst the centroid position shifts to higher energy ca. 0.15 eV. Again, in the presence of the co-catalyst this shift is prevented (within error). Interestingly the centroid positions follow opposite trends yet the FWHMs follow the same trend.

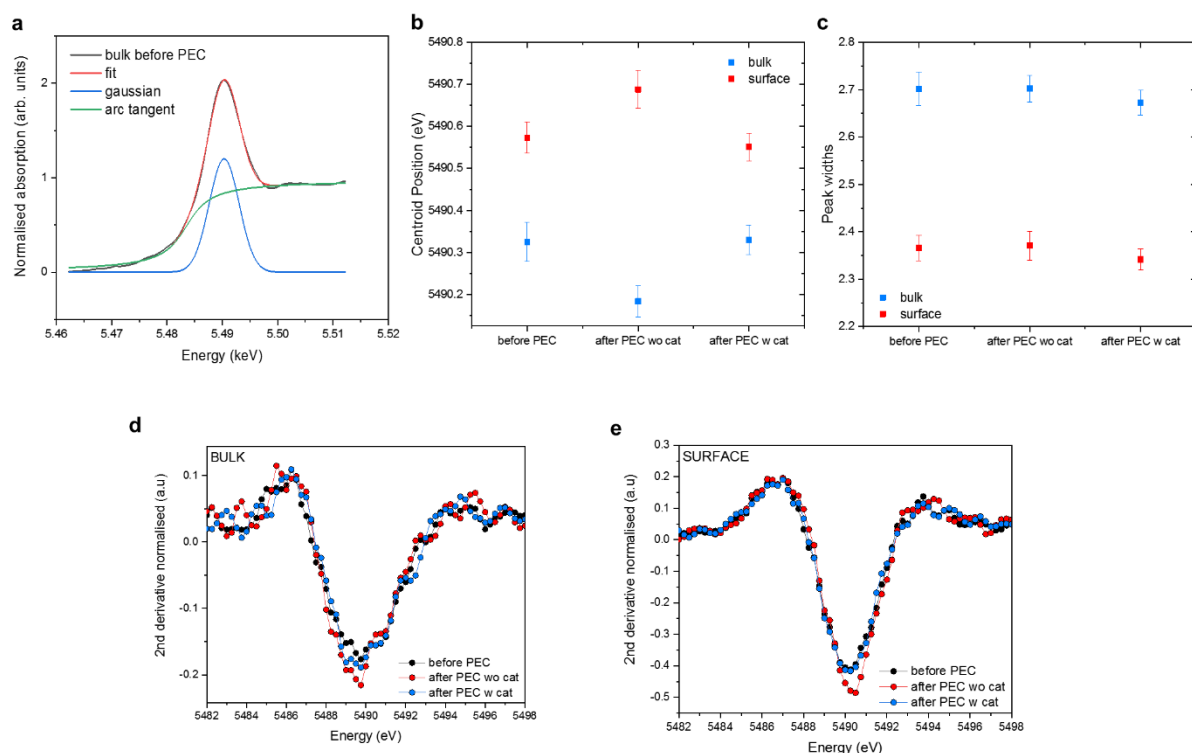


**Fig. 3.9.** (a) example of peak fitting for one of the La L<sub>3</sub> spectra, (b) centroid position of peak for each spectra from figure 3.6b-c, (c) peak FWHM, (d) second derivative for bulk XANES measurements, (e) second derivative for surface XANES measurements.

It can be seen that the peak widths in the bulk and surface measurements for LTON have FWHM ranges approximately between 2.65-2.75 and 2.3-2.4 respectively. However, comparing bulk vs surface is complicated since the bulk measurements suffer from dampening due to self-absorption in the thin film. The bulk measurements can be compared to one another performed at the same probe depth as the self-absorption effect would be equal for each measurement. It is also of note that the peak FWHMs do not change by very significant amounts and are within error. Compared to<sup>137</sup>, which looks at FWHM shifts of ca. 0.5 eV for differently coordinated species. Therefore although interesting, this approach may not be as useful/accurate enough as suggested to compare the coordination of La to further our understanding. A second study<sup>138</sup> looked at the white line intensity with respect to symmetry/disorder effects by changing coordination. They note differences in the second

derivatives between species due to changing coordination and degree of disorder of the La octahedral by looking at symmetry with respect to the  $t_{2g}$  and  $e_g$  splitting.

From the  $\text{LaTiO}_x\text{N}_y$  measurements it can be seen there are no significant changes again in the second derivatives plots after PEC without a catalyst. There is no evidence of strong disorder or symmetry changes of La at the surface or bulk before and after PEC just centroid position shifts in energy. There is a slight difference comparing the bulk and surface La – but one has to be wary comparing bulk and surface due to self-absorption. However, the bulk shows slight band splitting with two peak contributions whereas the surface shows one peak contribution. Following the logic bulk La would be less disordered than La at the surface. Which one would expect since surface terminations lead to changes in coordination compared to the bulk.

**Supplementary Tables****Table 3.** Neutron reflectometry layer fitting model before PEC

Parameter	Thickness(nm)	composition
LTON Surface	1.59	La1.03 Ti0.97 O2.7 N0.3
LTON bulk 1	28.40	La1.03 Ti0.97 O2.6 N0.4
LTON bulk 2	15.07	La1.03 Ti0.97 O2.5 N0.5
LTON bulk 3	58.17	La1.03 Ti0.97 O2.4 N0.6
TiON 2	12.09	Ti1 N 0.9 O0.1
TiN	87.69	Ti1 N1
TiON	19.00	Ti1 N0.95 O0.05

**Table 4.** Neutron reflectometry layer fitting model after PEC

Parameter	Thickness(nm)	composition
LTON Surface	4.49	La1.03 Ti0.97 O3
LTON bulk 1	5.34	La1.03 Ti 0.97 O2.9 N0.1
LTON bulk 2	37.50	La 1.03 Ti0.97 O2.8 N0.2
LTON bulk 3	49.26	La1.03 Ti0.97 O2.4 N0.6
LTON bulk 4	7.70	La1.03 Ti0.97 O2.42 N0.58
TiON 2	12.59	Ti1 N0.9 O0.1
TiN	87.89	Ti1 N1
TiON	18.71	Ti1 N0.95 O0.05

## Chapter 4: Oxygen and Nitrogen, the last two puzzle pieces

### 4.1. Preamble

This chapter looks at the surface modifications at the solid-liquid interface that occur during photoelectrocatalytic water splitting with respect to oxygen and nitrogen using X-ray photoelectron spectroscopy (XPS) for the oxynitride  $\text{LaTiO}_x\text{N}_y$ .

The XPS analysis for  $\text{LaTiO}_x\text{N}_y$  thin films has previously been published in *Advanced Functional Materials* and can be found here:

Pichler M, Si WP, Haydous F, Tellez H, Druce J, Fabbri E, *et al.*  $\text{LaTiO}_x\text{N}_y$  Thin Film Model Systems for Photocatalytic Water Splitting: Physicochemical Evolution of the Solid-Liquid Interface and the Role of the Crystallographic Orientation. *Advanced Functional Materials* 2017, **27**(20). <https://doi.org/10.1002/adfm.201605690>

However, the XPS analysis was not the main focus of the aforementioned manuscript, and without the benefit of hindsight. In conjunction with the previous findings for LTON in chapters 2 and 3, in this chapter we re-visit the XPS of LTON. To look again, whilst bearing in mind, the information we have obtained from the previous two chapters, to fully extract as much information as possible. The analysis and discussion included in this chapter will also be used to support chapter 5.

## 4.2. Introduction

In XPS, the photoemission process occurs according to the photoelectric effect (Eq.4

.1) described in Fig. 4.1.

$$E_B = E_K - h\nu - e\phi \quad (4.1)$$

Where, upon the absorption of an X-ray by an atom or molecule, an electron is then emitted from the sample with energy ( $E_K$ ). The magnitude of  $E_K$  depends on the excitation energy ( $h\nu$ ) and the binding energy ( $E_B$ ) of the ejected electron.

By measuring the  $E_K$  of the photoelectron with a hemispherical analyser (Fig. 4.1a), the  $E_B$  of the electron can be determined. Since the  $E_B$  depends on a number of factors, XPS provides the following information: a) elemental specificity – which element the electron was ejected from, b) orbital specificity – which orbital the electron was ejected from, and (c) the chemical state - the chemical environment of the electron.

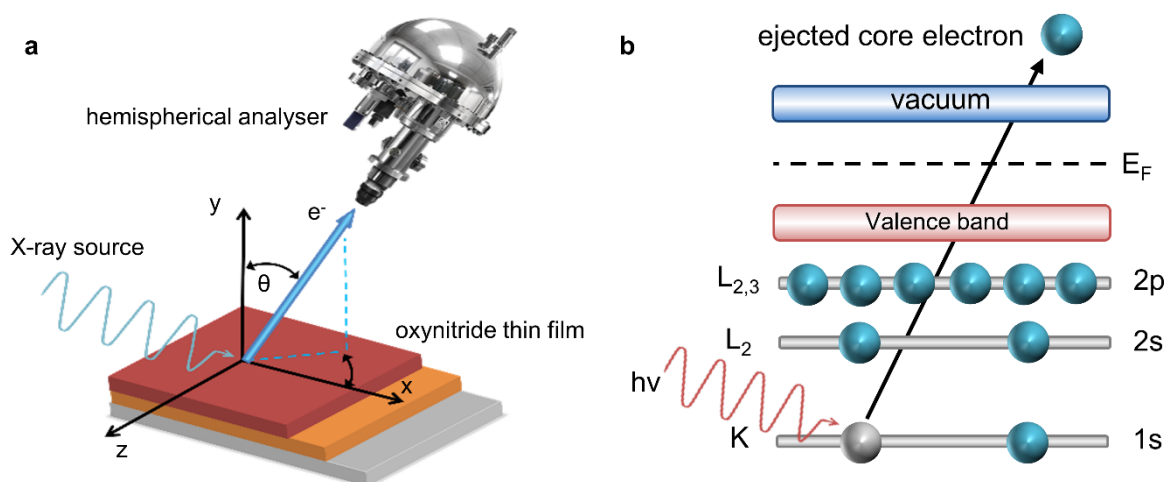


**Fig. 4.1.** (a) Schematic of an XPS experiment showing the photoemission, (b) the photoemission process.

In chapters 2 and 3, we discuss the surface modification of the oxynitride LTON thin films surface and electronic structure with respect to the cations, La and Ti. However, the energies of the anions, O and N, are too low to measure at a hard-XAS beamline, which is required to probe the cation energy ranges (chapter 3) and for *operando* studies in liquid environments (chapter 5). SX-ARPES provides indirect information regarding the degree of hybridisation between the cations and the O and N states, as discussed in chapter 2.

Whereas, XPS can provide direct information regarding O and N along with, La and Ti, for the LTON thin films *ex-situ*. In the following sections, the XPS analysis of LTON thin films before and after PEC characterisations are discussed with respect to the findings from chapters 2-3.

### 4.3. Oxygen

The before and after PEC comparison for the oxygen, O1s spectra are included in Fig. 4.2a, shown in blue and red, respectively. After PEC, there is a slight reduction in the main peak intensity, which corresponds to the lattice – O bond. There is a shoulder feature at ca. 532.5 eV that shifts to lower energy and increases in intensity after PEC. The shoulder itself also becomes less asymmetric on the higher energy side. Peak fitting analysis has been included and the fitting parameters are included in the appendix (section 4.8). For reference for peak fitting and discussion, sourced literature reported  $E_B$  ranges are included underneath the peak fit plots (Fig.4.2). The reported  $E_B$  and cited reference are included in the appendix.

The cumulative area for the O1s peak fitting suggest that after PEC there is an increase in the total oxygen content by ca. 17% on/at the LTON surface. The total increase in oxygen is due to the increased concentration of O species under OER conditions adsorbing/chemisorbing on the surface. A summary of O binding states and energies reported in literature are summarised in Fig. 4.2c-d.

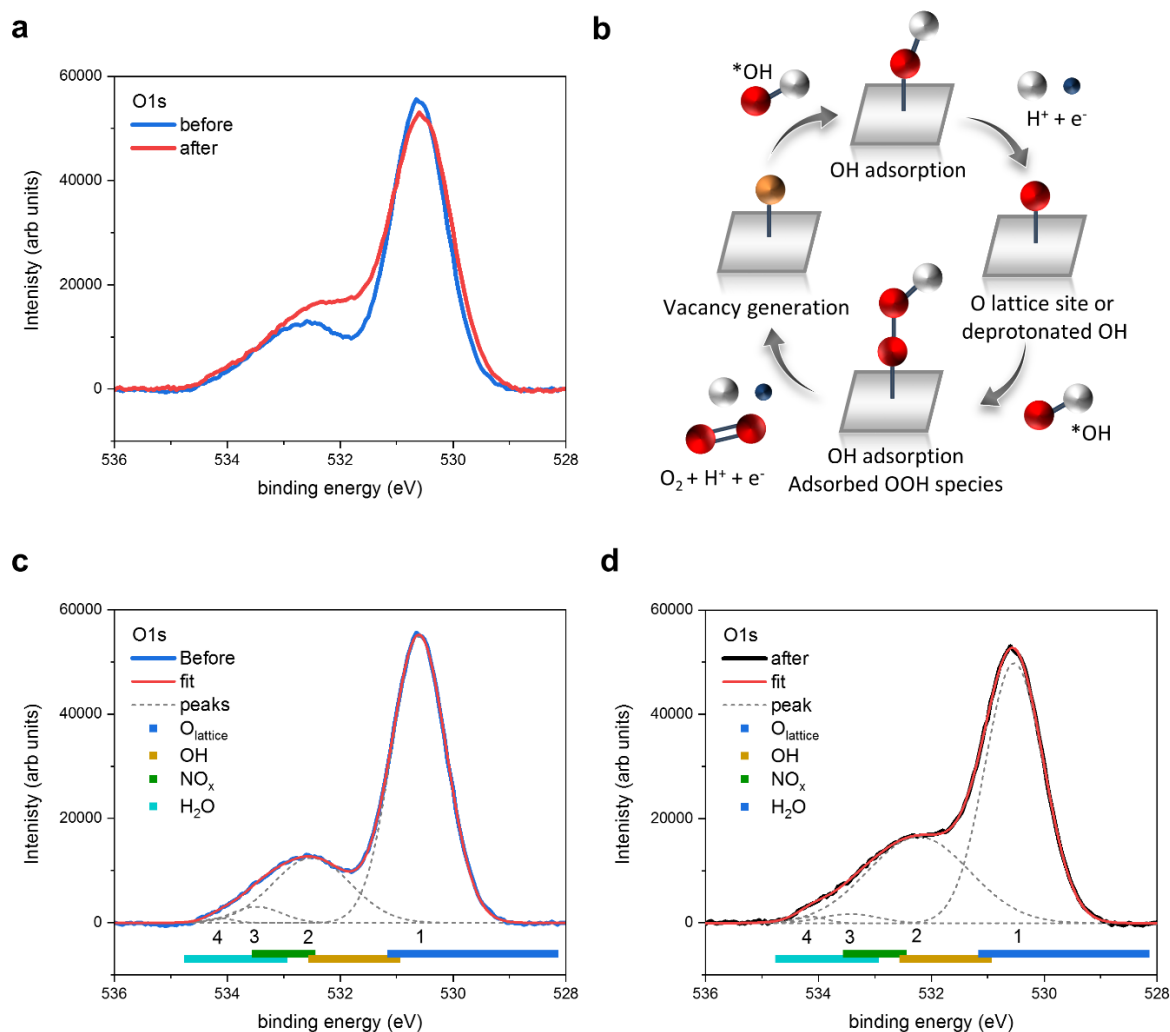


**Fig. 4.2.** (a) O1s XPS spectra before and after PEC comparison shown in blue and red respectively, (b) schematic representation of the OER mechanism, (c) peak fitting before PEC, (d) after PEC.

### Peak 1:

This peak corresponds to the lattice oxygen bond at ca. 530.6 eV. After PEC, there is a slight decrease in area and intensity yet a small increase in the FWHM suggesting that oxygen in the lattice structure is lost. This is likely due to  $O_2$  evolution and vacancy generation during OER reaction or the Lattice Oxygen Evolution Reaction (LOER).<sup>22</sup> Yet total oxygen contents increase due to adsorbed O species.



**Peak 2:**

This peak at ca. 532.5 eV would correspond to the metallic-OH environment which, is expected when exposed to ambient conditions. After PEC, there is ca. a 30% increase in both, the peak area and the FWHM. In conjunction, with a reductive shift to lower energy by ca. 2.8 eV. This is likely due to the changes that occur with respect to O and OH during the OER (Fig. 4.2d). Where, chemisorbed O would show different shielding to its OH counterpart; this would shift the binding energy as well as contributions to the FWHM increase.

**Peak 3:**

This peak at ca. 533.4 eV could represent a NO<sub>x</sub> type of environment according to the references. Discussion regarding nitrogen is included in the following section (4.4).

**Peak 4:**

This peak at ca. 534.1 eV corresponds to chemisorbed H<sub>2</sub>O on the surface. There is a small increase in this peaks contribution comparing with the after PEC sample. As expected, since the sample was exposed to the aqueous electrolyte and evolved O<sub>2</sub> at the surface.

#### **4.4. Nitrogen**

The nitrogen, N1s XPS spectra are included in Fig. 4.3a, comparing before and after PEC, shown in blue and red, respectively. Before PEC, four peaks are ascribed to the N1s spectrum (part b). After PEC (part c), there is a decrease in intensity of the main peak situated at ca. 397 eV. Followed by a slight change in ratios of all peaks. Two additional peaks not present in the before PEC spectra can be seen at ca. 403 eV and 408 eV. The peak fitting parameters are included in the appendix (section 4.8).

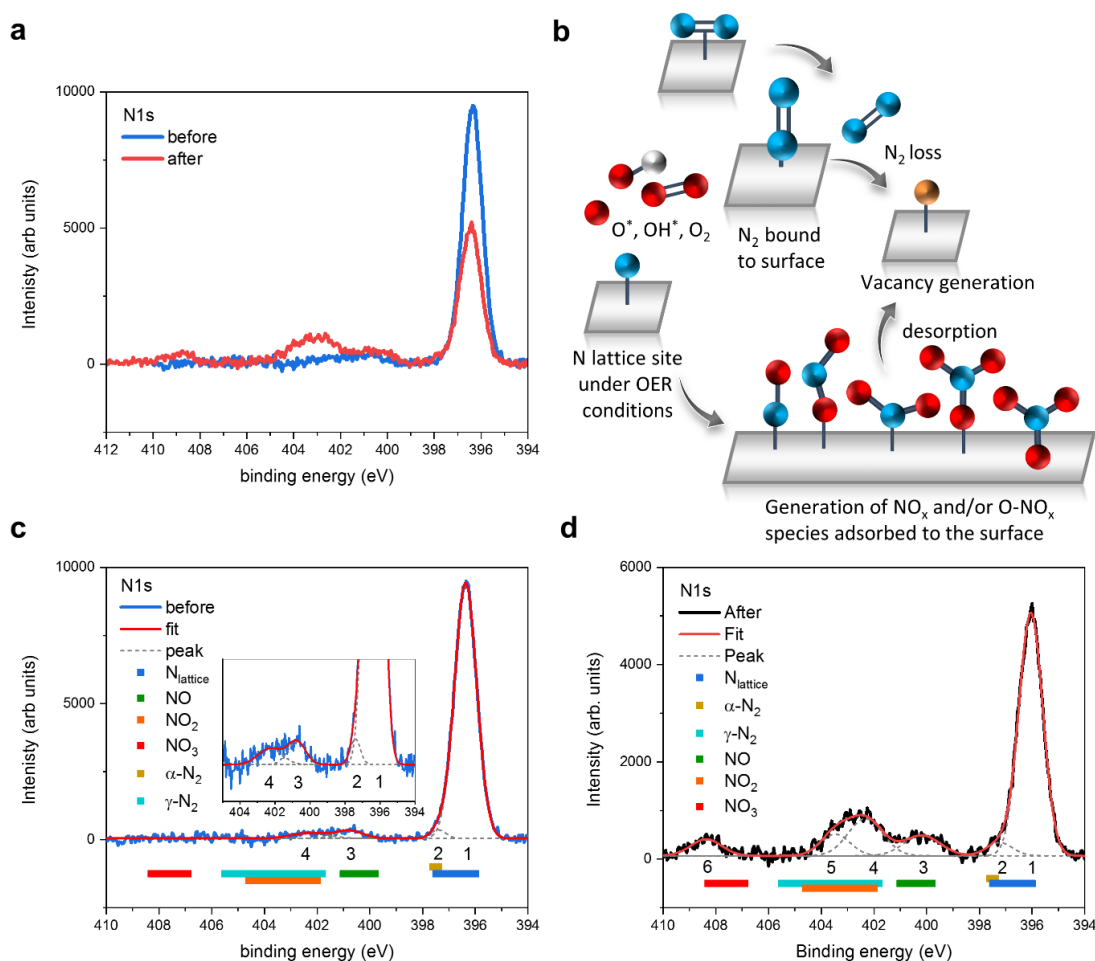


**Fig. 4.3.** (a) N1s XPS spectra before and after PEC comparison shown in blue and red respectively, (b) schematic representation of suggested changes to N states, (c) peak fitting before PEC, (d) after PEC.

### Peak 1:

This is the lattice Ti-N bond of the oxynitride situated at ca. 396.4 eV. After PEC, the FWHM increases slightly, suggesting slight disorder of the Ti-N bond lengths/angles of the  $Ti(O/N)_6$  octahedra. The area of the peak almost halves after PEC, suggesting significant amount of N leaves the lattice structure and remains either interstitial or chemisorbed – evidenced by the changes in the intensities of peaks 1-4, in addition to the emergence of 2 more peaks after PEC.

However, the cumulative areas of the N1s spectra suggest a loss of ca. 8% of the total N content at the surface.

**Peak 2:**

Literature suggests that this peak corresponds to chemisorbed  $\alpha$ -N<sub>2</sub> (Fig. 4.3). Before PEC, this contributes to ca. 2.5 % of the total N content. After PEC, this peak contribution increases by ca. 60 % suggesting that the applied potential and OER drives the loss of N from the lattice which is partially retained in the form as chemisorbed N<sub>2</sub>. The contribution of N<sub>2</sub> increases from ca. 2.5 % to ca. 4.5 % of the remaining total N content after PEC.

**Peak 3:**

Literature suggests that this peak corresponds to chemisorbed NO on the surface. After PEC, this peak contribution almost doubles. Perhaps signaling that after PEC small amounts of chemisorbed NO on the surface is formed/bound at the surface. The slight reductive shift could be due to the NO leaving the lattice structure and remaining chemisorbed to the surface. It is also worth noting that NO could be orientated differently on the surface, slightly deshielding the N.

**Peak 4:**

This represents chemisorbed N<sub>2</sub> on the surface of the oxynitride, which shows ca. a 3-fold increase after PEC. This would also agree with the loss of lattice N in peak 1 but the retention of the majority of the N content as chemisorbed N<sub>2</sub> and NO<sub>x</sub> species.

**Peak 5:**

This peak is assigned to chemisorbed NO<sub>2</sub>. Since this peak was only observed after PEC, and in conjunction with the large increase in NO (peak 3), the photocatalytic formation of NO<sub>2</sub> is more likely.

### Peak 6:

This peak is assigned to chemisorbed  $\text{NO}_3$ . Again like peak V, this peak was only observed after PEC, perhaps with the large increase in NO (peak 3) and  $\text{NO}_2$  (peak 5) the formation of  $\text{NO}_3$  ads is more likely.

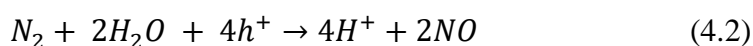
### The uncertainty with assigning peaks 4 and 5

In Fig. 4.3c-d, we can see that there are large ranges from ca. 401-406 eV for chemisorbed  $\gamma\text{-N}_2$  and chemisorbed  $\text{NO}_2$ . Therefore, it is hard to confidently, describe these two chemisorbed states to the two peaks that lie in this range. That said for this work we ascribe peak 4 to chemisorbed  $\gamma\text{-N}_2$  and peak 5 to chemisorbed  $\text{NO}_2$ . The justification for these assignments is as follows:

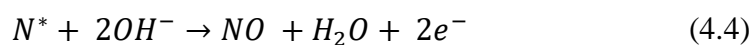
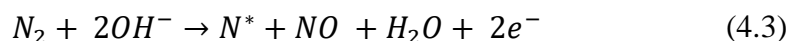
- $\alpha\text{-N}_2$  is slightly lower in energy than NO, therefore, it is assumed  $\gamma\text{-N}_2$  is also lower than  $\text{NO}_2$ .
- Since there is suggestion of  $\alpha\text{-N}_2$  before PEC, we would expect  $\gamma\text{-N}_2$  also to be present before PEC.
- Before PEC there is no evidence of peaks 5 and 6 – this could be the result of the photocatalytic formation of  $\text{NO}_2$  and  $\text{NO}_3$  during operation conditions.

For the oxynitride LTON, we observe increased hydrophilicity (XPS and SX-ARPES). However, contrary to oxides<sup>57</sup>, for oxynitrides this superficial BOH/BO(OH) enriched surface layer may have complications. We observe in the N 1s XPS spectra, the formation of  $\text{N}_2/\text{NO}_x$  chemisorbed species, which suggests, competitive reactions between the surface lattice N and the OER intermediates. Here the focus of discussion will be on the PEC nitrogen evolution reactions at the surface of the oxynitride, since the literature on this topic is scarce. Although, this process seems to have important consequences on the efficiency of the oxygen and hydrogen evolution half reactions.

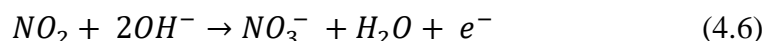
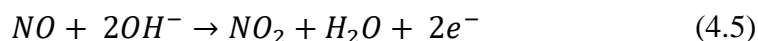
Photocatalytic nitrate formation on Ti dioxide surfaces irradiated by UV or sunlight irradiation under atmospheric N<sub>2</sub> and O<sub>2</sub> has been discussed by Yuan et al.<sup>99</sup> Where, the photogenerated holes on the Ti semiconductor surface catalyse the intermediary NO<sub>x</sub> species according to the following reactions:



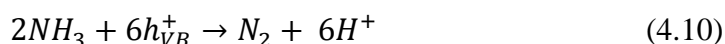
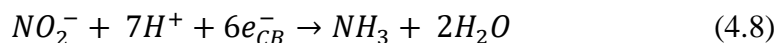
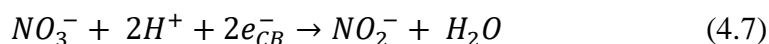
Dai et al<sup>101</sup> recently looked at the nitrogen oxidation reaction (NOR) catalysed by Fe/Co spinel oxides in alkaline electrolyte. Where they show that adsorbed N<sub>2</sub> is oxidised to intermediate NO<sub>x</sub> species by the adsorbed OH and the OER intermediate O(OH):



Where the intermediate NO<sub>x</sub> species are oxidised as follows:



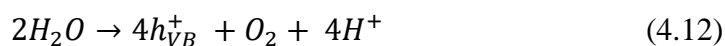
With the aid of theoretical calculation also, the authors note that Co shows increased hybridisation with the O 2p states, which aids in the stabilisation of OH<sup>-</sup> adsorption. This superficial CoO(OH) enriched surface layer has a beneficial effect on the OER for the oxides.<sup>57, 101</sup> However, in the presence of surface nitrogen based species, the stabilised CoO(OH) contribute to both the NOR and OER.<sup>101</sup> Kato and Kudo<sup>94</sup> looked at numerous tantalate oxide photocatalysts, and the authors observed nitrate reduction under UV irradiation in an aqueous environment. Where nitrate forms intermediate nitrite, dinitrogen and ammonia, even in the absence of a co-catalyst or reducing agents. The authors proposed the following mechanisms:



Where the photogenerated electrons in the CB reduce the nitrate and nitrite species (Eq. 4.7-4.8). Alternatively, the nitrate species can undergo photochemical decomposition (Eq. 4.9). The photogenerated holes in the VB can then oxidise ammonia to form dinitrogen (Eq. 4.10), which can form NO<sub>x</sub> species according to Eq. 4.1-4.4.

Wei et al.<sup>100</sup> recently reported increased photocatalytic activity for nitrite reduction on Ni<sub>2</sub>P modified tantalum nitride and tantalum oxynitride. Where the photogenerated holes in the VB of the two materials are involved in the water oxidation reaction (Eq. 4.12) and, the photogenerated electrons in the CB transfer to the Ni<sub>2</sub>P states where they are involved in the photocatalytic reduction of NO<sub>3</sub>.

Since the photocurrent is proportional to stoichiometric 2:1 H<sub>2</sub>/O<sub>2</sub> generation, according to the two half reactions of the water splitting process on a SC photocatalyst (Eq. 4.11-4.12).



As the applied potential increase and the forward reactions for O<sub>2</sub> generation proceed. O<sub>2</sub> generation should dominate since the nitrogen content at the surface is limited, compared to the high OH<sup>-</sup> content in the alkaline electrolyte. Once the nitrogen species desorbs from the surface, the OER could proceed on the now vacant active site and/or the adsorbed intermediates would no longer contribute to N<sub>2</sub>/NO<sub>x</sub> formation in competition.

## 4.5. Titanium

The titanium, Ti 2p XPS spectra are included in Fig. 4.4, comparing before and after PEC. Two peaks originate due to spin orbit coupling where the Ti 2p states are resolved as the  $2p_{3/2}$  (lower energy) and  $2p_{1/2}$  (higher energy) contributions. The spectra do not shift in position with respect to binding energy, suggesting that Ti does not change its formal oxidation state. Peak fitting analysis suggests two peaks contributions for both the  $2p_{3/2}$  (peaks 1 and 2) and  $2p_{1/2}$  (peaks 3 and 4) signals, the fitting parameters are included in the appendix (section 4.8). The two peaks suggest there are two environments for Ti:  $TiO_{5-x}N_{1+x}$  and  $TiO_6$  (Fig. 5.4b-c). There is no suggestion of titanium 3+ or mixed valence 3.5+, solely Ti 4+ in two different octahedra binding environments. Referencing to reported binding energies, we can assign the following peaks 1 and 3 to  $TiO_{5-x}N_{1+x}$ , and peaks 2 and 4 to a  $TiO_6$  environment. These peak positions do not shift in position after PEC suggesting that the valence state of Ti does not change. However, there are changes in the ratios of these peaks after PEC. These changes are likely due to the local structural change surrounding Ti when some nitrogen is lost and replaced with O changing the ratio of  $TiO_{5-x}N_{1+x}$  and  $TiO_6$  like environments in the oxynitride.

The splitting between peaks 1-3 and 2-4, both corresponds to 5.8 eV. For TiN (3+) the peak splitting is 6.0 eV and in  $TiO_2$  (4+) the peak splitting is 5.7 eV. This would support that Ti is more  $TiO_2$  like, with the 0.1 eV difference due to the N substitution and hybridisation with Ti, forming the oxynitride. After PEC, the peak splitting remains constant at 5.8 eV, also suggesting no oxidation or reduction of the titanium atoms. Further evidence for Ti stabilised in the 4+ and not mixed oxidation states is that upon the loss of nitrogen and replacing with O and even with O/N vacancy generation, Ti should reduce. Where,  $N^{3-}$  is replaced by either/or  $O^{2-}$  /  $Vo^{2+}$ . If we ascribe the peak contributions to 3+ and 4+, as seen common in literature. After PEC, one would expect the contributions of peaks 1 and 3 to increase and, peaks 2 and 4 should decrease. However, experimentally we see the opposite, suggesting N loss and increased O content, where the total electron density surrounding Ti does not change hence, why we observe no shift in the XPS or XAS spectra.

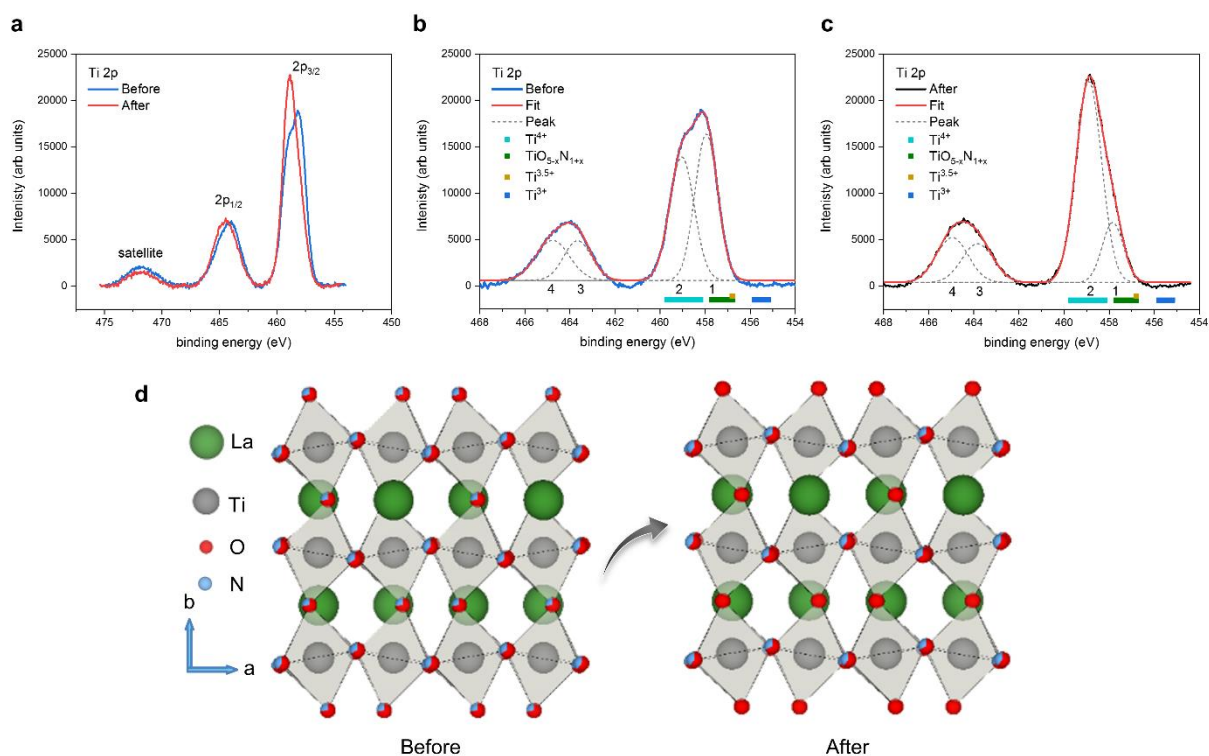


**Fig. 4.4.** (a) Ti 2p XPS spectra before and after PEC comparison shown in blue and red respectively, (b) peak fitting before PEC, (c) after PEC, (d) schematic representation of suggested changes to Ti octahedra.

### Titanium 3+ vs. Titanium 4+ debate

Suhadolnik et al.<sup>146</sup> show an example of titanium oxynitride (TiO<sub>x</sub>N<sub>y</sub>) samples measured by XPS where they report mixed oxidation states for Ti (2+, 3+, 4+), where it is apparent due to severe broadening of the Ti 2p peak, included below in Fig. 4.5. Where the difference in  $E_B$  between the 4+ and 3+ peak centroids corresponds to ca. 1.6 eV and between 3+ and 2+, ca. 1.2 eV (no access to the data). Avasarala and Haldar<sup>147</sup> looked at the electrochemical oxidation of TiN and noted broad Ti 2p XPS spectra due to the mixed oxidation states of Ti, included in Fig. 4.6 below. In LTON the peak separation between peak 1 and 2 corresponds to 1 eV, the separation does not change after PEC. Further evidence, that Ti in LTON has the formal 4+ oxidation state with a TiO<sub>6</sub> and a TiO<sub>5-x</sub>N<sub>1+x</sub> like environments. Neither reduced nor oxidised after PEC.



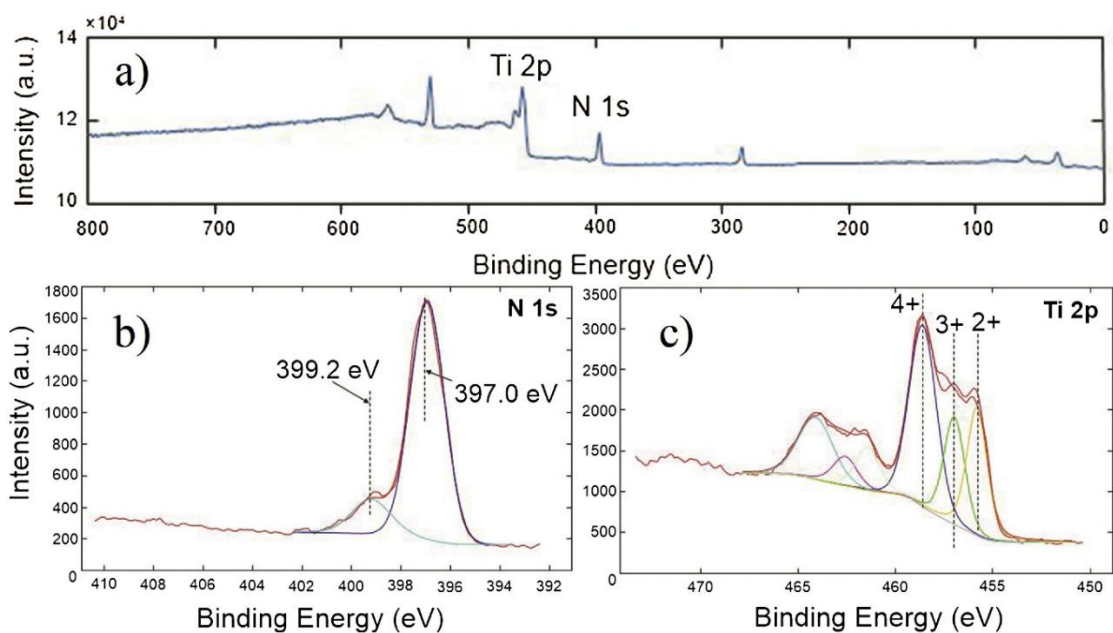


**Fig. 4.5.** (a) XPS spectra of titanium oxynitride electrocatalyst (a), N 1s spectrum (b) and Ti 2p spectrum (c). Reproduced from Ref<sup>146</sup>.

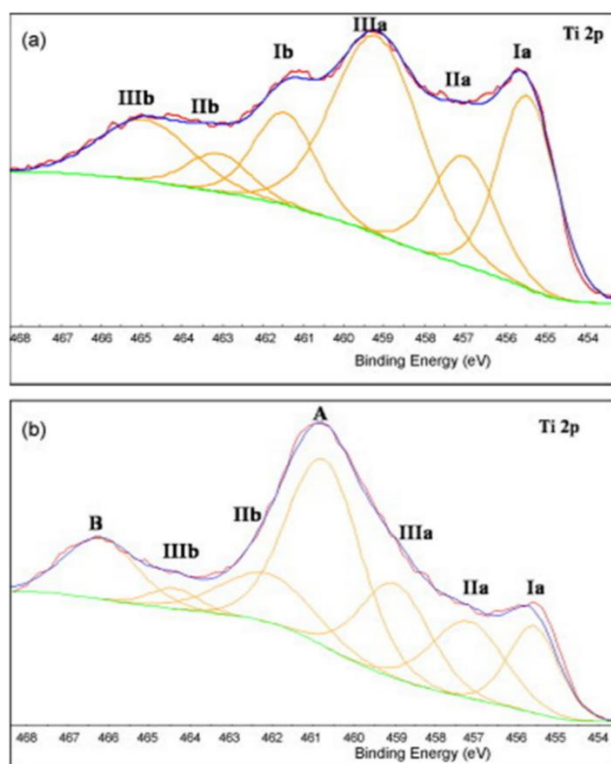


**Fig. 4.6.** Deconvoluted Ti 2p XPS spectra of: (a) untreated; (b) treated TiN NP electrode. Reproduced from Ref<sup>147</sup>.

## 4.6. Lanthanum

The La 3d spectra (Fig. 4.7) shows two doublet features due to spin-orbit coupling corresponding to the  $3d_{5/2}$  (835 eV) and the  $3d_{3/2}$  states (852 eV). The doublet features arise due to the three environments/final states after the photoemission of the La 3d electron. These correspond to  $3d^94f^0$  and  $3d^94f^1L$  bonding and the  $3d^94f^1L$  antibonding environments corresponding to solid, dashed and dotted lines respectively for both the  $3d_{5/2}$  and  $3d_{3/2}$  states. Where L represents charge donated from a ligand valence orbital, O 2p in this case. The peak separations  $\Delta E_1$  and  $\Delta E_2$  depend on the bonding and anti-bonding character of the interactions. Smaller energy differences reflect increased mixing and hybridisation between the La states and the ligand O2p states.

The peak fitting models shown in parts b and c are in good agreements with the data however, the La 3d spectra also include the contributions of lanthanum Auger peaks.<sup>148</sup> Since the XPS data was not measured using both Al  $K\alpha$  and Mg  $K\alpha$  radiation sources, the peak fitting models do not include the estimation of the Auger peaks. Therefore, due to uncertainty, we have not considered the peak areas, FWHM's and ratios.

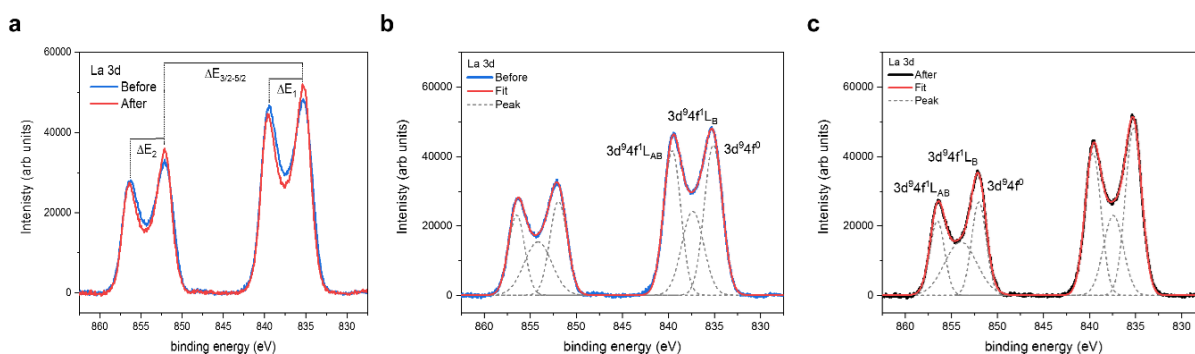


**Fig. 4.7.** (a) La 3d XPS spectra before and after PEC comparison shown in blue and red respectively, (b) peak fitting before PEC, (c) after PEC.

The peak separation,  $\Delta E_{5/2-3/2}$ , between the two main peaks remains constant. However, the peak separation for both doublets slightly increases in energy by ca. 0.1 eV. Due to the increased contributions of the  $3d^9 4f^1 L$  bonding final states (middle peaks). Where, there is increased charge transfer between the ligand and the La 4f states. This effect is also, reflected in the intensities of the two doublet peaks showing a decrease for the antibonding  $3d^9 4f^1 L$  contributions and an increase in the  $3d^9 4f^0$  main peaks. This suggests two things; changes in La – O 2p / N 2p hybridisation and secondly, changes in charge transfer between the L the 4f states after PEC. This, in conjunction with the SX-ARPES, and the XPS O 1s spectra, also suggests changes in La – O 2p hybridisation, after the loss of La - N 2p states.

The La 4d spectra before and after PEC comparisons are included in Fig. 4.8a. Two peaks can be seen at ca. 102.8 and 105.8 eV corresponding to the La  $4d_{5/2}$  and  $4d_{3/2}$  spin orbit coupling. As mentioned previously due to La auger peaks, and the fact that the peak fitting model should include a minimum of 6 considering the final states:  $4d^9 4f^0$  and the  $4d^9 4f^1 L$  bonding and antibonding states as previously discussed<sup>149</sup>. However, since many states overlap (Fig. 4.8b-c) there is a degree of uncertainty that should be taken into account. That said, qualitatively the peak separation increases slightly and the intensity of the antibonding final state contributions decrease, similar to the effect seen for the La 3d spectra.

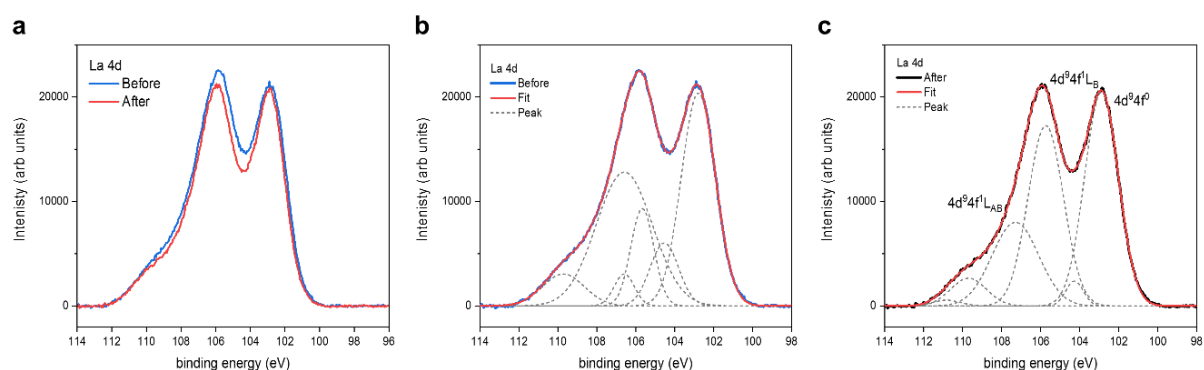


**Fig. 4.8.** (a) La 4d XPS spectra before and after PEC comparison shown in blue and red respectively, (b) peak fitting before PEC, (c) after PEC.

However, the antibonding states have greater intensity for the La 3d states compared to the La 4d states (Fig. 4.7-4.8), with respect to their ratios with the main peaks. This effect has

previously been described by <sup>149</sup> as a weaker interaction between the core hole and the 4f orbitals for the outer core levels with lower binding energy (4d vs 3d). Therefore, the 4f orbitals should have less hybridisation and interaction with the valence band states, explaining the lower intensities between the La 3d and La 4d states.

The La 4p spectra are included in Fig. 4.9, with peak fitting before and after PEC shown in parts b and c, respectively. Peak analysis of La 4p is again difficult, due to the final states and the fluctuation of the  $4p^1$  electron with d and f states upon photoemission of a core electron. The main peak is attributed to the final state  $4p^15d^0$ , the two satellites at higher binding energy correspond to the  $4p^15d^1L$  bonding and antibonding contributions (ignoring any f final state contributions). In general, lanthanum is complex due to the existence of the f orbitals. Where, the f final states create uncertainty in peak fitting. However, generally for the La 3d, 4d and 4p spectra we see a slight shift in energy of the main peaks by ca. 0.1 eV and a decrease in the antibonding satellites suggesting changing hybridisation with the N 2p and O 2p states.

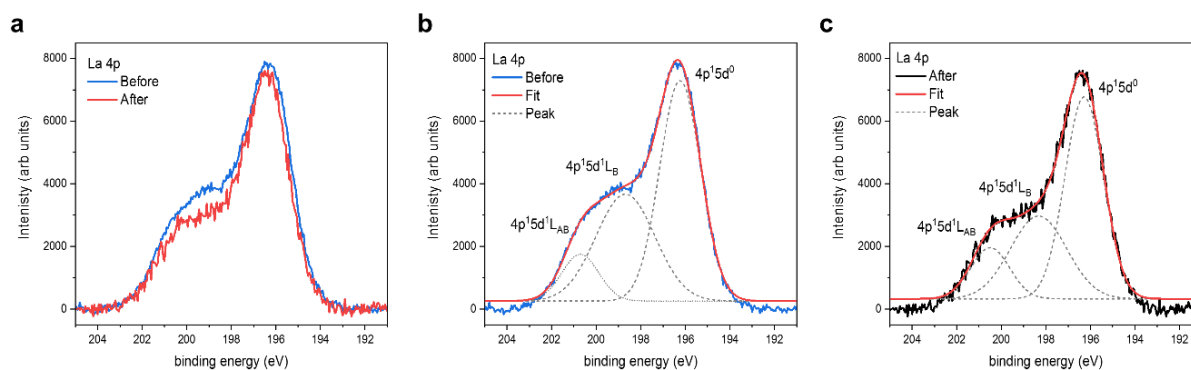


**Fig. 4.9.** (a) La 4p XPS spectra before and after PEC comparison shown in blue and red respectively, (b) peak fitting before PEC, (c) after PEC.

#### 4.7. Conclusion

The cumulative area for the O1s peak fitting suggests that, after PEC there is an increase in the total oxygen content by ca. 17% on/at the LTON surface. The total increase in oxygen is due to the increased concentration of O species under OER conditions adsorbing/chemisorbing on the surface. We observe in the N 1s XPS spectra, the formation of N<sub>2</sub>/NO<sub>x</sub> chemisorbed species, which suggests, competitive reactions between the surface lattice N and the OER intermediates.

As the applied potential increases and the forward reactions for O<sub>2</sub> generation proceed, O<sub>2</sub> generation should dominate since the nitrogen content at the surface is limited, compared to the high OH<sup>-</sup> content in the alkaline electrolyte. Once the nitrogen species desorbs from the surface, the OER could proceed on the now vacant active site and/or the adsorbed intermediates would no longer contribute to N<sub>2</sub>/NO<sub>x</sub> formation in competition.

The titanium, Ti 2p XPS peaks do not shift in position with respect to binding energy, suggesting that Ti does not change its formal oxidation state (as suggested in chapter 2 and 3). However, there are changes in the ratios of these peaks after PEC. These changes are likely due to the local structural change surrounding Ti when nitrogen is lost and replaced with O changing the ratio of TiO<sub>5-x</sub>N<sub>1+x</sub> and TiO<sub>6</sub> like environments in the oxynitride.

In general, the XPS, XAS and SX-ARPES data suggest an increase in La – O 2p hybridisation likely due to La – OH formation and secondly, changes in charge transfer between the La 4f states. We also observe changes in electron density (binding energy shifts), suggesting that La retains partial 5d<sup>1</sup> electron density and behaves like a transition metal, albeit a weak one. Where it is then likely then that the formation of LaOH/LaO(OH) would then not only contribute to overall O<sub>2</sub> evolution<sup>144</sup> but possibly also help to stabilise and/or minimise, vacancy induced surface reconstruction.<sup>145</sup> However, as discussed for Ti, it then likely would also facilitate in N<sub>2</sub>/NO<sub>x</sub> formation and drive the N loss from the surface layer(s).

## 4.8. Appendix

### C 1s XPS calibration

The XPS spectra in this work were all calibrated using the C1s peak signal situated at 285.9 eV for the comparison between before and after PEC characterisation. The C1s spectra is included below in Fig. 4.10a. The carbon signal arises, due to adventitious carbon (surface contamination of hydrocarbons) due to exposure to air. In part b, the time-dependent SX-ARPES measurements show small changes upon exposure to the X-ray beam, previously associated to the slight oxidation of hydrocarbons.

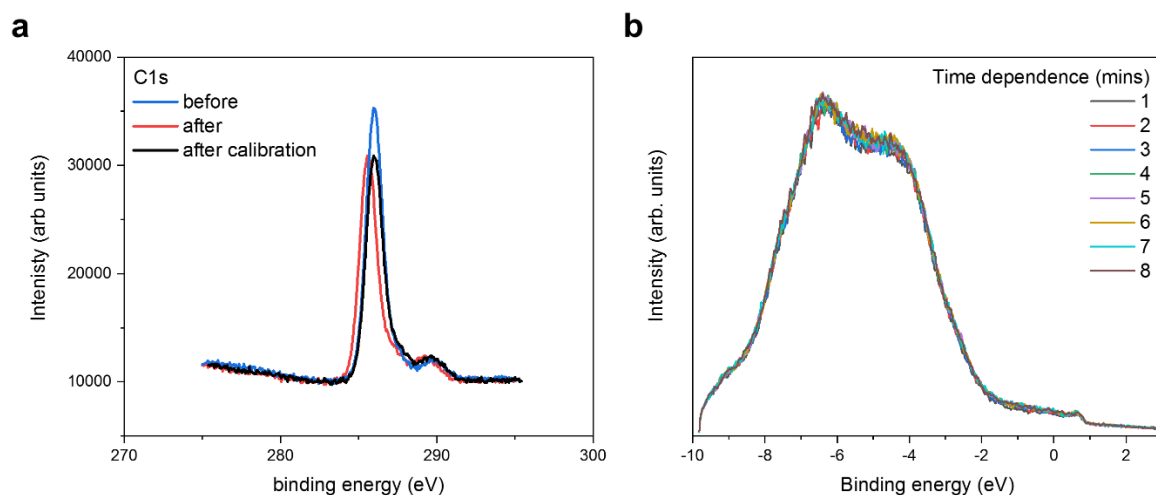


**Fig. 4.10.** (a) C 1s XPS spectra showing adventitious carbon, before and after PEC comparison used as calibration, (b) Angle-integrated plot of the LTON VB measured at the Ti L3 edge after exposure to the X-ray beam over time (as shown in Fig. 3.7).

## Supplementary Tables

**Table 5.** Peak fitting parameters for O1s before and after PEC

Component	Energy (eV)	Before PEC Area	FWHM	Energy (eV)	After PEC Area	FWHM
Peak 1	530.6	66186	1.13	530.5	64366	1.22
Peak 2	532.5	21127	1.62	532.2	36607	2.11
Peak 3	533.4	3165	1.02	533.4	1927	1.16
Peak 4	534.1	459	0.55	534.1	3569	0.58
		90937			106469	

**Table 6.** Literature sourced XPS data for O 1s. Where (L), (C) and (i) correspond to lattice, chemisorbed and interstitial respectively.

Peak	Component	Energy (eV)	Reference
1	TiO <sub>2</sub> (L)	528.2-531.1	150, 151, 152, 153, 154, 155, 156, 157, 158, 159, 160, 161
2	Ti-N-O(L)	531.0	156
		531.3	159
		531.4	150
		531.6	155
		531.6 - .7	162
		532	154
	OH	530.9-532	163
		531.3	159
		531.4	150
		531.5	157
3-4	NO <sub>x</sub> (c)	532.5-533.5	163
		533.2	164
	H <sub>2</sub> O(c)	533.0	160
		533.3	158
		533.7	161
		533.9	153
		534.7	165

**Table 7.** Peak fitting parameters for N1s before and after PEC

Component	Before			After		
	Energy (eV)	Area	FWHM	Energy (eV)	Area	FWHM
Peak 1	396.3	10012	0.99	396.4	5816	1.07
Peak 2	397.4	277	0.73	397.4	453	1.36
Peak 3	400.7	445	1.35	400.6	875	1.82
Peak 4	402.2	460	1.92	402.5	1439	1.65
Peak 5	-	-	-	403.6	785	1.46
Peak 6	-	-	-	408.3	644	1.59
		11092			10012	

**Table 8.** Literature sourced XPS data for N1s.

Peak	Component	Energy (eV)	Reference
1	N <sub>(L)</sub>	396-397.5	150, 164, 166, 167, 168, 169, 170, 171, 172, 173
2	$\alpha$ -N <sub>2(c)</sub>	397.5	164
3	NO <sub>(i)</sub>	399.8	170
	NO <sub>(c)</sub>	400	174
		400.4	169
		400.9	175
		401	168
4	$\gamma$ -N <sub>2(c)</sub>	401.8	150
		403	170
		405	164
		405.5	176
5	NO <sub>2(c)</sub>	402	168
		403.5	168
		403.6	173
		404.6	177
6	NO <sub>3(c)</sub>	406.9	178
		407	151
		407.2	171
		407.4	173
		408.3	



**Table 9.** Peak fitting parameters for Ti2p before and after PEC

Component	Energy (eV)	Before PEC Area	FWHM	Energy (eV)	After PEC Area	FWHM
Peak 1	457.9	21703	1.22	457.9	8563	1.15
Peak 2	459.0	20058	1.33	459.0	32203	1.35
Peak 3	463.7	8271	1.59	463.7	8552	1.74
Peak 4	464.8	10084	1.93	464.8	9830	1.75
		<u>60116</u>			<u>60148</u>	

**Table 10.** Literature sourced XPS data for Ti 2p<sub>3/2</sub>.

Peak	Component	Energy (eV)	Reference
	Ti 3+	455.2	179
		455.3	150, 171
		455.5	158, 159
		455.6	152
		455.8	162
		456.5	151
		456.7	170, 172
	Ti 3.5+		
		456.8	171
1	TiO <sub>5-δ</sub> N <sub>1+δ</sub>	456.8	158, 159
		457.1	152
		457.4	179
		457.6	162, 179
		457.7	172
2	Ti 4+		
		458.2	151
		458.3	154
		458.5	156
		458.6	171
		458.8	152, 153, 170
		458.9	158, 159, 172
		459.0	179
		459.1	150

**Table 11.** Peak fitting parameters for La 3d before and after PEC

<b>Component</b>	<b>Energy (eV)</b>	<b>Before PEC Area</b>	<b>FWHM</b>	<b>Energy (eV)</b>	<b>After PEC Area</b>	<b>FWHM</b>
Peak 1	835.1	106931	2.32	835.2	108443	2.11
Peak 2	837.3	72393	2.80	837.4	62195	2.54
Peak 3	839.6	97325	2.19	839.5	90121	2.06
Peak 4	851.9	63314	2.20	852.0	53497	1.86
Peak 5	854.1	57943	3.53	853.9	67021	4.12
Peak 6	856.5	50524	2.05	856.5	41953	1.84

**Table 12.** Peak fitting parameters for La 4d before and after PEC

<b>Component</b>	<b>Energy (eV)</b>	<b>Before PEC Area</b>	<b>FWHM</b>	<b>Energy (eV)</b>	<b>After PEC Area</b>	<b>FWHM</b>
Peak 1	102.8	45351	2.07	102.9	44850	2.05
Peak 2	104.0	2409	1.27	103.9	255	0.40
Peak 3	105.6	323	0.61	104.4	2137	0.98
Peak 4	105.7	49837	2.46	105.7	35055	2.08
Peak 5	107.5	24095	3.16	107.1	27705	3.00
Peak 6	109.9	2727	2.34	109.9	6802	2.35

**Table 13.** Peak fitting parameters for La 4p before and after PEC

<b>Component</b>	<b>Energy (eV)</b>	<b>Before PEC Area</b>	<b>FWHM</b>	<b>Energy (eV)</b>	<b>After PEC Area</b>	<b>FWHM</b>
Peak 1	196.2	17562	2.21	196.3	15590	2.11
Peak 2	198.7	13164	3.28	198.3	10542	3.25
Peak 3	200.7	4183	2.19	200.5	4761	2.35

## Chapter 5: Experimental platform for *operando* GIXAS at the solid-liquid interface

### 5.1. Preamble

This chapter focuses on the design and fabrication of a reactor cell for *operando* GIXAS at the solid-liquid interface. As a case example, we study the surface modification of SrTaO<sub>x</sub>N<sub>y</sub> oxynitride, building on what we have learnt from the previous chapters. Opening up, an experimental platform for *operando* GIXAS measurements at the solid-liquid interface of thin films, not limited to oxynitrides.

The results in this chapter will be submitted for publication by the following authors: Craig Lawley, Zahra Pourmand Tehrani, Adam H. Clark, Olga V. Safonova, Max Döbeli, Vladimir N. Strocov, Thomas J. Schmidt, Thomas Lippert, Maarten Nachtegaal and Daniele Pergolesi.

Entitled: “*Protagonists and spectators during photocatalytic solar water splitting with SrTaO<sub>x</sub>N<sub>y</sub> oxynitride.*” (In preparation).

### Author Contributions

Conceptualisation, C.L., A.C., O.S., M.N., and D.P.; Investigation, C.L., A.C., Z.P., O.S., V.S., M.D.; Formal Analysis, C.L., A.C., Z.P., V.S.; M.D.; Writing – Original Draft, C.L. and D.P.; Writing – Review & Editing, C.L., A.C., Z.P., O.S., M.N., V.S., M.D., T.S., D.P. and T.L.; Funding Acquisition, D.P., M.N., T.S., V.S., and T.L.; Supervision, D.P., M.N., T.S., V.S., and T.L.

## 5.2. Introduction

Independence from the reliance on fossil and nuclear fuels requires the sustainable production of green energy and chemicals. As an alternative, utilisation of solar energy is possible by several means: solar thermal applications,<sup>7</sup> the direct conversion to electricity (photovoltaic),<sup>8</sup> or storage in the form of chemical energy as solar fuels.<sup>10</sup> One promising clean energy carrier and renewable fuel source is hydrogen harvested from photoelectrochemical (PEC) water splitting.<sup>1, 2, 11</sup>

PEC water splitting requires the use of semiconductor (SC) photocatalysts that utilise solar light energy to generate electron/hole pairs. After reaching the surface, in contact with water, these charge carriers can be used to dissociate water molecules directly into molecular hydrogen and oxygen<sup>17</sup>. Perovskite oxynitrides are a promising class of SC materials for solar light driven water splitting. These materials have the general formula  $ABO_{3-x}N_x$  (where A can be La, Sr, Ba, Ca, etc., and the B site: Ti, Ta, or Nb for example). The substitution of N into the O site of the precursor oxides affect the energy position of the band edges, reducing the band gap down to the visible light energy range.<sup>180</sup> Moreover, in this class of compounds, the photogenerated electrons and holes, both possess enough energy to promote the hydrogen and oxygen evolution reaction, respectively.

The majority of studies to date focus on the characterisation of the photocatalytic properties of these materials in the form of powders,<sup>30, 63, 64</sup> since powder development and optimisation is the primary way to device design and engineering. However, with powder samples, probing specific material properties is challenging. For example, the polycrystalline oxynitride powders do not provide well-defined surfaces to allow detailed studies of the solid-liquid interface, where the electrochemical reactions take place. The understanding of the catalytic process at the solid-liquid interface of oxynitride materials is therefore limited, as a result. A way to circumvent this limitation is the growth of thin films. By physical or chemical vapour deposition methods, it is possible to fabricate thin films with well-defined and atomically flat surfaces,

therefore representing ideal model systems that allow the investigation of the surface and interface properties.

In this work, we present an *operando* study of the evolution of the photocatalyst semiconductor/water interface during photoelectrochemical solar water splitting using SrTaO<sub>x</sub>N<sub>y</sub> (STON) thin films. Grazing incidence X-ray absorption spectroscopy (GIXAS) coupled with modulation excitation (ME)-XAS were used to increase the surface sensitivity, whilst probing epitaxially grown STON thin films with a custom designed *operando* reactor cell. This technique and experimental setup allow us to probe, during operation conditions, the changes of the local chemical and geometric environment surrounding the A- and B-cations of perovskite oxynitrides near and at the solid-liquid interface.

Due to the attenuation of X-rays by the aqueous electrolyte, it is not feasible to extend this study to the O and N anions, since the O 1s and N 1s edges are too low in energy (543.1 eV and 409.9 eV, respectively). Therefore, complimentary *ex-situ* X-ray photoelectron spectroscopy (XPS) has been included in conjunction with *operando* GIXAS, to observe all four elements (Sr, Ta, O, and N) in their initial and final states. With this experimental strategy, we are able to show that it is possible to achieve a better understanding of the physicochemical processes occurring at the oxynitride-liquid interface, leading to a degradation of the photocatalytic activity. Our findings can be of great importance for the rational design of stable oxynitride SC's for solar water splitting

### 5.3. Photoelectrochemical Water Splitting

The splitting of water into molecular H<sub>2</sub> and O<sub>2</sub> is an energetically unfavourable reaction. It requires a standard Gibbs free energy change of + 237.2 kJ mol<sup>-1</sup>, which also corresponds to a potential of 1.23 eV per electron. Moreover, for both half reactions of the solar water splitting process to proceed, that is the hydrogen evolution reaction (HER) and oxygen evolution reaction (OER), first the kinetic overpotentials must be overcome. Therefore, a suitable SC material for visible light PEC water splitting should have (a) a band gap ( $E_g = E_{CB} - E_{VB}$ ) in the

range of 1.6 – 2.4 eV to sufficiently utilise the solar spectrum and drive the reactions, and (b) energy position of the band edges appropriately aligned with respect to the HER and OER redox potentials.

As mentioned above, a number of oxynitride perovskite materials possess these characteristics, making them ideal candidates for PEC solar water splitting.<sup>30, 63, 76, 180, 181</sup> Thin films of these materials provide excellent model systems to probe the physical and chemical evolution of the surface of the SC, in contact with water. Fig. 5.1 shows the energy diagram schematic for PEC water splitting using a STON thin film as a light harvesting SC photocatalyst and TiN as the current collector. In Fig. 5.1a, we see that upon light irradiation with photons with an energy ( $h\nu$ ) > 1.23 eV, the photon is absorbed promoting a photoexcited electron ( $e^-$ ) from the valence band (VB) to the conduction band (CB). The photoelectrons travel via a TiN current collector layer and external circuit where they are involved in the HER using a platinum counter electrode (cathode). The generation of a photoelectron leaves behind a photogenerated electron hole ( $h^+$ ) which migrates towards the surface of the SC oxynitride where it is then involved in the OER.

Fig. 5.1b shows the three-electrode configuration used in this work, where the STON SC photocatalyst is used as a photoanode to study the OER, a platinum counter electrode used for the HER half reaction, and a Ag/AgCl reference electrode is used to control the applied potential on the working electrode. The electronic current between the working and counter electrodes is called the photocurrent and the photocurrent is proportional to the amount of molecular  $H_2$  and  $O_2$  produced. The photocurrent is defined as the current response under light conditions minus the current response under dark conditions. More in-depth experimental details are included in the corresponding methods section.

Fig. 5.1c shows the PEC performance of the STON oxynitride thin films, the initial photocurrent reaches a photocurrent density of ca.  $12 \mu A cm^{-1}$  at 1.5 V vs. reversible hydrogen electrode (RHE). This value is in line with previous reports on oxynitride thin films using the bare SC material without surface decoration with co-catalyst, which dramatically facilitate hole extraction. On the one hand, the N content of textured thin films is typically lower than the stoichiometric value that can be obtained with powder samples.<sup>182</sup> This reduces the thin films

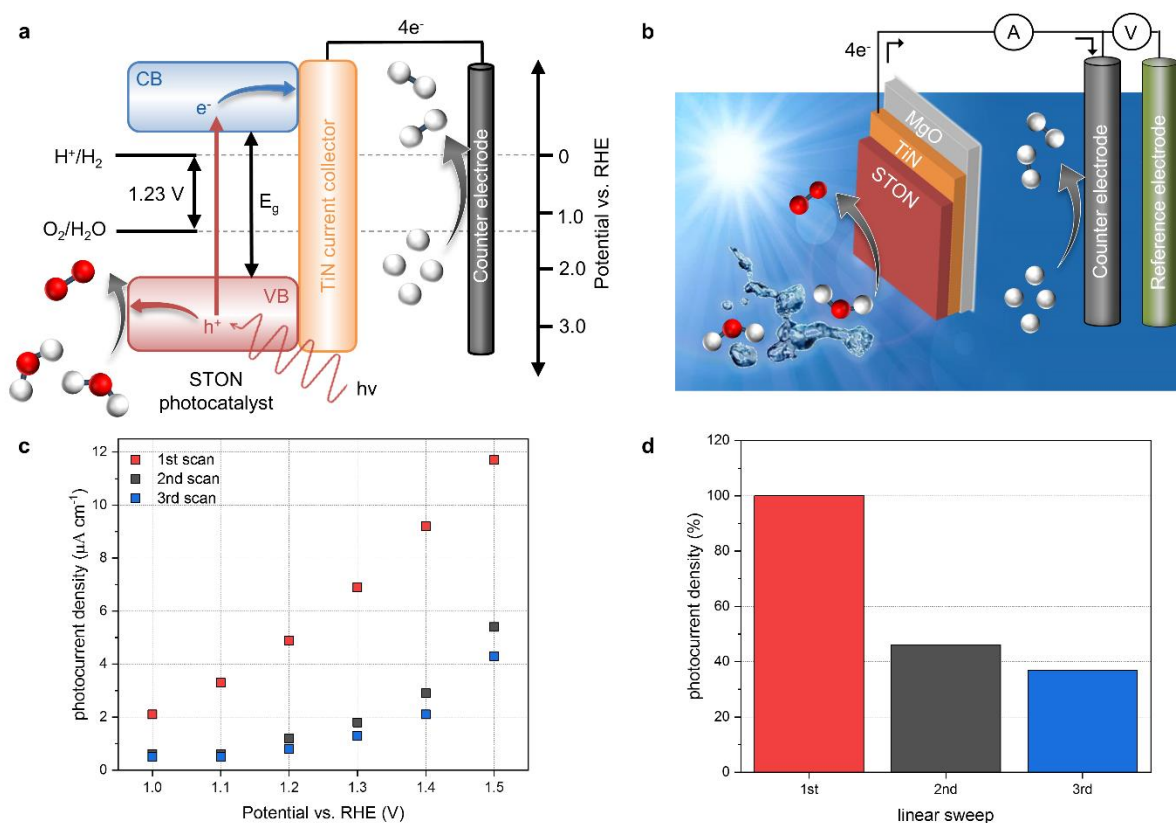


**Fig. 5.1.** (a) Energy diagram for photocatalytic water splitting, (b) experimental schematic of the photoelectrochemical three-electrode cell. The working, counter and reference electrodes are the oxynitride thin film, platinum wire and Ag/AgCl respectively, (c) photocurrent densities for STON for the first three-potentiodynamic measurements, (d) photocurrent degradation from part c, values taken at 1.5 V vs. RHE.

photoresponse to visible light illumination. On the other, the thin films possess atomically flat surfaces compared to the corresponding oxynitride powders. Therefore, the surface area is ca. 20 times smaller than it would be in their powder forms.<sup>62</sup>

However, after successive measurements (potentiodynamic sweeps) the material shows significant degradation in its initial performance. The stabilised photocurrent density shows values ca. 40% of its initial value. The sudden and large degradation in performance is a huge hindrance for the application of a material that initially seems quite promising. Some studies have already looked at ways of improving the performance and long-term stability of STON<sup>64</sup>.

<sup>183, 184</sup> by doping constituent elements and/or decorating the surface with co-catalyst nanoparticles. Probing the physicochemical evolution of the surface under operation conditions will provide insight into what physical and chemical processes occur at the surface during the OER and therefore, allow a rational design of stable STON.

#### 5.4. Oxynitride thin films

The STON thin films were fabricated using a modified pulsed laser deposition technique described in previous works,<sup>72</sup> followed by post annealing in NH<sub>3</sub> for 1 hour. The epitaxial oxynitride STON films were deposited on titanium nitride (TiN) coated magnesium oxide single crystal substrates (001) oriented. Rutherford back scattering (RBS) and Elastic recoil detection analysis (ERDA) determined the chemical compositions of the STON thin films as Sr<sub>0.94</sub>Ta<sub>1.06</sub>O<sub>2.80</sub>N<sub>0.31</sub>. The experimental uncertainties for Sr and Ta are ± 2% (RBS) and ± 7% for O and N (ERDA). The full results have been included in Fig. 6.2. The O:N ratio of ca. 10 is in line with previous examples of highly ordered oxynitride thin films, since there is a trade-off between overall nitrogen content and crystalline quality,<sup>70</sup> where films with larger N contents tend to be more disordered.

From Fig. 5.3, it can be seen that the TiN buffer layer grows (001) epitaxially oriented on the MgO substrate. The (002) reflex of TiN is visible as a shoulder on the left-hand side of the peak of the substrate (part b). Fig. 5.3, also shows that STON grows epitaxially on the TiN buffer layer<sup>72</sup> with the (hkl) reflexes (002) and (004) appearing at 2θ values of ca. 21.8° and 44.2°, respectively. The angular position of the (00l) reflexes of the perovskite SrTaO<sub>2</sub>N have been marked in blue as reference from the Inorganic Crystal Structure Database (ICSD). Both the 002 and 004 reflexes of the STON thin film are slightly shifted to lower 2θ values compared to the SrTaO<sub>2</sub>N reflexes.

This is due to the combined effect of a difference in N content to the stoichiometric reference and the crystalline constrain (lattice mismatch between the substrate and film) induced by the TiN-coated MgO substrate. The perovskite structure of STON remains stable, within a large



range of N content. However, the cell parameters can be significantly affected since the N content affects the Ta-O-Ta dihedral bond angle and ultimately, the overall distortion of the cell. To characterise how the OER modifies the physicochemical properties of the surface of our STON films, we first used XPS to compare changes of the oxidation state of all four elements before and after PEC testing.

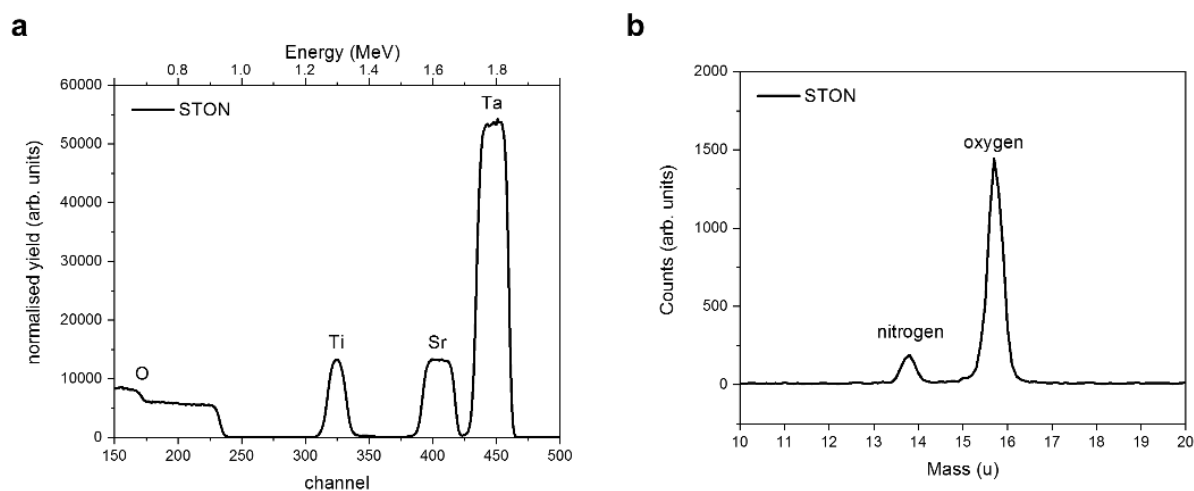


**Fig. 5.2.** (a) Rutherford backscattering (RBS) spectrum, (b) elastic recoil detection analysis (ERDA) spectrum. The cation ratios were determined by RBS and the O:N ratio by ERDA.

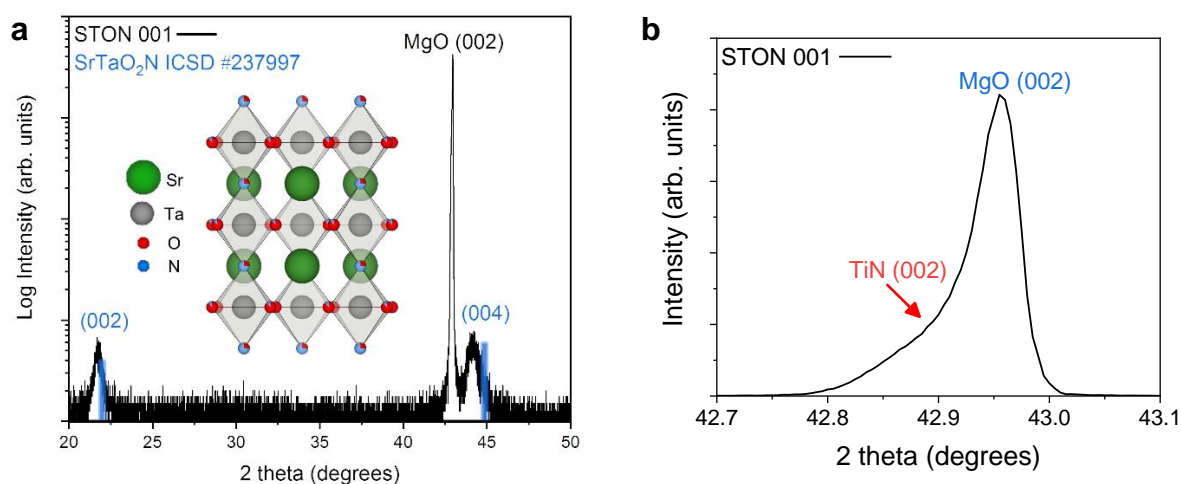


**Fig. 5.3.** (a) XRD pattern of the epitaxially grown STON film, the  $\theta/2\theta$  scan is shown in black, with the angular position of the (001) reflexes of SrTaO<sub>2</sub>N shown in blue for reference. The inset shows the crystal structure of SrTaO<sub>2</sub>N, (b) Magnified region from data shown in part a.

## 5.5. X-ray Photoelectron Spectroscopy

The XPS spectra for all four elements are shown in Fig 5.4, for peak fitting analysis the reader can refer to supplementary Fig. 5.11 and the supplementary tables. Fig 5.4a shows the carbon signals that arise due to adventitious carbon, present during the ex-situ transfer of the samples. After PEC, the intensity of the main peak reduces suggesting the oxidation/loss of the carbon-based surface contaminates after exposure to the electrolyte and/or X-ray beam. The shoulder features result from C-O and O-C=O like environments. Although, the intensities of the main peak reduce in intensity after PEC, suggesting that the total number of C based species are reduced after PEC, the peak fit suggest that the shoulder C-O contribution increases after PEC, likely due to oxidation during the PEC reaction. With respect to oxygen, after PEC, the O 1s spectra (Fig. 5.4b) exhibits a large increase in the intensity of the main peak and shoulder feature(s). The shoulder feature is observable on the high-energy side of the asymmetric O 1s lattice peak at ca. 531.5-534 eV. It is likely in reality that there exists a number of O based chemical environments (lattice O, SrO, C-O, OH and H<sub>2</sub>O). Trying to estimate these environments would produce a high degree of uncertainty in the peak fit models. However, peak fitting suggests a minimum of two chemical environments likely associated with chemisorbed OH and/or H<sub>2</sub>O species. In addition, after PEC the integrated area under of the shoulder increases, suggesting an increase in hydrophilicity of the surface. The increased O content suggests that any lattice vacancies generated at the surface/surface layers are self-healed under OER conditions by oxygen based species.<sup>114</sup>

For the Sr 3d spectra (Fig.5.4c), peak fitting suggests that the epitaxial STON thin films as grown exhibit a preferential AO (SrO) termination, also noted for various perovskites using low energy ion scattering (LEIS)<sup>93, 115, 116, 117, 139</sup> and XPS<sup>93, 185, 186</sup>. Under ambient conditions/aqueous environment, Sr should be covered in OH adsorbates. After deprotonation (slow step) the OER would proceed, leaving vacant oxygen cavity on Sr, assuming the traditional 4-step mechanism for the OER.<sup>187</sup> However, SrO is partially soluble in water to form ionic Sr<sup>2+</sup> and 2 OH<sup>-</sup>. Therefore, dissolution and leaching of Sr<sup>2+</sup> into the electrolyte would be expected<sup>188</sup>. Especially, in an alkaline medium such as NaOH/H<sub>2</sub>O with a pH of 13.

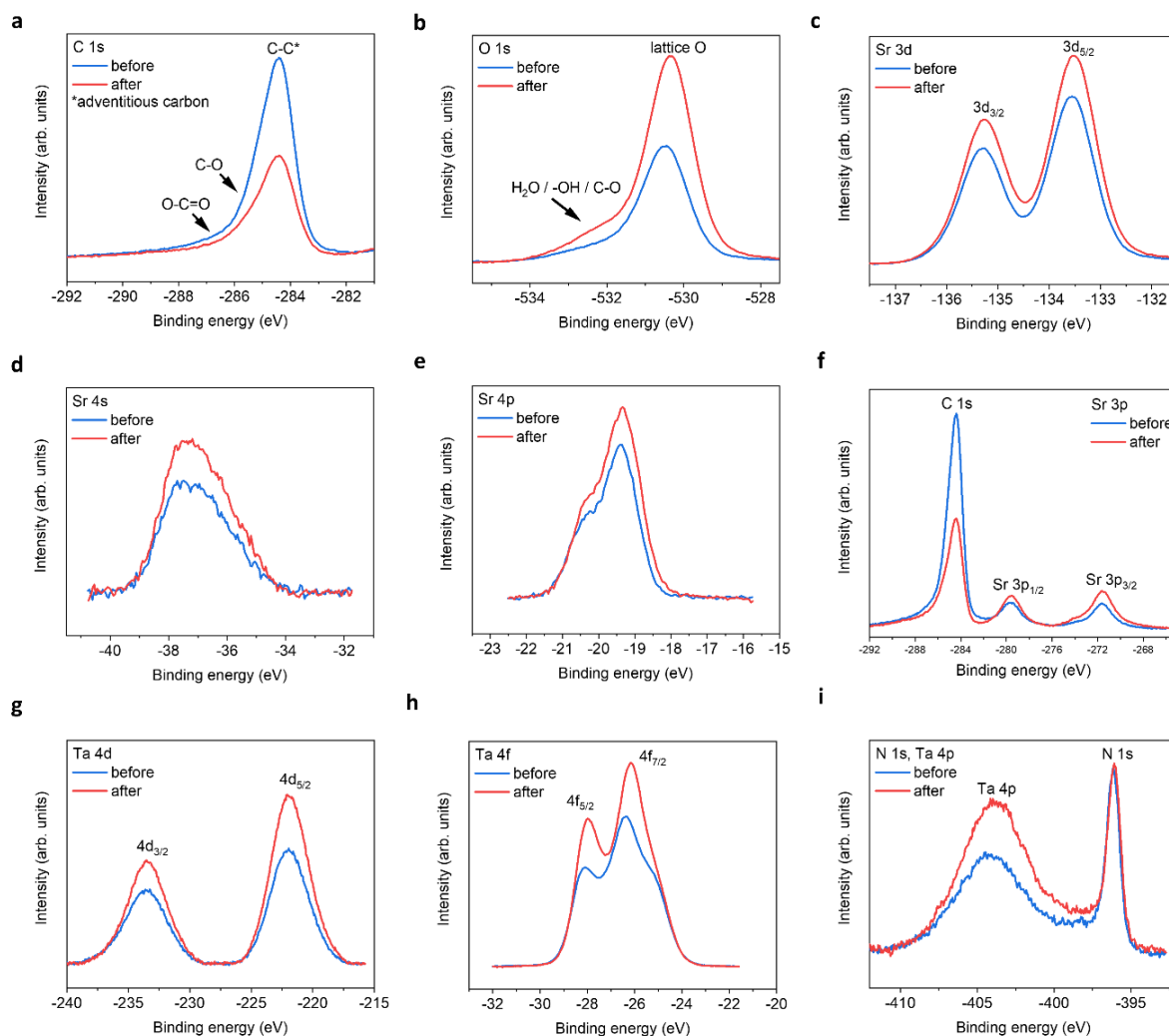


**Figure 5.4.** STON thin film XPS spectra before and after PEC. (a) C 1s, (b) O 1s, (c) Sr 3d, (d) Sr 4s, (e) Sr 4p, (f) Sr 3p, (g) Ta 4d, (h) Ta 4f, (i) N 1s and Ta 4p edges.

After PEC, the peak fitting suggests a large decrease in the SrO content at the surface and an overall increase in peak area and intensity for the remaining Sr XPS spectra (Fig 5.4c-f). It has previously been shown, that an increase in XPS peak intensity can result from Sr segregation/accumulation<sup>189, 190</sup> as well as, with increased doping concentrations<sup>191</sup>. Peak intensity/area increases are also observed due to Sr particle/Sr surface species formation.<sup>189, 190</sup> Therefore, the increase in Sr signal in this work is likely due to the loss of SrO and the apparent enrichment of the Sr lattice contribution.

Fig. 5.4g-i, include the Ta 4d, Ta 4f, and Ta 4p edges respectively. From peak fitting the Ta 4d spectra suggests one binding environment, which is the lattice Ta contribution. After the PECR, this intensity and area of the Ta 4d peak increases as seen for the lattice Sr contributions. This suggests that after the loss of SrO the underlying lattice Ta appears enriched by XPS. The Ta 4f spectra (Fig. 5.4h) exhibits two peaks due to the Ta 4f<sub>5/2</sub> and 4f<sub>7/2</sub> contributions. The peak fitting analysis suggests that there are two Ta binding environments for both the 5/2 and 7/2 peaks corresponding to TaO<sub>x</sub> and TaO<sub>x</sub>N<sub>y</sub> like environments (supplementary Fig. 5.11) which, after the PECR, the peak contributions of TaO<sub>x</sub>N<sub>y</sub> decrease and those of TaO<sub>x</sub> increase. Again, like the O1s spectra, suggesting a slight loss of nitrogen and an increase in the overall oxygen content at the surface/surface layers of the thin film. The energy positions of the peaks suggest a slight reductive shift by ca. +0.15 eV. However, the Ta 4d spectra in Fig. 5.4d show an increase in the FWHM and peak intensities, but no shift in energy position or peak separation. The shift in the Ta 4f spectra may then also be related to the changing O/N, resulting in disorder and differences in the charge transfer between the Ta 4f final states and the O 2p / N 2p orbitals. This then shifts the mid gap f band higher towards the CB or above,<sup>192</sup> leaving the 4d core states unchanged. The increase in intensity observed could be a result of apparent lattice Ta enrichment due to the O/N vacancy generation exposing the subsurface B sites.<sup>139</sup> It could also be a result of SrO leaching, also exposing the subsurface Ta on average. Since Sr is more soluble than Ta and, it has been shown that Ta is passive in alkaline electrolytes with concentrations 2.5x stronger than used in this work.<sup>193</sup>

The electronic configuration of Ta<sup>0</sup> is [Xe] 4f<sup>14</sup>5d<sup>3</sup>6s<sup>2</sup> and that for Ta<sup>5+</sup> should then consist of [Xe] 4f<sup>14</sup>. This may then explain, the changes in charge transfer and hybridisation between the Ta 4f and O/N 2p atomic orbitals as observed in this work and suggested by the peak fitting analysis. This is also interesting as the f orbitals are typically ignored when considering the density of states (DOS) using density functional theory (DFT) calculations for materials due to the complexity, time and cost involved in the computation of the f states.

The Ta 4p<sub>3/2</sub> is observed as a broad peak at ca. 404-405 eV (Fig. 5.4e). However, the Ta 4p<sub>3/2</sub> spectrum overlaps with the N 1s signal in the energy region at ca. 402-408 eV which contains the N 1s information regarding interstitial and/or chemisorbed NO, NO<sub>2</sub>, NO<sub>3</sub> and N<sub>2</sub>, making

the peak analysis difficult. The N 1s Ta-N lattice signal can be seen as a sharp peak at ca. 396.1 eV. After the PECR, the broad peak in the region, which contains the convoluted N 1s and Ta 4p<sub>3/2</sub> signals increases significantly suggesting an increase in the number of electronically decoupled N states. As well as, the apparent lattice Ta enrichment as seen previously.

At ca. 407.5 eV there is a small but obvious increase in intensity belonging to a different Ta/N binding state, which is likely a contribution due to chemisorbed NO<sub>3</sub> according to literature reports (supplementary Fig. 5.11). It is therefore assumed that NO and NO<sub>2</sub> would contribute to the overall increased intensity/peak area observed, where the O(OH) OER intermediate formed during the reaction likely oxidise the NO<sub>x</sub> species in competition with O<sub>2</sub> evolution. This would reduce the overall efficiency of the material, and chemisorbed NO<sub>x</sub> species would occupy possible active sites. This, in conjunction with the surface reconstruction after the loss of SrO and the changing N/O content, could explain the large degradation in initial photocurrent observed. Likely hampered by side reactions and charge recombination.

Clearer evidence of NO<sub>x</sub> formation for the oxynitride LaTiO<sub>x</sub>N<sub>y</sub> can be seen by XPS in a previous work<sup>70</sup>, and as discussed in chapter 4. Where, Ta does not convolute the N 1s signal. We also observe evidence for the depletion of N states from the lattice structure using SX-ARPES (chapter 2). Overall, the XPS analyses of the initial and final state of the STON photocatalyst suggest that STON suffers from a surface degradation and reconstruction, which lead to a dramatic decrease in photocurrent (Fig. 5.1c). This process involves (a) loss of N from the structure (including interstitial N), where N remains partially chemisorbed as N<sub>2</sub>/NO<sub>x</sub> species, (b) an increase in electron density on Sr (c) Ta enrichment/exposure with an increase in disorder of its local environment due to changes in hybridisation with the N and O 2p states. Next, we explore the effect of several external stimuli (applied potential and light) on the surface of the oxynitride SC under oxygen evolution reaction conditions by *operando* XAS in liquid phase.

### 5.6. *Operando* reactor cell

The *operando* XAS measurements were performed in a custom-built reactor cell designed and fabricated at the Paul Scherrer Institute for the specific purpose of *operando* GIXAS in aqueous electrolytes for thin films. The cell design is included in Fig. 5.5. The cell is made of polyether ether ketone (PEEK), a thermoplastic with high mechanical and chemical stability, allowing the use of most common acidic/alkali based aqueous electrolytes.

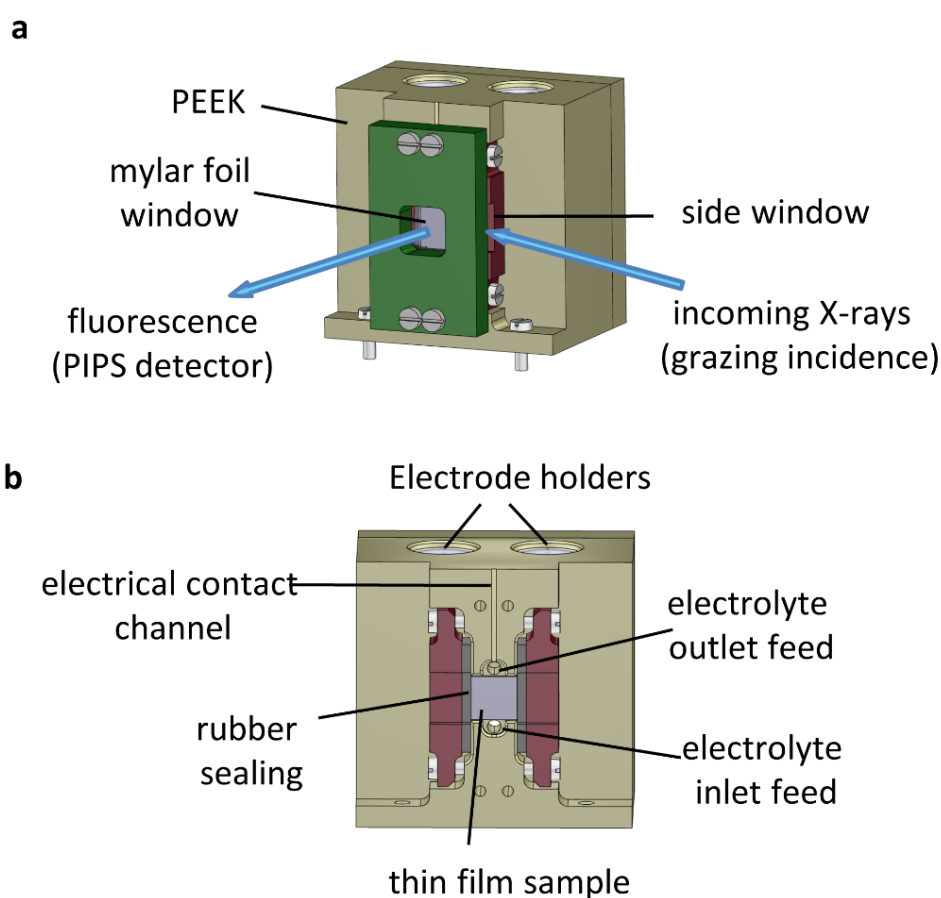


**Fig 5.5.** (a) trimetric view of the cell and GIXAS geometry used during measurements, where the grazing incident X-rays enter through a Mylar foil covered side window, (b) cross sectional internal view. Where, PIPS denotes a passivated implanted planar silicon detector.

The X-ray beam illuminates the surface of the sample at grazing angle and the fluorescent signal is detected as a cone along the surface normal, as shown in Fig. 5.5a. The surface sensitivity that can be achieved in grazing angle geometries considering the incident energy of the X-rays is ca. 3 nm.<sup>66</sup> The cell is designed to hold thin films grown onto standard substrate sizes. Typically, 10 x 5 mm or 10 x 10 mm with a substrate thickness of 0.5-1.0 m. The window material used is an optically clear Mylar foil ( $t= 0.19\text{mm}$ ), which allows the transmission of visible light onto the sample whilst also allowing  $> 90\%$  X-ray transmission at the energy ranges used in this work (Fig. 5.6).

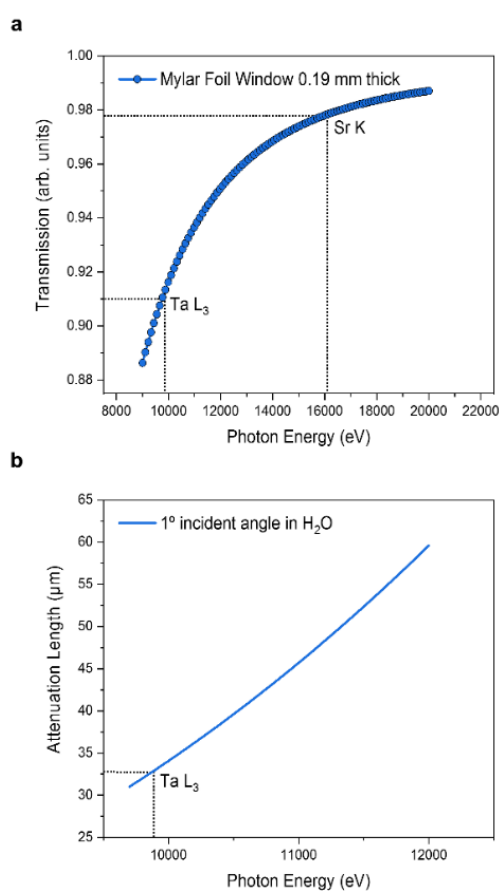


**Fig. 5.6.** (a) Transmission of X-rays through optically clear Mylar used as a window material for X-rays and visible light, (b) attenuation length of X-rays in pure H<sub>2</sub>O at an incident angle of 1°. Ta L<sub>3</sub> edge (9881 eV) has been labelled (Sr K edge at 16105 eV is not shown). Values taken from.<sup>136</sup>

The use of Mylar foil as a window provides flexibility in enabling visible light to shine onto the sample whilst detecting the fluorescence signal, as well as allowing grazing incidence angles of  $< 1$  degree onto the sample surface in an aqueous environment. Synthetic rubber pieces clamped into position seal the Mylar foil window to prevent leaks (Fig. 5.5b). On the backside (Fig. 5.7) are two threaded openings, allowing the use of an external electrolyte reservoir as well as connecting a peristaltic pump or a syringe pump system to circulate the electrolyte as required. Alternatively, the cell can use an internal electrolyte reservoir situated behind the sample. The cells' internal reservoir can house both the counter and reference electrodes.

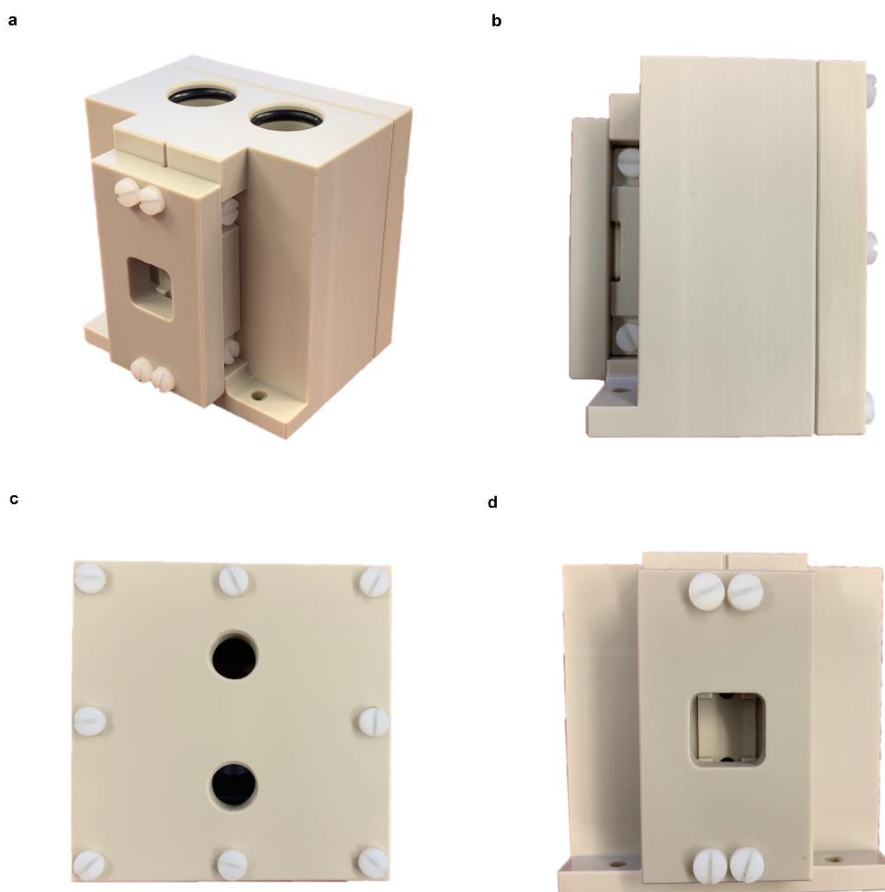


**Fig. 5.7.** (a) Trimetric view, (b) side view, (c) back side with fittings for a peristaltic pump or for sealing, (d) front view. The cell was designed and fabricated at the Paul Scherrer Institute as part of this work.



5.7. Tantalum L<sub>3</sub> Edge XANES

Fig. 5.8a shows the XANES spectra recorded *ex-situ* at the Ta L<sub>3</sub> edge ( $E_0 = 9881$  eV) for BaTaO<sub>2</sub>N (BTON), STON, and KTaO<sub>3</sub> powder samples. These measurements are used as reference to understand the corresponding GIXAS measurements performed during OER using the STON thin films, as shown in

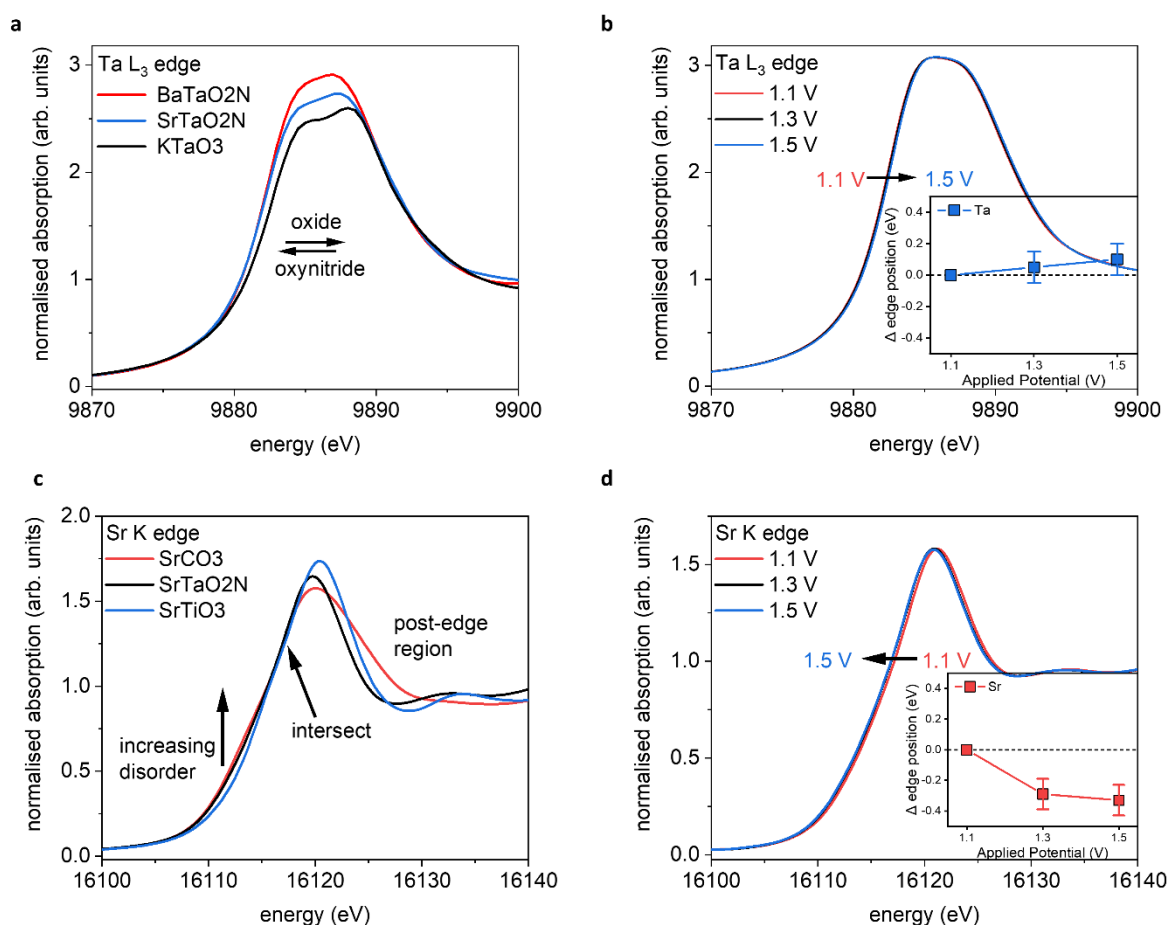


**Figure 5.8. Operando GIXAS at the STON-liquid interface** (a) Reference spectra for Ta<sup>5+</sup> oxide and oxynitride powders, (b) *operando* Ta measurements for STON thin film, (c) reference spectra for Sr<sup>2+</sup> containing powders, (d) *operando* Sr measurements. The *operando* characterisations were performed during the chronoamperometry (1 hour) measurements, with stepped applied potential. The error bars included in the magnified insert correspond to  $\pm 0.1$  eV.

Fig. 5.8b. We use  $\text{KTaO}_3$  as a reference for this work since the parent oxide of STON, which would be  $\text{Sr}_2\text{Ta}_2\text{O}_7$ , possesses a different crystal structure, therefore, the electronic structure would differ significantly.  $\text{KTaO}_3$  has a cubic crystal structure like  $\text{SrTaO}_2\text{N}$  and  $\text{BaTaO}_2\text{N}$ . Moreover, in all three cases Ta exists in the 5+ oxidation state, therefore allowing a sensible comparison of their electronic structures (Fig. 5.8a). We can see that, compared to  $\text{KTaO}_3$ , for the oxynitride powders there is a shift of the edge position ( $E_0$ ) to lower energies by ca.  $0.5 \text{ eV} \pm 0.1$ . This shift of the absorption edge is not due to the reduction of Ta but rather due to the downward shifting of the CB minimum of STON and BTON compared to  $\text{KTaO}_3$ . Since, the CB is comprised of Ta 5d orbitals for all three materials,<sup>144</sup> The substitution of nitrogen into the oxygen sites affects the Ta-O/N-Ta dihedral bond angle and the overall electronegativity of the anions. Both these effects can explain the downward shift in energy of the CBM<sup>60, 61</sup>.

The increase in intensities for the XANES spectra most likely result from the nitrogen substitution. In the cubic perovskite oxide  $\text{KTaO}_3$ , the Ta-O-Ta angle is 180 deg. In the orthorhombic oxynitride perovskites, the dihedral bond angle is distorted and its value depends on the total N content and the size of the A cation. Therefore, with the lowering of symmetry and increased p-d orbital mixing, the 2p-5d transition will be more favourable and reflected in the relative intensities of the peaks.

Fig. 5.8b shows the *operando* XANES measurements performed on STON thin films during the chronoamperometry measurements (measuring the photocurrent at a fixed applied potential over time). We can see that for all applied potentials, there is no significant change in the spectral shape or in the edge position, indicating no change in formal oxidation state. When inspecting the magnified inset, there are small shifts in the edge positions to higher energies when moving from 1.1 to 1.3 and 1.3 to 1.5 V vs. RHE, corresponding to ca. 0.05 and 0.1 eV respectively. It has previously been shown that for various compounds which all contain formally  $\text{Ta}^{5+}$  species, the edge position can vary by ca.  $1.4 \text{ eV}$ <sup>194</sup> due to the variation of the electronic structure and the relative position of the Ta 5d states. Therefore, the small shifts seen in edge position for Ta are unlikely to be oxidation of Ta at the surface. Even though oxidation states are often valid interpretations due to the correlation between formal oxidation state and edge position,<sup>59, 195, 196</sup> the changes shown here are first, within error and second, any small

change is likely due to the slight loss of lattice nitrogen and/or the possible formation of  $\text{NO}_x$  species at the surface of the STON thin film as suggested by the XPS analysis in this work. As previously discussed, upon partial N loss in the surface layer, it will also result in a local loss of hybridisation between the Ta 5d and the N 2p states at the VB maximum (Fig. 5.8c). As a result, a more ‘oxide-like’ electronic structure forms at the surface as the potential is increased.

It is reasonable to assume that Ta will tend to fulfil its full coordination sphere upon loss of N by replacing with O under OER conditions.<sup>114</sup> This would also explain why there is no significant change in the spectral shape for Ta. There is instead, a slight shift to higher energy of the absorption edge. However, the replacement of  $\text{N}^{3-}$  with  $\text{O}^{2-}$  should see a reductive shift to lower energy for Ta. This again suggests that the charge around Ta is stabilised, like for Ti in  $\text{LaTiO}_x\text{N}_y$ <sup>66</sup>, but due to slight changing O/N concentrations at the surface, the Ta octahedra undergo a slight disorder. Since the CBM is comprised of delocalised Ta 5d states in STON<sup>197</sup>, the resulting changes in the O/N-Ta-O/N dihedral bond angle and degree of hybridisation, affect the conduction band minimum position.<sup>60</sup>

### Strontium K edge XANES

Fig. 5.8c shows the XANES spectra measured at the Sr K edge ( $E_0 = 16105$  eV) for Sr containing oxide ( $\text{SrTiO}_3$ ), carbonate ( $\text{SrCO}_3$ ) and oxynitride (STON) powders. Small changes in the post edge region and in the intensities of the main peak (16120-16140 eV) can be observed and are due to the differences in coordination environment surrounding the Sr cations.<sup>198</sup> There are also changes of intensity of a broad shoulder in the pre-edge region at ca. 16108-16115 eV. Pre edge features relate to changes in the local geometry and degree of disorder surrounding the absorbing element of interest. Therefore, as one moves away from a perfect octahedral environment the pre-edge intensities increase<sup>199</sup> and this is observed from the perfect octahedral environment surrounding Sr in  $\text{SrTiO}_3$ , to the increasingly disordered octahedra in  $\text{SrTaO}_2\text{N}$  and  $\text{SrCO}_3$ , respectively.

Fig. 5.8d shows the *operando* XANES measurements performed on the STON films during the chronoamperometry measurements as described previously. Unlike for the Ta B site, here we observe a more significant shift in the edge position due to an increase of electron density on  $\text{Sr}^{2+}$ , with increasing the applied potential from 1.1 to 1.3 V vs. RHE. Increasing the potential further from 1.3V to 1.5 V does not show any further significant modification of either the local coordination or electronic structures around the Sr cations. The observed shift in edge position with potential is not constant, unlike observed for Ta.

Many of these oxides and oxynitride perovskites tend to typically exhibit AO (SrO) surface terminations<sup>115, 139, 200</sup> rather than  $\text{BO}_2$  ( $\text{TaO}_2$ ). As previously discussed, a Sr/SrO<sub>x</sub> surface initially covered by oxygen adsorbates, would then initially contribute to overall O<sub>2</sub> generation.<sup>144</sup> As the potential increases to 1.3 V, the Sr starts to reduce (Fig. 5.8d) likely associated with the decoupling of the OER intermediates leaving the adsorption site on Sr vacant<sup>144</sup> before further adsorption.

However, the degradation in the initial performance of STON and the XPS and XAS results, suggests these changes on Sr are permanent and detrimental. When changing the applied potential from 1.3 to 1.5 V, we see no significant change, except an overall further reductive shift albeit, at a reduced magnitude (Fig. 5.8d insert) within error. This observation could be explained by the earlier discussion regarding the deprotonation of Sr as the overpotential determining step (ODS). As the potential increases the majority of the Sr species reduce, followed by Sr/SrO/SrOH leaching. This disorder would also lead to defect Ta 5d states near the CBM which will then trap electrons,<sup>201</sup> leading to charge-recombination.<sup>202</sup> This, in conjunction with changes seen for Sr and the generation of N species in competition with O<sub>2</sub> generation, can explain why there is unusually large degradation in the initial photoelectrochemical performance of STON before the material stabilises.

### Modulation Excitation X-ray Absorption Spectroscopy

In a different and complementary experimental strategy, we performed modulation excitation XAS (ME-XAS) to monitor the real time effects of the chemical modification of the surface using light as the external stimulus. The description of the experiment can be seen in Fig. 5.9a, where the thin film sample is stimulated by periodic modulation of light (chopped illumination) whilst time resolved XAS measurements are performed and data collected simultaneously during operation conditions at different, fixed potentials. Spectral changes induced by external stimuli (light in this case) are often small and/or prone to overshadowing by noise and background signals due to the experimental set-up.<sup>203</sup> One can improve the signal-to-noise ratio by averaging data sets over several modulation periods. Furthermore, improvements in signal-to-noise ratio can be achieved through analysis of ME-XAS with phase sensitive detection (PSD).<sup>204, 205, 206, 207</sup> PSD converts time-resolved XAS data into a set of phase ( $\phi^{\text{PSD}}$ ) resolved data akin to a digital lock-in amplifier, enhancing the sensitivity of the ME-XAS experiment to spectral responses that match the frequency of the chopped light stimulus. More information on the PSD approach is included in the Supplementary Discussion.

Fig. 5.9b shows the chronoamperometry measurements at 1.1, 1.3, and 1.5 V vs. RHE where the incident light was modulated with 120-second periods (60 seconds on, 60 seconds off). Fig. 5.9b has been adapted for sake of clarity, where the photocurrent spikes (labelled light ON/OFF), are minimised. At 1.1 V, the photocurrent response is limited, but as the potential is increased further the photocurrent response also increases, as expected. However, at 1.3 V there is a large increase in the dark current response compared to 1.1 V. This increase degrades over time, before minimising after ca. 3000 s. When the potential is stepped to 1.5 V, there is an initial increase in the dark current response, which stabilises ca. 1/3 faster than at 1.3 V. There is also an overall increase in the stabilised dark current response compared to 1.1 and 1.3 V. These increases in the dark current at 1.3 V also coincide with the changes seen in the *operando* XAS data measured at 1.3 V, with the increase of electron density on Sr, resulting in increased overpotentials.

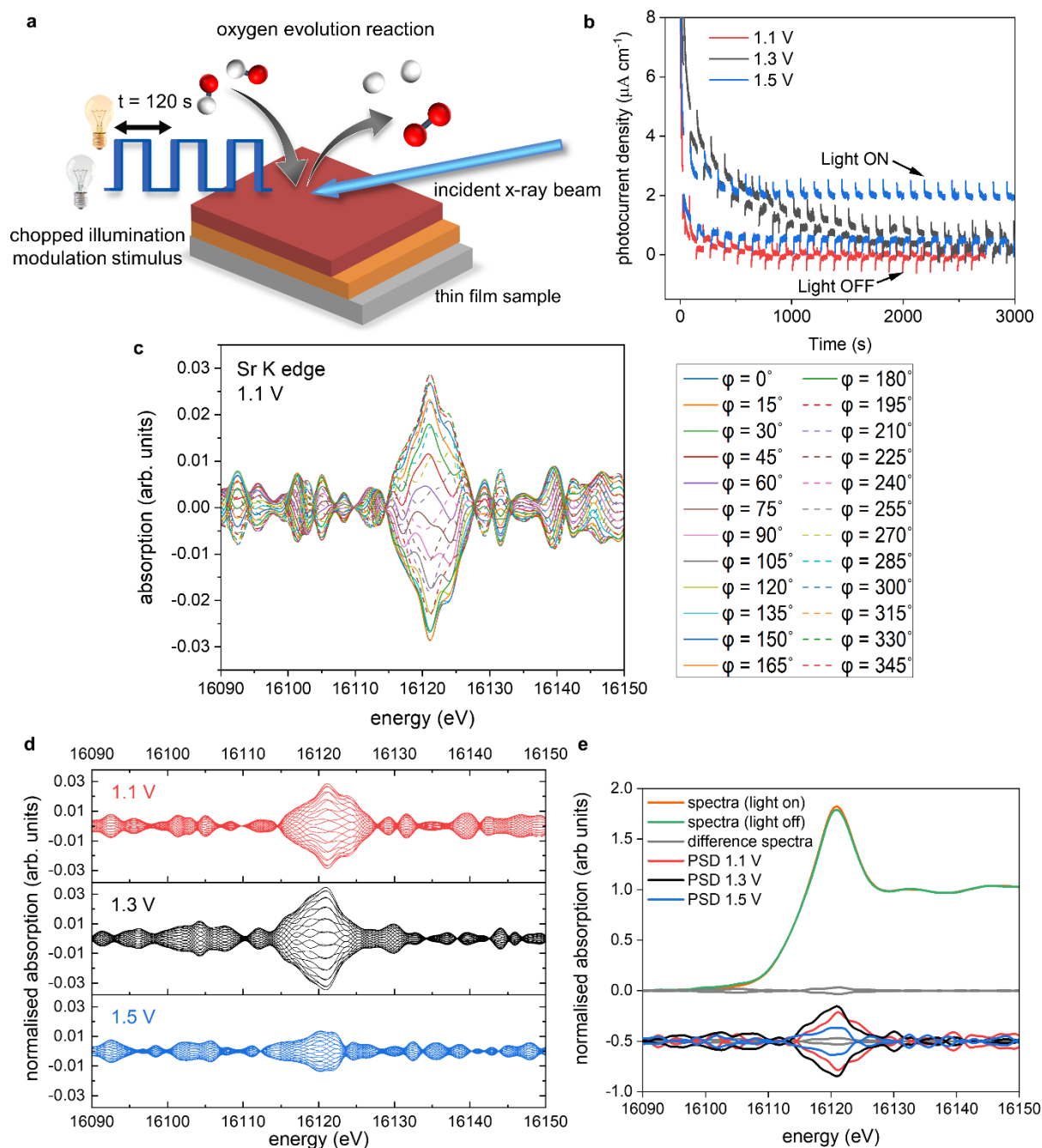


**Figure 5.9. Operando ME-XAS at the STON-liquid interface.** (a) schematic of the experiment, (b) chronoamperometry measurements performed at 1.1 V, 1.3 V and 1.5V vs. RHE, (c) phase resolved spectra ( $\phi^{\text{PSD}} = 0^\circ - 345^\circ$ ) obtained from the modulation experiment measured at 1.1 V at the Sr K edge, (d) phase resolved spectra for Sr K edge measured at 1.1 V, 1.3 V and 1.5 V vs. RHE shown in red, black and blue, respectively, (e) average of spectra recorded under illumination and under dark conditions, with the difference and PSD spectra at each potential.

Fig. 5.9c shows, as an example, the PSD data analysis of data acquired at the Sr K edge for STON measured at 1.1 V. The benefit of PSD is the significantly enhanced signal-to-noise ratios, as it contains primarily only the signals from the changes due to the external light stimulus,<sup>208, 209</sup> while spurious effects from inactive species, spectators and noise are filtered out.

Fig. 5.9d includes the phase resolved spectra for Sr measured at 1.1, 1.3, and 1.5 V in red, black and blue, respectively. Not only can we see that there are small changes due to stimulus with light, but there is also a potential dependence. The spectra collected at 1.5 V show decreased sensitivity (smaller differences) due to the modulated light stimulus compared to 1.1 and 1.3 V. Fig. 5.9e shows an example of averaged spectra collected under illumination and dark conditions at one potential, along with the difference of the two plots shown as a solid grey line and the PSD spectra shown below.

Upon irradiation with light, photons with sufficient energy are absorbed; generating electrons and electron hole pair charge carriers. The charge carriers are subsequently consumed in the water splitting process or recombine. The promotion of electrons from the valence band to the conduction band will induce small changes in the overall electronic system. This is reflected by the change in intensity of the Sr K-edge main peak under illumination (Fig. 5.9e).

We saw for the XANES (Fig 5.8d) that when the Sr species reduce, there is a gain of electron density surrounding Sr with applied potential. The electronic configuration for Sr should reflect [Kr] 5s<sup>2</sup> and that for oxidised Sr<sup>2+</sup> represented by [Kr]. Therefore, as Sr reduces with applied potential, one would expect the lower lying energy 5s orbitals to be partially filled compared to the 4d states, according to Hund's rule. Typically, the intensity, especially in the case of L edges, is assumed to be related to holes in the d-band. Therefore, an oxidised species with electron holes in the d-band would typically exhibit larger intensity of that of a more reduced species with a filled d band.<sup>210</sup> The Sr K edge transition includes dipole s to p transitions like the L edges previously mentioned, however, it also includes quadrupole transitions s > d and p > f, complicating the interpretation further. Especially, as these quadrupole transitions should

be forbidden due to selection rules. However, due to disorder and p-d orbital mixing, the forbidden  $s > d$  transitions are observable in the K edge spectra. According to p-DOS, the CB for STON is comprised of primarily Ta d states, but also Sr d states and with increasing energy, the Sr p and s states.<sup>197</sup>

This can be reflected visually in Fig.5.8d with the pre-edge features of various Sr containing species with, the local coordination surrounding the absorbing Sr showing signs of disorder from the perfect octahedral. With increasing degrees of disorder and orbital mixing, the intensity of the pre-edge features increases, as the usually forbidden  $s > d$  transitions are now allowed. Therefore, the main peak intensity may not be solely related to oxidation state and holes in the d band, like for the L edges, but also to the effect of the Sr s and p states and, the local coordination surrounding Sr. As previously mentioned, due to the highly crystalline nature of the epitaxial films, diffraction renders the EXAFS data unreliable to investigate any changes in the local coordination environment of Sr. Future work will look at ways to circumvent this limitation.

As electron density on Sr increases, the reduced intensity of the PSD data at 1.5 V (Fig. 5.9d) may then be related to a) reduced probability for an electron to promote to the Sr states in the CB, as they are now partially occupied and/or b) increased recombination of electron hole pairs due to the surface reconstruction and the proceeding of the forwards reaction of the OER.

The suggested changes to the surface stoichiometry would result in a surface reconstruction that affects the binding energies of the intermediate products (\*OH, \*O, \*OOH). produced during OER conditions. The intermediates that adsorb too weakly or too strongly will reduce the overall kinetics and, increase the overpotential of the OER.<sup>114, 211</sup> At 1.5 V, the applied potential overcomes the increased overpotentials, reflected in the increased photocurrent response.

Both the A (Sr) and B (Ta) are both described as active sites for the OER mechanism to proceed on.<sup>144</sup> With Sr covered in OH adsorbates contributing to O<sub>2</sub> generation. Deprotonation was



shown to be the ODS for STON,<sup>144</sup> Therefore, upon deprotonation, most Sr species would exist as SrO which, as previously discussed, is partially soluble in the electrolyte. However, unlike Sr, the Ta PSD signals never increase above the level of noise (supplementary Fig.5.10). This suggests either two things: 1) Ta is not responsive to the light and not involved in the photo absorption process, a hypothesis which would contradict available literature<sup>144, 182 212</sup> or, 2) the kinetics for Ta are faster than those for Sr<sup>144</sup> therefore Ta evolves O<sub>2</sub> at faster rates.

## Conclusion

In this work, we employed *operando* grazing incidence and modulated excitation X-ray absorption spectroscopy to study the effect of several stimuli on STON oxynitride thin films during photoelectrochemical water splitting. A comparison with *ex-situ* XPS of the samples in their initial and final states is also included. The XPS analysis suggests (a) partial dissolution of SrO<sub>x</sub> into the alkaline electrolyte, (b) an increase in electron density on Sr, (c) lattice Sr and Ta enrichment at the surface, (d) changes in hybridisation with the N 2p and O 2p states. (e) Increase in surface hydrophilicity, evidenced by the increased adsorbed OH/O(OH)/H<sub>2</sub>O content, (f) slight loss of N from the structure where N remains chemisorbed as N<sub>2</sub>/NO<sub>x</sub> species.

Surface reconstruction under OER conditions has previously been discussed for Sr and Co containing perovskite oxide catalysts<sup>57, 145, 213, 214</sup> where, the OER proceeds under applied potential together with the lattice-oxygen evolution reaction.<sup>22, 57</sup> This has been shown to have a beneficial effect with respect to the OER due to the formation of an enriched BOH/BO(OH) surface, increased hydrophilicity and an increase in catalytic activity.<sup>57, 92</sup> For the oxynitride STON, we also observe surface enrichment of the B cation (Ta) and increased hydrophilicity. However, contrary to oxides, this superficial BOH/BO(OH) enriched surface layer may have complications for the oxynitrides. Since, the N 1s XPS analysis of LTON and STON oxynitride thin films before and after the PECR, evidence N<sub>2</sub>/NO<sub>x</sub> chemisorbed species. As discussed previously, likely formed in competitive reactions from the surface lattice N and the OER intermediates.

*Operando* GIXAS determined that the surface reconstruction occurs when the applied potential increases above 1.3 V vs. RHE. ME-XAS-PSD measurements with modulated light as an external stimulus. It was previously shown for LaTiOxNy that light and the electrolyte do not contribute to the degradation of the material.<sup>66</sup> However, we observe small changes in the light response for Sr, with respect to its electronic structure and its evolution as a function of applied potential. Here we show that the nature of the A cation and the evolution of its electronic and geometric environment at the solid/liquid interface has large impacts on the overall stability and catalytic activity of the material during operation conditions.

We also note that nitrogen determines the bulk electronic structure of oxynitrides and in turn, the light absorption properties of the photocatalysts. However, at the surface, the nitrogen species take on a more apparent antagonistic role, competing with the OER. To improve the performance of semiconductor photocatalysts, it is important to understand on a fundamental level what is occurring at the photocatalyst surface during operation.

This study presents the first *operando* surface sensitive characterisation of the solid-liquid interface during the visible light driven oxygen evolution reaction. An important advance, for future work to explore in *operando*, the effect of applied potential and the synergistic effects first row transition metal-based co-catalysts have on the performance and stability of the oxynitride photocatalyst templates, where it has been shown that passivation layers and co-catalysts can prevent/minimise the detrimental surface reconstruction. The *operando* studies are not limited to the visible-light responsive oxynitrides thin film photocatalysts. *Operando* surface sensitive characterisations and comparisons can also be made with thin films representative UV-only responsive, wide band gap oxides.

## 5.12. Experimental

### Crystalline Properties

XRD measurements were performed using a Seifert X-ray Diffractometer with characteristic Cu K $\alpha$  radiation 0.154 nm. Theta-2theta scans were performed to determine the out-of-plane orientations of the films.

### Thin Film Deposition

Three sets of films used in this work were grown using pulsed laser deposition (PLD). A KrF excimer laser (Lambda Physik LPX 300, 30 ns pulse width,  $\lambda = 248$  nm) was used to ablate a target of Sr<sub>2</sub>Ta<sub>2</sub>O<sub>7</sub> fabricated in our laboratory. The target to substrate distance was set at 5 cm. The laser was focused on a spot of 1.1 mm<sup>2</sup> with a laser fluence of ca. 3 J cm<sup>-2</sup> and laser repetition rate of 10 Hz. Commercially available (001)-oriented MgO was used as a substrate (10 x 10 x 0.5 mm). Platinum paste was applied between the substrates and heating stage to provide good thermal conductivity. The substrate temperature of 750°C was measured via a pyrometer. N<sub>2</sub> background partial pressure of 8.0 x 10<sup>-4</sup> mbar was set via a gas inlet line to the vacuum chamber. NH<sub>3</sub> gas was injected through a nozzle near the laser spot at the target. The titanium nitride current collector layer was grown in situ, prior to the deposition of the oxynitride film, by conventional PLD using a commercially available TiN target under vacuum with a base pressure of ca. 5 x 10<sup>-6</sup> mbar. The substrate to target distance, substrate temperature, laser repetition and fluence were the same as above.

### Photoelectrochemical Characterisation

Photoelectrochemical (PEC) measurements were performed using a three-electrode configuration in the *operando* reactor cell described in Fig. 3. The working and counter electrode were the STON thin films and Pt wire respectively. A KCl saturated Ag/AgCl electrode was used as the reference. An aqueous solution of 0.5 molar NaOH (pH = 13) was used as an electrolyte. For the electrical contact of the STON films a wire was adhered to the TiN current collector to apply the electrical contact to the potentiostat (Metrohm Autolab). The electrically connected area was then insulated with epoxy and the sample then immersed into the electrolyte in the cell. The samples were illuminated with a 405 nm laser diode (Laser2000)

which has a 5mW power output and spot size of ca. 0.0308 cm<sup>2</sup>. The corresponding light intensity is ca. 130 mW cm<sup>-2</sup>. To measure the dark and light current the laser diode was modulated for 60 second periods (60 seconds on, 60 seconds off). The potentiodynamic measurements were performed at a scan rate of 10 mV s<sup>-1</sup> under chopped illumination with 4 second periods.

### **Chemical Composition**

Rutherford Backscattering (RBS) and Elastic Recoil Detection Analysis (ERDA) were employed to determine the chemical compositions of the STON thin films. RBS provides the metal ratios and oxygen content whereas, ERDA provides nitrogen-to-oxygen ratio. The RBS measurements were performed using a 2 MeV He beam and a silicon PIN diode detector. ERDA was carried out with a 13 MeV <sup>127</sup>I beam and the combination of a time-of-flight spectrometer with a gas ionisation detector. RBS data was analysed using RUMP.<sup>131</sup>

### **X-ray Photoelectron Spectroscopy**

The XPS measurements were performed at the SX-ARPES endstation<sup>126</sup> of the Advanced Resonant Spectroscopies (ADDRESS) beamline<sup>215</sup> situated at the Swiss Light Source, Paul Scherrer Institute, Switzerland. The photon flux was ca. 10<sup>13</sup> photons s<sup>-1</sup> and focused into a spot size of 30 × 75 μm<sup>2</sup> on the sample surface at an X-ray grazing incidence angle of 20°. The energy resolution was set to 50 meV and the sample temperature was kept at 298 K. Spectra were calibrated using the C 1s signal due to adventitious carbon situated at 284.8 eV.

### **X-ray Absorption Spectroscopy**

The time resolved XAS were measured using the quickXAS method<sup>207</sup> at the SuperXAS beamline at the SLS, Paul Scherrer Institute in Switzerland. The polychromatic beam of the 2.9 Tesla superbend was collimated by a Si-coated collimating mirror and subsequently monochromatised by a Si(111) channel-cut crystal of the quickXAS monochromator, which oscillated at 1 Hz frequency with an acquisition time of 500 milliseconds per spectrum. Energy calibration was performed using Pb (L<sub>1</sub> edge E<sub>0</sub> = 15861 eV) and Zn (K edge E<sub>0</sub> = 9659 eV)

thin foils for the Sr K ( $E_0 = 16105$  eV) and Ta  $L_3$  ( $E_0 = 9881$  eV) edges, respectively. A focused beam was used with a spot size of  $100 \times 100 \mu\text{m}^2$ . The samples were fixed into the cell and the cell was mounted in grazing incidence to the incoming X-ray beam, with an incident angle between 0-1 degrees. Data analysis was performed using the ProQEXAFS,<sup>216</sup> Athena<sup>217</sup> and Larch<sup>218</sup> software packages.

### 5.13. Appendix

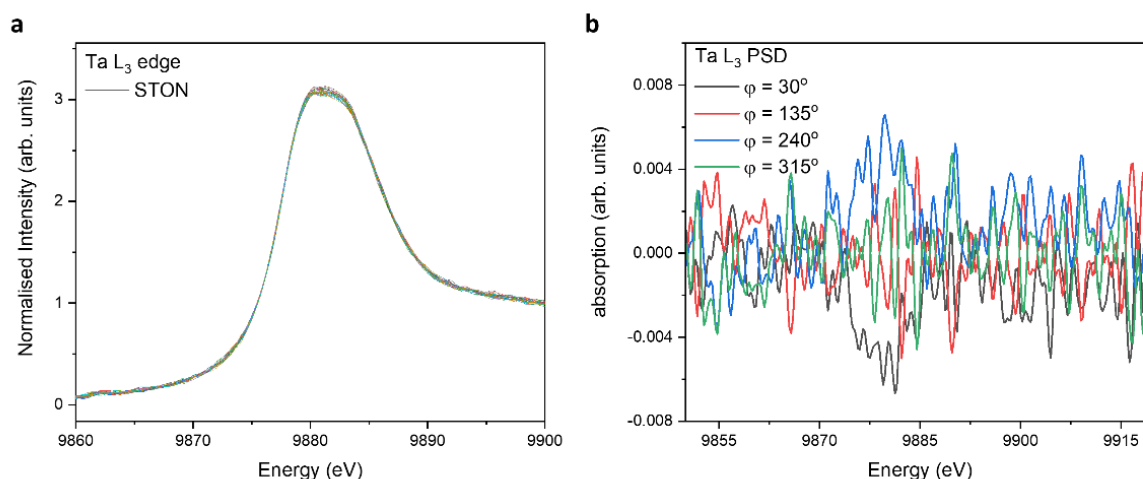


**Fig. 5.10.** The Ta PSD signal does not exhibit any changes larger than the noise of the experiments. This does not suggest that Ta is not active, rather that the changes in electron density and the kinetics of the OER are much faster than those for Sr due to the fact that Ta is a transition metal and Sr, an alkaline earth element.

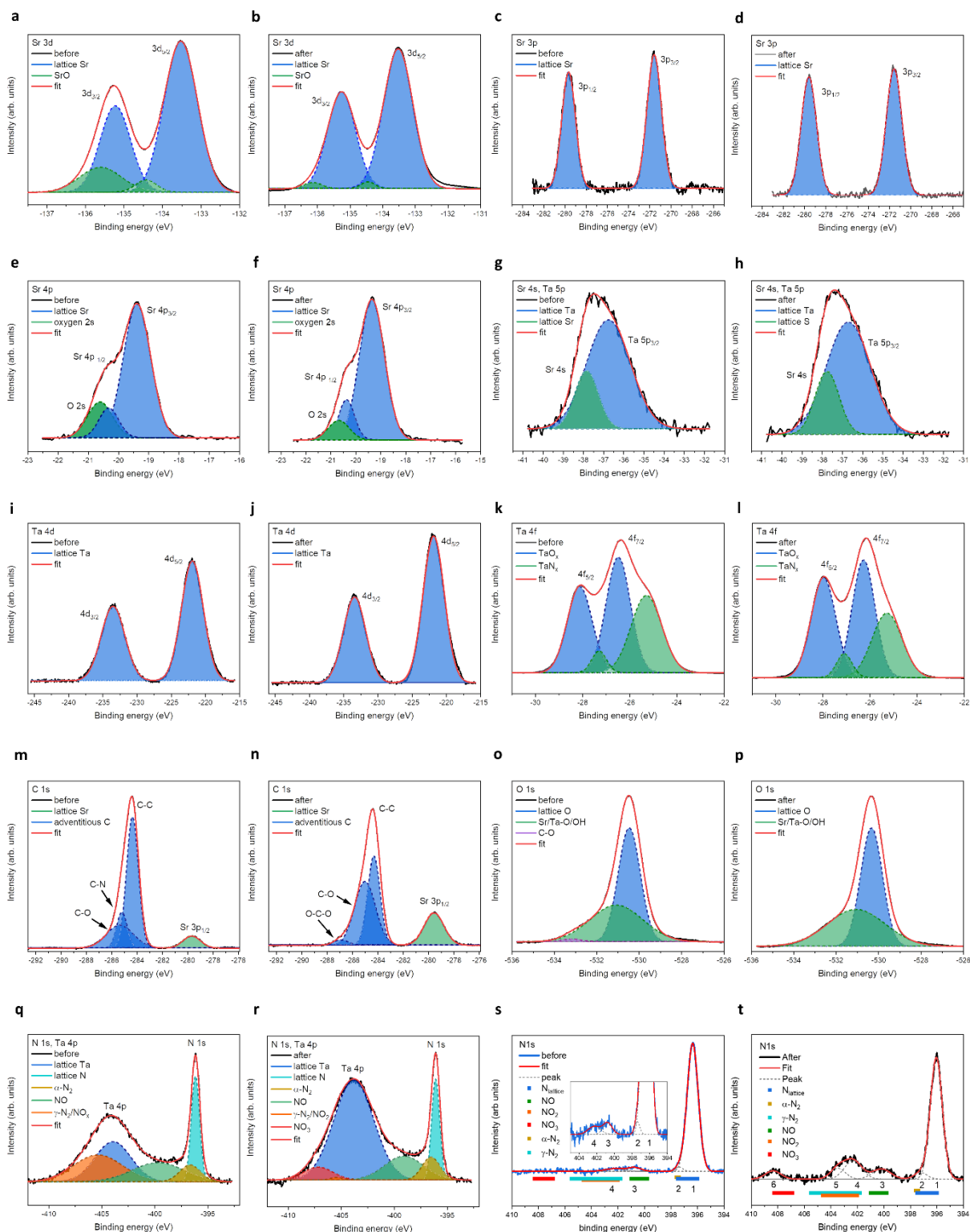


**Fig. 5.11** (a-r) STON before and after PEC, (s-t) LTON N1s before and after PEC, respectively. Reference values for binding energies given in supplementary tables.

**Table 14.** Ion Beam Analysis for STON films

<b>Composition</b>	<b>Sr:Ta</b>	<b>O:N</b>
Sr <sub>0.94</sub> Ta <sub>1.06</sub> O <sub>2.80</sub> N <sub>0.31</sub>	0.89 (0.02)	9.03(0.07)

**Table 15.** Literature sourced XPS data for Ta 4f<sub>7/2</sub>.

<b>Component</b>	<b>Energy (eV)</b>	<b>Reference</b>
Ta	21.6-22	80, 219, 220, 221, 222, 223, 224, 225, 226, 227
TaO <sub>x</sub>	26.0	228
	26.2	229
	26.5	80, 230, 231, 232
	26.6	227
	26.9	233
TaN <sub>x</sub>	23.5	80
	24.7	229
	24.8	227, 232, 234
	25.1	233, 234
	25.3	231
TaO <sub>x</sub> N <sub>y</sub>	25.0	80
	25.5	229
	25.7	234
	25.8	227, 232
	25.9	234
	26.0	233
	26.1	234

**Table 16.** Literature sourced XPS data for Ta 4f<sub>5/2</sub>.

Component	Energy (eV)	Reference
Ta	23.70	227, 235
TaO <sub>x</sub>	28.4	231
	28.5	227
	28.7	233
TaN <sub>x</sub>	26.7	227
	26.9	233
	27.2	231
TaO <sub>x</sub> N <sub>y</sub>	27.7	227, 233

**Table 17.** Literature sourced XPS data for Ta 4p<sub>3/2</sub>.

Component	Energy (eV)	Reference
TaN <sub>x</sub>	400.8	236
	402	237
	403	238
TaO <sub>x</sub> N <sub>y</sub>	403.1	239
	403.5	231
	403.9	239
	404	240
	404.5	227

**Table 18.** Sr 3p Peak Fit Before PEC

Peak	1	2
<b>Centroid (eV)</b>	-279.65322 ± 0.00457	-271.58483 ± 0.00409
<b>FWHM (eV)</b>	1.291 ± 0.0096	1.36436 ± 0.00861
<b>Area</b>	24249.73794 ± 170.28232	29469.15676 ± 176.22869
<b>R-Square</b>	0.99493	



**Table 19.** Sr 3p Peak Fit After PEC

Peak	1	2
<b>Centroid (eV)</b>	-279.57941 ± 0.00317	-271.53526 ± 0.003
<b>FWHM (eV)</b>	1.4441 ± 0.00672	1.47716 ± 0.00637
<b>Area</b>	42598.5652 ± 189.56348	46526.0029 ± 192.31561
<b>R-Square</b>	0.99776	

**Table 20.** Sr 3d Peak Fit Before PEC

Peak	1	2	3	4
<b>Centroid (eV)</b>	--133.52559 ± 0.01414	-134.42294 ± 0.15156	-135.22127 ± 0.04092	-135.60325 ± 5.33923
<b>FWHM (eV)</b>	0.86754 ± 0.02092	0.55329 ± 0.30998	0.79233 ± 0.55571	1.09281 ± 2.65848
<b>Area</b>	220674.28476 ± 6504.05398	11457.0213 ± 2241.51213	115215.53577 ± 54773.7724	6112.76107 ± 5108.96732
<b>R-Square</b>	0.98726			

**Table 21.** Sr 3d Peak Fit After PEC

Peak	1	2	3	4
<b>Centroid (eV)</b>	-133.52371 ± 0.00375	-134.44716 ± 0.07153	-135.25871 ± 0.00981	136.13358 ± 0.15463
<b>FWHM (eV)</b>	0.90477 ± 0.00793	0.4245 ± 0.15984	0.86069 ± 0.04955	0.5591 ± 0.19969
<b>Area</b>	232332.42423 ± 1776.72603	5212.77251 ± 4145.0633	153051.89003 ± 8408.25997	45995.00203 ± 1424.5185
<b>R-Square</b>	0.99609			

**Table 22.** Sr 4p and O 2s Peak Fit Before PEC

Peak	1	2	3
Centroid (eV)	$-19.38482 \pm 0.01864$	$-20.3163 \pm 0.10708$	$-20.61054 \pm 1.16868$
FWHM (eV)	$0.9026 \pm 0.01591$	$0.64963 \pm 0.43078$	$0.83051 \pm 0.52531$
Area	$11953.29605 \pm 495.33252$	$1912.54469 \pm 1122.8581$	$2959.82432 \pm 1170.0807$
R-Square	0.99918		

**Table 23.** Sr 4p and O 2s Peak Fit After PEC

Peak	1	2	3
Centroid (eV)	$-19.34974 \pm 0.01268$	$-20.36315 \pm 0.04252$	$-20.68429 \pm 1.15995$
FWHM (eV)	$1.00048 \pm 0.013$	$0.63186 \pm 0.18837$	$0.84706 \pm 0.57905$
Area	$16509.95251 \pm 391.78648$	$2985.39928 \pm 654.02432$	$1944.41958 \pm 690.44717$
R-Square	0.99918		

**Table 24.** Sr 4s and Ta 5p Peak Fit Before PEC

Peak	1	2
Centroid (eV)	$-37.83893 \pm 0.01823$	$-36.75281 \pm 0.06538$
FWHM (eV)	$1.16559 \pm 0.07543$	$2.17036 \pm 0.06255$
Area	$4220.6715 \pm 803.01647$	$14750.36267 \pm 922.61298$
R-Square	0.99446	

**Table 25.** Sr 4s and Ta 5p Peak Fit After PEC

Peak	1	2
Centroid (eV)	$-37.75081 \pm 0.01553$	$-36.69728 \pm 0.05493$
FWHM (eV)	$1.19942 \pm 0.06123$	$2.19563 \pm 0.05015$
Area	$6106.5987 \pm 926.47299$	$19927.18315 \pm 1056.30328$
R-Square	0.9963	

**Table 26.** Ta 4d Peak Fit Before PEC

Peak	1	2
Centroid (eV)	$-233.5189 \pm 0.00585$	$-221.91514 \pm 0.0035$
FWHM (eV)	$3.48002 \pm 0.01311$	$3.2174 \pm 0.00777$
Area	$102869.76637 \pm 398.19966$	$152900.35078 \pm 376.43228$
R-Square	0.99841	

**Table 27.** Ta 4d Peak Fit After PEC

Peak	1	2
Centroid (eV)	$-233.41751 \pm 0.00665$	$-221.85157 \pm 0.0038$
FWHM (eV)	$3.27951 \pm 0.01474$	$3.13172 \pm 0.00839$
Area	$132220.62551 \pm 602.56733$	$215880.03097 \pm 583.29846$
R-Square	0.998	

**Table 28.** Ta 4f Peak Fit Before PEC

Peak	1	2	3	4
<b>Centroid (eV)</b>	$-25.28531 \pm 0.01644$	$-27.2936 \pm 0.0139$	$-26.48192 \pm 0.0056$	$-28.12081 \pm 0.00614$
<b>FWHM (eV)</b>	$1.30442 \pm 0.01537$	$0.63056 \pm 0.03194$	$1.03484 \pm 0.02117$	$1.0662 \pm 0.00779$
<b>Area</b>	$125778.64569 \pm 3126.10392$	$17090.70087 \pm 2890.97467$	$149256.04267 \pm 5148.01471$	$114674.56033 \pm 1192.47262$
<b>R-Square</b>	0.99987			

**Table 29.** Ta 4f Peak Fit After PEC

Peak	1	2	3	4
<b>Centroid (eV)</b>	$-25.26927 \pm 0.03279$	$-27.08503 \pm 0.01872$	$-26.26536 \pm 0.00667$	$-27.9737 \pm 0.00524$
<b>FWHM (eV)</b>	$1.26866 \pm 0.02643$	$0.97409 \pm 0.02477$	$0.66245 \pm 0.03494$	$1.05826 \pm 0.00665$
<b>Area</b>	$132232.36396 \pm 7017.27026$	$185156.91357 \pm 10048.03592$	$25633.93592 \pm 4493.3563$	$171320.72122 \pm 1535.28089$
<b>R-Square</b>	0.99987			

**Table 30.** C 1s Peak Fit Before PEC

Peak	1	2	3	4
<b>Centroid (eV)</b>	$-279.69471 \pm 0.00839$	$-284.3548 \pm 0.00767$	$-285.18928 \pm 0.02152$	$-285.35279 \pm 0.0267$
<b>FWHM (eV)</b>	$1.39118 \pm 0.01775$	$0.93911 \pm 0.00887$	$0.82405 \pm 0.0233$	$2.13579 \pm 0.03022$
<b>Area</b>	$29309.94428 \pm 357.69729$	$214157.2881 \pm 4433.23097$	$51158.70353 \pm 4217.75904$	$84350.46265 \pm 2540.20022$
<b>R-Square</b>	0.99976			

**Table 31.** C 1s Peak Fit After PEC

Peak	1	2	3	4
<b>Centroid (eV)</b>	-279.57921 ± 0.00335	-284.31246 ± 0.00388	-285.01138 ± 0.02467	-286.92129 ± 0.06273
<b>FWHM (eV)</b>	1.55878 ± 0.00715	0.97561 ± 0.00901	1.64606 ± 0.01545	1.1534 ± 0.08275
<b>Area</b>	50003.16423 ± 221.61098	86330.86346 ± 2788.01509	103841.19401 ± 2414.48879	5983.695 ± 764.23011
<b>R-Square</b>	0.99971			

**Table 32.** O 1s Peak Fit Before PEC

Peak	1	2	3
<b>Centroid (eV)</b>	-530.46148 ± 0.00178	-531.07071 ± 0.0374	-533.18451 ± 0.05187
<b>FWHM (eV)</b>	1.04254 ± 0.00626	2.48263 ± 0.0627	0.9018 ± 0.17859
<b>Area</b>	165610.48771 ± 2829.38261	126647.74654 ± 1471.86872	3398.38014 ± 1501.12366
<b>R-Square</b>	0.99979		

**Table 33.** O 1s Peak Fit After PEC

Peak	1	2
<b>Centroid (eV)</b>	-530.32002 ± 0.00106	-531.04871 ± 0.00807
<b>FWHM (eV)</b>	1.03305 ± 0.00275	2.73542 ± 0.01428
<b>Area</b>	295971.82056 ± 1368.69256	243648.68368 ± 1828.90827
<b>R-Square</b>	0.99983	

**Table 34.** N 1s and Ta 4p Peak Fit Before PEC

Peak	1	2	3	4
<b>Centroid (eV)</b>	-396.15118 ± 0.00378	-396.65639 ± 0.09367	-399.67412 ± 1.88024	-403.92705 ± 0.10212
<b>FWHM (eV)</b>	0.79614 ± 0.00996	1.94654 ± 0.21381	4.87092 ± 1.3796	3.38278 ± 1.1459
<b>Area</b>	21611.22085 ± 568.30918	8370.54043 ± 2479.53865	22418.31898 ± 5377.99719	96803.94916 ± 10607.91758

Peak	5
<b>Centroid (eV)</b>	-405.35034 ± .28803
<b>FWHM (eV)</b>	4.61057 ± 3.03883
<b>Area</b>	31680.48163 ± 15843.03548
<b>R-Square</b>	0.99653

**Table 35.** N 1s and Ta 4p Peak Fit After PEC

Peak	1	2	3	4
<b>Centroid (eV)</b>	-396.0752 ± 0.00465	-396.51934 ± 0.07196	-399.06478 ± 0.30341	-403.80418 ± 0.08599
<b>FWHM (eV)</b>	0.76585 ± 0.01237	1.68271 ± 0.13794	3.65362 ± 0.59233	3.76847 ± 0.31262
<b>Area</b>	19835.05122 ± 748.6462	9909.66385 ± 1928.76987	22418.31898 ± 5377.99719	96803.94916 ± 10607.91758

Peak	5	6
<b>Centroid (eV)</b>	-405.41358 ± 0.21635	-407.1659 ± 0.48547
<b>FWHM (eV)</b>	1.14905 ± 0.65182	2.78483 ± 0.39213
<b>Area</b>	750.00707 ± 1037.78766	9226.66389 ± 6274.80751
<b>R-Square</b>	0.99764	

## Chapter 6: Conclusion and Outlook

### 6.1. Conclusion

The work in this thesis can be divided into two halves, the first, concerned with the fundamental understanding of the electronic structure of oxynitride SC photocatalysts and their evolution at the solid-liquid interface. The second, an experimental platform for *operando* GIXAS at the solid-liquid interface using a custom designed reactor cell, providing a platform for future work to continue.

In chapter 2, this work demonstrates that SX-ARPES can resolve the electronic structure and its evolution for the oxynitride type materials, where no information regarding oxynitrides with respect to ARPES exists to date. Not only have we determined the electronic structure of the oxynitride LTON photocatalysts used in this work, we also monitored the evolution of the electronic structure of LTON, as a consequence of the OER. Using SX-ARPES, we could

observe that the VBM consists of primarily Ti – N 2p states but it also has small contribution due to La – N 2p states. After PEC, these states deplete due to the loss of nitrogen from the surface of the lattice during operation conditions. Exposure to the light, electrolyte and/or the X-ray beam do not affect the electronic structure of LTON. The summary of the findings are as follows: (a) the depletion of Ti- and La-N 2p states, (b) disorder surrounding the local environment of Ti, whilst, the total charge surrounding Ti is conserved, (c) a reductive shift in the XAS spectra for the La and an increase in the spin orbit coupling of the La d states, (d) the creation of additional Ti- and La - O 2p states.

In chapter 3, we applied complementary NR and surface sensitive GIXAS techniques to probe the detrimental surface modifications associated with oxynitrides that occur during operation. We show that thin films are ideal model systems for surface sensitive studies where one can more easily distinguish the surface signals from the bulk contributions. The physiochemical modification of the oxynitride surface was limited to the first 3nm of the bare thin film. The addition of the IrO<sub>2</sub> co-catalyst not only increases the performances of the oxynitride sample by a factor of two but also protects the surface by preventing the observed surface modification as a direct consequence of the water splitting process. The surface modification involves the oxidation of the La A cations and a disordering of the local environment surrounding the Ti B cations. Whereas, La undergoes a reduction in the bulk and Ti remains unaffected. These findings were unexpected because we have evidence that the A site plays a significant role in the OER and La does not exist solely in the nominal +3 valence state. To the best of our knowledge, this is the first depiction of what is occurring at the surface and the extent of the changes with respect to each cation as a function of depth during photocatalytic water splitting.

The findings in this chapter are also in agreement with those in Chapter 2 where, s-XAS and SX-ARPES suggested (a) the loss of N states, (b) charge conservation surrounding Ti but disorder to its local environment, (c) reductive shift for La and an increase in spin orbit coupling and, (d) increased O2p hybridisation. Here, NR suggests this effect is limited within the first 3 nm of the samples, GIXAS shows that La acts as a weak transition metal and, the Ti 3d states in the conduction band shows signs of disorder, due to vacancy generation, changing O/N and the disorder of the O/N-B-O/N dihedral bond angles.



In chapter 4, the cumulative area for the O1s peak fitting suggest that after PEC there is an increase in the total oxygen content by ca. 17% on/at the LTON surface. The total increase in oxygen is due to the increased concentration of O species under OER conditions adsorbing/chemisorbing on the surface. We observe in the N 1s XPS spectra, the formation of N<sub>2</sub>/NO<sub>x</sub> chemisorbed species, which suggests, competitive reactions between the surface lattice N and the OER intermediates. The titanium, Ti 2p XPS peaks do not shift in position with respect to binding energy, suggesting that Ti does not change its formal oxidation state (as suggested in chapters 2 and 3). However, there are changes in the ratios of these peaks after PEC. These changes are likely due to the local structural change surrounding Ti when nitrogen is lost and replaced with O changing the ratio of TiO<sub>5-x</sub>N<sub>1+x</sub> and TiO<sub>6</sub> like environments in the oxynitride.

In chapter 5, we employed *operando* grazing incidence and modulated excitation X-ray absorption spectroscopy to study the effect of several stimuli on STON oxynitride thin films during photoelectrochemical water splitting. A comparison with *ex-situ* XPS of the samples in their initial and final states is also included. Overall, the XPS analysis of the initial and final state of the STON photocatalyst suggests that STON suffers from a surface degradation and reconstruction as evidenced with respect to the decrease in initial photocurrent. The XPS data suggests that STON undergoes a) slight loss of N from the structure where N remains bound as N<sub>2</sub>/NO<sub>x</sub> species. b) The increase in electron density and segregation of Sr. c) apparent Ta enrichment at the surface due to the changing O/N, d) Increased hydrophilicity.

*Operando* GIXAS corroborates the XPS findings, determining that the surface reconstruction occurs when the applied potential increases above 1.3 V vs. RHE. ME-XAS-PSD measurements, with modulated light as an external stimulus we show that other than the generation of charge carriers, the light has minimal effect on the system, where it was previously shown in chapter 3 that for LaTiO<sub>x</sub>N<sub>y</sub> that light and the electrolyte do not contribute to the degradation of the material. However, we observe changes in the light response for Sr, with respect to its electronic structure and its evolution as a function of applied potential.

Indicating that the kinetics of the OER are much faster on the Ta site than for Sr. However, when the potential is increased to 1.5V, the rate of the OER on the reduced Sr sites increase, where Sr behaves more like a transition metal and less ionic in nature.

These observations can be explained by increases in surface hydrophilicity and the formation of a superficial OH/O(OH) surface layer. This beneficial effect normally associated with the perovskite oxides, adopts a more counterproductive role with respect to the oxynitrides in the presence of N at the surface. Where nitrogen is lost from the lattice structure in the surface layer(s), and remains chemisorbed on the surface as N<sub>2</sub> and NO<sub>x</sub> species. The OER intermediates (OH/O(OH)) and charge carriers are then in competition between the desired H<sub>2</sub> and O<sub>2</sub> generation, unfavourable charge recombination and the self-degradation and formation of N<sub>2</sub> and NO<sub>x</sub> species during the OER. Where, the generation of defects limit the overall kinetics and charge transfer efficiency for efficient water splitting using oxynitrides in their bare form.

Our findings also support the idea that that La behaves as a transition metal although, a weak one, compared to Ti. It is likely then that the formation of LaOH/LaO(OH) would then not only contribute to overall O<sub>2</sub> evolution during the OER, but also help to stabilise and/or minimise, vacancy induced surface reconstruction. However, as discussed for Ti, it then can also facilitate N<sub>2</sub>/NO<sub>x</sub> formation and drive the N loss from the surface layer on the Ti site. We show that the nature of the A cation and the evolution of its electronic and geometric environment at the solid/liquid interface has large impacts on the overall stability and catalytic activity of the material during operation conditions. We also note that nitrogen determines the bulk electronic structure of the oxynitrides and in turn, the light absorption properties of the photocatalysts. However, at the surface the nitrogen species take on a more apparent antagonistic role, competing with the OER.

## 6.2. Outlook

To improve the performance of semiconductor photocatalysts, it is important to understand on a fundamental level what is occurring at the photocatalyst surface during operation. Future work plans to explore *operando*, the effect of applied potential and the synergistic effects first row transition metal based co-catalysts have on the performance and stability of the oxynitride photocatalyst templates, where it has been shown that passivation layers<sup>65</sup> and co-catalysts can prevent/minimise the detrimental surface reconstruction (chapter 3).

In this work, we have compared epitaxially orientated oxynitride thin films, however, we have recently observed that for thin films grown with different crystallographic orientations (not possible with randomly orientated polycrystalline powders) exhibit large differences in the kinetics, charge extraction and, in turn the photocatalytic performance. The effect of orientation also has consequences on the usual enhancement seen when decorated with a co-catalyst (Fig. 6.1). Future work can aim to build on what we have learnt, with respect to the work in this thesis, to study a number oxynitride materials for the determination of their electronic structures at the surface and their evolution whilst, trying to rationalise the observed orientation dependence on their photocatalytic performance. These experiments are not limited to oxynitrides or, bare semiconductor photocatalyst templates. The semiconductor-co-catalyst and/or buried semiconductor-passivation layer interface play crucial roles in the charge injection and transfer processes.

With the advantage of the enhanced probing depth, and chemical state specificity, NR, SX-ARPES, XPS and GIXAS provide unique opportunities to explore both materials and the interface properties, as well as their reactivity and/or evolution. Chemical state specificity is not limited to oxynitrides and, the measurements are feasible with thin films used in various applications. Based on the findings in this work (with respect to La and Sr), it would be of personal interest to investigate materials such as  $\text{La}_{1-x}\text{Sr}_x\text{CoO}_{3-\delta}$ . Where the effect of doping concentration between Sr and La can be explored with respect to the stability and activity of the materials as well as, the evolution with respect to Sr and La at the A sites.

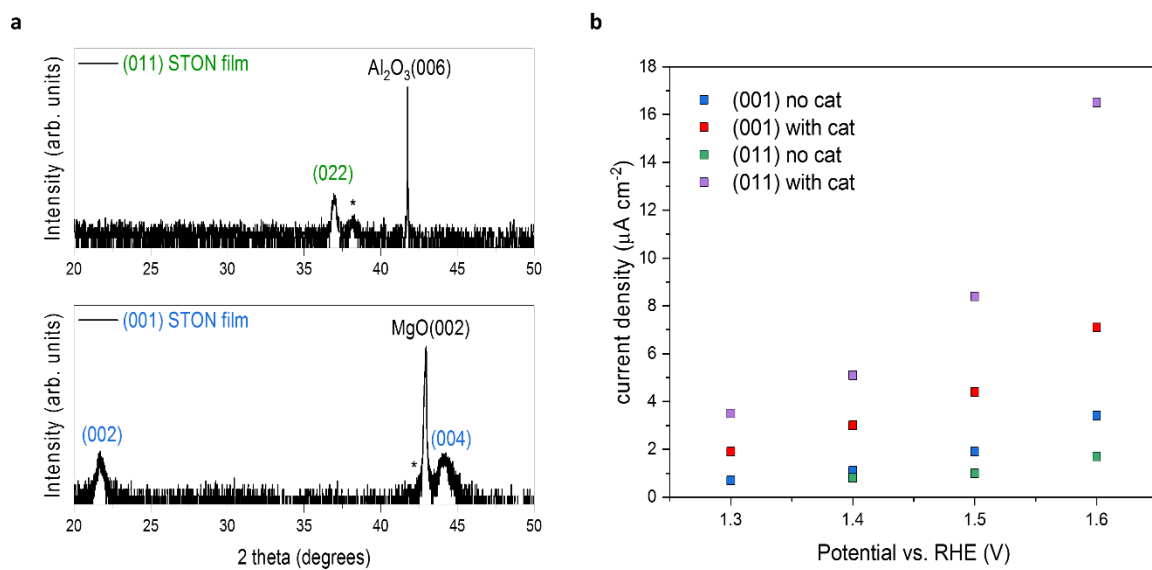


**Fig. 6.1.** (a) XRD for 001 and 011 orientated STON oxynitride thin films, (b) the PEC performance of the two orientated film, with and without a NiO co-catalyst.

## List of Figures

- Fig. 1.1 (a) comparison of solar energy with other energy sources, (b) worldwide mean solar irradiance variation, (c) solar thermal plant, (d) silicon photovoltaic (PV) panels and wind turbines, (e) Dye-sensitised solar cells (DSSC), (f) biofuel production – bioethanol from corn, (g) photoelectrochemical water splitting for solar hydrogen production. Reproduced from Ref.<sup>2</sup>. 11
- Fig. 1.2 Electrolysis of water. Adapted from Ref.<sup>14</sup> 12
- Fig. 1.3 Schematic representation of the photoexcitation 14
- Fig. 1.4 The band positions of various semiconductors relative to the NHE and aligned to the vacuum level for a more accurate comparison between materials. pH = 0, 298.15K, 1 bar Reproduced from Ref.<sup>25</sup> 16
- Fig. 1.5 (a) wide bandgap oxide semiconductor, (b) spectral irradiance of the sun, reproduced from Ref.<sup>31</sup> 18
- Fig. 1.6 Energy diagrams of photocatalytic water splitting based on (a) one-step excitation and (b) two-step excitation (Z-scheme); and PEC water splitting using (c) a photoanode, (d) photocathode, and (e) photoanode and photocathode in tandem configuration. The band gaps are depicted smaller in (b) and (e) to emphasize that semiconductors with a narrow band gap can be employed.<sup>17</sup> 19
- Fig. 1.7 ABX<sub>3</sub> perovskite structure. Reproduced from Ref.<sup>46</sup> 20
- Fig. 1.8 Bandgap engineering with nitrogen substitution 21
- Fig. 1.9 (a) TEM cross-section of oxynitride thin film, adapted from Ref.<sup>66</sup>, (b) SEM for CaNbO<sub>x</sub>N<sub>y</sub> oxynitride powders, reproduced from Ref.<sup>65</sup> 23

- Fig. 1.10 Upper panel: schematic diagram of the principal of PRCLA. PV = pulsed valve; AT = ablation target; AE = adiabatic pulsed expansion; AP = ablation plume; IR = interaction region; SH = substrate heater; dVA = distance from pulsed valve nozzle to point of ablation on target.  $\Delta t$  is the adjustable delay between the pulsed valve trigger and laser trigger. Lower panel: the visual effect of crossing a gas pulse with an ablation plume for a Cu plasma and an N<sub>2</sub>O gas pulse. The left-hand image shows the appearance of the plume propagating into vacuum or when  $\Delta t$  is set so that the plume and gas pulse “miss” each other temporally. The right-hand image shows the increase in plume brightness due to its collisional excitation in passing through the densest part of the gas pulse. If one uses a constant background pressure of 20 Pa instead of a pulsed expansion, the plume also becomes brighter, but it is more localized around the point of ablation because of quenching. Reproduced from Ref.<sup>69</sup> 24
- Fig. 2.1 (a) Schematic of an ARPES experiment showing the photoemission geometry, (b) 3-electrode configuration for the photoelectrochemical characterisations. 31
- Fig. 2.2 (a) XRD pattern of the epitaxially grown LTON film, the  $\theta/2\theta$  scan is shown in black, with the angular position of the (00l) reflexes of LaTiO<sub>2</sub>N shown in blue for reference. The inset shows the crystal structure of LaTiO<sub>2</sub>N, (b) zoomed region around the MgO substrate reflex for data shown in part a, (c) Rutherford backscattering (RBS) spectrum, (d) elastic recoil detection analysis (ERDA) spectrum. The cation ratios were determined by RBS and the O:N ratio by ERDA. 34
- Fig. 2.3 (a) Energy diagram for photocatalytic water splitting, (b-c) photocurrent densities for LTON for the first four-potentiodynamic measurements. 36
- Fig. 2.4 (a) soft-XAS spectra for LTON showing the Ti  $L_2$  and  $L_3$  edge before and after the PECR, shown in blue and red, respectively, (b) SX-ARPES Ti 2p resonance (angle integrated) intensity map before the PECR, (c) after PEC. 36

- The solid white lines are the XAS spectra overlaid from part a. The white dashed line marks  $E_F$ . (d) schematic representation of the transition of the  $L_3$  and  $L_2$  absorption bands, (e) graphic representation for the observed changes occurring to the band structure of the surface layers of the LTON photocatalyst. Where  $E_F$ ,  $h\nu$ ,  $E_g$  and VBM denote the fermi level, visible-light photons, the band gap and the VB maximum, respectively. 38
- Fig. 2.5 (a-b) Ti  $L_3$ -edge high-statistics ARPES images acquired at  $h\nu = 465.3$  eV before (a) and after (b) the PECR; (c) angle-integrated ARPES images from a-b, (d-e) the ARPES data from a-b represented in the second derivative -  $d^2I/dE_B^2$  to enhance the band dispersions. The integrated angle range corresponds to  $-7.6:8.1$  degrees. The Ti  $L_2$  edge is included in the appendix Fig. 2.11. 40
- Fig. 2.6 (a) Soft-XAS spectra for LTON showing the La  $M_5$  and  $M_4$  edges, respectively, (b) schematic representation of the transitions of the  $M_4$  and  $M_5$  absorption bands, (c) schematic representation of the La contribution to the band structure of LTON, (d) La resonance (angle-integrated) intensity map before PEC, (e) after PEC, (f) angle-integrated plots for data shown in parts d-e. 43
- Fig. 2.7 Off-resonant angle-integrated ARPES spectra measured below (a) the Ti  $L_3$  edge (averaged over  $h\nu = 452-454$  eV) and (b) the La  $M_5$  edge ( $h\nu = 828-830$  eV) representing the total DOS; Resonant weight (resonant minus off-resonant spectral intensity) at (a) the Ti  $L_3$  edge ( $h\nu = 460.2$  eV) and (b) the La  $M_5$  edge ( $h\nu = 835$  eV) representing the Ti and La partial DOS, respectively. The spectra (a-d) are measured before and after the PECR; Theoretical (e) total and partial DOS for  $\text{LaTiO}_2\text{N}$  and (f) total DOS for  $\text{LaTiO}_2\text{N}$ ,  $\text{LaTiO}_3$  and  $\text{La}_4\text{Ti}_4\text{O}_9\text{N}_3$ , aligned to the fermi level. 43
- Fig. 2.8 Total DOS (a)  $\text{LaTiO}_2\text{N}$  (b)  $\text{LaTiO}_3$  (c)  $\text{La}_4\text{Ti}_4\text{O}_9\text{N}_3$  aligned to their respective fermi levels. 53

- Fig. 2.9 (a) Ti L<sub>2</sub> edge high-statistic before PEC, acquired at 465.3 eV, (b) Ti L<sub>2</sub> edge high-statistic after PEC, (c) normalised angle integrated plots for data shown in parts a-b, (d) smoothed data from part a, (e) smoothed data from part b. The integrated angle range corresponds to -7.6:8.1 degrees. 54
- Fig. 2.10 Angle-integrated plot of the LTON VB measured at the Ti L<sub>3</sub> edge after exposure to the X-ray beam over time. 54
- Fig. 3.1 (a) crystal structure of LaTiO<sub>2</sub>N, (b) XRD pattern of the epitaxial LTON film, the  $\theta/2\theta$  is shown in black, with LaTiO<sub>2</sub>N and MgO substrate reflexes shown below in red and green for reference. Reflections are labelled using the (hkl) notation, (c) TEM cross section of the LTON – TiN film grown on MgO, (d) High-angle annular darkfield (HAADF) image; a grain boundary (GB) is tracked with asterisks, (e) O:N ratio determined by TEM/EELS analysis. 58
- Fig. 3.2 (a) Rutherford backscattering (RBS) spectrum, (b) elastic recoil detection analysis (ERDA) spectrum. The cation ratios were determined by RBS whereas, the O:N ratios were determined by ERDA 59
- Fig. 3.3 (a) instrument description for AMOR time-of-flight neutron reflectometer at SINQ/PSI, (b) neutron reflectometry measurement for multilayer thin films, (c-d) surface sensitive GIXAS measurement, side view and top down respectively, (e) penetration depth of X-rays for LTON at the Ti K edge energy range as a function of incident angle, the error bars correspond to the penetration depth at a given incident angle with an error of  $\pm 0.1$  degrees. Values taken from.<sup>136</sup> 61
- Fig. 3.4 (a) energy diagram for the LTON semiconductor photocatalyst, (b) photoelectrochemical 3 electrode cell, (c) 3 consecutive potentiodynamic scans for LTON without catalyst, (d) stabilised photocurrent for the bare LTON film and IrO<sub>2</sub> decorated LTON film shown in red and blue respectively, (e) the degradation from the initial photocurrent with



- successive potentiodynamic linear sweeps comparing the bare and IrO<sub>2</sub> decorated LTON films values taken at 1.5 V vs RHE. 62
- Fig. 3.5 (a) Reflectivity plot for a LTON film exposed to electrolyte and light intensity, yet no external bias was applied to the sample and showed no photoelectrochemical performance, (b) with applied bias, (c) experimental and corresponding model fit for data shown in b, shown by the solid and dashed lines respectively, (d) the inferred scattering length density profile as a function of depth from the corresponding fit. The inset shows the magnified region at and near to the surface of LTON, (e) depth profile of the samples before and after PEC. 65
- Fig. 3.6 (a) La containing references, (b) LTON bulk comparing La before and after PEC, (c) LTON surface comparing La before and after PEC, (d) Ti containing references, (e) LTON bulk comparing Ti before and after PEC, (f) LTON surface comparing Ti before and after PEC. 67
- Fig. 3.7 (a) the bare LTON film surface before and after PEC and the differential spectra shown in black, red and blue respectively, (b) differential spectra and corresponding peak fitting analysis, (c) peak fitting analysis for measured TiO<sub>2</sub> anatase as a reference for peak assignments, (d) Ti(O/N)<sub>6</sub> octahedra and the possible axial and equatorial positions for vacancy generation and adsorption sites, (e) schematic representation of the OER mechanism. 70
- Fig. 3.8 Transmission Electron Microscopy (TEM) cross sectional image for a LTON film. 79
- Fig. 3.9 (a) example of peak fitting for one of the La L<sub>3</sub> spectra, (b) centroid position of peak for each spectra from figure 5b-c, (c) peak FWHM, (d) second derivative for bulk XANES measurements, (e) second derivative for surface XANES measurements. 80

- Fig. 4.1 (a) Schematic of an XPS experiment showing the photoemission, (b) the photoemission process. 84
- Fig. 4.2 (a) O1s XPS spectra before and after PEC comparison shown in blue and red respectively, (b) schematic representation of the OER mechanism, (c) peak fitting before PEC, (d) after PEC. 86
- Fig. 4.3 (a) N1s XPS spectra before and after PEC comparison shown in blue and red respectively, (b) schematic representation of suggested changes to N states, (c) peak fitting before PEC, (d) after PEC. 88
- Fig. 4.4 (a) Ti 2p XPS spectra before and after PEC comparison shown in blue and red respectively, (b) peak fitting before PEC, (c) after PEC, (d) schematic representation of suggested changes to Ti octahedra. 94
- Fig. 4.5 (a) XPS spectra of titanium oxynitride electrocatalyst (a), N 1s spectrum (b) and Ti 2p spectrum (c). Reproduced from Ref<sup>146</sup>. 95
- Fig. 4.6 Deconvoluted Ti 2p XPS spectra of: (a) untreated; (b) treated TiN NP electrode. Reproduced from Ref<sup>147</sup>. 95
- Fig. 4.7 (a) La 3d XPS spectra before and after PEC comparison shown in blue and red respectively, (b) peak fitting before PEC, (c) after PEC. 96
- Fig. 4.8 (a) La 4d XPS spectra before and after PEC comparison shown in blue and red respectively, (b) peak fitting before PEC, (c) after PEC. 97
- Fig. 4.9 (a) La 4p XPS spectra before and after PEC comparison shown in blue and red respectively, (b) peak fitting before PEC, (c) after PEC. 98
- Fig. 4.10 (a) C 1s XPS spectra showing adventitious carbon, before and after PEC comparison used as calibration, (b) Angle-integrated plot of the LTON VB measured at the Ti L3 edge after exposure to the X-ray beam over time (as shown in Fig. 3.7). 100
- Fig. 5.1 (a) Energy diagram for photocatalytic water splitting, (b) experimental schematic of the photoelectrochemical three-electrode

- cell. The working, counter and reference electrodes are the oxynitride thin film, platinum wire and Ag/AgCl respectively, (c) photocurrent densities for STON for the first three-potentiodynamic measurements, (d) photocurrent degradation from part c, values taken at 1.5 V vs. RHE. 109
- Fig. 5.2 (a) Rutherford backscattering (RBS) spectrum, (b) elastic recoil detection analysis (ERDA) spectrum. The cation ratios were determined by RBS and the O:N ratio by ERDA. 111
- Fig. 5.3 (a) XRD pattern of the epitaxially grown STON film, the  $\theta/2\theta$  scan is shown in black, with the angular position of the (00l) reflexes of SrTaO<sub>2</sub>N shown in blue for reference. The inset shows the crystal structure of SrTaO<sub>2</sub>N, (b) Magnified region from data shown in part a. 111
- Fig. 5.4 STON thin film XPS spectra before and after PEC. (a) C 1s, (b) O 1s, (c) Sr 3d, (d) Sr 4s, (e) Sr 4p, (f) Sr 3p, (g) Ta 4d, (h) Ta 4f, (i) N 1s and Ta 4p edges. 113
- Fig. 5.5 (a) trimetric view of the cell and GIXAS geometry used during measurements, where the grazing incident X-rays enter through a Mylar foil covered side window, (b) cross sectional internal view. Where, PIPS denotes a passivated implanted planar silicon detector. 116
- Fig. 5.6 (a) Transmission of X-rays through optically clear Mylar used as a window material for X-rays and visible light, (b) attenuation length of X-rays in pure H<sub>2</sub>O at an incident angle of 1°. Ta L<sub>3</sub> edge (9881 eV) has been labelled (Sr K edge at 16105 eV is not shown). Values taken from.<sup>136</sup> 117
- Fig. 5.7 (a) Trimetric view, (b) side view, (c) back side with fittings for a peristaltic pump or for sealing, (d) front view. The cell was designed and fabricated at the Paul Scherrer Institute as part of this work. 118

- Fig. 5.8 (a) Reference spectra for Ta<sup>5+</sup> oxide and oxynitride powders, (b) *operando* Ta measurements for STON thin film, (c) reference spectra for Sr<sup>2+</sup> containing powders, (d) *operando* Sr measurements. The *operando* characterisations were performed during the chronoamperometry (1 hour) measurements, with stepped applied potential. The error bars included in the magnified insert correspond to  $\pm 0.1$  eV. 119
- Fig. 5.9 (a) schematic of the experiment, (b) chronoamperometry measurements performed at 1.1 V, 1.3 V and 1.5V vs. RHE for 60 minutes under chopped illumination with 60 second periods, (c) phase resolved spectra ( $\phi$ PSD= 0° - 345°) obtained from the modulation experiment measured at 1.1 V at the Sr K edge, (d) phase resolved spectra for Sr K edge measured at 1.1 V, 1.3 V and 1.5 V vs. RHE shown in dark grey, light grey and black respectively, (e) average of spectra recorded under illumination and under dark conditions, with the difference and PSD spectra at each potential. 124
- Fig. 5.10 Ta L<sub>3</sub> spectra recorded under illumination and under dark conditions. The Ta signal does not exhibit any changes larger than the noise of the experiments. 131
- Fig. 5.11 (a-r) STON before and after PEC, (s-t) LTON N1s before and after PEC, respectively. Reference values for binding energies given in supplementary tables. 132
- Fig. 6.1 (a) XRD for 001 and 011 orientated STON oxynitride thin films, (b) the PEC performance of the two orientated film, with and without a NiO co-catalyst. 147

## List of Tables

Table 1	Compositions of LTON thin films determined by RBS and ERDA.	60
Table 2	Pre edge peak positions and assignments for TiO <sub>2</sub> and LTON.	71
Table 3	Neutron reflectometry layer fitting model before PEC	82
Table 4	Neutron reflectometry layer fitting model after PEC	82
Table 5	Peak fitting parameters for O1s before and after PEC	101
Table 6	Literature sourced XPS data for O 1s.	101
Table 7	Peak fitting parameters for N1s before and after PEC	102
Table 8	Literature sourced XPS data for N1s.	102
Table 9	Peak fitting parameters for Ti2p before and after PEC	103
Table 10	Literature sourced XPS data for Ti 2p <sub>3/2</sub> .	103
Table 11	Peak fitting parameters for La 3d before and after PEC	104
Table 12	Peak fitting parameters for La 4d before and after PEC	104
Table 13	Peak fitting parameters for La 4p before and after PEC	104
Table 14	Ion Beam Analysis for STON films	133
Table 15	Literature sourced XPS data for Ta 4f <sub>7/2</sub>	133
Table 16	Literature sourced XPS data for Ta 4f <sub>5/2</sub> .	134
Table 17	Literature sourced XPS data for Ta 4p <sub>3/2</sub> .	134
Table 18	Sr 3p Peak Fit Before PEC	134
Table 19	Sr 3p Peak Fit After PEC	135
Table 20	Sr 3d Peak Fit Before PEC	135
Table 21	Sr 3d Peak Fit After PEC	135
Table 22	Sr 4p and O 2s Peak Fit Before PEC	136
Table 23	Sr 4p and O 2s Peak Fit After PEC	136

Table 24	Sr 4s and Ta 5p Peak Fit Before PEC	136
Table 25	Sr 4s and Ta 5p Peak Fit After PEC	137
Table 26	Ta 4d Peak Fit Before PEC	137
Table 27	Ta 4d Peak Fit After PEC	137
Table 28	Ta 4f Peak Fit Before PEC	138
Table 29	Ta 4f Peak Fit After PEC	138
Table 30	C 1s Peak Fit Before PEC	138
Table 31	C 1s Peak Fit After PEC	139
Table 32	O 1s Peak Fit Before PEC	139
Table 33	O 1s Peak Fit After PEC	139
Table 34	N 1s and Ta 4p Peak Fit Before PEC	140
Table 35	N 1s and Ta 4p Peak Fit After PEC	140

## Acknowledgements

For the last three and a half years, I have had the wonderful opportunity to conduct my Ph.D. in the Thin Films and Interfaces group, led by Professor Thomas Lippert at the Paul Scherrer Institute (PSI) and the Laboratory of Inorganic Chemistry (LAC) at ETH Zürich (ETH). This project was also part of a PSI CROSS collaboration; therefore, my special thanks go to the PSI as well as, to all of the co-proposers and their respective teams. Without your effort, this project would likely, not have been viable. The co-proposers are as follows:

- Dr. Daniele Pergolesi (NUM/ENE),
- Dr. Maarten Nachtegaal (PSD/*SuperXAS*),
- Dr. Jochen Stahn (NUM/AMOR)
- Dr. Davide Ferri (ENE).

During this time, as part of my education and work, I have had the chance to meet and, get acquainted with numerous, talented and interesting people. Who, have helped and supported me during my project and education, resulting in this work. Therefore, my special thanks go to and, in no particular order:

Prof. Dr. Thomas Lippert (PSI/ETH) for their supervision of my PhD and to both, Prof. Dr. Thomas J. Schmidt (PSI/ETH) and Prof. Dr. Gunnar Jeschke (ETH) for taking the time to be my co-examiners and to review my thesis. Unfortunately, due to the current social restrictions at the time of writing this, I will have to delay an Apéro, so I can pass on my gratitude in person.

Dr. Adam H. Clark (PSD/*SuperXAS*), regardless that we share the same nationality, it was a pleasure to get to know you. I believe that you are a great asset to PSI and the wider XAS community, which has shown by your help and support with the GIXAS measurements and data

analysis included in this work, as well as your support with many other projects which you collaborate on. I wish you all the best on your recent promotion and future at PSI.

Dr. Olga. V. Safonova (PSD/SuperXAS), for your support with the experimental set up, data analysis and discussions. Also, for your help with my education during the Cook and Look: Synchrotron Techniques, ETH Zürich course held at PSI.

Dr. Maarten Nachtegaal (PSD/SuperXAS), we may not have always been on the same page at times, however, in the end, I think we have had a fruitful and interesting collaboration during these last few years. I will be forever grateful for your support during this time, your contribution to this work and my education with respect to XAS. It seems a lifetime ago that I attended the Cook and Look course, which piqued my curiosity, transitioning from the classroom to application. You have a good team and I wish you all well for the future.

Dr. Jochen Stahn (NUM/AMOR), for your assistance with respect to the neutron reflectometry measurements, data analysis and discussion included in this work, carried out at AMOR (SINQ-PSI). I also appreciate your personal time and sharing your expertise as part of my education and enabling this collaboration before the shutdown and upgrade of the SINQ. I look forward to hearing about the emerging science coming from the SINQ now operation is making good progress.

Dr. Davide Ferri (ENE), I will be eternally grateful for your personal recommendation, without which, this would not have been possible for me. I definitely owe you a nice bottle of French Wine :). I also wish you and Dr. Thibault Fovanna congratulations on your success as part of the CROSS project and his PhD defence. I have a sneaking suspicion that Thibault would not object to French wine :)



I would also like to pass my thanks to Andreas Keller, Marcel Locher and Patrick Widmann of the PSI workshop east. Who were patient with my attempts to converse in 1/3 High German, 1/3 Swiss German and 1/3 English and helped enormously with the design modifications and technical parts related to the realisation of the *operando* cell. Patrick has since finished his apprenticeship at PSI and, I wish him all the best in his bright future.

I would also like to thank every member of the thin films and interfaces group (past and present); this is not a final goodbye, but a closing of a chapter for myself. This year (2020) has been a difficult and trying year for all and, due to remote work; we have not been as close, as in previous years, unfortunately. Therefore, I have not had the opportunity to fully welcome and get to know the new members (Andrew and Jan); I wish you both well on your ambitious projects and look forward to reading about it in the near future.

To Zahra, I cannot thank you enough for your help and support on various parts of this project and I hope that you benefit from our collaboration as much as I have from you. I wish you all the best with your remaining time at PSI. I have no concerns that you will not be able to make a success of your project.

To Christof, even though our projects did not overlap directly, I will always be grateful for your support in the group. Whether, helping with equipment, lab set ups and discussions regarding science or more relaxing and equally interesting topics.

To Thomas and Daniele, thank you for both believing in me and providing me with this opportunity. I hope that I have been an asset to the group and not too taxing to manage. I will be eternally grateful for your support over the last 3.5 years and even though some times were extremely hard, frustrating and even de-motivating during my project, I will cherish every moment and appreciate both of your support.

To all the current members of the thin films and interfaces group for their continuous support, helping hands in our laboratories and the relaxed environments during our coffee breaks, where we could unwind and get to know one another better, separate from work. In alphabetic order:

Andrew, Banani; Christof, Daniele; Elisa, Eric; Gesara, Jan; Luca, Natacha, Thomas and Zahra.

- Best of luck for the remainder of your time at PSI.

Previous members: Alan, Alexandra, Fatima, Maria, Marina, Valentina, Venkat, Veronica, Wenping, Xi and Xiang

– I hope you are all excelling in whichever path you chose to follow since.

This project also grew during the last 3.5 years to include further internal and external collaborators and I would like to share my appreciation:

Dr. Vladimir N. Strocov (LSC, PSI) for his support and great help with respect to the SX-ARPES measurements and discussions regarding data analysis, interpretation and general discussion. I have learnt a tremendous amount during our collaboration in this short time and look forward to the possibilities in the future.

Dr. Max Döbeli (Laboratory of Ion Beam Physics, ETH), for his work and support with respect to the Rutherford Backscattering (RBS) and Elastic Recoil Detection Analysis (ERDA) measurements for the compositions of the samples used in this work. Thank you for all your support and for introducing these topics as part of my education at ETH Zürich.

Prof. Aleksandar T. Staykov from the Kyushu University (International Institute for Carbon-Neutral Energy Research (I2CNER), Electrochemical Energy Conversion Division, Japan) for your support with respect to discussion, analysis and the theoretical DFT calculations included in this work, used to help support and bridge the gap that sometimes exists between theory and experiment. I hope things have improved in Japan since we last spoke.

Dr. Vladimir Roddatis (GFZ Postdam - Interface Geochemistry) for his support with respect to the TEM analysis included in this work. I wish you all the best with your relatively recent move to GFZ.

Lastly, but not least, my deepest gratitude belongs also to my two families. My family back in the UK and my family here in Switzerland (including my cats and dog - famous on PSI Zoom meetings). Due to the intensive nature of a Ph.D and the current climate in the year of writing this, unfortunately, I have not been able to see my family back in the UK as much as I would have liked. However, I wish you all to know (those on the continent and those not), that this was only possible due to your love and support on my way through life and during the time of my Ph.D. I may have detoured during my teens and made mistakes in life. However, I do not look back with regret. I look back with a kind of wisdom, knowing that all my life experiences have formed me into who I am now and, taught me to appreciate what is important in life.

I hope that I have been, a good son/son-in-law, partner, grandson, friend, student, colleague and pack leader (pets). As you all, have been to me.

Thank you all, CRL.

# Curriculum Vitae

Craig Richard Lawley

Born on 03.02.1988

Citizen of the United Kingdom

## Education

- 23.05.2017 – Ph.D. Laboratory of Inorganic Chemistry (LAC), Department of Chemistry and Applied Biosciences (D-CHAB), ETH Zürich and, the Thin Films and Interfaces group, Laboratory for Multiscale Materials Experiments (LMX), Paul Scherrer Institute (PSI).  
16.12.2020
- 20.09.2010 – MChem (Master of Chemistry) – Department of Chemistry at the University of Bath, United Kingdom  
30.06.2016
- 01.09.2008 – A levels (Biology, Chemistry, Physics) – Greenwich Community College, United Kingdom  
30.06.2010
- 01.09.2004 – 9 GCSEs – Bexley Grammar School, United Kingdom  
30.06.2006

## Professional Experience

- 23.05.2017 – Thin Films and Interfaces group at the Paul Scherrer Institute (PSI) – Ph.D. student, supervisor Prof. Dr. T. Lippert  
16.12.2020
- 06.2018 - ETH Zürich and PSI - Teaching assistant: “701-1336-00L Cook and Look: Synchrotron Techniques”.  
06.2018
- 09.2015 – University of Bath – Master student research project, supervisor Prof. Dr. P. Raithby  
06.2016
- 08.2015 – University of Bath – Internship: Final year B.Sc. advanced Inorganic laboratory course experiment design and Testing, Supervisor Dr. A. Buchard  
09.2015
- 06.2015 – Royal Society of Chemistry (RSC) undergraduate research bursary –  
08.2015 University of Bath, Supervisor Dr. A. Buchard

## Conference presentation contributions

Craig Lawley, Maarten Nachtegaal, Daniele Pergolesi, Thomas Lippert

*Surface sensitive X-ray absorption spectroscopy on oxynitride thin film photoanodes for visible light driven water splitting.*

EMRS 2019 Fall Meeting, Warsaw University of Technology, Warsaw, Poland

Craig Lawley, Maarten Nachtegaal, Daniele Pergolesi, Thomas Lippert

*SOIFIT: X-ray spectroscopy at the Paul Scherrer Institute*

Solid Oxide Interfaces for Faster Ion Transport (SOIFIT) 2018 Summer Meeting – Paul Scherrer Institute, Switzerland.

### Poster contributions

Craig Lawley, Wenping Si, Markus Pichler, Fatima Haydous, Uli Aschauer, Silviya Ninova, Daniele Pergolesi, Thomas Lippert.

*LaTiO<sub>x</sub>N<sub>y</sub> thin film model systems for photocatalytic water splitting: physicochemical evolution of the solid-liquid interface and the role of the crystallographic orientation*

PSI-FoKo NUM/BIO 2017 Meeting – Paul Scherrer Institute, Switzerland.

### Publications

Lawley C, Nachtegaal M, Stahn J, Roddatis V, Döbeli M, Schmidt TJ, *et al.* Examining the surface evolution of LaTiO<sub>x</sub>N<sub>y</sub> an oxynitride solar water splitting photocatalyst. *Nature Communications* 2020, **11**(1): 1178. <https://doi.org/10.1038/s41467-020-15519-y>

Craig Lawley, Arian Arab; Aleksandar Staykov, Max Döbeli; Daniele Pergolesi, Thomas Lippert; and Vladimir N. Strocov. Entitled: “*Momentum-resolved electronic structure of LaTiO<sub>x</sub>N<sub>y</sub> photocatalysts by resonant soft-X-ray ARPES*” (Manuscript in preparation).

Craig Lawley, Zahra Pourmand Tehrani, Adam H. Clark, Olga V. Safonova, Max Döbeli, Vladimir N. Strocov, Thomas J. Schmidt, Thomas Lippert, Maarten Nachtegaal and Daniele Pergolesi. Entitled: “*Protagonists and spectators during photocatalytic solar water splitting with SrTaO<sub>x</sub>N<sub>y</sub> oxynitride.*” (Under Review).

Craig Lawley, Zahra Pourmand Tehrani, Aleksandar Staykov, Jakub Szlachetko, Maarten Nachtegaal, Thomas J. Schmidt, Daniele Pergolesi, Thomas Lippert. Entitled: “From oxide to oxynitride: How nitrogen substitution determines the electronic structure. (*manuscript in preparation*)

## References

1. Hisatomi T, Domen K. Reaction systems for solar hydrogen production via water splitting with particulate semiconductor photocatalysts. *Nature Catalysis* **2**, 387-399 (2019).
2. Kim JH, Hansora D, Sharma P, Jang JW, Lee JS. Toward practical solar hydrogen production - an artificial photosynthetic leaf-to-farm challenge. *Chem Soc Rev* **48**, 1908-1971 (2019).
3. Perera F, Ashrafi A, Kinney P, Mills D. Towards a fuller assessment of benefits to children's health of reducing air pollution and mitigating climate change due to fossil fuel combustion. *Environ Res* **172**, 55-72 (2019).
4. Lei R, Feng S, Lauvaux T. Country-scale trends in air pollution and fossil fuel CO<sub>2</sub> emissions during 2001-2018: confronting the roles of national policies and economic growth. *Environmental Research Letters*, (2020).
5. Sippel S, Meinshausen N, Fischer EM, Székely E, Knutti R. Climate change now detectable from any single day of weather at global scale. *Nature Climate Change* **10**, 35-41 (2020).
6. Landrigan PJ. Air pollution and health. *The Lancet Public Health* **2**, e4-e5 (2017).
7. Tian Y, Zhao CY. A review of solar collectors and thermal energy storage in solar thermal applications. *Applied Energy* **104**, 538-553 (2013).
8. Parida B, Iniyar S, Goic R. A review of solar photovoltaic technologies. *Renewable and Sustainable Energy Reviews* **15**, 1625-1636 (2011).
9. Kim JY, Lee JW, Jung HS, Shin H, Park NG. High-Efficiency Perovskite Solar Cells. *Chem Rev* **120**, 7867-7918 (2020).
10. Montoya JH, Seitz LC, Chakhranont P, Vojvodic A, Jaramillo TF, Norskov JK. Materials for solar fuels and chemicals. *Nat Mater* **16**, 70-81 (2016).

11. Pinaud BA, *et al.* Technical and economic feasibility of centralized facilities for solar hydrogen production via photocatalysis and photoelectrochemistry. *Energy & Environmental Science* **6**, (2013).
12. Dau H, Limberg C, Reier T, Risch M, Roggan S, Strasser P. The Mechanism of Water Oxidation: From Electrolysis via Homogeneous to Biological Catalysis. *ChemCatChem* **2**, 724-761 (2010).
13. Leung DY, *et al.* Hydrogen production over titania-based photocatalysts. *ChemSusChem* **3**, 681-694 (2010).
14. *Electrolysis*. Encyclopædia Britannica (2007).
15. Zhou H, *et al.* Water splitting by electrolysis at high current densities under 1.6 volts. *Energy & Environmental Science* **11**, 2858-2864 (2018).
16. Kreysa G, Ota K-i, Savinell RF. *Encyclopedia of Applied Electrochemistry* (2014).
17. Hisatomi T, Kubota J, Domen K. Recent advances in semiconductors for photocatalytic and photoelectrochemical water splitting. *Chem Soc Rev* **43**, 7520-7535 (2014).
18. Song J, *et al.* A review on fundamentals for designing oxygen evolution electrocatalysts. *Chem Soc Rev* **49**, 2196-2214 (2020).
19. Weng SX, Chen X. A hybrid electrolyzer splits water at 0.8 V at room temperature. *Nano Energy* **19**, 138-144 (2016).
20. Tee SY, *et al.* Recent Progress in Energy-Driven Water Splitting. *Adv Sci (Weinh)* **4**, 1600337 (2017).
21. Weng B, Qi M-Y, Han C, Tang Z-R, Xu Y-J. Photocorrosion Inhibition of Semiconductor-Based Photocatalysts: Basic Principle, Current Development, and Future Perspective. *ACS Catalysis* **9**, 4642-4687 (2019).
22. Fabbri E, Schmidt TJ. Oxygen Evolution Reaction—The Enigma in Water Electrolysis. *ACS Catalysis* **8**, 9765-9774 (2018).

23. Fujishima A, Honda K. Electrochemical photolysis of water at a semiconductor electrode. *Nature* **238**, 37-38 (1972).
24. Kudo A, Miseki Y. Heterogeneous photocatalyst materials for water splitting. *Chem Soc Rev* **38**, 253-278 (2009).
25. Chen S, Wang L-W. Thermodynamic Oxidation and Reduction Potentials of Photocatalytic Semiconductors in Aqueous Solution. *Chemistry of Materials* **24**, 3659-3666 (2012).
26. Ning X, Lu G. Photocorrosion inhibition of CdS-based catalysts for photocatalytic overall water splitting. *Nanoscale* **12**, 1213-1223 (2020).
27. Sheng P, *et al.* A novel method for the preparation of a photocorrosion stable core/shell CdTe/CdS quantum dot TiO<sub>2</sub> nanotube array photoelectrode demonstrating an AM 1.5G photoconversion efficiency of 6.12%. *Journal of Materials Chemistry A* **1**, (2013).
28. Tang Y, Hu X, Liu C. Perfect inhibition of CdS photocorrosion by graphene sheltering engineering on TiO<sub>2</sub> nanotube array for highly stable photocatalytic activity. *Phys Chem Chem Phys* **16**, 25321-25329 (2014).
29. Su J, *et al.* CdTe-Based Photoanode for Oxygen Evolution from Water under Simulated Sunlight. *J Phys Chem Lett* **8**, 5712-5717 (2017).
30. Maeda K, Domen K. Oxynitride materials for solar water splitting. *MRS Bulletin* **36**, 25-31 (2011).
31. Fondriest Environmental I. "Solar Radiation and Photosynthetically Active Radiation." *Fundamentals of Environmental Measurements*. (ed<sup>^</sup>(eds) (2014).
32. Hu C, Chu K, Zhao Y, Teoh WY. Efficient photoelectrochemical water splitting over anodized p-type NiO porous films. *ACS Appl Mater Interfaces* **6**, 18558-18568 (2014).
33. Ros C, Andreu T, Morante JR. Photoelectrochemical water splitting: a road from stable metal oxides to protected thin film solar cells. *Journal of Materials Chemistry A* **8**, 10625-10669 (2020).



34. Wei Y, *et al.* Enhanced photoelectrochemical water-splitting effect with a bent ZnO nanorod photo anode decorated with Ag nanoparticles. *Nanotechnology* **23**, 235401 (2012).
35. Wick R, Tilley SD. Photovoltaic and Photoelectrochemical Solar Energy Conversion with Cu<sub>2</sub>O. *The Journal of Physical Chemistry C* **119**, 26243-26257 (2015).
36. Berglund SP, Flaherty DW, Hahn NT, Bard AJ, Mullins CB. Photoelectrochemical Oxidation of Water Using Nanostructured BiVO<sub>4</sub> Films. *The Journal of Physical Chemistry C* **115**, 3794-3802 (2011).
37. Seabold JA, Choi KS. Efficient and stable photo-oxidation of water by a bismuth vanadate photoanode coupled with an iron oxyhydroxide oxygen evolution catalyst. *J Am Chem Soc* **134**, 2186-2192 (2012).
38. Kim TW, Choi KS. Improving Stability and Photoelectrochemical Performance of BiVO<sub>4</sub> Photoanodes in Basic Media by Adding a ZnFe<sub>2</sub>O<sub>4</sub> Layer. *J Phys Chem Lett* **7**, 447-451 (2016).
39. Abdi FF, van de Krol R. Nature and Light Dependence of Bulk Recombination in Co-Pi-Catalyzed BiVO<sub>4</sub> Photoanodes. *The Journal of Physical Chemistry C* **116**, 9398-9404 (2012).
40. Fàbrega C, *et al.* Efficient WO<sub>3</sub> photoanodes fabricated by pulsed laser deposition for photoelectrochemical water splitting with high faradaic efficiency. *Applied Catalysis B: Environmental* **189**, 133-140 (2016).
41. Zheng JY, *et al.* Facile Fabrication of WO<sub>3</sub> Nanoplates Thin Films with Dominant Crystal Facet of (002) for Water Splitting. *Crystal Growth & Design* **14**, 6057-6066 (2014).
42. Su J, Feng X, Sloppy JD, Guo L, Grimes CA. Vertically aligned WO<sub>3</sub> nanowire arrays grown directly on transparent conducting oxide coated glass: synthesis and photoelectrochemical properties. *Nano Lett* **11**, 203-208 (2011).
43. Sivula K, Le Formal F, Gratzel M. Solar water splitting: progress using hematite (α-Fe<sub>2</sub>O<sub>3</sub>) photoelectrodes. *ChemSusChem* **4**, 432-449 (2011).

44. Kim JY, *et al.* Single-crystalline, wormlike hematite photoanodes for efficient solar water splitting. *Sci Rep* **3**, 2681 (2013).
45. Pena MA, Fierro JL. Chemical structures and performance of perovskite oxides. *Chem Rev* **101**, 1981-2017 (2001).
46. Santomauro FG, *et al.* Localized holes and delocalized electrons in photoexcited inorganic perovskites: Watching each atomic actor by picosecond X-ray absorption spectroscopy. *Struct Dyn* **4**, 044002 (2017).
47. Sasaki S, Prewitt CT, Bass JD, Schulze WA. Orthorhombic perovskite CaTiO<sub>3</sub> and CdTiO<sub>3</sub>: structure and space group. *Acta Crystallographica Section C Crystal Structure Communications* **43**, 1668-1674 (1987).
48. Zhou W, *et al.* Structural properties of PbVO<sub>3</sub> perovskites under hydrostatic pressure conditions up to 10.6 GPa. *J Phys Condens Matter* **24**, 435403 (2012).
49. Oka K, Koyama T, Ozaaki T, Mori S, Shimakawa Y, Azuma M. Polarization rotation in the monoclinic perovskite BiCo(1-x)Fe(x)O<sub>3</sub>. *Angew Chem Int Ed Engl* **51**, 7977-7980 (2012).
50. Guerrero A, Bisquert J. Perovskite semiconductors for photoelectrochemical water splitting applications. *Current Opinion in Electrochemistry* **2**, 144-147 (2017).
51. Khan R, *et al.* Role of perovskites as a bi-functional catalyst for electrochemical water splitting: A review. *International Journal of Energy Research* **44**, 9714-9747 (2020).
52. Li W, *et al.* Origin of Improved Photoelectrochemical Water Splitting in Mixed Perovskite Oxides. *Advanced Energy Materials* **8**, (2018).
53. Abdi M, Mahdikhah V, Sheibani S. Visible light photocatalytic performance of La-Fe co-doped SrTiO<sub>3</sub> perovskite powder. *Optical Materials* **102**, (2020).
54. Wang W, Xu M, Xu X, Zhou W, Shao Z. Perovskite Oxide Based Electrodes for High-Performance Photoelectrochemical Water Splitting. *Angew Chem Int Ed Engl* **59**, 136-152 (2020).

55. Hu Z, Lin Z, Su J, Zhang J, Chang J, Hao Y. A Review on Energy Band-Gap Engineering for Perovskite Photovoltaics. *Solar RRL* **3**, (2019).
56. Sun J, Zhong DK, Gamelin DR. Composite photoanodes for photoelectrochemical solar water splitting. *Energy & Environmental Science* **3**, (2010).
57. Fabbri E, *et al.* Dynamic surface self-reconstruction is the key of highly active perovskite nano-electrocatalysts for water splitting. *Nat Mater* **16**, 925-931 (2017).
58. Vojvodic A, Norskov JK. Optimizing perovskites for the water-splitting reaction. *Science* **334**, 1355-1356 (2011).
59. Cheng X, Kim BJ, Fabbri E, Schmidt TJ. Co/Fe Oxyhydroxides Supported on Perovskite Oxides as Oxygen Evolution Reaction Catalyst Systems. *ACS Appl Mater Interfaces* **11**, 34787-34795 (2019).
60. Aguiar R, Logvinovich D, Weidenkaff A, Rachel A, Reller A, Ebbinghaus SG. The vast colour spectrum of ternary metal oxynitride pigments. *Dyes and Pigments* **76**, 70-75 (2008).
61. Pichler M, *et al.* Determination of Conduction and Valence Band Electronic Structure of LaTiOx Ny Thin Film. *ChemSusChem* **10**, 2099-2106 (2017).
62. Haydous F, *et al.* Oxynitride Thin Films versus Particle-Based Photoanodes: A Comparative Study for Photoelectrochemical Solar Water Splitting. *ACS Applied Energy Materials* **2**, 754-763 (2019).
63. Takata T, Domen K. Development of non-oxide semiconductors as light harvesting materials in photocatalytic and photoelectrochemical water splitting. *Dalton Trans* **46**, 10529-10544 (2017).
64. Seo J, *et al.* Photoelectrochemical Water Splitting on Particulate ANbO<sub>2</sub>N (A = Ba, Sr) Photoanodes Prepared from Perovskite-Type ANbO<sub>3</sub>. *Chemistry of Materials* **28**, 6869-6876 (2016).

65. Haydous F, *et al.* Improved Photoelectrochemical Water Splitting of CaNbO<sub>2</sub>N Photoanodes by CoPi Photodeposition and Surface Passivation. *The Journal of Physical Chemistry C* **123**, 1059-1068 (2018).
66. Lawley C, *et al.* Examining the surface evolution of LaTiOxNy an oxynitride solar water splitting photocatalyst. *Nature Communications* **11**, 1178 (2020).
67. Craciun F, Lippert T, Dinescu M. Pulsed Laser Deposition: Fundamentals, Applications, and Perspectives. In: *Handbook of Laser Micro- and Nano-Engineering* (ed<sup>^</sup>(eds) (2020).
68. Stender D, *et al.* Tracing the plasma interactions for pulsed reactive crossed-beam laser ablation. *Journal of Applied Physics* **118**, (2015).
69. Willmott PR. Pulsed reactive crossed-beam laser ablation. *Appl Phys a-Mater* **69**, S437-S440 (1999).
70. Pichler M, *et al.* LaTiOxNy Thin Film Model Systems for Photocatalytic Water Splitting: Physicochemical Evolution of the Solid-Liquid Interface and the Role of the Crystallographic Orientation. *Advanced Functional Materials* **27**, (2017).
71. Le Paven-Thivet C, *et al.* Photoelectrochemical Properties of Crystalline Perovskite Lanthanum Titanium Oxynitride Films under Visible Light. *J Phys Chem C* **113**, 6156-6162 (2009).
72. Pichler M, *et al.* TiN-buffered substrates for photoelectrochemical measurements of oxynitride thin films. *Applied Surface Science* **369**, 67-75 (2016).
73. Marozau I, *et al.* Pulsed laser deposition and characterisation of perovskite-type LaTiO<sub>3-x</sub>N<sub>x</sub> thin films. *Acta Materialia* **59**, 7145-7154 (2011).
74. Davidse PD. Theory and practice of RF sputtering. *Vacuum* **17**, 139-145 (1967).
75. Xie R-J, Bert Hintzen HT, Johnson D. Optical Properties of (Oxy)Nitride Materials: A Review. *Journal of the American Ceramic Society* **96**, 665-687 (2013).

76. Moriya Y, Takata T, Domen K. Recent progress in the development of (oxy)nitride photocatalysts for water splitting under visible-light irradiation. *Coordination Chemistry Reviews* **257**, 1957-1969 (2013).
77. Minegishi T, Nishimura N, Kubota J, Domen K. Photoelectrochemical properties of LaTiO<sub>2</sub>N electrodes prepared by particle transfer for sunlight-driven water splitting. *Chemical Science* **4**, (2013).
78. Maeda K, Domen K. Photocatalytic Water Splitting: Recent Progress and Future Challenges. *The Journal of Physical Chemistry Letters* **1**, 2655-2661 (2010).
79. Damascelli A, Hussain Z, Shen ZX. Angle-resolved photoemission studies of the cuprate superconductors. *Reviews of Modern Physics* **75**, 473-541 (2003).
80. Cristea D, *et al.* Tantalum Oxynitride Thin Films: Assessment of the Photocatalytic Efficiency and Antimicrobial Capacity. *Nanomaterials (Basel)* **9**, (2019).
81. Seo J, *et al.* The effects of annealing barium niobium oxynitride in argon on photoelectrochemical water oxidation activity. *Journal of Materials Chemistry A* **7**, 493-502 (2019).
82. Hsu J-C, Lin Y-H, Wang PW. X-ray Photoelectron Spectroscopy Analysis of Nitrogen-Doped TiO<sub>2</sub> Films Prepared by Reactive-Ion-Beam Sputtering with Various NH<sub>3</sub>/O<sub>2</sub> Gas Mixture Ratios. *Coatings* **10**, (2020).
83. Powell CJ, Jablonski A, Tilinin IS, Tanuma S, Penn DR. Surface sensitivity of Auger-electron spectroscopy and X-ray photoelectron spectroscopy. *Journal of Electron Spectroscopy and Related Phenomena* **98**, 1-15 (1999).
84. Molodtsov SL, Richter M, Danzenbächer S, Wieling S, Steinbeck L, Laubschat C. Angle-Resolved Resonant Photoemission as a Probe of Spatial Localization and Character of Electron States. *Physical Review Letters* **78**, 142-145 (1997).
85. Kobayashi M, *et al.* Unveiling the impurity band induced ferromagnetism in the magnetic semiconductor (Ga,Mn)As. *Physical Review B* **89**, (2014).
86. Chikina A, *et al.* Orbital Ordering of the Mobile and Localized Electrons at Oxygen-Deficient LaAlO<sub>3</sub>/SrTiO<sub>3</sub> Interfaces. *ACS Nano* **12**, 7927-7935 (2018).

87. Maegli AE, *et al.* Perovskite-Type LaTiO<sub>2</sub>N Oxynitrides for Solar Water Splitting: Influence of the Synthesis Conditions. *Energy Procedia* **22**, 61-66 (2012).
88. Groot Fd. Multiplet effects in X-ray spectroscopy. *Coordination Chemistry Reviews* **249**, 31-63 (2005).
89. Degroot FMF, Figueiredo MO, Basto MJ, Abbate M, Petersen H, Fuggle JC. 2p X-Ray Absorption of Titanium in Minerals. *Phys Chem Miner* **19**, 140-147 (1992).
90. Krüger P. Multichannel multiple scattering calculation of L<sub>2,3</sub>-edge spectra of TiO<sub>2</sub> and SrTiO<sub>3</sub>: Importance of multiplet coupling and band structure. *Physical Review B* **81**, (2010).
91. Olson CG, Benning PJ, Schmidt M, Lynch DW, Canfield P, Wieliczka DM. Valence-band dispersion in angle-resolved resonant photoemission from LaSb. *Phys Rev Lett* **76**, 4265-4268 (1996).
92. Sun X, Wu F, Liu G, Xu X. Enabling efficient visible light photocatalytic water splitting over SrTaO<sub>2</sub>N by incorporating Sr in its B site. *Journal of Materials Chemistry A* **6**, 20760-20768 (2018).
93. Chen Y, *et al.* Segregated Chemistry and Structure on (001) and (100) Surfaces of (La<sub>1-x</sub>Sr<sub>x</sub>)<sub>2</sub>CoO<sub>4</sub> Override the Crystal Anisotropy in Oxygen Exchange Kinetics. *Chemistry of Materials* **27**, 5436-5450 (2015).
94. Kato H, Kudo A. Photocatalytic reduction of nitrate ions over tantalate photocatalysts. *Physical Chemistry Chemical Physics* **4**, 2833-2838 (2002).
95. Yuan L-D, Deng H-X, Li S-S, Wei S-H, Luo J-W. Unified theory of direct or indirect band-gap nature of conventional semiconductors. *Physical Review B* **98**, (2018).
96. Makula P, Pacia M, Macyk W. How To Correctly Determine the Band Gap Energy of Modified Semiconductor Photocatalysts Based on UV-Vis Spectra. *J Phys Chem Lett* **9**, 6814-6817 (2018).

97. Cooper JK, *et al.* Indirect Bandgap and Optical Properties of Monoclinic Bismuth Vanadate. *The Journal of Physical Chemistry C* **119**, 2969-2974 (2015).
98. Castelli IE, Pandey M, Thygesen KS, Jacobsen KW. Band-gap engineering of functional perovskites through quantum confinement and tunneling. *Physical Review B* **91**, (2015).
99. Yuan SJ, Chen JJ, Lin ZQ, Li WW, Sheng GP, Yu HQ. Nitrate formation from atmospheric nitrogen and oxygen photocatalysed by nano-sized titanium dioxide. *Nat Commun* **4**, 2249 (2013).
100. Wei L, Adamson MAS, Vela J. Ni<sub>2</sub>P-Modified Ta<sub>3</sub>N<sub>5</sub> and TaON for Photocatalytic Nitrate Reduction. *Chemnanomat* **6**, 1179-1185 (2020).
101. Dai C, Sun Y, Chen G, Fisher AC, Xu ZJ. Electrochemical Oxidation of Nitrogen towards Direct Nitrate Production on Spinel Oxides. *Angew Chem Int Ed Engl* **59**, 9418-9422 (2020).
102. Tanner PA, Duan C-K. Luminescent lanthanide complexes: Selection rules and design. *Coordination Chemistry Reviews* **254**, 3026-3029 (2010).
103. Kaya Ç, *et al.* Influence of Gallium Substitution on the Crystal and Electronic Properties of Li<sub>5</sub>Ca<sub>1-x</sub>Ga<sub>x</sub>La<sub>3</sub>Zr<sub>2</sub>O<sub>12</sub> Solid State Battery Electrolyte. *Journal of Electron Spectroscopy and Related Phenomena* **226**, 45-52 (2018).
104. Lagarde P, Flank AM, Ogasawara H, Kotani A. Resonant photoemission of La and Yb at the 3d absorption edge. *Journal of Electron Spectroscopy and Related Phenomena* **128**, 193-204 (2003).
105. Loble MW, *et al.* Covalency in lanthanides. An X-ray absorption spectroscopy and density functional theory study of LnCl<sub>6</sub>(x-) (x = 3, 2). *J Am Chem Soc* **137**, 2506-2523 (2015).
106. Wu J, *et al.* A systematic evaluation of the role of lanthanide elements in functional complex oxides; implications for energy conversion devices. *Journal of Materials Chemistry A* **6**, 11819-11829 (2018).

107. Ritzmann AM, Dieterich JM, Carter EA. Density functional theory + U analysis of the electronic structure and defect chemistry of LSCF ( $\text{La}_{0.5}\text{Sr}_{0.5}\text{Co}_{0.25}\text{Fe}_{0.75}\text{O}_{3-\delta}$ ). *Phys Chem Chem Phys* **18**, 12260-12269 (2016).
108. Lee Y-L, Morgan D. Ab initio defect energetics of perovskite (001) surfaces for solid oxide fuel cells: A comparative study of  $\text{LaMnO}_3$  versus  $\text{SrTiO}_3$  and  $\text{LaAlO}_3$ . *Physical Review B* **91**, (2015).
109. Akbay T, Staykov A, Druce J, Téllez H, Ishihara T, Kilner JA. The interaction of molecular oxygen on LaO terminated surfaces of  $\text{La}_2\text{NiO}_4$ . *Journal of Materials Chemistry A* **4**, 13113-13124 (2016).
110. Lindroos M, Sahrakorpi S, Bansil A. Matrix element effects in angle-resolved photoemission from  $\text{Bi}_2\text{Sr}_2\text{CaCu}_2\text{O}_8$ : Energy and polarization dependencies, final state spectrum, spectral signatures of specific transitions, and related issues. *Physical Review B* **65**, (2002).
111. Ninova S, Aschauer U. Anion-order driven polar interfaces at  $\text{LaTiO}_2\text{N}$  surfaces. *Journal of Materials Chemistry A* **7**, 2129-2134 (2019).
112. Yashima M, Saito M, Nakano H, Takata T, Ogisu K, Domen K. Imma perovskite-type oxynitride  $\text{LaTiO}_2\text{N}$ : structure and electron density. *Chem Commun (Camb)* **46**, 4704-4706 (2010).
113. Shi J, *et al.*  $\text{LaTiO}_2\text{N}$ - $\text{LaCrO}_3$ : continuous solid solutions towards enhanced photocatalytic  $\text{H}_2$  evolution under visible-light irradiation. *Dalton Trans* **46**, 10685-10693 (2017).
114. Ouhbi H, Aschauer U. Nitrogen Loss and Oxygen Evolution Reaction Activity of Perovskite Oxynitrides. *Acs Mater Lett* **1**, 52-57 (2019).
115. Druce J, *et al.* Surface termination and subsurface restructuring of perovskite-based solid oxide electrode materials. *Energy Environ Sci* **7**, 3593-3599 (2014).
116. Staykov A, Téllez H, Akbay T, Druce J, Ishihara T, Kilner J. Oxygen Activation and Dissociation on Transition Metal Free Perovskite Surfaces. *Chemistry of Materials* **27**, 8273-8281 (2015).



117. Rupp GM, *et al.* Surface chemistry of La<sub>0.6</sub>Sr<sub>0.4</sub>CoO<sub>3-δ</sub> thin films and its impact on the oxygen surface exchange resistance. *Journal of Materials Chemistry A* **3**, 22759-22769 (2015).
118. Ninova S, Aschauer U. Surface structure and anion order of the oxynitride LaTiO<sub>2</sub>N. *Journal of Materials Chemistry A* **5**, 11040-11046 (2017).
119. Singh RB, *et al.* Trapped state sensitive kinetics in LaTiO<sub>2</sub>N solid photocatalyst with and without cocatalyst loading. *J Am Chem Soc* **136**, 17324-17331 (2014).
120. Zhang Z, Yates JT, Jr. Band bending in semiconductors: chemical and physical consequences at surfaces and interfaces. *Chem Rev* **112**, 5520-5551 (2012).
121. Tosi E, Comedi D, Zampieri G. Band bending at the ZnO(0001)-Zn surface produced by electropositive, electronegative and atmospheric adsorbates. *Applied Surface Science* **495**, (2019).
122. Yamakata A, Kawaguchi M, Nishimura N, Minegishi T, Kubota J, Domen K. Behavior and Energy States of Photogenerated Charge Carriers on Pt- or CoO<sub>x</sub>-Loaded LaTiO<sub>2</sub>N Photocatalysts: Time-Resolved Visible to Mid-Infrared Absorption Study. *The Journal of Physical Chemistry C* **118**, 23897-23906 (2014).
123. Maeda K. Photocatalytic water splitting using semiconductor particles: History and recent developments. *Journal of Photochemistry and Photobiology C: Photochemistry Reviews* **12**, 237-268 (2011).
124. Hu C, Zhang L, Gong J. Recent progress made in the mechanism comprehension and design of electrocatalysts for alkaline water splitting. *Energy & Environmental Science* **12**, 2620-2645 (2019).
125. Strocov VN, *et al.* Soft-X-ray ARPES at the Swiss Light Source: From 3D Materials to Buried Interfaces and Impurities. *Synchrotron Radiation News* **27**, 31-40 (2014).
126. Strocov VN, *et al.* Soft-X-ray ARPES facility at the ADDRESS beamline of the SLS: concepts, technical realisation and scientific applications. *J Synchrotron Radiat* **21**, 32-44 (2014).

127. Hammer B, Hansen LB, Nørskov JK. Improved adsorption energetics within density-functional theory using revised Perdew-Burke-Ernzerhof functionals. *Physical Review B* **59**, 7413-7421 (1999).
128. Smidstrup S, *et al.* QuantumATK: an integrated platform of electronic and atomic-scale modelling tools. *J Phys Condens Matter* **32**, 015901 (2020).
129. Doumont J, Tran F, Blaha P. Limitations of the DFT-1/2 method for covalent semiconductors and transition-metal oxides. *Physical Review B* **99**, (2019).
130. Jacobs R, Booske J, Morgan D. Understanding and Controlling the Work Function of Perovskite Oxides Using Density Functional Theory. *Advanced Functional Materials* **26**, 5471-5482 (2016).
131. Doolittle LR. A Semiautomatic Algorithm for Rutherford Backscattering Analysis. *Nucl Instrum Meth B* **15**, 227-231 (1986).
132. Clemens D, Gross P, Keller P, Schlumpf N, Konnecke M. AMOR - the versatile reflectometer at SINQ. *Physica B* **276**, 140-141 (2000).
133. Schmitt J, Grunewald T, Decher G, Pershan PS, Kjaer K, Losche M. Internal Structure of Layer-by-Layer Adsorbed Polyelectrolyte Films - a Neutron and X-Ray Reflectivity Study. *Macromolecules* **26**, 7058-7063 (1993).
134. Strauß F, Jerliu B, Geue T, Stahn J, Schmidt H. Short range atomic migration in amorphous silicon. *Journal of Applied Physics* **119**, (2016).
135. Owejan JE, Owejan JP, DeCaluwe SC, Dura JA. Solid Electrolyte Interphase in Li-Ion Batteries: Evolving Structures Measured In situ by Neutron Reflectometry. *Chemistry of Materials* **24**, 2133-2140 (2012).
136. Henke BL, Gullikson EM, Davis JC. X-Ray Interactions: Photoabsorption, Scattering, Transmission, and Reflection at  $E = 50\text{-}30,000$  eV,  $Z = 1\text{-}92$ . *Atomic Data and Nuclear Data Tables* **54**, 181-342 (1993).
137. Asakura H, Shishido T, Teramura K, Tanaka T. Local structure and La L1 and L3-edge XANES spectra of lanthanum complex oxides. *Inorg Chem* **53**, 6048-6053 (2014).

138. Aritani H, Yamada H, Yamamoto T, Tanaka T, Imamura S. XANES study of Li-MgO and Li-La<sub>2</sub>O<sub>3</sub>-MgO catalysts for oxidative coupling of methane. *Journal of Synchrotron Radiation* **8**, 593-595 (2001).
139. Staykov A, Tellez H, Druce J, Wu J, Ishihara T, Kilner J. Electronic properties and surface reactivity of SrO-terminated SrTiO<sub>3</sub> and SrO-terminated iron-doped SrTiO<sub>3</sub>. *Sci Technol Adv Mater* **19**, 221-230 (2018).
140. Burriel M, *et al.* Absence of Ni on the outer surface of Sr doped La<sub>2</sub>NiO<sub>4</sub> single crystals. *Energy Environ Sci* **7**, 311-316 (2014).
141. Wu ZY, Ouyard G, Gressier P, Natoli CR. Ti and O K edges for titanium oxides by multiple scattering calculations: Comparison to XAS and EELS spectra. *Physical Review B* **55**, 10382-10391 (1997).
142. Hanley TL, Luca V, Pickering I, Howe RF. Structure of titania sol-gel films: A study by X-ray absorption spectroscopy. *J Phys Chem B* **106**, 1153-1160 (2002).
143. Rossi TC, *et al.* X-ray absorption linear dichroism at the Ti K edge of anatase TiO<sub>2</sub> single crystals. *Physical Review B* **100**, (2019).
144. Ouhbi H, Aschauer U. Water oxidation chemistry of oxynitrides and oxides: Comparing NaTaO<sub>3</sub> and SrTaO<sub>2</sub>N. *Surface Science* **677**, 258-263 (2018).
145. Das T, Nicholas JD, Qi Y. Polaron size and shape effects on oxygen vacancy interactions in lanthanum strontium ferrite. *Journal of Materials Chemistry A* **5**, 25031-25043 (2017).
146. Suhadolnik L, Lašič Jurković D, Likozar B, Bele M, Drev S, Čeh M. Structured titanium oxynitride (TiO N ) nanotube arrays for a continuous electrocatalytic phenol-degradation process: Synthesis, characterization, mechanisms and the chemical reaction micro-kinetics. *Applied Catalysis B: Environmental* **257**, (2019).
147. Avasarala B, Haldar P. Electrochemical oxidation behavior of titanium nitride based electrocatalysts under PEM fuel cell conditions. *Electrochimica Acta* **55**, 9024-9034 (2010).

148. Teterin YA, Teterin AY. Structure of X-ray photoelectron spectra of lanthanide compounds. *Russian Chemical Reviews* **71**, 347-381 (2002).
149. Sunding MF, Hadidi K, Diplas S, Løvvik OM, Norby TE, Gunnæs AE. XPS characterisation of in situ treated lanthanum oxide and hydroxide using tailored charge referencing and peak fitting procedures. *Journal of Electron Spectroscopy and Related Phenomena* **184**, 399-409 (2011).
150. Saha NC, Tompkins HG. Titanium nitride oxidation chemistry: An x-ray photoelectron spectroscopy study. *Journal of Applied Physics* **72**, 3072-3079 (1992).
151. Rodriguez JA, Jirsak T, Liu G, Hrbek J, Dvorak J, Maiti A. Chemistry of NO<sub>2</sub> on oxide surfaces: formation of NO<sub>3</sub> on TiO<sub>2</sub>(110) and NO<sub>2</sub>↔O vacancy interactions. *J Am Chem Soc* **123**, 9597-9605 (2001).
152. Esaka F, *et al.* Comparison of surface oxidation of titanium nitride and chromium nitride films studied by x-ray absorption and photoelectron spectroscopy. *Journal of Vacuum Science & Technology A: Vacuum, Surfaces, and Films* **15**, 2521-2528 (1997).
153. Lu G, Bernasek SL, Schwartz J. Oxidation of a polycrystalline titanium surface by oxygen and water. *Surface Science* **458**, 80-90 (2000).
154. Chen X, Burda C. Photoelectron Spectroscopic Investigation of Nitrogen-Doped Titania Nanoparticles. *The Journal of Physical Chemistry B* **108**, 15446-15449 (2004).
155. György E, Pérez del Pino A, Serra P, Morenza JL. Depth profiling characterisation of the surface layer obtained by pulsed Nd:YAG laser irradiation of titanium in nitrogen. *Surface and Coatings Technology* **173**, 265-270 (2003).
156. Guillot J, *et al.* Nitrogen plasma pressure influence on the composition of TiN<sub>x</sub>O<sub>y</sub> sputtered films. *Surface and Interface Analysis* **33**, 577-582 (2002).
157. Bertoti I, Mohai M, Sullivan JL, Saied SO. Surface Characterization of Plasma-Nitrided Titanium - an Xps Study. *Applied Surface Science* **84**, 357-371 (1995).
158. Mohan L, Anandan C. Effect of gas composition on corrosion behavior and growth of apatite on plasma nitrided titanium alloy Beta-21S. *Applied Surface Science* **268**, 288-296 (2013).

159. Mohan L, Anandan C, Rajendran N. Effect of plasma nitriding on structure and biocompatibility of self-organised TiO<sub>2</sub> nanotubes on Ti–6Al–7Nb. *RSC Advances* **5**, 41763-41771 (2015).
160. de Sena LA, Rocha NCC, Andrade MC, Soares GA. Bioactivity assessment of titanium sheets electrochemically coated with thick oxide film. *Surf Coat Tech* **166**, 254-258 (2003).
161. Lee B-H, Kim YD, Lee KH. XPS study of bioactive graded layer in Ti–In–Nb–Ta alloy prepared by alkali and heat treatments. *Biomaterials* **24**, 2257-2266 (2003).
162. Delegan N, Dagherir R, Drogui P, El Khakani MA. Bandgap tailoring of in-situ nitrogen-doped TiO<sub>2</sub> sputtered films intended for electrophotocatalytic applications under solar light. *Journal of Applied Physics* **116**, (2014).
163. Briggs D. Handbook of X-ray Photoelectron Spectroscopy C. D. Wanger, W. M. Riggs, L. E. Davis, J. F. Moulder and G. E. Muilenberg Perkin-Elmer Corp., Physical Electronics Division, Eden Prairie, Minnesota, USA, 1979. 190 pp. \$195. *Surface and Interface Analysis* **3**, v-v (1981).
164. Shinn ND, Tsang KL. Strain-induced surface reactivity: Low temperature Cr/W(110) nitridation. *Journal of Vacuum Science & Technology A: Vacuum, Surfaces, and Films* **9**, 1558-1562 (1991).
165. Ganguly A, Sharma S, Papakonstantinou P, Hamilton J. Probing the Thermal Deoxygenation of Graphene Oxide Using High-Resolution In Situ X-ray-Based Spectroscopies. *The Journal of Physical Chemistry C* **115**, 17009-17019 (2011).
166. Asahi R, Morikawa T, Irie H, Ohwaki T. Nitrogen-doped titanium dioxide as visible-light-sensitive photocatalyst: designs, developments, and prospects. *Chem Rev* **114**, 9824-9852 (2014).
167. Lynch J, Giannini C, Cooper JK, Loiudice A, Sharp ID, Buonsanti R. Substitutional or Interstitial Site-Selective Nitrogen Doping in TiO<sub>2</sub> Nanostructures. *The Journal of Physical Chemistry C* **119**, 7443-7452 (2015).

168. Rodriguez JA, Jirsak T, Dvorak J, Sambasivan S, Fischer D. Reaction of NO<sub>2</sub> with Zn and ZnO: Photoemission, XANES, and Density Functional Studies on the Formation of NO<sub>3</sub>. *The Journal of Physical Chemistry B* **104**, 319-328 (2000).
169. Sugai S, Watanabe H, Miki H, Kioka T, Kawasaki K. Chemisorption of No on Pd Single-Crystals Studied by Ups, Aes and Xps. *Vacuum* **41**, 90-92 (1990).
170. Zatsepin DA, *et al.* Structural defects and electronic structure of N-ion implanted TiO<sub>2</sub>: Bulk versus thin film. *Applied Surface Science* **355**, 984-988 (2015).
171. Nambu A, Graciani J, Rodriguez JA, Wu Q, Fujita E, Sanz JF. N doping of TiO<sub>2</sub>(110): photoemission and density-functional studies. *J Chem Phys* **125**, 094706 (2006).
172. Cheung SH, Nachimuthu P, Joly AG, Engelhard MH, Bowman MK, Chambers SA. N incorporation and electronic structure in N-doped TiO<sub>2</sub>(110) rutile. *Surface Science* **601**, 1754-1762 (2007).
173. Nanayakkara CE, Jayaweera PM, Rubasinghe G, Baltrusaitis J, Grassian VH. Surface photochemistry of adsorbed nitrate: the role of adsorbed water in the formation of reduced nitrogen species on alpha-Fe<sub>2</sub>O<sub>3</sub> particle surfaces. *J Phys Chem A* **118**, 158-166 (2014).
174. Breitschafter MJ, Umbach E, Menzel D. An Electron Spectroscopic Investigation of the Adsorption of No on Ni(111). *Surface Science* **109**, 493-511 (1981).
175. Jirsak T, Dvorak J, Rodriguez JA. Adsorption of NO<sub>2</sub> on Rh(111) and Pd/Rh(111): photoemission studies. *Surface Science* **436**, L683-L690 (1999).
176. Shinn ND, Tsang KL. Anomalous nitrogen-metal bonding on Cr(110) and Cr/W(110) overlayers. *Journal of Vacuum Science & Technology A: Vacuum, Surfaces, and Films* **8**, 2449-2453 (1990).
177. Chen C, Bai H, Chang C. Effect of Plasma Processing Gas Composition on the Nitrogen-Doping Status and Visible Light Photocatalysis of TiO<sub>2</sub>. *The Journal of Physical Chemistry C* **111**, 15228-15235 (2007).

178. Rodriguez JA, Jirsak T, Chaturvedi S, Dvorak J. Chemistry of SO<sub>2</sub> and NO<sub>2</sub> on ZnO(0001)-Zn and ZnO powders: changes in reactivity with surface structure and composition. *Journal of Molecular Catalysis A: Chemical* **167**, 47-57 (2001).
179. Milosev I, Strehblow HH, Navinsek B, Metikoshukovic M. Electrochemical and Thermal-Oxidation of Tin Coatings Studied by Xps. *Surface and Interface Analysis* **23**, 529-539 (1995).
180. Takata T, Pan C, Domen K. Recent progress in oxynitride photocatalysts for visible-light-driven water splitting. *Sci Technol Adv Mater* **16**, 033506 (2015).
181. Navarro Yerga RM, Alvarez Galvan MC, del Valle F, Villoria de la Mano JA, Fierro JL. Water splitting on semiconductor catalysts under visible-light irradiation. *ChemSusChem* **2**, 471-485 (2009).
182. Zhong Y, *et al.* Enhanced Water-Splitting Performance of Perovskite SrTaO<sub>2</sub>N Photoanode Film through Ameliorating Interparticle Charge Transport. *Advanced Functional Materials* **26**, 7156-7163 (2016).
183. Wang Y, Wei S, Xu X. SrTaO<sub>2</sub>N-CaTaO<sub>2</sub>N solid solutions as efficient visible light active photocatalysts for water oxidation and reduction. *Applied Catalysis B: Environmental* **263**, (2020).
184. Kawashima K, *et al.* Perovskite Sr<sub>1-x</sub>BaxW<sub>1-y</sub>Tay(O,N)<sub>3</sub>: synthesis by thermal ammonolysis and photocatalytic oxygen evolution under visible light. *Materials for Renewable and Sustainable Energy* **6**, (2017).
185. Cai Z, Kubicek M, Fleig J, Yildiz B. Chemical Heterogeneities on La<sub>0.6</sub>Sr<sub>0.4</sub>CoO<sub>3-δ</sub> Thin Films—Correlations to Cathode Surface Activity and Stability. *Chemistry of Materials* **24**, 1116-1127 (2012).
186. Bucher E, Sitte W, Klauser F, Bertel E. Oxygen exchange kinetics of La<sub>0.58</sub>Sr<sub>0.4</sub>Co<sub>0.2</sub>Fe<sub>0.8</sub>O<sub>3</sub> at 600°C in dry and humid atmospheres. *Solid State Ionics* **191**, 61-67 (2011).
187. Wang F, *et al.* Recent advances in transition-metal dichalcogenide based nanomaterials for water splitting. *Nanoscale* **7**, 19764-19788 (2015).

188. Wang H, *et al.* Mechanisms of Performance Degradation of (La,Sr)(Co,Fe)O<sub>3-δ</sub> Solid Oxide Fuel Cell Cathodes. *Journal of The Electrochemical Society* **163**, F581-F585 (2016).
189. Opitz AK, *et al.* The Chemical Evolution of the La<sub>0.6</sub>Sr<sub>0.4</sub>CoO<sub>3-δ</sub> Surface Under SOFC Operating Conditions and Its Implications for Electrochemical Oxygen Exchange Activity. *Top Catal* **61**, 2129-2141 (2018).
190. Koo B, Kim K, Kim JK, Kwon H, Han JW, Jung W. Sr Segregation in Perovskite Oxides: Why It Happens and How It Exists. *Joule* **2**, 1476-1499 (2018).
191. Pramana SS, *et al.* Crystal structure and surface characteristics of Sr-doped GdBaCo<sub>2</sub>O<sub>6-δ</sub> double perovskites: oxygen evolution reaction and conductivity. *Journal of Materials Chemistry A* **6**, 5335-5345 (2018).
192. Mullica DF, Lok CK, Perkins HO, Young VV. X-ray photoelectron final-state screening in La(OH)<sub>3</sub>: A multiplet structural analysis. *Phys Rev B Condens Matter* **31**, 4039-4042 (1985).
193. Robin A. Corrosion behaviour of tantalum in sodium hydroxide solutions. *Journal of Applied Electrochemistry* **33**, 37-42 (2003).
194. Paek S-M, Kim Y-I. Ta L<sub>3</sub>-edge XANES study of perovskite oxynitrides ATaO<sub>2</sub>N (A=Ca, Sr, Ba). *Journal of Alloys and Compounds* **587**, 251-254 (2014).
195. Ibidunni AO, Masaitis RL, Opila RL, Davenport AJ, Isaacs HS, Taylor JA. Characterization of the Oxidation of Tantalum Nitride. *Surface and Interface Analysis* **20**, 559-564 (1993).
196. Wu TS, *et al.* Correlation between oxygen vacancies and magnetism in Mn-doped Y<sub>2</sub>O<sub>3</sub> nanocrystals investigated by defect engineering techniques. *Applied Physics Letters* **101**, (2012).
197. Mahmood A, *et al.* Cation effect on electronic, optical and thermoelectric properties of perovskite oxynitrides: Density functional theory. *Materials Science in Semiconductor Processing* **107**, (2020).



198. Greigor RB, Pingitore NE, Jr., Lytle FW. Strontianite in coral skeletal aragonite. *Science* **275**, 1452-1454 (1997).
199. Farges F. Coordination of Ti in crystalline and glassy fresnoites: A high-resolution XANES spectroscopy study at the Ti K-edge. *J Non-Cryst Solids* **204**, 53-64 (1996).
200. Staykov A, Fukumori S, Yoshizawa K, Sato K, Ishihara T, Kilner J. Interaction of SrO-terminated SrTiO<sub>3</sub> surface with oxygen, carbon dioxide, and water. *Journal of Materials Chemistry A* **6**, 22662-22672 (2018).
201. Lee J, Lu WD, Kioupakis E. Electronic and optical properties of oxygen vacancies in amorphous Ta<sub>2</sub>O<sub>5</sub> from first principles. *Nanoscale* **9**, 1120-1127 (2017).
202. Wen X, *et al.* Defect trapping states and charge carrier recombination in organic-inorganic halide perovskites. *Journal of Materials Chemistry C* **4**, 793-800 (2016).
203. Abe H, *et al.* Improving the quality of XAFS data. *J Synchrotron Radiat* **25**, 972-980 (2018).
204. Ferri D, Newton MA, Nachtegaal M. Modulation Excitation X-Ray Absorption Spectroscopy to Probe Surface Species on Heterogeneous Catalysts. *Topics in Catalysis* **54**, 1070-1078 (2011).
205. Chiarello GL, Ferri D. Modulated excitation extended X-ray absorption fine structure spectroscopy. *Phys Chem Chem Phys* **17**, 10579-10591 (2015).
206. König CFJ, van Bokhoven JA, Schildhauer TJ, Nachtegaal M. Quantitative Analysis of Modulated Excitation X-ray Absorption Spectra: Enhanced Precision of EXAFS Fitting. *The Journal of Physical Chemistry C* **116**, 19857-19866 (2012).
207. Nachtegaal M, Müller O, König C, Frahm R. QEXAFS: Techniques and Scientific Applications for Time-Resolved XAS. In: *X-Ray Absorption and X-Ray Emission Spectroscopy* (ed<sup>^</sup>(eds Bokhoven JAV, Lamberti C). John Wiley & Sons (2016).
208. Baurecht D, Fringeli UP. Quantitative modulated excitation Fourier transform infrared spectroscopy. *Review of Scientific Instruments* **72**, 3782-3792 (2001).

209. Urakawa A, Bürgi T, Baiker A. Sensitivity enhancement and dynamic behavior analysis by modulation excitation spectroscopy: Principle and application in heterogeneous catalysis. *Chemical Engineering Science* **63**, 4902-4909 (2008).
210. Yoshida H, Nonoyama S, Hattori YYT. Quantitative Determination of Platinum Oxidation State by XANES Analysis. *Phys Scripta*, (2005).
211. Fabbri E, Habereder A, Waltar K, Kötz R, Schmidt TJ. Developments and perspectives of oxide-based catalysts for the oxygen evolution reaction. *Catal Sci Technol* **4**, 3800-3821 (2014).
212. Zhang P, Zhang J, Gong J. Tantalum-based semiconductors for solar water splitting. *Chem Soc Rev* **43**, 4395-4422 (2014).
213. Deng X, Tüysüz H. Cobalt-Oxide-Based Materials as Water Oxidation Catalyst: Recent Progress and Challenges. *ACS Catalysis* **4**, 3701-3714 (2014).
214. May KJ, *et al.* Influence of Oxygen Evolution during Water Oxidation on the Surface of Perovskite Oxide Catalysts. *The Journal of Physical Chemistry Letters* **3**, 3264-3270 (2012).
215. Strocov VN, *et al.* High-resolution soft X-ray beamline ADDRESS at the Swiss Light Source for resonant inelastic X-ray scattering and angle-resolved photoelectron spectroscopies. *J Synchrotron Radiat* **17**, 631-643 (2010).
216. Clark AH, Imbao J, Frahm R, Nachtegaal M. ProQEXAFS: a highly optimized parallelized rapid processing software for QEXAFS data. *Journal of Synchrotron Radiation* **27**, 551-557 (2020).
217. Ravel B, Newville M. ATHENA, ARTEMIS, HEPHAESTUS: data analysis for X-ray absorption spectroscopy using IFEFFIT. *Journal of Synchrotron Radiation* **12**, 537-541 (2005).
218. Newville M. Larch: An Analysis Package for XAFS and Related Spectroscopies. *Journal of Physics: Conference Series* **430**, (2013).
219. Gruzalski GR, Zehner DM. Defect states in substoichiometric tantalum carbide. *Phys Rev B Condens Matter* **34**, 3841-3848 (1986).

220. Badrinarayanan S, Sinha S. X-ray photoelectron spectroscopy studies of the reaction of N<sup>+</sup>2-ion beams with niobium and tantalum metals. *Journal of Applied Physics* **69**, 1141-1146 (1991).
221. van der Veen JF, Himpsel FJ, Eastman DE. Chemisorption-induced 4f-core-electron binding-energy shifts for surface atoms of W(111), W(100), and Ta(111). *Physical Review B* **25**, 7388-7397 (1982).
222. Thomas JH, Hammer LH. A Photoelectron Spectroscopy Study of CF<sub>4</sub> / H<sub>2</sub> Reactive Ion Etching Residue on Tantalum Disilicide. *Journal of The Electrochemical Society* **136**, 2004-2010 (1989).
223. Wagner CD, Joshi A. The Auger Parameter, Its Utility and Advantages - a Review. *Journal of Electron Spectroscopy and Related Phenomena* **47**, 283-313 (1988).
224. Baba Y, Sasaki TA, Takano I. Preparation of nitride films by Ar<sup>+</sup>-ion bombardment of metals in nitrogen atmosphere. *Journal of Vacuum Science & Technology A: Vacuum, Surfaces, and Films* **6**, 2945-2948 (1988).
225. DeLouise LA. Investigation of the chemical mechanisms of Ta(110) /Ta(110)-suboxide etch selectivity using Cl<sub>2</sub> molecular beams. *Surface Science* **324**, 233-248 (1995).
226. Prieto P, Galan L, Sanz JM. Changes Induced in the Secondary-Electron Emission Properties of Tantalum Nitride by Ar<sup>+</sup> Bombardment and Oxygen Exposure. *Applied Surface Science* **70-1**, 186-190 (1993).
227. Chun WJ, *et al.* Conduction and valence band positions of Ta<sub>2</sub>O<sub>5</sub>, TaON, and Ta<sub>3</sub>N<sub>5</sub> by UPS and electrochemical methods. *J Phys Chem B* **107**, 1798-1803 (2003).
228. Ho SF, Contarini S, Rabalais JW. Ion-Beam-Induced Chemical-Changes in the Oxyanions (MO<sub>y</sub><sup>n-</sup>) and Oxides (MO<sub>x</sub>) Where M = Cr, Mo, W, V, Nb, and Ta. *J Phys Chem-Us* **91**, 4779-4788 (1987).
229. Yang X, *et al.* Tantalum Nitride Electron-Selective Contact for Crystalline Silicon Solar Cells. *Advanced Energy Materials* **8**, (2018).

230. Sarma DD, Rao CNR. XPS Studies of Oxides of Second- and Third-Row Transition Metals Including Rare Earths. *Journal of Electron Spectroscopy and Related Phenomena* **20**, 25-45 (1980).
231. Khan S, *et al.* Structural, optical and photoelectrochemical characterizations of monoclinic Ta<sub>3</sub>N<sub>5</sub> thin films. *Phys Chem Chem Phys* **17**, 23952-23962 (2015).
232. Ishihara A, Doi S, Mitsushima S, Ota K-i. Tantalum (oxy)nitrides prepared using reactive sputtering for new nonplatinum cathodes of polymer electrolyte fuel cell. *Electrochimica Acta* **53**, 5442-5450 (2008).
233. Yang X, *et al.* Controlled nitridation of tantalum (oxy)nitride nanoparticles towards optimized metal-support interactions with gold nanocatalysts. *RSC Advances* **5**, 89282-89289 (2015).
234. Narkeviciute I, Jaramillo TF. Effects of Ta<sub>3</sub>N<sub>5</sub> Morphology and Composition on the Performance of Si-Ta<sub>3</sub>N<sub>5</sub> Photoanodes. *Solar RRL* **1**, (2017).
235. Rodgers JD, Sundaram VS, Kleiman GG, Castro SGC, Douglas RA, Peterlevitz AC. High resolution study of the M45N67N67 and M45N45N67 Auger transitions in the 5d series. *Journal of Physics F: Metal Physics* **12**, 2097-2102 (1982).
236. Lamour P, *et al.* Direct measurement of the nitrogen content by XPS in self-passivated Ta<sub>x</sub>N<sub>x</sub> thin films. *Surface and Interface Analysis* **40**, 1430-1437 (2008).
237. Alishahi M, *et al.* Structural properties and corrosion resistance of tantalum nitride coatings produced by reactive DC magnetron sputtering. *RSC Advances* **6**, 89061-89072 (2016).
238. Zaman A, Meletis E. Microstructure and Mechanical Properties of TaN Thin Films Prepared by Reactive Magnetron Sputtering. *Coatings* **7**, (2017).
239. Fu H, Zhang S, Zhang L, Zhu Y. Visible-light-driven NaTaO<sub>3</sub>-xN<sub>x</sub> catalyst prepared by a hydrothermal process. *Materials Research Bulletin* **43**, 864-872 (2008).
240. Shi X, Ma D, Ma Y, Hu A. N-doping Ta<sub>2</sub>O<sub>5</sub> nanoflowers with strong adsorption and visible light photocatalytic activity for efficient removal of methylene blue. *Journal of Photochemistry and Photobiology A: Chemistry* **332**, 487-496 (2017).



